Growth and structural characterization of III-V semiconductor nanowires

Von der Fakultät für Mathematik, Informatik und Naturwissenschaften der RWTH Aachen University zur Erlangung des akademischen Grades eines Doktors der Naturwissenschaften genehmigte Dissertation

vorgelegt von

Master of Science

Torsten Rieger

aus Hamburg, Deutschland

Berichter: Universitätsprofessor Dr. rer. nat. D. Grützmacher
Universitätsprofessor Dr. rer. nat. M. Morgenstern

Tag der mündlichen Prüfung: 11. September 2015

Rieger, Torsten:
Growth and structural characterization of III-V semiconductor nanowires
PhD thesis, 2015
carried out at the Forschungszentrum Jülich GmbH, Peter Grünberg Institute 9.

Declaration of originality

I certify that the work in this thesis has not previously been submitted for a degree nor has it been submitted as part of requirements for a degree except as fully acknowledged within the text.
I also certify that the thesis has been written by me. Any help that I have received in my research work and the preparation of the thesis itself has been acknowledged. In addition, I certify that all information sources and literature used are indicated in the thesis.

Jülich, 1st December 2015

Contents

Abstract

In this thesis, the growth and structural properties of III-V semiconductor nanowires and nanowire heterostructures are studied. These nanowires represent structures suitable for both fundamental physics and applications in electronic devices such as (tunnel) field effect transistors. The III-V nanowires are grown with molecular beam epitaxy, high κ dielectric layers are deposited conformally around the nanowires by atomic layer deposition. The morphological and structural characteristics of the obtained structures are analyzed by scanning and transmission electron microscopy as well as x-ray diffraction.
InAs nanowires are grown via two different growth mechanisms on both GaAs and Si (111) substrates. The growth proceeds either in the vapor-liquid-solid mechanism involving a liquid In droplet or via the vapor-solid growth mechanism without the use of any catalyst particle. A thorough analyzes of the impact of the substrate preparation on the nanowire growth is conducted and optimal parameters for the *in situ* and *ex situ* substrate preparations are identified. The vapor-solid grown InAs NWs exhibit a high density of stacking defects while the growth via the vapor-liquid-solid mechanism results in zinc blende twinning super lattices with a short wurtzite segment below the catalyzing In droplet. This wurtzite segment is attributed to a nucleation at the triple phase line between the vapor, the liquid droplet and the solid crystal. After developing a kinetic model for the presence of the wurtzite phase below the droplet, it becomes possible to include wurtzite segments of various lengths in GaAs and InAs nanowires grown via the vapor-liquid-solid mechanism.
The growth of InAs and GaAs nanowires is successfully transferred to Si (100) substrates applying a texturing process to the Si substrate. This produces pyramids bound by {111} facets. An alignment of the pyramids with respect to the effusion cells allows us to control the nanowire growth direction and to study the impact of the growth parameters within a single growth experiment. Furthermore, the textured substrates enable a simultaneous integration of GaAs and InAs nanowires on the very same sample.
Nanowire heterostructures are investigated by means of almost lattice matched combinations (InAs, GaSb and AlSb) as well as highly lattice mismatched heterostructures (GaAs/InAs and GaAs/InSb). The latter exhibit a lattice mismatch of 7% and 14%, respectively, resulting in the presence of misfit dislocations already for very thin shells. For zinc blende core-shell nanowires, three types of dislocations are identified: perfect dislocation, Frank partial dislocations and Shockley partial dislocations. Contrary, for the wurtzite core-shell segments only Frank partial dislocations are observed. GaAs/InAs core-shell NWs exhibit a pronounced morphological characteristic at the nanowire tip: the absence of the growth of the InAs shell. This is correlated with the presence of the wurtzite crystal phase. In combination with the control of the crystal phases in GaAs nanowires, we study the growth of the InAs shell in the vicinity of the wurtzite segment. A model is developed to describe the absence of the InAs shell on wurtzite GaAs and the impact of stacking faults and twin boundaries on the growth. GaAs/InSb heterostructure nanowires exhibit two growth regimes: an axial growth at high substrate temperatures and a radial growth at low temperatures. The axial growth is governed by the nucleation of an In droplet on the flat top facet of a GaAs nanowire stem. The radial growth evidences an additional mechanism of strain relaxation via tiled lattice planes. For both GaAs/InSb heterostructures, geometric phase analyzes reveal an abrupt and complete strain relaxation. Core-shell nanowires composed

of InAs, GaSb and AlSb are free of misfit dislocations, the shell thicknesses significantly exceed the critical thicknesses of planar heterostructures.
InAs nanowire junctions based on the combination of several individual nanowires are obtained via the growth on Si (100) substrates with V-grooves. Three basic junctions are identified: L-shaped, T-shaped and X-shaped. In the junctions, the crystal structure is modified from a stacking fault rich structure to a zinc blende crystal structure via a solid phase transformation involving Shockley partial dislocations.
A passivation of the nanowires is obtained by depositing Al_2O_3 and HfO_2 high κ dielectrics by atomic layer deposition. The mismatch in thermal expansion coefficients between the semiconductor and the Al_2O_3 induces a compressive strain in the III-V nanowire. HfO_2 covering InAs nanowires contain significant amounts of crystalline phases which are expected to influence the dielectric properties. The presence of crystalline phases is suppressed by laminate structures based on Al_2O_3 and HfO_2.

Kurzfassung

In dieser Arbeit werden das Wachstum und die strukturellen Eigenschaften von III-V Halbleiternanodrähten und Nanodrahtheterostrukturen untersucht. Bei diesen Nanodrähten handelt es sich um Strukturen, die sowohl für fundamentale Physik als auch elektronische Bauelemente, wie (Tunnel-)Feldeffekttransistoren, geeignet sind. Die III-V Nanodrähte sind mittels Molekularstrahlepitaxie gewachsen, dielektrische Schichten sind per Atomlagenabscheidung konform um die Nanodrähte deponiert. Die morphologischen und strukturellen Eigenschaften der Strukturen werden mit Raster- und Transmissionselektronenmikroskopie sowie Röntgenbeugung untersucht. InAs Nanodrähte werden über zwei verschiedene Wachstumsmechanismen auf GaAs und Si (111) Substraten hergestellt. Das Wachstum erfolgt entweder über einen Gas-Flüssig-Fest Mechanismus mit einem flüssigen In-Tropfen oder über einen Gas-Fest Wachstumsmechanismus ohne einen Katalysator. Eine gründliche Untersuchung des Einflusses der Substratvorbereitung wird durchgeführt und die optimalen Parameter für die *in situ* und die *ex situ* Substratvorbereitung werden bestimmt. Die InAs Nanodrähte, die per Gas-Fest-Mechanismus gewachsen sind, haben eine hohe Dichte an Stapelfehlern während das Wachstum per Gas-Flüssig-Fest-Mechanismus in einer Überstruktur aus Zinkblendezwillingen sowie einem kurzen Wurtzitsegment unter dem Tropfen führt. Dieses Wurtzitsegment wird auf die Nukleation an der Dreiphasengrenze zwischen dem Gas (Vakuum), dem flüssigen Tropfen und dem Kristall zurückgeführt. Nachdem ein kinetisches Modell für das Vorhandensein der wurtzitischen Phase unter dem Tropfen entwickelt ist, können Wurtzitsegmente mit variabler Länge in GaAs und InAs Nanodrähten eingebaut werden.
Das Wachstum von InAs und GaAs Nanodrähten wird erfolgreich auf Si (100) Substrate durch Anwendung einer Substrattexturierung transferiert. Diese Texturierung erzeugt Pyramiden, die von {111} Facetten begrenzt sind. Eine Ausrichtung der Pyramiden zu den Effusionszellen ermöglicht eine Kontrolle der Wachstumsrichtung der Nanodrähte und eine Untersuchung des Einflusses der Wachstumsparameter in einem Experiment. Zusätzlich ermöglichen die texturierten Substrate die simultane Integration von GaAs und InAs Nanodrähten auf der selben Probe.
Nanodrahtheterostrukturen werden in Form der nahezu gitterangepassten Kombination aus InAs, GaSb und AlSb und Heterostrukturen mit Gitterfehlpassung (GaAs/InAs und GaAs/InSb) untersucht. Letztere haben Gitterfehlpassungen von 7% und 14%, diese erzeugen Versetzungen bereits für dünne Hüllen. In Zinkblende Kern-Hülle Nanodrähten werden drei verschiedene Versetzungen erkannt: Perfekte Versetzungen sowie Frank und Shockley Partialversetzungen. In Wurtzit Kern-Hülle Nanodrähten sind hingegen nur Frank Partialversetzungen vorhanden. GaAs/InAs Kern-Hülle Nanodrähte zeigen eine auffällige morphologische Charakteristik an der Drahtspitze: das Nichtvorhandensein der InAs Hülle. Dies ist korreliert mit der wurtzitischen Kristallstruktur. In Kombination mit der Kontrolle der Kristallphasen der GaAs Nanodrähte wird das Wachstum der InAs Hülle in der Umgebung der Wurtzitsegmente untersucht. Ein Modell wird entwickelt um das Nichtvorhandensein der InAs Hülle auf Wurtzit-GaAs und den Einfluss von Stapelfehlern und Zwillingsgrenzen auf das Wachstum zu beschreiben. Zwei Wachstumsregime für GaAs/InSb Heterostrukturnanodrähte sind vorhanden: axiales Wachstum bei hohen Temperaturen und radiales Wachstum bei niedrigen Temperaturen. Das axiale Wachstum erfolgt durch die Nukleation einen In-Tropfens auf der flachen Topfacette des GaAs Nanodrahts. Das radiale Wachstum zeigt einen zusätzlichen Mechanismus der Verspannungsrelaxation durch

verkippte Gitterebenen. Geometrische Phasenanalyse verdeutlicht eine abrupte und komplette Verspannungsrelaxation für beide GaAs/InSb Heterostrukturen. Kern-Hülle Nanodrähte aus InAs, GaSb und AlSb sind versetzungsfrei. Die Hüllendicke übersteigt die kritische Schichtdicke in planaren Heterostrukturen.
InAs Nanodrahtverbindungen, basierend auf der Kombination von mehreren individuellen Nanodrähten, werden über das Wachstum auf Si (100) Substraten mit V-Gräben erreicht. Drei grundlegende Verbindungen sind vorhanden: die L-Form, die T-Form und die X-Form. Die Kristallstruktur in den Verbindungen ist über einen Festphasenmechanismus mit Shockley Partialversetzungen von einer stapelfehlerreichen zu einer Zinkblende-Struktur modifiziert.
Eine Passivierung der Nanodrähte erfolgt durch die Abscheidung von Al_2O_3 und HfO_2 Dielektrika mittels Atomlagenabscheidung. Die unterschiedlichen thermischen Ausdehnungskoeffizienten des Halbleiters und des Al_2O_3 induzieren eine kompressive Verspannung im III-V Nanodraht. HfO_2 Hüllen um InAs Nanodrähte haben signifikante Anteile an kristallinen Phasen, welche die dielektrischen Eigenschaften beeinflussen. Die kristallinen Phasen werden durch Schichtstrukturen basierend auf Al_2O_3 und HfO_2 unterdrückt.

List Of Publications

Most of the results presented in this thesis have been published in scientific manuscripts listed below. The corresponding references used in the thesis are given in brackets.

- **T. Rieger**, M. Luysberg, T. Schäpers, D. Grützmacher, and M. I. Lepsa. *Molecular beam epitaxy growth of GaAs/InAs core-shell nanowires and fabrication of InAs nanotubes.* Nano letters, 12(11):5559-64, 2012. Ref. [262]

- A. Biermanns, **T. Rieger**, G. Bussone, U. Pietsch, D. Grützmacher, and M. Ion Lepsa. *Axial strain in GaAs/InAs core-shell nanowires.* Applied Physics Letters, 102(4):043109, 2013. Ref. [25]

- **T. Rieger**, M. I. Lepsa, T. Schäpers, and D. Grützmacher. *Controlled wurtzite inclusions in self-catalyzed zinc blende III-V semiconductor nanowires.* Journal of Crystal Growth, 378:506-510, 2013. Ref. [261]

- **T. Rieger**, D. Grützmacher, and M. I. Lepsa. *Si substrate preparation for the VS and VLS growth of InAs nanowires.* physica status solidi (RRL) - Rapid Research Letters, 7(10):840-844, 2013. Ref. [256]

- **T. Rieger**, T. Schäpers, D. Grützmacher, and M. I. Lepsa. *Crystal Phase Selective Growth in GaAs/InAs Core-Shell Nanowires.* Crystal Growth & Design, 14(3):1167-1174, 2014. Ref. [264]

- T. Wenz, M. Rosien, F. Haas, **T. Rieger**, N. Demarina, M. I. Lepsa, H. Lüth, D. Grützmacher, and T. Schäpers. *Phase coherent transport in hollow InAs nanowires.* Applied Physics Letters, 105(11):113111, 2014. Ref. [329]

- **T. Rieger**, T. Jörres, J. Vogel, A. Biermanns, U. Pietsch, D. Grützmacher, and M. I. Lepsa. *Crystallization of HfO_2 in InAs/HfO_2 core-shell nanowires.* Nanotechnology, 25(40):405701, 2014. Ref. [260]

- **T. Rieger**, D. Grützmacher, and M. I. Lepsa. *Misfit dislocation free InAs/GaSb core-shell nanowires grown by molecular beam epitaxy.* Nanoscale, 7(1):356-64, 2015. Ref. [258]

- **T. Rieger**, D. Rosenbach, G. Mussler, T. Schäpers, D. Grützmacher, and M. I. Lepsa. *Simultaneous Integration of Different Nanowires on Single Textured Si (100) Substrates.* Nano Letters, 15(3):1979-1986, 2015. Ref. [263]

- **T. Rieger**, D. Grützmacher, and M. I. Lepsa. *InAs nanowires with $Al_xGa_{1-x}Sb$ shells for band alignment engineering.* Journal of Crystal Growth, 425:80-84, 2015. Ref. [257]

- **T. Rieger**, D. Grützmacher and M.I. Lepsa, "*Abrupt axial heterostructures in self-catalyzed III-V nanowires*". Manuscript in preparation.

- **T. Rieger**, F. J. Hackemüller, P. Zellekens, T. Schäpers, D. Grützmacher and M.I. Lepsa, "*Strain relaxation in GaAs/InSb core-shell nanowires with 14% lattice mismatch*". Manuscript in preparation.

- **T. Rieger**, D. Rosenbach, S. Heedt, D. Vakulov, Th. Schäpers, D. Grützmacher and M.I. Lepsa, "*Crystal phase transformation in self-assembled InAs nanowire junctions on patterned Si substrates*". Manuscript in preparation.

Other publications

- H. Wang, J. Yuan, **T. Rieger**, P. J. van Veldhoven, P. Nouwens, T. J. Eijkemans, T. de Vries, B. Smalbrugge, E. J. Geluk, and R. Nötzel. *Distribution control of 1.55 μm InAs quantum dots down to small numbers on truncated InP pyramids grown by selective area metal organic vapor phase epitaxy.* Applied Physics Letters, 94(14):143103, 2009. Ref. [322]
- J. Yuan, H. Wang, P. J. van Veldhoven, **T. Rieger**, P. Nouwens, T. J. Eijkemans, T. de Vries, B. Smalbrugge, E. J. Geluk, and R. Nötzel. *1.55 μm InAs quantum dot distribution on truncated InP pyramids and regrowth by selective area epitaxy.* IOP Conference Series: Materials Science and Engineering, 6(1):012004, 2009. Ref. [346]
- **T. Rieger**, S. Heiderich, S. Lenk, M. I. Lepsa, and D. Grützmacher. *Ga-assisted MBE growth of GaAs nanowires using thin HSQ layer.* Journal of Crystal Growth, 353(1):39-46, 2012. Ref. [259]
- C. Blömers, **T. Rieger**, P. Zellekens, F. Haas, M. I. Lepsa, H. Hardtdegen, O. Gül, N. Demarina, D. Grützmacher, H. Lüth, and T. Schäpers. *Realization of nanoscaled tubular conductors by means of GaAs/InAs core/shell nanowires.* Nanotechnology, 24(3):035203, 2012. Ref. [28]
- F. Haas, K. Sladek, A. Winden, M. von der Ahe, T. E. Weirich, **T. Rieger**, H. Lüth, D. Grützmacher, T. Schäpers, and H. Hardtdegen. *Nanoimprint and selective-area MOVPE for growth of GaAs/InAs core/shell nanowires.* Nanotechnology, 24(8):085603, 2013. Ref. [117]
- T. Grap, **T. Rieger**, C. Blömers, T. Schäpers, D. Grützmacher, and M. I. Lepsa. *Self-catalyzed VLS grown InAs nanowires with twinning superlattices.* Nanotechnology, 24(33):335601, 2013. Ref. [109]
- C. Blömers, **T. Rieger**, T. Grap, M. Raux, M. I Lepsa, H. Lüth, D. Grützmacher, and T. Schäpers. *Gate-induced transition between metal-type and thermally activated transport in self-catalyzed MBE-grown InAs nanowires.* Nanotechnology, 24(32):325201, 2013. Ref. [27]
- A. Davydok, **T. Rieger**, A. Biermanns, M. Saqib, T. Grap, M. I. Lepsa, and U. Pietsch. *Alloy formation during molecular beam epitaxy growth of Si-doped InAs nanowires on GaAs[111]B.* Journal of Applied Crystallography, 46(4):893-897, 2013. Ref. [62]
- O. Gül, N. Demarina, C. Blömers, **T. Rieger**, H. Lüth, M. I. Lepsa, D. Grützmacher, and T. Schäpers. *Flux periodic magnetoconductance oscillations in GaAs/InAs core/shell nanowires.* Physical Review B, 89(4):045417, 2014. Ref. [111]
- A. Haab, M. Mikulics, E. Sutter, J. Jin, T. Stoica, B. Kardynal, **T. Rieger**, D. Grützmacher, and H. Hardtdegen. *Evolution and characteristics of GaN nanowires produced via maskless reactive ion etching.* Nanotechnology, 25(25):255301, 2014. Ref. [115]
- Ö. Gül, H. Y. Günel, H. Lüth, **T. Rieger**, T. Wenz, F. Haas, M. I. Lepsa, G. Panaitov, D. Grützmacher, and T. Schäpers, Giant Magnetoconductance Oscillations in Hybrid Superconductor-Semiconductor Core/Shell Nanowire Devices., Nano letters, 14(11):6269-6274, 2014. [112]
- D. Grützmacher, S. Wirths, **T. Rieger**, D. Buca, T. Stoica, M. I. Lepsa, Q.-T. Zhao, and S. Mantl. *(Keynote) Epitaxy-Based Strain-Engineering Methods for Advanced Devices.* ECS Transactions, 64(11):85-96, 2014. Ref. [110]

List Of Presentations

Conference contributions

- PDI Topical Workshop on MBE-grown Arsenide Nanowires, Berlin, Germany, September 8-9 2011; oral presentation "*Self-catalyzed growth and characterization of GaAs nanowires, InAs nanowires and their heterostructures*"

- Deutscher MBE Workshop 2011, Berlin, Germany, October 5-6 2011; oral presentation "*Droplet-assisted and droplet-free growth of InAs nanowires*"

- 17th International Winterschool on New Developments in Solid State Physics, Mauterndorf, Austria, February 13-17 2012; poster presentation "*Heterostructures in self-catalyzed III-As nanowires* "

- Jahrestagung der Deutschen Physikalischen Gesellschaft, Berlin, Germany, March 25-30 2012; oral presentation "*Growth of an InAs shell around GaAs nanowires*"; poster presentation "*Analysis of defects in GaAs/InAs core/shell nanowires by means of Moiré pattern*"; poster presentation "*Vapor-solid growth of InAs nanowires on GaAs substrates by MBE*"

- Nanowire Growth Workshop 2012, St Petersburg, Russia, June 4-6 2012, oral presentation "*Self-catalyzed MBE grown GaAs/InAs core/shell nanowires*"

- Deutscher MBE Workshop 2012, Hannover, Germany, September 11-12 2011; oral presentation "*Growth of GaAs/InAs core-shell nanowires*"

- 17th Internation Conference on Molecular Beam Epitaxy, Nara, Japan, September 23-28 2012; oral presentation "*Controlled wurtzite inclusions in self-catalyzed zinc blende III-V semiconductor nanowires* "; Best student paper award

- 17th European Molecular Beam Epitaxy workshop, Levi, Finland, March 11-13 2013; oral presentation "*Crystal phase selective growth: the way to core - axial heterostructured shell nanowires*"

- Nanowire Growth Workshop 2013, Lausanne, Switzerland, June 10-12 2013; poster presentation "*Crystal phase selective growth in GaAs/InAs core-shell nanowires*"

- 5th International Conference on One dimensional Nanomaterials, Annecy, France, September 23-26 2013; poster presentation "*High-k/III-V semiconductor nanowires investigated by means of TEM and XRD*"

- Nanowires 2013, Rehovot, Israel, November 12-15 2013; oral presentation "*Broken gap core-shell heterostructure nanowires*"; poster presentation "*Core-shell nanowire structures*"

- Dutch Nanowire Day 2014, Eindhoven, Netherlands, February 3 2014; oral presentation "*Dislocation-free type II and type III core-shell nanowires*"

- ESPS-NIS 2014, Traunkirchen, Austria, July 20-23 2014; oral presentation "*InAs nanowires on textured Si (100) substrates*"
- Nanowire Growth Workshop 2014, Eindhoven, Netherlands; August 25-27 2014; poster presentation "*MBE growth of InAs nanowires on textured Si (100) substrates*"
- Nanowires 2014, Eindhoven, Netherlands; August 27-29 2014; poster presentation "*GaAs/InSb heterostructure nanowires: axial nucleation and radial overgrowth*"
- 18th Internation Conference on Molecular Beam Epitaxy, Flagstaff, USA, September 7-12, 2014; oral presentation "*Transition from Axial Nucleation to Radial Growth in GaAs/InSb Heterostructure Nanowires*"; oral presentation "*Radial InAs-GaSb-AlSb Heterostructure Nanowires*"
- 18th European Molecular Beam Epitaxy workshop, Canazei, Italy, March 15-18 2015; oral presentation "*Self-assembled nanowire junctions on patterned Si substrates* "; poster presentation "*Axial and radial growth of GaAs/InSb heterostructure nanowires*"
- 41st Micro and nano engineering,The Hague, The Netherlands, September 21-24 2015; oral presentation "*GaAs/InSb core-shell nanowires and InSb nanotubes*"
- Nanowires, Barcelona, Spain, October 26-30 2015; oral presentation "*Self-assembled InAs nanowire junctions on Si substrates*"

Other presentations

- University of Regensburg, February 6 2013, "*Nanowire engineering: From GaAs and InAs nanowires to tubular conductors*"
- Ernst Ruska Centre, December 9 2013, "*III-V nanowires @ PGI9*"
- University of Siegen, April 17 2014, "*MBE grown type I, II and III core-shell nanowires*"

1 Chapter 1. Introduction

As a consequence of the on going demand for high speed and low power consumption electronic equipment such as mobile phones, notebooks and tablet computers, semiconductor devices have to become smaller and more efficient. Therefore, not only the lateral dimensions of the structures need to be shrinked, in the same time also material properties such as the carrier mobility and gate dielectric constant need to be improved. In the Si technology, this can be achieved by using strained Si [236] and replacing the SiO_2 with alternative gate oxides such as Al_2O_3 and HfO_2 [172]. Although long postponed, at some point, the active Si regions need to be exchanged with a different material, e.g. SiGe [331], GeSn [333] or III-V semiconductors. The last offer a large variety of materials with suitable properties for electronic and optoelectronic devices: very high electron mobilites (e.g. ~ 40000 cm^2/Vs for InAs and ~ 77000 cm^2/Vs for InSb), direct band gaps and the formation of high quality heterostructures. Integrating these materials on low cost Si substrates is mandatory, ideally on Si (100) substrates. This integration requires the growth of high quality structures on Si substrates, but only GaP and AlP are nearly lattice matched with Si. The other III-V semiconductors have significantly larger lattice constants, resulting finally in three dimensional growth (quantum dots) or dislocations [93, 294, 320]. Additionally, the binary III-V semiconductors can form anti-phase domains when grown on Si [11]. Both, dislocations and anti-phase domains can be avoided using nanostructures instead of layers. III-V nanowires (NWs) are known to grow preferentially along the [111]B direction (As-terminated) and, due to the small lateral dimensions, dislocations can be suppressed. This makes them ideal candidates for an integration of III-V semiconductors on Si substrates. NW growth was first demonstrated by Wagner and Ellis for the growth of Si NWs using Au catalysts [321]. Au is, however, not compatible with Si technology as it introduces deep level defects [35] and may be either incorporated during NW growth [14] or decorate the side facets of the NWs [34, 60]. This is the point where the Au-free growth mechanisms that are used in this thesis become important. The self-assisted NW growth has been demonstrated by Fontcuberta i Morral *et al.* for GaAs NWs [90] and Koblmüller *et al.* for InAs NWs [177]. Commonly, (111) oriented substrates are used for the NW growth. This is not the standard orientation in Si technology and apparently, growing NWs on Si (100) substrates is preferable. The NWs should then grow either along the [100] direction or along one specific and defined $\langle 111 \rangle$ direction.

Although the growth of foreign catalyst free III-V NWs dates back to 2008 [90], deep knowledge about the growth mechanism, the formation of the different crystal structures and, apart

from the GaAs/AlGaAs core-shell configuration, NW heterostructures is missing.

Several aspects regarding the growth mechanism, the NW nucleation, the effective growth front, the impact of adatom diffusion and the role of liquid group III particles on top of the NWs are under debate. Thin oxide layers providing pinholes as nucleation sites and different sticking coefficients on the oxide and the semiconductor are generally considered to be essential [90, 177, 202], but NWs grown on oxide-free surfaces have been reported as well [80]. Since the axial NW growth rate is significantly higher than the equivalent planar growth rate [55, 80, 177], the adatom migration to the NW tip represents an important contribution to the NW growth. Group III atoms have reasonable sticking coefficients (close to unity) and are typically regarded to be very mobile, the sticking coefficient of group V atoms (especially As) is low resulting in a negligible contribution of diffusion [103, 186]. The high axial growth rate of NWs is obtained not only by direct impingement and diffusion, but secondary adsorption of group III and group V atoms [103, 186, 259, 275]. Finally, the role of liquid Ga or In droplets on the top of GaAs or InAs NWs and their impact on the crystal structure is under investigation and is discussed by many groups. While some groups report the presence of droplets catalyzing the growth [90, 205], others report the absence of droplets during the entire growth [128, 270] or its presence only during NW nucleation [24, 80]. A droplet being present would represent the liquid sink for adatoms and covers the growth front of the NW. Consequently, it should not only determine the composition of ternary or quaternary alloys [125] and the incorporation of dopants [44, 85, 168] but also the crystal structure [182]. The crystal structure is one of the most studied properties of NWs since two or even more crystal structures are often present within a single NW [3, 73, 106, 134, 204, 235]. These crystal structures are zinc blende (ZB, *.. ABCABC..* stacking sequence; the thermodynamic stable crystal structure of most III-V semiconductors), wurtzite (WZ, *..ABABAB..* stacking sequence; the high pressure phase) and more complex stacking sequences such as 4H (*..ABCBABCB..*) and 6H. The crystal structures differ e.g. in lattice constants and band gap [10, 167, 189, 235, 300]. Stacking faults and twins can act as scattering centers [300] or form quantum wells with different emission energies [292]. Having knowledge about the existence and composition of the droplet and its role in defining the crystal structure is essential to fabricate phase-pure NWs or to switch between the crystal structures in a controlled manner. Crystal phase control, i.e. pure ZB NWs, was demonstrated for GaAs NWs grown from a Ga droplet [186] while the crystal structure of InAs NWs grown without a droplet remained almost unaffected by any changes of the growth parameters [283].

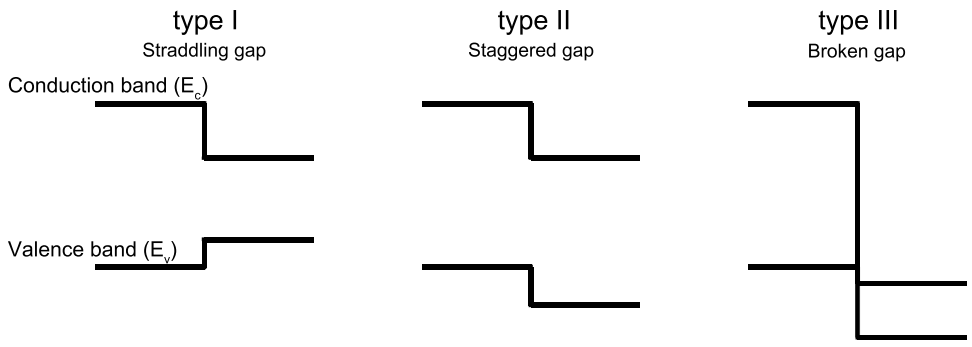

Figure 1.1.: *Schematic illustration of the three different types of band alignment in semiconductor heterostructures: straddling gap (type I), staggered gap (type II) and broken gap (type III)*

Combining different semiconductors into heterostructures enlarge the area of possible applications for NWs, but also make the growth more complex. Unlike planar structures, the NW geometry allows two different configurations of heterostructures: axial heterostructures where different semiconductors are stacked on top of each other or radial heterostructures. In the latter, one or multiple shells cover the initial NW (i.e. the NW core). Such heterostructures have already been used to demonstrate different electronic and optoelecctronic nanodevices e.g. lasers [210], solar cells [184, 341], tunneling field effect transistors (TFETs) [72], circular two dimensional electron gases [30, 284, 293] and single photon emitters [254]. In these heterostructures two properties are important: the band alignment and the strain induced by the lattice mismatch between the semiconductors. Three different band alignments are possible: the type I straddling gap, the type II staggered gap and the type III broken gap. These band alignments are displayed schematically in Fig. 1.1. The type I alignment is found for example between GaAs and $Al_xGa_{1-x}As$ [16] as well as GaAs and InAs [28, 228]. It results in the confinement of both carriers, electrons and holes, in the semiconductor with the smaller band gap. Accordingly, $Al_xGa_{1-x}As$ is used to passivate GaAs NWs and avoid non-radiative recombination at the surface of the GaAs [68]. The photoluminescence intensity is increased significantly by the presence of the $Al_xGa_{1-x}As$ shell [68, 210]. If an InAs NW is covered by GaAs, the carriers are also confined in the core and surface effects may be circumvented [164]. Embedding a small band gap semiconductor in another semiconductor with larger band gap (maintaining the type I band alignment, e.g. InAsP in InP) a quantum dot can be positioned into a NW wave guide. This configuration is used as single photon sources [254]. The staggered band gap alignment (type II) is frequently observed in NWs since it is present between the ZB and WZ crystal phases e.g. in GaAs [292] and InAs [300]. Accordingly, crystal phase control is important in order to obtain a high electron mobility in InAs NWs [300] or a clean light emission in GaAs NWs [1, 95, 123, 292]. A combination of InAs and $Al_xGa_{1-x}Sb$ with $x \geq 0.4$ can produce high electron mobilities since electrons are confined in the InAs [17, 18, 198, 310]. Moreover, InAs/$Al_xGa_{1-x}Sb$ NW heterostructures represent an interesting combination for TFETs [176]. For InAs/$Al_xGa_{1-x}Sb$ heterostructures with $x \leq 0.4$ as well as pure InAs/GaSb heterostructures, the band alignment is of type III which enables efficient band to band tunneling from the InAs conduction band to the $Al_xGa_{1-x}Sb$ valence band. TFETs are promising as future ultra low power FETs allowing a subthreshold slope below the thermal limit of 60 mV/dec [61, 146]. The InAs/$Al_xGa_{1-x}Sb$ combination is of additional high interest due its low lattice mismatch in the range between 0.6% and 1.2%. According to the classical theory for the critical thickness t_c developed by Matthews and Blakeslee [208] and People and Bean [240], t_c is $\sim$ 20 nm for planar InAs/GaSb heterostructures and $\sim$ 10 nm for InAs/AlSb. For low dimensional structures, the critical thickness is enhanced significantly since the strain accommodation is more efficient [137] and plastic deformation e.g. by a roughening of the surface can take place [2, 58, 163, 234]. The critical dimensions for single [104, 342] and double [100] axial heterostructure NWs as well as core-shell NWs [116, 252, 253] have been predicted and several NW heterostructures were investigated. These have mostly been limited to almost lattice matched systems such as GaAs/$Al_xGa_{1-x}As$ core-shell NWs [124, 210]. Self-seeded NWs with axial heterostructures were restricted to the GaAs/$In_xGa_{1-x}As$ system with low In contents ($\leq$ 4 %) [125] and GaAs/$GaAs_{1-x}Sb_x$ heterostructures with Sb contents below 30% [68, 220, 244]. These represent structures with relatively small lattice mismatches and usually exhibit graded changes in the composition. Such graded changes in the composition are also often observed in Au-catalyzed NW heterostructures [233] and are correlated with the droplet acting as a reservoir [74]. However, abrupt axial heterostructures with larger lattice mismatches have been reported in Au-catalyzed NWs as well [65, 74]. When the NW dimensions exceed the critical dimensions for coherent growth, the strain is relaxed plastically by the introduction

of misfit dislocations [163]. Information about the formation of dislocations in axial and radial heterostructures are reported only rarely [2, 64, 163].

When aimed for an integration in future devices, the electrical and optical properties of the NWs need to be reproducible and constant during operation. As shown by Blömers *et al.* [27], the conductivity of InAs NWs changes in time when stored in air or after an exposure to an electron beam. This was attributed to changes on the surfaces of the NWs such as absorbents or an increased oxidation. To avoid this, the NWs need to be passivated either with another semiconductor (e.g. GaAs NWs passivated with an $Al_xGa_{1-x}As$ shell [68]) or an oxide layer. This oxide layer can then act simultaneously as a passivation and gate dielectric in FETs. Oxide layers can be deposited by atomic layer deposition (ALD). The deposition conditions strongly influence their properties (leakage current, dielectric constant ...) and may also affect the semiconductor.

The passivation of NWs is one of the main aspects for the integration of NWs in industry. Another two are the growth on (100) Si substrates and the possibility to obtain NWs of different composition on the same sample, e.g. GaAs NWs as well as InAs NWs. The growth on (100)-oriented substrates was reported only in few publications, either by using Au catalyst particles [323] or a nanotube template [160]. NWs from different materials on the same sample have not yet been produced.
Finally, to explore new possible applications for NWs [9] or investigate novel physical phenomena [7], the NW morphology needs to be modified towards more complex structures based on several NWs forming junctions. Such complex structures are often called "nanotrees" and were obtained by depositing Au droplets on existing NWs [75, 296]. Recently, NW junctions were grown by merging two or more Au-catalyzed NWs during the growth [41, 157, 246]. NW junctions or nanotrees without the use of foreign catalyst particles have not been investigated.

1.1. Scope of this work

The objective of this thesis is to evaluate the molecular beam epitaxial growth and the structural and morphological properties of self-assisted NWs, NW heterostructures and NW junctions. This includes the preparation of silicon (111) and (100) substrates prior to the growth, the exploration of the growth parameters as well as the control of the crystal structure in the NWs. Special emphasis is given to the critical dimensions and strain relaxation in core-shell NWs composed of almost lattice matched as well as highly lattice mismatched III-V semiconductors. An additional focus lies on the deposition of high κ dielectrics, namely Al_2O_3 and HfO_2, by atomic layer deposition on III-V NWs.

Although the detailed analyzes of the impact of the growth parameters and the search for the appropriate ones is one of the most important challenges in the growth of NWs, the thesis mainly focuses on the morphological and structural characteristics of the obtained NWs. An overview of the growth parameters and substrate preparations is given in the Appendix A.1.
The thesis is structured as follows:

- The growth, deposition and characterization techniques used in this thesis are shortly described in Chapter 2.

- Chapter 3 discusses the critical thickness in planar structures and shows critical thickness maps for core-shell NWs of the semiconductor combinations used in this thesis:

GaAs/InAs, InAs/GaSb, InAs/AlSb and GaAs/InSb. The results are based on the model of Raychaudhuri and Yu [252, 253].

- In Chapter 4, the growth and structural characteristics of GaAs and InAs NWs are presented, including the vapor solid growth of InAs NWs on GaAs (111)B substrates, the investigation of necessary substrate preparations to achieve the growth of InAs NWs on Si substrates and the role of group III liquid droplets in determining the crystal structure.
- Chapter 5 is dedicated to core-shell NWs which are entirely based on group III-As materials. It presents the structural properties of lattice mismatched GaAs/InAs core-shell NWs and InAs nanotubes. Furthermore, the growth of InAs on the WZ phase of GaAs is described.
- Chapter 6 refers to heterostructure NWs containing antimony. These heterostructures are either based on InAs/$Al_xGa_{1-x}Sb$ or GaAs/InSb. For the first case, only radial heterostructures are taken into account while the second material combination is discussed for both radial and axial heterostructures.
- In Chapter 7, the growth of InAs and GaAs NWs on faceted Si (100) substrates is presented. InAs and GaAs NWs grown on textured Si substrates enable determining the impact of the fluxes on the NW density and growth rate and allow the growth of NWs from different semiconductors on the same substrate. Using V-grooves, branched InAs NWs are produced and their structural and electrical characteristics are investigated.
- High κ dielectrics covering III-V NWs are investigated in Chapter 8, focusing on the impact of the thermal mismatch between Al_2O_3 and GaAs and the structure of HfO_2 on InAs NWs.
- A summary of the achieved results together with an outlook for future work is given in Chapter 9.

Chapter 2.
2 Growth and characterization techniques

In order to grow the NWs, deposit the high κ dielectrics as well as to analyze the morphological and structural characteristics of the structures, different techniques have been used. In the following, the most relevant methods are briefly described. These are molecular beam epitaxy (MBE) for the growth of the III-V semiconductors, atomic layer deposition (ALD) for high κ dielectrics and transmission electron microscopy (TEM) used for the analyzes of the NWs. Apart from the techniques described below, mainly scanning electron microscopy (SEM) and X-ray diffraction (XRD) have been used.

2.1. Molecular beam epitaxy

The NWs presented in this thesis have been grown by molecular beam epitaxy. For the MBE growth, a growth chamber is evacuated to ultra high vacuum (UHV) and a substrate and several source materials are heated. The high purity of the sources materials in combination with the UHV results in a high purity and quality of the grown layers. An additional advantage is the low growth rate of about 1 µm/h giving the opportunity to control the thickness on the atomic layer or even below. In order to maintain the UHV conditions, the chamber is pumped using a cryo pump, an ion getter pump as well as a cryo shield. The cryo shield not only acts as a pump but also serves as a thermal isolation of the effusion cells.
For the work presented in this thesis, two MBE systems have been used. The first one, MBE1, is a *Varian GenII MBE* equipped with an As cracker, two Ga effusion cells, one In effusion cell, one Al effusion cell as wells as Si and Be cells for doping. The other system, MBE2, is also a *Varian GenII MBE* which is equipped with one As and one Sb cracker as well as Ga, In and Al effusion cells and Si and C doping cells. Both system are connected to each other via a buffer chamber having two load locks. MBE1 was used for the growth of the NWs presented in Chapters 4, 5, 7 and 8. The NWs discussed in Chapter 6 have been grown in MBE2. Ga, Al and In deposition rates are given as the planar growth rates under As rich growth conditions on GaAs (100) substrates. As and Sb fluxes correspond to the beam equivalent pressures measured at the position of the substrate. Substrate temperatures above 400°C are measured with a pyrometer while temperatures below 400°C are taken from the thermocouple.

2.2. Atomic layer deposition

To deposit very thin layers a modified chemical vapor deposition system can be used. The precursor gases are not supplied simultaneously but separately. Thus, for the deposition of a layer of composition A_nB_m, first only the precursor for the A element is provided, followed by an evacuation of the deposition chamber. Subsequently, the precursor containing the B element is offered and again the system is pumped. This sequence, the "deposition cycle", corresponds to the deposition of one layer of A_nB_m. The thickness of the deposited material is controlled by the number of repetitions of the deposition cycle. This deposition method is named atomic layer deposition (ALD). ALD is a commonly used technique to deposit high κ films such as Al_2O_3 and HfO_2 but also single elements like tungsten [174] or nickel [271] can be deposited. For the work presented in this thesis, a *SVTA NorthStar ALD* with trimethylaluminum (TMA), tetrakis(dimethylamino)hafnium (TDMAH), tetrakis(ethylmethylamino)hafnium (TEMAH) and ozone precursors was used.

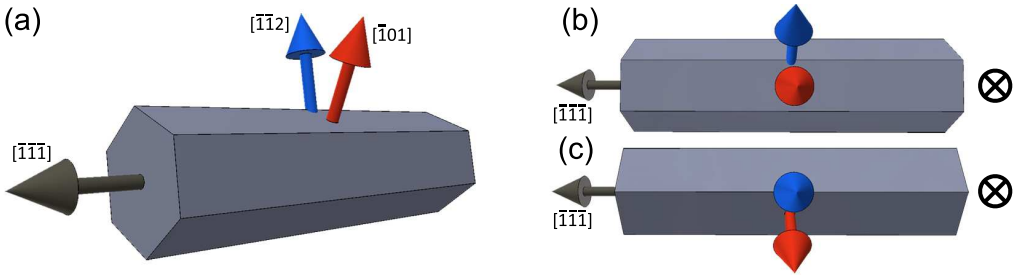

Figure 2.1.: *NW alignment with respect to the electron beam in the TEM. (a) Typical shape of the NWs. (b) Alignment to the* ⟨110⟩ *zone axis. (c) Alignment to the* ⟨211⟩ *zone axis. The direction of the electron beam is indicated by* ⊗.

2.3. Transmission electron microscopy

Analyzes of the crystal structure, structural defects (dislocations, stacking faults), NW morphology and chemical composition was performed by transmission electron microscopy. A *FEI Tecnai G2F20* located at the "Ernst Ruska Centre for Microscopy and Spectroscopy with Electrons" was used. The acceleration voltage was kept constant at 200 kV for all investigations. For the analyzes, the NWs are mechanically transferred to copper TEM grids with holey carbon films. Different modes of operation have been used: bright field imaging, selective area electron diffraction and scanning transmission electron microscopy (STEM). In the latter, high angle annular dark field (HAADF) images were acquired and energy dispersive x-ray spectroscopy (EDX) serves for the detection of the chemical composition. Selective area electron diffraction was performed on regions as small as 200 nm in diameter[1]. In general, the NWs were aligned to the ⟨110⟩ zone axis or the the ⟨211⟩ zone axis of the ZB structure[2]. Figure 2.1a schematically displays a NW with a hexagonal cross section and {110} side facets, the NW growth direction is [$\overline{111}$]B. The NWs presented in this thesis have similar side facets and the same growth direction. The two different alignments of the NW, in the ⟨110⟩ zone axis or the the ⟨211⟩ zone axis, are displayed in Fig. 2.1b,c, respectively. The directions differ by a rotation of 30° around the [$\overline{111}$]B

[1] The smallest diffraction aperture has a diameter of 200 nm.
[2] The corresponding zone axes in hexagonal notation are: ⟨$\bar{2}$110⟩ (equivalent to the cubic ⟨110⟩ zone axis) and ⟨1$\bar{1}$00⟩ (equivalent to the cubic ⟨211⟩ zone axis).

NW growth axis.

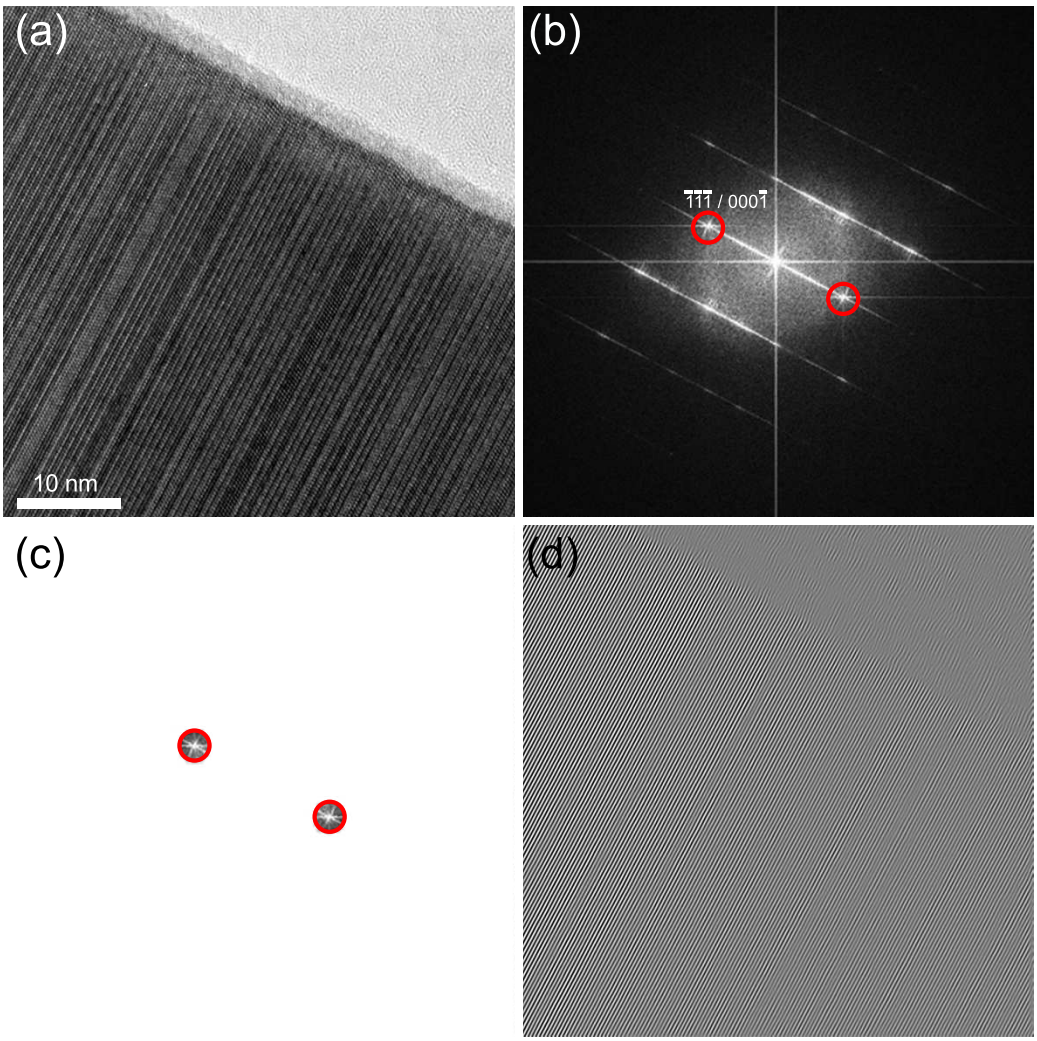

Figure 2.2.: *General procedure to obtain FFT-filtered TEM micrographs. (a) HRTEM micrograph. (b) FFT of the HRTEM micrograph depicted in (a). Red circles denote the (111) lattice planes. (c) Mask applied to the FFT shown in (b). Only the (111) reflections are maintained. (d) Inverse FFT of (c) only displaying the (111) lattice planes.*

In several cases, high resolution (HR) TEM micrographs undergo a post processing as described below.

FFT-filtered TEM images Distinct lattice planes are extracted by applying a filter to the fast Fourier transform (FFT) of the original image. The procedure is exemplary depicted in Fig. 2.2. The HRTEM image is displayed in (a). The image is taken from an InAs NW containing both crystal phases, i.e. WZ and ZB, and several stacking faults (see Sec. 4.1). The zone axis is $\langle 110 \rangle$. The FFT of the image evidences diffraction spots and streaks (Fig. 2.2(b)). The diffraction spots belonging to the $(\overline{111})$ (ZB notation) or $(000\overline{1})$ (WZ notation) lattice planes are marked by red circles. Applying a mask maintaining only these spots generates the image displayed in Fig. 2.2(c). The inverse FFT of this filtered image produces an image only containing the $(\overline{111})$ / $(000\overline{1})$ lattice planes, it is the FFT-filtered TEM micrograph shown in Fig. 2.2(d). The

technique is also often referred to as "Bragg filtering". In these images, misfit dislocation are easily identified as terminating lattice planes. The scale bar of the HRTEM image is always also valid for the FFT-filtered image.

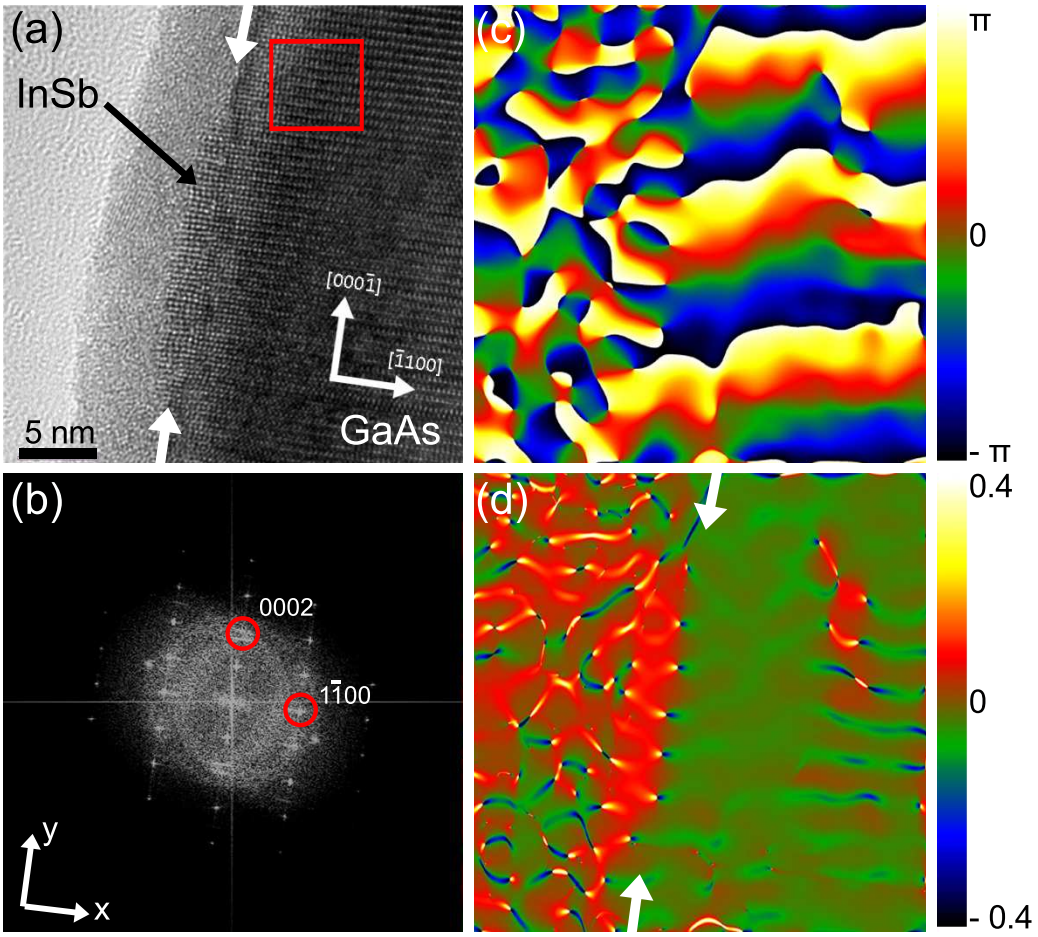

Figure 2.3.: *Procedure to perform the geometric phase analyses. (a) HRTEM micrograph of an InSb island on a WZ section in a GaAs NW. The red rectangle refers to the reference region of unstrained material. (b) FFT of the HRTEM image. Red circle denote the WZ* $(1\bar{1}00)$ *(x) and* (0002) *(y) reflections. (c) Phase image.(d)* ϵ_{yy} *strain map. White arrows in (a) and (d) indicate the interface from the GaAs to the InSb.*

Geometric phase analyses Dislocations as well as variations in the lattice constants can be identified by a technique referred to as "geometric phase analyses" (GPA). This method was developed by Hÿtch *et al.* [142, 143]. An image of a perfect crystal can be described as a Fourier sum:

$$I(\vec{r}) = \sum_g H_g \exp\{2\pi \vec{g} \cdot \vec{r}\} \tag{2.1}$$

$I(\vec{r})$ refers to the intensity at the position $\vec{r}$, $\vec{g}$ corresponds to the Bragg reflection of a reference lattice. The Fourier coefficients H_g are given by $H_g = A_g \exp\{iP_g\}$. Here, A_g is the amplitude of the lattice fringe $\vec{g}$ and P_g is the phase. In real images, H_g can be a function of the position $\vec{r}$, that is

$$H_g(\vec{r}) = A_g(\vec{r}) \exp\{iP_g(\vec{r})\} \tag{2.2}$$

The intensity $I(\overrightarrow{r})$ is then described by

$$I(\overrightarrow{r}) = A_0 + \sum_{g>0} 2A_g(\overrightarrow{r}) \cos\{2\pi \overrightarrow{g} \cdot \overrightarrow{r} + P_g(\overrightarrow{r})\} \tag{2.3}$$

A particular set of Bragg fringes is given by

$$B_g(\overrightarrow{r}) = 2A_g(\overrightarrow{r}) \cos\{2\pi \overrightarrow{g} \cdot \overrightarrow{r} + P_g(\overrightarrow{r})\} \tag{2.4}$$

With a displacement field $\overrightarrow{u}(\overrightarrow{r})$, Eq. 2.4 is changed to

$$B_g(\overrightarrow{r}) = 2A_g(\overrightarrow{r}) \cos\{2\pi \overrightarrow{g} \cdot \overrightarrow{r} - 2\pi \overrightarrow{g} \cdot \overrightarrow{u}\} \tag{2.5}$$

Accordingly,

$$P_g(\overrightarrow{r}) = -2\pi \overrightarrow{g} \cdot \overrightarrow{u}(\overrightarrow{r}) \tag{2.6}$$

$P_g(\overrightarrow{r})$ is the phase shift. Figure 2.3(a) displays a HRTEM micrograph of an InSb island grown on the WZ section of a GaAs NW. The white arrows indicate the interface between both semiconductors. The red rectangle marks the reference region in the GaAs. The FFT of the HRTEM image is depicted in Fig. 2.3(b). The Bragg reflections $\overrightarrow{g}$ corresponding to the (0002) and $(1\overline{1}00)$ lattice planes are encircled, that are the y and x directions. The resulting phase images is shown in Fig. 2.3(c). The uniform gradient (or a uniform color) in the reference region indicates that the lattice is not distorted. Phase jumps are either caused by lattice distortions (strain, dislocations), regions being slightly tilted away from the zone axis or thicker regions.

Strain maps are the derivative of the displacement field u_i along i (x- or y-direction), that is $\epsilon_{ij} = \frac{\delta u_i}{\delta j}$ [142].

Figure 2.3(d) depicts the ϵ_{yy} strain map. The image displays the strain with respect to the reference region. Dislocations are identified as point-like changes of the color. In this particular case, six dislocations are present. Color changes at the right part of this image are caused by the a slight misalignment of the NW with respect to the electron beam and the corresponding phase jumps seen in the phase image (see Fig. 2.3c). The GPA is performed using the "FRWRtools plugin" for Digital Micrograph™ provided by the *Electron and Ion Microscopy group at Ulm University*. The scale bar of the HRTEM image is always also valid for the phase and strain maps.

3 Chapter 3. Critical thickness in semiconductor heterostructures

By combining semiconductors with different band gaps into heterostructures, efficient devices can be fabricated. However, due to the fact that the different materials have different lattice constants, strain develops in the structure. When the strain exceeds a certain value, the structure relaxes by the formation of dislocations [92]. This critical strain value corresponds to a critical thickness t_c: below this critical thickness coherent growth is possible. Apart from strain relaxation by the formation of dislocations, roughening of the surface can reduce the strain. In this case, a Stranski-Krastanov or Volmer-Weber growth takes place. These growth modes typically result in self-assembled quantum dots.
In this chapter, first two models for the critical thickness in layered structures are presented and the possible dislocations in zinc blende and wurtzite materials are introduced. The model to determine coherency limits in core-shell NWs developed by Raychaudhuri and Yu is shortly described [252, 253]. Finally, the model is applied to the different material combinations used in this thesis.

3.1. Critical thickness

The critical thickness t_c was firstly introduced by Frank and van der Merwe as the thickness beyond which it is energetically favorable to form a dislocation [92]. Below t_c, the layers are coherently strained and pseudomorphic growth takes place as displayed in the schematic in Fig. 3.1 a. Once the critical thickness is reached, dislocations form in order to relax the strain (see Fig. 3.1a).
Several models were developed in order to calculate the critical thickness, the first one developed

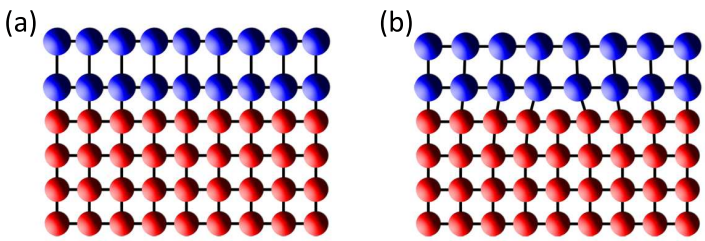

Figure 3.1: *Schematic illustration of the combination of two materials with different lattice constants, either the epitaxial layer is strained (a) or relaxed by the inclusion of misfit dislocations (b).*

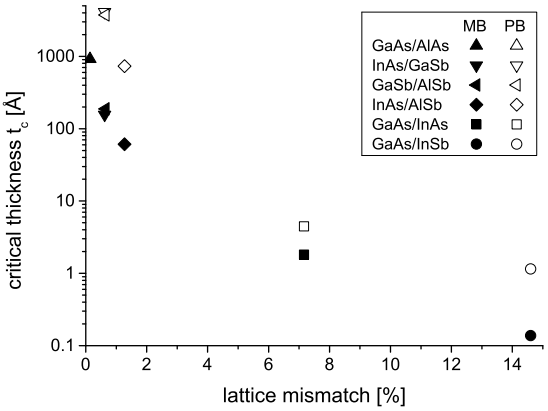

Figure 3.2: *Critical thickness as a function of the lattice mismatch. The critical thicknesses were calculated using the model by Matthews and Blakeslee (MB, filled symbols) [208] and People-Bean (PB, open symbols) [240].*

by van der Merwe [318]. Applying this model, almost no agreement between the theory and experiments was observed. Consequently, a more accurate model based on mechanical-equilibrium theory was developed by Matthews and Blakeslee [208]. The critical thickness t_c is given by

$$t_c \cong \frac{b}{f}\frac{1}{4\pi(1-\nu)}\left[\ln\left(\frac{t_c}{b}\right)+1\right] \tag{3.1}$$

Here, b is the Burgers vector of the dislocation, f is the lattice mismatch and ν Poission's ratio ($\nu \approx 0.3$). The model overestimated the critical thickness for large lattice mismatches while it underestimated it for low mismatches [240]. People-Bean improved the model by an energy balance approach, resulting in [240]:

$$t_c \cong \frac{1-\nu}{1+\nu}\frac{1}{16\pi\sqrt{2}}\left[\frac{b^2}{a}\right]\left[\frac{1}{f^2}\ln\left(\frac{t_c}{b}\right)\right] \tag{3.2}$$

With this model, People and Bean obtained a good agreement with experiments [240]. Comparing the models developed by Matthews-Blakeslee and People-Bean one can see that the critical thickness scales with $1/f$ and $1/f^2$, respectively. Figure 3.2 shows the critical thickness for different combinations of III-V semiconductors. Most of these combinations are used in this thesis.
All these models assumed a thin film grown on an infinite thick substrate. Huang investigated the impact of the substrate thickness, demonstrating an increase in the critical thickness when the substrate thickness decreased [137]. In fact, this situation is already comparable to core-shell nanowires where a thin NW core acts as the substrate for the shell.

3.2. Dislocations in zinc blende and wurtzite lattices

A dislocation is characterized by its line vector l, its Burgers vector b and the glide plane. The line vector can vary on a dislocation whereas the Burgers vector is constant for a given dislocation. If the Burgers vector is a translation vector of the lattice, the dislocation is called "perfect dislocation", otherwise it is a "partial dislocation". Table 3.1 lists Burgers vectors and corresponding glide planes of dislocations in ZB and WZ lattices. The energy of a dislocation is proportional to b^2, thus when a perfect dislocation splits into partial ones, the energy decreases. However, these partial dislocations modify the stacking sequence and therefore create a stacking fault. The energy of this stacking fault has to be taken into account as well. The Burgers vector

	zinc blende	wurtzite
perfect	$1/2\langle 110\rangle\{111\}$ $1/2\langle 100\rangle\{100\}$	$1/3\langle 11\bar{2}0\rangle\{0001\}$ $1/3\langle 11\bar{2}0\rangle\{10\bar{1}0\}$ $\langle 0001\rangle\{10\bar{1}0\}$ $\langle 0001\rangle\{11\bar{2}0\}$
Shockley	$1/6\langle 112\rangle\{111\}$	$1/3\langle 10\bar{1}0\rangle\{0001\}$
Frank	$1/3\langle 111\rangle$	$1/2\langle 0001\rangle$
Frank-Shockley		$1/6\langle 20\bar{2}3\rangle$

Table 3.1.: *Burgers vectors and corresponding glide planes in zinc blende and wurtzite lattices [179, 229, 230, 315].*

of the Shockley partial dislocation lies in the plane of the fault, thus the dislocation is glissile. Contrary, the Frank partial dislocation is sessile and can only climb.

Considering axial strain relaxation in core-shell NWs, the Burgers vector b of the dislocation needs to have a component in the ZB $[\bar{1}\bar{1}\bar{1}]$ or in the WZ $[000\bar{1}]$ direction. In a ZB lattice, this can be achieved by perfect dislocations with Burgers vector $b = a/2\langle 110\rangle$, Frank partial dislocations with $b = a/3\langle 111\rangle$ or Shockley partials with $b = a/6\langle 112\rangle$.

In WZ lattices, the axial strain can also be relaxed by perfect dislocations with $b = c\langle 0001\rangle$ or Frank partial dislocations with $b = c/2\langle 0001\rangle$. The Frank partial dislocation again creates a stacking fault.

3.3. Core-shell nanowire model

Raychaudhuri and Yu published a model to predict the critical dimensions in core-shell NWs, both for ZB and WZ structures [253, 252]. The NW growth axis is the $[\overline{111}]$B direction in the ZB system and the $[000\overline{1}]$B in the WZ case. The model assumes cylindrical NWs without any faceting. It is based on an energetic approach considering on the one hand the strain energy in the NW and on the other hand the energy associated with dislocations. For certain dimensions (core radius and shell thickness) it becomes energetically favorable to form dislocations.
The model is shortly described in the Appendix A.2. Details about the model can be found in Refs. [252] and [253].

3.4. Application to GaAs/InAs, InAs/$Al_xGa_{1-x}Sb$ and GaAs/InSb core-shell nanowires

In the following, the model to predict the critical thickness of core-shell NWs is applied to the different material combinations used in this work. These are the highly lattice mismatched systems GaAs/InAs ($\sim$ 7% lattice mismatch) and GaAs/InSb ($\sim$ 14% lattice mismatch) as well as InAs/GaSb and InAs/AlSb having low lattice mismatches ($\sim$ 0.6% and $\sim$ 1.2% lattice mismatch).

Figure 3.3 shows the critical dimensions maps of the highly lattice mismatched materials GaAs/InAs and GaAs/InSb for the ZB lattices. As seen, the predicted critical shell thicknesses are in the order of just a few atomic layers and almost independent on the core radius. Only core radii of $\sim$ 1 nm would result in coherent growth of a thick shell. Such thin III-V NWs have not yet been reported. Considering the different types of dislocations (Frank partial dislocations

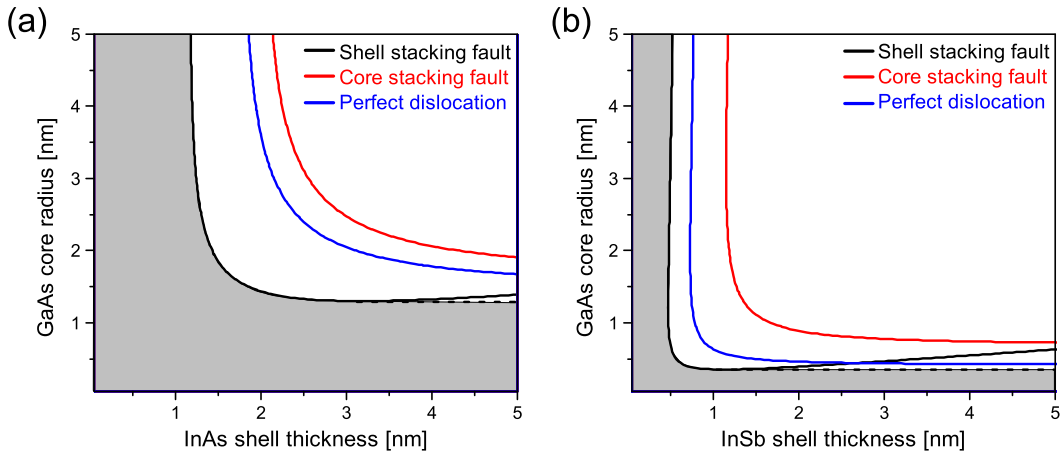

Figure 3.3.: *Critical dimension maps of (a) GaAs/InAs and (b) GaAs/InSb core-shell NWs. The black lines indicate the critical dimension for shell stacking faults, red line for core stacking faults and blue lines for perfect dislocations. The grey regions corresponding to misfit dislocation free structure.*

and perfect dislocations), it is seen that Frank partial dislocations producing a stacking fault in the shell are the energetically preferred type, followed by perfect dislocations.

InAs cores with shells of either GaSb or AlSb have significantly lower lattice mismatches, 0.6% and 1.2% respectively. Therefore, larger critical dimensions are expected. Figure 3.4a,b show the critical thickness maps for ZB and WZ InAs/GaSb core-shell NWs. Coherent growth is theoretically expected within a range of core radii below 40 nm or shell thicknesses below 35 nm. In a certain window of NW dimensions, Frank partial dislocations with a stacking fault in the core are the theoretically preferred type of dislocations. Such dislocations have not yet been observed experimentally, only stacking faults in the shell were found [164, 165, 247]. The formation of a stacking fault in the core requires an additional energy since existing atoms need to be shifted. Accordingly, especially the critical dimensions line defined by "core stacking fault" is regarded as a lower boundary. Considering the critical dimensions defined by "core stacking fault" no major difference between ZB and WZ core-shell NWs is observed. Neglecting this type of dislocation, coherent WZ InAs/GaSb core-shell NWs with infinite shell thickness are expected for core radii up to 70 nm while the critical core radius is only $\sim$ 60 nm for ZB wires. For this particular system, WZ InAs/GaSb core-shell NWs may accommodate the strain slightly better than ZB ones. It should be mentioned that neither the elastic constants nor the lattice parameters of WZ InAs or GaSb are know and are only taken from theory [206, 235]. Replacing GaSb with AlSb, the lattice mismatch increases to 1.2 % and the critical dimensions decrease roughly by a factor of 2-4, as seen in Fig. 3.4c. For thin cores, Frank partial dislocations with a stacking fault located in the core are again expected to be the preferred type. Neglecting this type, ZB core-shell NWs with thin core radii of about 26 nm give rise to coherent growth independent on the shell thickness.

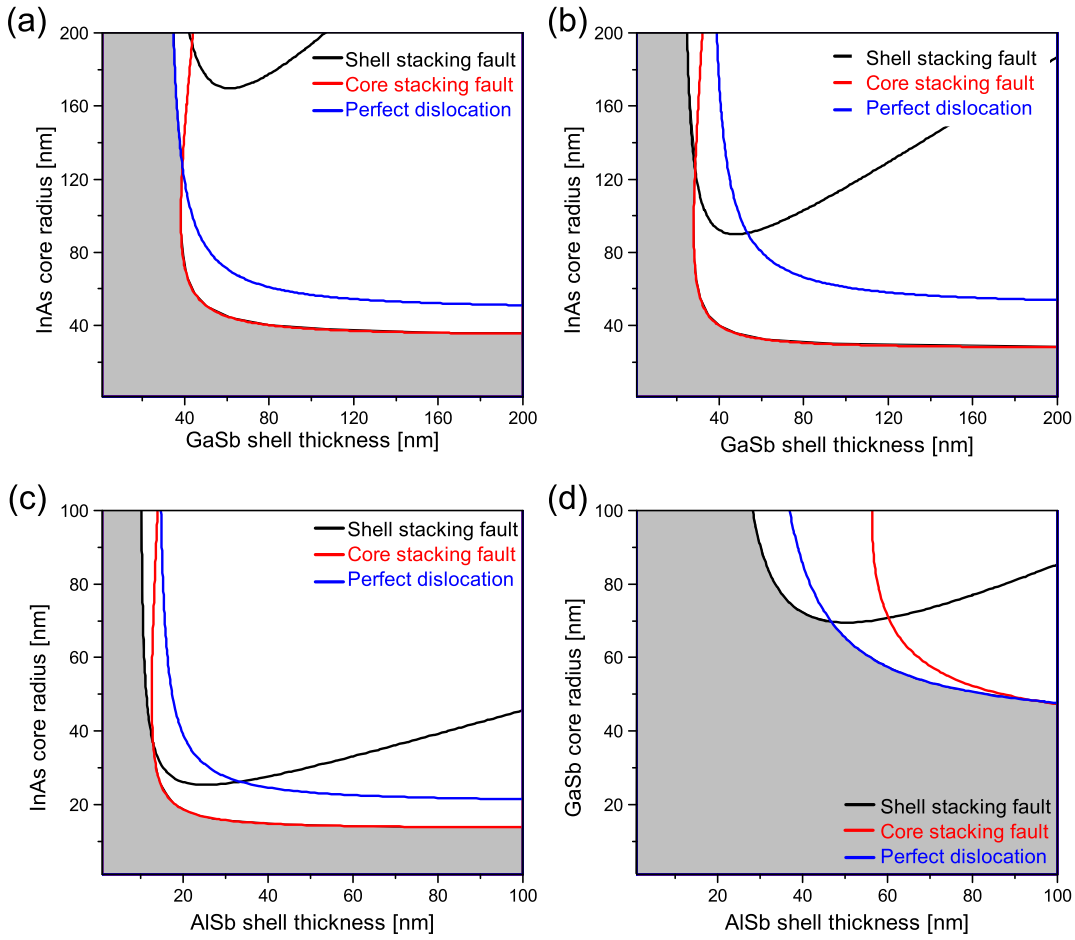

Figure 3.4.: *Critical dimension maps of (a) ZB InAs/GaSb, (b) WZ InAs/GaSb, (c) ZB InAs/AlSb and (d) ZB GaSb/AlSb core-shell NWs. The black lines indicate the critical dimension for shell stacking faults, red line for core stacking faults and blue lines for perfect dislocations. The grey regions corresponding to misfit dislocation free structure.*

4 Chapter 4. Group III-Arsenide nanowires

In this chapter, the growth of group III-As NWs is discussed. If the NW growth via Au catalyst particles should be avoided, two growth schemes are possible: a vapor-liquid-solid (VLS) mechanism with the group III element acting as a liquid catalyst (self-catalyzed growth) and a vapor-solid (VS) growth mechanism which does not require any catalyst. In 2008, Fontcuberta *et al.* demonstrated the growth of GaAs NWs via the VLS mechanism using GaAs substrates covered by a thin layer of silicon oxide [90]. Subsequently, this technique was adopted by several groups and transferred to Si substrates, e.g. in Refs. [244, 273]. Details about this growth are e.g. found in Refs. [55]. A similar mechanism for the growth of InAs NWs was reported by our group [109], whereas others reported only about the growth of VS InAs NWs [80, 177, 202]. The growth conditions for both differ strongly and reported substrates for the growth are different as well. For the VLS growth the substrate is GaAs with a thin oxide layer [109, 205] whereas it is Si with an oxide layer for the VS growth [177, 202]. The first part of this chapter discusses the growth of InAs NWs on both GaAs and Si substrates and in doing so, explains the different growth modes and substrate preparations in the VLS and VS case.
In the second part of this chapter, the advantage of a good control of the crystal structure in VLS grown NWs is used to include short WZ segments within the (twinned) ZB crystal structure of GaAs and InAs NWs.
Several results presented in this chapter have been published in Refs. [256, 261, 264].

4.1. Vapor-solid InAs nanowire growth on GaAs (111)B substrates

Compared to the VLS mechanism, doping as well as the growth of ternary alloys are expected to be more simple when a droplet is not involved in the NW growth. In general, the presence of a catalyzing droplet results in the formation of a core-shell system: the composition grown from the droplet, defined by the concentration in the droplet, differs from the composition grown radially by direct impingement [85]. Using a VS growth mechanism, the formation of an unintentionally grown core-shell NW is expected to be reduced. Studying the growth of such VS InAs NWs is therefore e.g. especially interesting for NW heterostructures, ternary materials and doped NWs. Basic growth parameters were already evaluated in Ref. [255]. There it was shown that especially the silicon oxide on the substrate has a major influence on the NW growth. Very thin oxides favored the growth of high density, vertical NWs while thicker oxides resulted in significant lower NW densities as well as a high number of tilted NWs. This

	standard value	varied range
As_4 flux [Torr]	$2 \cdot 10^{-5}$	$0.5 \cdot 10^{-5} - 3.5 \cdot 10^{-5}$
In rate [µm/h]	0.1	$0.001 - 0.3$
Substrate temperature [°C]	490	$450 - 530$
growth time [min]	60	$0.5 - 120$

Table 4.1.: *Standard growth parameters and varied range for the VS growth of InAs NWs on GaAs substrates*

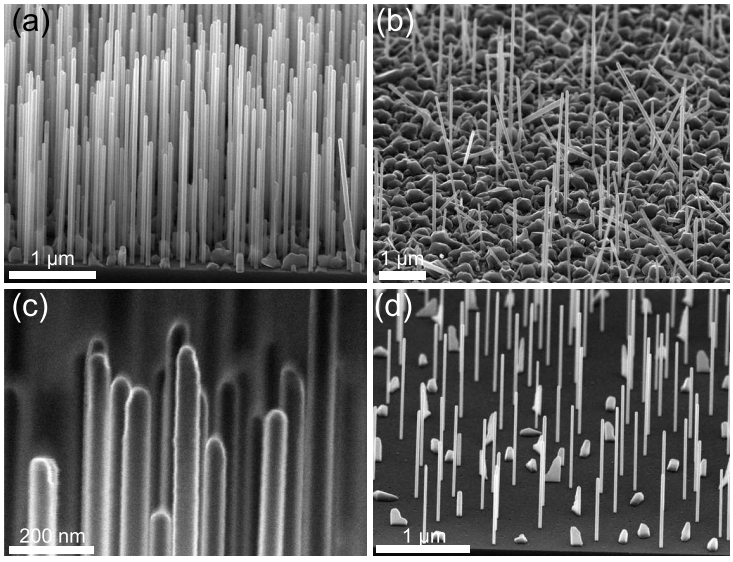

Figure 4.1: *SEM micrographs of vapor solid InAs NWs grown on GaAs (111)B substrates. (a) InAs NWs on GaAs (111)B substrates with a 4 nm thick SiO_x layer. (b) InAs NWs on GaAs (111)B substrates with a 6 nm thick SiO_x layer. (c) Top of the InAs NWs showing the round or faceted shape. (d) Low density NWs obtained by reducing the In flux.*

is also seen in Fig. 4.1a,b. Consequently, GaAs (111)B substrate were covered by a very thin layer of SiO_x. The SiO_x was obtained by spin-coating a hydrogen silsesquioxane (HSQ) : methyl isobutyl ketone (MIBK) solution at 6000 rpm on the wafer and a subsequent annealing at 300°C. The HSQ:MIBK dilution was 1:40 resulting in a SiO_x thickness of about 4 nm, as measured by ellipsometry.
In the following, the influence of the different growth parameters on the NW growth is described, finally also giving the limitations of this growth mechanism. Apart from the NW dimensions, two further parameters are important for future devices: the ability to tailor the conductivity as well as the crystal structure. Thus, the impact of an additional Si flux on the NW growth is described and the crystal structure of the NWs is discussed.

4.1.1. Impact of the growth parameters on the nanowire growth

A thorough study of the impact of the growth parameters, namely the In rate, the As flux, the substrate temperature and the growth time, was performed. The standard growth conditions are listed in Tab. 4.1. For each investigated condition, the mean and maximal NW length, the NW diameter, the NW density and the overall substrate coverage were determined by analyzing SEM micrographs. The coverage is a good indicator for the number of crystallites since even extraordinary high NW densities (40 NWs/µm^2) of rather thick NWs ($\sim$ 100 nm) result only in a coverage of about 25%. As it will be shown later, the NW diameters in this study are usually below 100 nm and the NW density does not exceed 40 NWs/µm^2. Accordingly, the substrate coverage is dominated by the amount of crystallites. Figure 4.1a,c,d show exemplary (60° tilted view and top view) SEM micrographs of samples grown with the standard growth conditions (a,c) as well as a low In rate of 0.005 µm/h (d). The NW density and their diameter

are strongly reduced by decreasing the In flux. The NWs have a hexagonal morphology with side facets belonging to the {110} family. The top of the NWs is characterized by a rounded, rough shape which is seen in Fig. 4.1c. Similar observations were made by Hertenberger *et al.* for the growth of self-seeded InAs NWs on Si substrates [128] whereas Dimakis *et al.* [80] observed flat top facets of InAs NWs grown on bare Si substrates. The round shape on top of the NWs is the growth front of the NW and will therefore determine the crystal structure as well as the abruptness and shape of axial heterostructures. A more detailed description of the top region is given in Section 4.1.3.

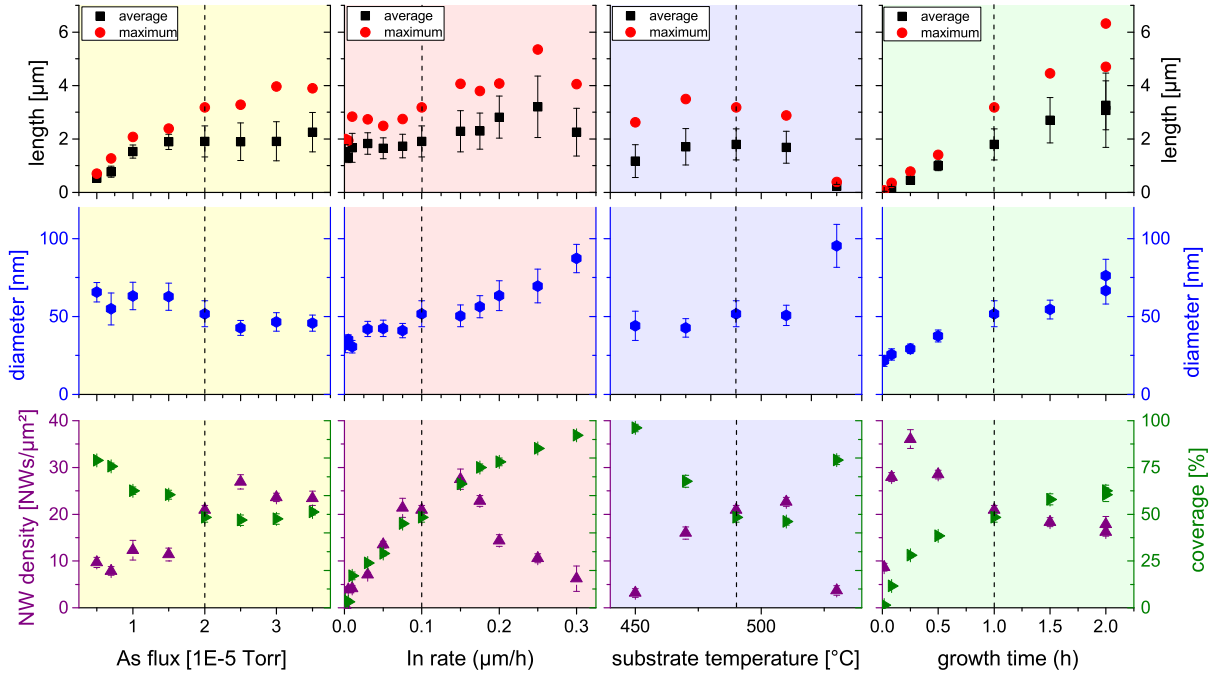

Figure 4.2.: *InAs NW length (average ■, maximum ●), diameter ●, density ▲ and coverage ► depending on the As flux, the In rate, the substrate temperature and the growth time. The dashed vertical lines represent the standard growth parameters.*

The results of the variation of the growth parameters are plotted in Fig. 4.2. Two regimes for the influence of the As_4 flux were identified. Below $1.5 \cdot 10^{-5}$ Torr, the NW length increases linearly with the As_4 flux, above it saturates. The NW diameter decreases until $1.5 \cdot 10^{-5}$ Torr and is constant above. The NW density increases by a factor of 2 up to 25 NWs/µm^2 between As_4 fluxes of $1.5 \cdot 10^{-5}$ and $2 \cdot 10^{-5}$ Torr while the coverage, i.e. the number of crystallites, decreases. In general, As_4 fluxes above $2 \cdot 10^{-5}$ Torr do not change the NW morphology and density: the growth is limited by the arrival of In atoms. As seen by the coverage, In rich growth conditions, that are low As fluxes, favor the formation of crystallites in between the NWs.
Similarly to the As_4 flux, two regimes for the influence of the In rate are identified. When the In rate is below 0.1 µm/h, both NW length and diameter show almost no dependence on the In rate. Only at very low rates of 0.005 and 0.001 µm/h both decrease slightly. Above In rates of 0.1 µm/h, the NW length and diameter increase nearly linearly. From 0.1 µm/h to 0.3 µm/h the diameter is doubled, while the NW length is increased at maximum only by about 50%. In contrast to the diameter, the NW length decreases for In rates above 0.25 µm/h. In order to fully understand the growth phenomena, the NW density and coverage have to be taken into account. The NW density first increases from $\sim$ 1 NWs/µm^2 up to $\sim$ 30 NWs/µm^2 with an increase of

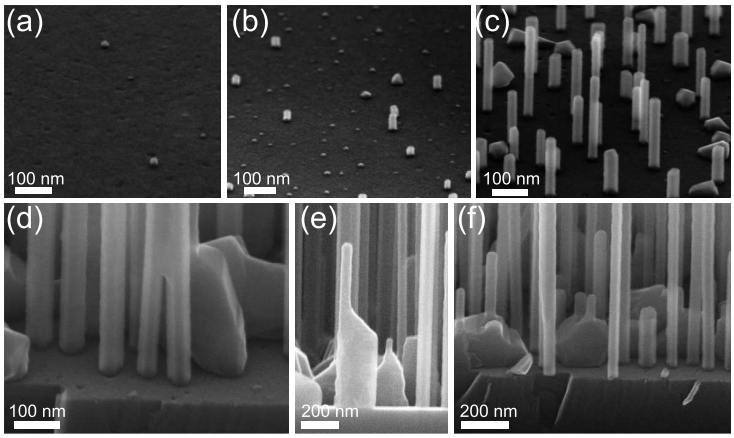

Figure 4.3: *(a)-(c): SEM micrographs showing the early stages of NW growth. The images in (a), (b) and (c) are taken after 30 s, 1 min and 5 min of growth, respectively. (d)-(f): SEM micrographs showing the origin of NW density reduction with the growth time. (d) and (e) show coalesced NWs and in (e) and (f) NWs being buried by crystallites are seen.*

the In rate, while it decreases when the In rate is above 0.15 µm/h. The coverage simultaneously increases monotonically up to almost 100%. As already described, In rich conditions favor the growth of crystallites rather than NWs. Thus, the reduced length at the highest In rate is due to a strong competition for the adatoms between the crystallites and the NW. The constant NW length and diameter below 0.1 µm/h are accompanied by the increasing NW density and coverage. Accordingly, the additional In atoms nucleate further NWs and crystallites rather than increase the dimensions of the existing ones. Above 0.1 µm/h, both NW density and coverage are already very high resulting in a strong competition for the adatoms between the structures. This is evident by the large error bars of the NW length and diameter. Additionally supplied In does not anymore nucleate further NWs but grows on crystallites and existing NWs.
The substrate temperature plays a minor role during the NW growth as seen in Fig. 4.2. Between 470°C and 510°C there is almost no influence on the NW length, diameter, density and coverage. The lower limit for the growth of vertical NWs was found to be 450°C: many NWs are tilted and the NW density strongly decreases while the coverage increases. Thus, the temperature is too low to nucleate the NWs. The upper limit was found to be 530°C. This is the temperature were VLS InAs NWs are grown on oxide covered GaAs substrates by much smaller As_4 fluxes [109]. Using high As_4 fluxes, only few short and thick InAs stems are found. However, recently Hertenberger *et al.* reported that the temperature regime for VS InAs NWs can be increased significantly by increasing the As_4 flux [126].

The mean NW length was found to increase sublinear with the growth time, although the maximal NW length increases linear. After two hours of growth, the maximal length is around 6.5 µm giving a growth rate of 3.2 µm/h whereas the mean NW length is only 3 µm corresponding to a growth rate of 1.5 µm/h. The strong fluctuation in NW length, visible due to the increasing error bars, can be attributed to shading effects being present despite of the substrate rotation: short NWs receive less material due to shadowing while long ones collect In adatoms by direct impingement, diffusion and reabsorption. Consequently, the short NWs grow slower which finally increases the spread in NW length. Additionally, due to the high NW and crystallite density, the competition between NWs and crystallites for adatoms is high. Compared to the NW length, the diameter distribution is narrower but even there it is visible that the spread increases with the growth time. The NW density has a maximum after 15 min growth, subsequently decreasing by 50% to 15-20 NWs/µm^2. The coverage increases monotonically and saturates at about 60%. The increase of the coverage is explained by a lateral expansion of both NWs and crystallites. After a certain growth time and NW length, the substrate is shadowed and only very few atoms can contribute to the expansion of the crystallites. To understand the maximum in NW density after

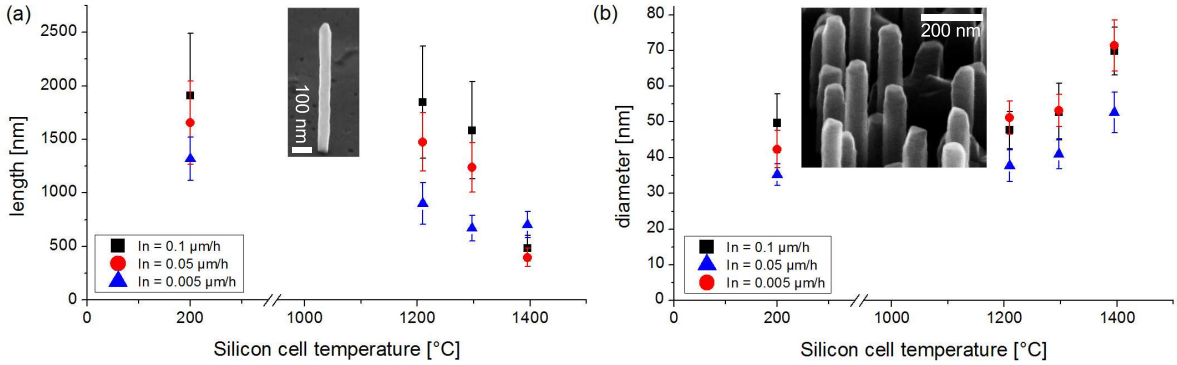

Figure 4.4.: *InAs NW length and diameter as a function of the Si cell temperature for NWs grown with three different In rate of ■ 0.1 µm/h, ● 0.05 µm/h and ▲ 0.005 µm/h.*

15 min, SEM micrographs taken after short growth times as well as detailed micrographs after long growth times are depicted in Fig. 4.3. The NW density increases rapidly between 0.5 and 5 min (see Figs. 4.3a-c), the number of crystallites being small. After 5 minutes, the NW density is already in the range of 25-30 NW/µm^2. After 15 min of growth, the NW density is further increased to 35 NW/µm^2. When the growth time is prolonged, the NW density decreases due to two effects. First, short NWs are buried by the parasitic growth of crystallites. Typical SEM micrographs of such buried NWs are shown in Fig. 4.3e,f. Second, neighboring NWs coalesce resulting in non-hexagonal NWs. Here, two additional situations can be distinguished. In the first one, the neighboring NWs are completely coalesced (Fig. 4.3e). In the second situation, a part at the NW bottom remains non coalesced (Fig. 4.3d). Due to the coalescence and burying of NWs, the measured NW density decreases. A similar decrease of the NW density was also observed in other system where the NW density is very high [38].

4.1.2. Impact of Si doping on the nanowire dimensions

For any future devices, NW doping and therefore a control of the conductivity is essential. Consequently, the impact of Si doping on the growth of InAs was investigated. InAs NWs with different Si fluxes have been grown for 1h. Three different In rates were used in order to understand whether the absolute Si flux or the Si flux relative to the In flux influence the growth. In Fig. 4.4a,b the NW lengths and diameters are plotted as a function of the temperature of the Si cell. Si cell temperatures of 1210°C, 1297°C and 1395°C correspond to dopant concentrations of $5 \cdot 10^{16}$, $5 \cdot 10^{17}$ and $5 \cdot 10^{18}$ cm^{-3} in (100) GaAs layers, respectively. A Si cell temperature of 200°C represents the undoped NWs. As seen in Fig. 4.4, high Si fluxes reduce the NW lengths and increase their diameters, independent on the supplied In rate. The NW side facets roughen (see inset in Fig. 4.4a) and clear flat top facets develop (see inset in Fig. 4.4b) being in contrast to undoped NWs. The Si dopant atoms reduce the diffusion length of both In and Ga adatoms [62, 81, 82], explaining the increasing NW diameter and decreasing length. Consequently, diffusion of adatoms from the NW side facets to the top represents one of the major contributions to the axial growth. If this adatom diffusion is decreased, the axial growth rate decreases and the radial one increases. The roughening of the side facets can be caused by an enhanced nucleation on the side facets being induced by the reduced diffusion length. The flat top facet may develop due to a reduced axial growth rate. Recently, Dimakis *et al.* confirmed the incorporation of Si in VS grown InAs NWs by Raman scattering and showed that it is incorporated only on the In lattice sites, thus as an n-dopant [81]. Transport in Si-doped Au-free InAs NWs was investigated by Wirths *et al.* for MOVPE grown NWs [334]. This study

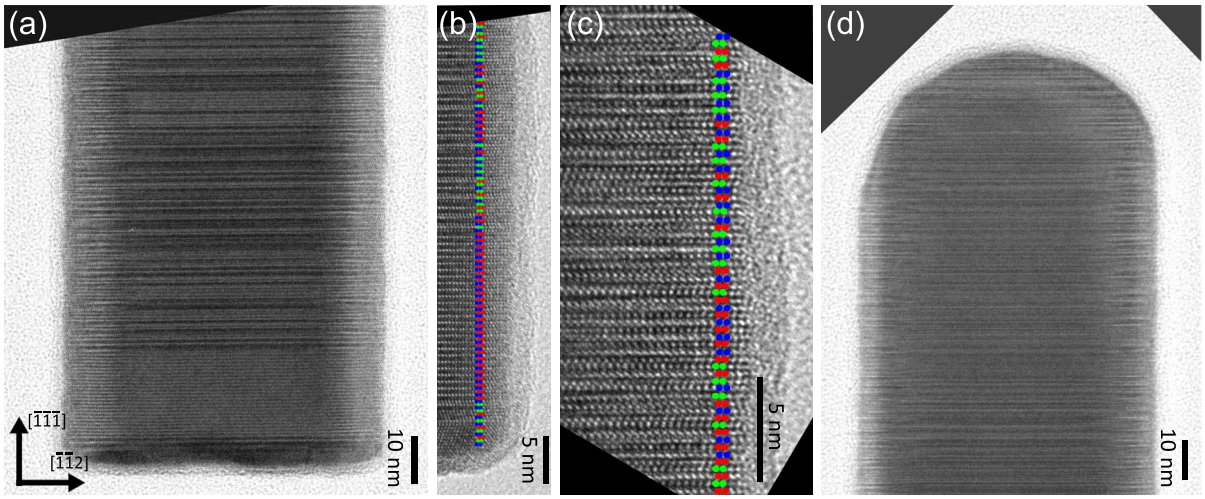

Figure 4.5.: *TEM micrographs of InAs NWs grown via the VS method showing the bottom (a,b), the middle part (c) and the top part (d). Colored dots in (b) and (c) indicate the different layers A ●, B ● and C ●.*

also verified the NWs to be n-type with an increasing donor concentration for increasing Si supplies. Both authors observed similar changes of the NW morphology by the addition of Si to the growth. Thus, the results demonstrate that high Si fluxes strongly influence the growth of InAs NWs by decreasing their aspect ratio. This limits the possibilities for InAs NWs doped with Si to rather short and thick devices.

4.1.3. Crystal structure

Figure 4.5 shows exemplary TEM micrographs of a VS InAs NW. The images are taken at the bottom of the NW (a,b), in the center (c) as well as at the top (d). Colored circles shown as an overlay in (b) and (c) indicate the different stacking position A, B and C. The stacking is arbitrary without any preference of the ZB crystal structure, WZ crystal structure or another polytype (4H, 6H ...). Only at the bottom of the NW, a short segment of ZB phase followed by about 20 nm of WZ is found. Similar results are obtained for all growth conditions. The change of the crystal structure at the bottom may indicate different growth process being involved. Dimakis *et al.* suggested that the nucleation takes place by locally In-rich conditions, most likely In droplets [80]. These In-rich conditions subsequently turn into As-rich conditions favoring the axial growth. For VLS grown InAs it was shown that the crystal structure is periodically twinned ZB with a WZ top being attributed to a nucleation at the triple phase line vapor-droplet-solid induced by the consumption of the In droplet [109, 345]. Our TEM results, in fact, support the nucleation model assumed by Dimakis *et al.* [80]: In droplets form on the substrate and are consumed rapidly resulting in a pure crystal structure without stacking faults. Subsequently, the growth takes place without a droplet, as demonstrated by Hertenberger *et al.* [128].
The arbitrary stacking is a typical characteristic of VS grown InAs NWs: Sladek investigated the growth of InAs NWs using SA-MOVPE and performed a thorough study on the influence of growth parameters on the crystal structure [283]. There, it was found that the V/III ratio has a small impact on the structure, meaning that the relative amount of ZB or WZ increases but without having a pure crystal structure.

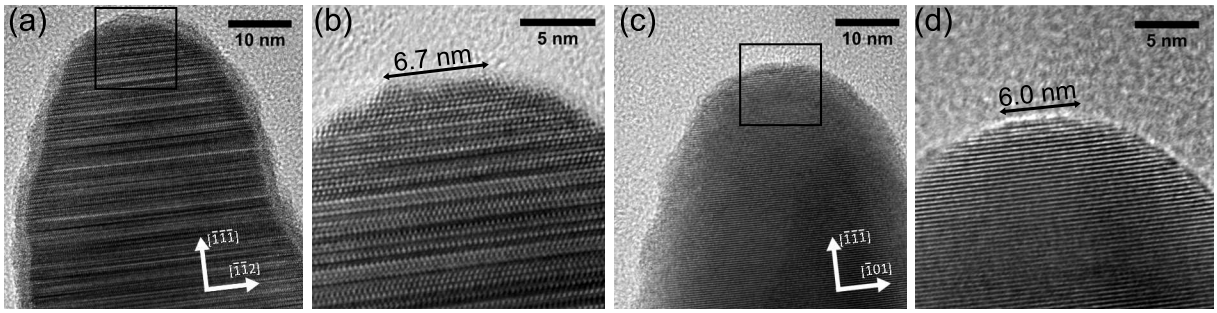

Figure 4.6.: *TEM micrographs of the faceted top region of VS InAs NWs viewed from the* ⟨110⟩ *(a,b) and* ⟨211⟩ *(c,d) zone axes. The width of the uppermost layer is given in (b) and (c).*

Typically, the defective structure of NWs is explained by the supersaturation of the catalyzing droplet and improvements in the crystal structure are achieved by modifying the supersaturation [83]. In case of VS grown NWs, no droplet is involved in the NW growth and therefore this explanation is not applicable. By drastically reducing the lateral dimensions of the NWs, the WZ structure should become stable due to the lower energy of the side facets compared to the ZB structure [3, 97]. The critical radius/diameter is in the order of $\sim 5 - 15$ nm and thus, much smaller than the NWs shown here. However, as already shown in the SEM micrographs in Fig. 4.1c, the top region of the NWs is tapered and faceted. In order to further analyze whether the dimensions at the top are small enough to enable the formation of both crystal structures, the top part was analyzed more detailed by HRTEM and HAADF images. Figure 4.6 shows the top layers of a VS InAs NW. The mean NW diameter is around 80 nm, while the diameter continuously decreases to less than 15 nm at the top, being close to the critical diameter for the transition from ZB to WZ. In fact, the upper layers being the effective axial growth front of the NW may be even smaller but are not clearly seen due to oxidation. From the HRTEM micrographs these upper layers can be approximated to ~ 7 nm along the ⟨211⟩ direction (b, ⟨110⟩ zone axis) and ~ 6 nm along the ⟨110⟩ direction (d, ⟨211⟩ zone axis). A faceting of the top region is investigated by HAADF images. Figure 4.7a and d show HAADF images of the top region taken from the ⟨110⟩ and ⟨211⟩ zone axes, respectively. The intensity in a HAADF image depends on square of the atomic number Z of the element as well as the thickness. Since the image contains only InAs, Z is constant. Hence, changes in the intensity are caused by variations in the thickness and in a first approximation, the intensity increases linearly with the thickness [317]. Lehmann *et al.* demonstrated a method to identify NW facets using intensity profiles perpendicular to the NW growth axis [194]. By combining the ⟨110⟩ and ⟨211⟩ zone axes, a quasi three-dimensional structure is reconstructed. Figure 4.7b shows intensity profiles taken from the main, untapered part of the NW. The facets are identified to be {110} type facets, similar as expected from SEM analyses. In Fig. 4.7c, e, f intensity profiles taken from the tapered top region are plotted. As seen, the profiles changed significantly, indicating the presence of additional facets. Especially in the last profile taken at the uppermost possible position no clear evidence of {110} is found. The profile matches roughly with the existence of higher index facets like the {211} facets. Consequently, the effective growth front of the NWs is strongly different from its mean diameter and stable ⟨110⟩ side facets.

Recently, it was shown that the crystal structure of MBE-grown VS InAs NWs switches to twinned ZB when adding small amounts of Sb, resulting in InAsSb NWs with about 7% Sb [288, 353]. This Sb concentration is almost independent on the Sb flux. The Sb flux influenced the growth by decreasing the aspect ratio of the NWs. The electron mobility was significantly enhanced.

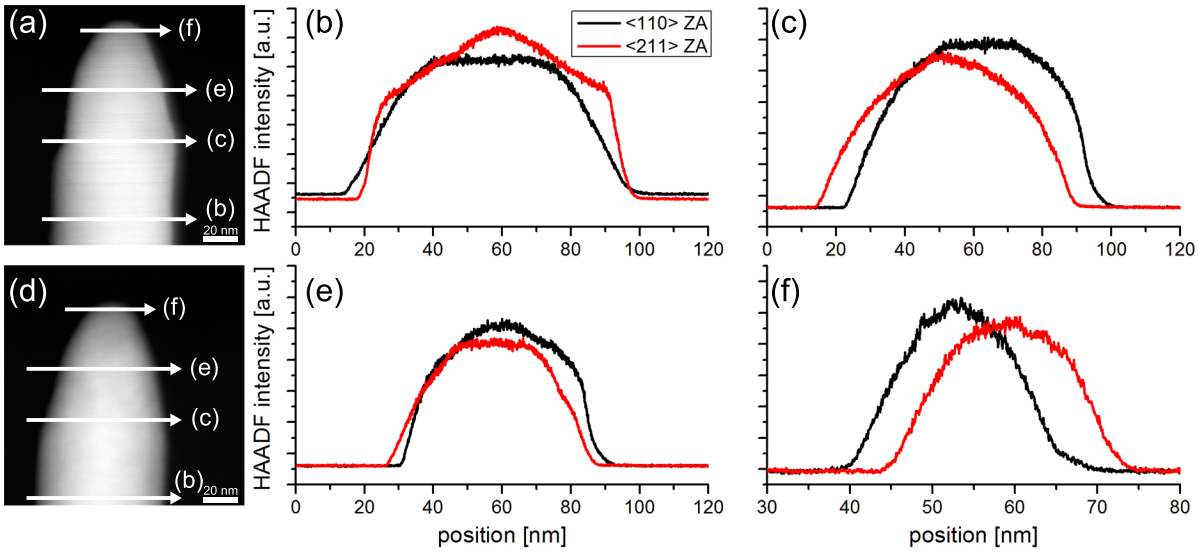

Figure 4.7.: *HAADF images of the top region of InAs NWs from the (a) ⟨110⟩ zone axis (ZA), (d) the ⟨211⟩ zone axis (ZA). HAADF profiles taken at different positions as indicated in the HAADF images: (b) central part of the NW, (c) lower part of the faceted region, (e) mid part of the faceted regions and (f) upper part of the faceted region*

4.2. Vapor-solid and vapor-liquid-solid growth of InAs nanowires on Si substrates

Self-catalyzed GaAs NWs are usually grown on Si substrates which do not receive any special treatment prior to the growth of the NWs [231, 244, 273]. Thus, the substrates are covered with a thin native silicon oxide. This native oxide layer typically has a thickness in the range 7 – 20 Å [202, 214, 216, 244, 249, 335]. For the growth of self-assisted InAs NWs on Si substrates, oxides with a thickness in the range of $\sim$ 1 nm are required [202] and certainly the way to obtain these thin oxide layers needs to be reproducible. Commonly, these thin oxides were created by wet chemical thinning of a thicker layer [177] or by a Ga-assisted deoxidation at high temperatures [202]. The latter suffers from the high thermal budget as well as a temperature gradient and corresponding gradient of the oxide thickness along the wafer. The first method requires both a precise deposition of the initial oxide layer as well as a controlled etching. Building up a new, thin layer of SiO_x at low temperatures is the preferential method. This possibility is evaluated first. The second section is dedicated to the VLS growth of InAs NWs on Si (111) substrates which has not yet been reported. The origin of the absence of the VLS growth of InAs NWs on Si substrates is investigated and it is overcome by an *in situ* etching of the surface.

4.2.1. Hydrogen-peroxide assisted reoxidation of Si substrates for the vapor solid growth of InAs nanowires[1]

Madsen *et al.* reported about an optimal silicon oxide thickness of 9 Å for the growth of InAs NWs on Si (111) substrates [202]. This thickness was achieved by a Ga-assisted deoxidation at high temperatures, resulting in an oxide thickness profile along the wafer being caused by a

[1] Most of the results of this section have been published in T. Rieger, D. Grützmacher, and M. I. Lepsa. *Si substrate preparation for the VS and VLS growth of InAs nanowires.* physica status solidi (RRL) - Rapid Research Letters, 7(10):840-844, 2013. Ref. [256]

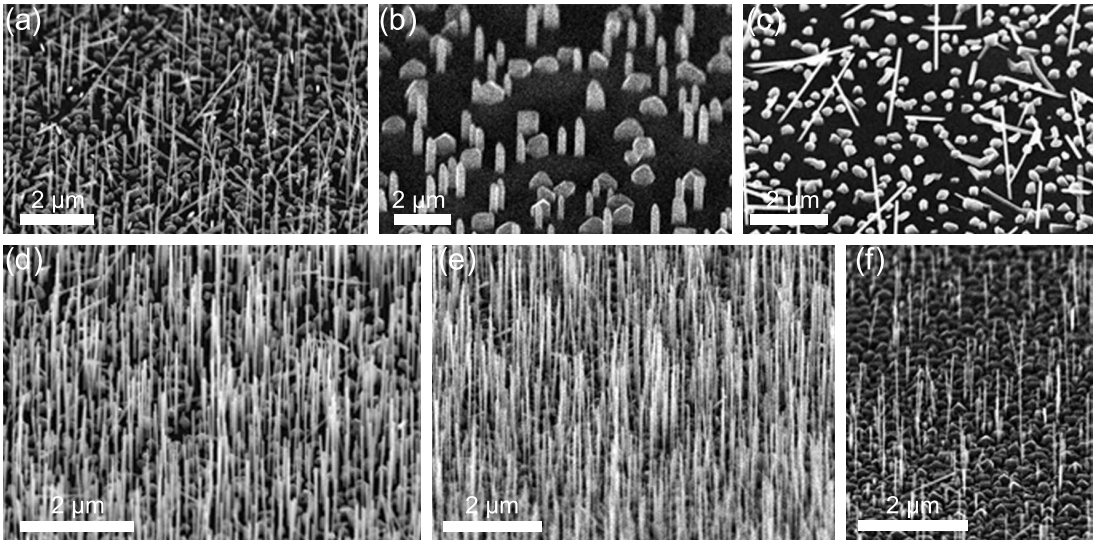

Figure 4.8.: *(a)-(f) SEM micrographs of VS InAs NWs grown on Si substrates with different substrate preparations: (a) after 1 day oxidation in air, (b) only HF cleaned, in (c)-(f), the substrates were HF cleaned and subsequently stored in H_2O_2 for durations of 30 min (c), 5 min (d), 1 min (e), 30 s (f). The samples were tilted by 60° relative to the substrate normal. Published in [256].*

temperature gradient from the center of the wafer to its edge [202]. Koblmüller *et al.* have used an etched SiO_x layer of 2.5 - 6 nm thickness [177]. The native silicon oxide has a thickness in the range of 20 Å, depending on the storing atmosphere and time [202, 214, 216, 244, 249, 335]. Accordingly, the native silicon oxide in principle has a thickness which is in the same range as the above listed values. Growing InAs on such native oxide covered Si substrates results in NWs. However, as seen in Fig. 4.8a, these are of low density and not well aligned. They grow with a random orientation and are therefore not suitable for a future integration into devices. The upper mentioned top-down methods for obtaining a suitable oxide thickness have the drawback of low reproducibility and high temperature treatment of the sample. Both these drawbacks can be circumvented when the oxide is build-up from a clean, H-terminated Si surface. Neuwald *et al.* have reported a wet chemical oxidation of Si (111) surfaces using hydrogen peroxide (H_2O_2) [222]. Silicon oxides with very low thicknesses were prepared due to significant different oxidation rates for the first and second Si bilayers. A 10 min reoxidation of the hydrogen passivated Si surface created a silicon oxide of about 5 Å thickness. After rather long reoxidation times, the oxide thickness saturated at a thickness corresponding to 2 Si bilayers. We adopted this method for obtaining well controlled SiO_2 thicknesses and have cleaned Si (111) samples using piranha solution and HF. After rinsing the sample in DI water, it was placed in H_2O_2 for a certain time t_{reox}. Subsequently, it was rinsed again in DI water and loaded immediately into the loadlock of the MBE system. The reoxidation time t_{reox} was varied between 30s and 24h. For comparison, one sample was prepared without the reoxidation step, thus a bare Si (111) surface, and a second one with one day reoxidation in ambient air. The samples were degased at 600°C for 10 minutes prior to the growth. After cool down to 490 °C, the growth of the NWs was initiated by opening the As and In shutters. The In rate and the As_4 flux were set to 0.035 µm/h and $2 \cdot 10^{-5}$ Torr, respectively. The growth time was 1 h. As described in Section 4.1.1, these growth conditions give rise to a droplet-free growth mechanism of InAs NWs: the growth proceeds in the vapor-solid growth mode. The low In flux is expected to result in a reasonable NW density in the range of 10 NWs/µm^2 (see Sec. 4.1.1).

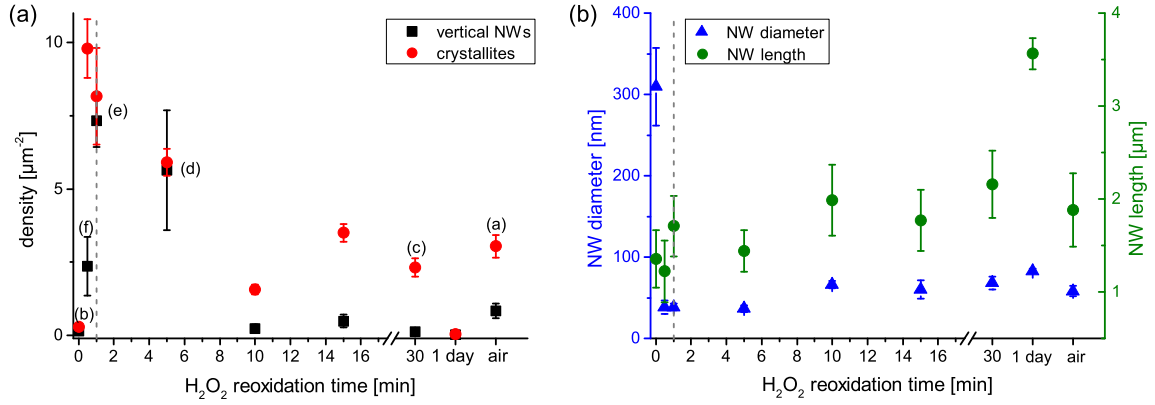

Figure 4.9.: *(a) Density of vertical NWs ■ and crystallites ● and (b) NW diameter ▲ and length ● as a function of the H_2O_2 reoxidation time. The optimum reoxidation time is 1 min and is marked by a dashed grey line. Labels in (a) refer to the corresponding SEM micrographs in Fig. 4.8. Published in [256].*

In Fig. 4.8a-f, SEM micrographs from samples with different reoxidation times are shown. The density of vertical NWs and crystallites as well as the diameter and length of the NWs were determined from the SEM images and are plotted as a function of the reoxidation time in Fig. 4.9a and b. Native oxides result in a low density of NWs, most of them being tilted (see Fig. 4.8a). The observed NWs were long and thin. However, many crystallites in-between the NWs were observed. Without any oxide, NWs grow perpendicular to the substrate and their density decreases (see Fig. 4.8b and 4.9a). These NWs are short and the diameter is significantly larger than that of the previous ones (see Fig. 4.9b). A significant improvement of the NW growth is observed when the substrate is treated with H_2O_2 prior to the growth. In Fig. 4.8c-f, the storing times in H_2O_2 continuously decrease from 30 min to 30 s. After a one day storage in H_2O_2 and subsequent growth, almost no NWs are found on the sample, indicating that the oxide layer is too thick. Also the number of crystallites is very low. A reduction of the storage time to 30 min enhances both the number of crystallites and NWs, being comparable with the substrate covered by a native oxide (see Fig. 4.8c and 4.9a). However, the NWs grow mainly tilted. An substantial improvement is observed when the reoxidation time is below 10 min. Figure 4.8d and e show SEM micrographs taken from samples where the H_2O_2 reoxidation times are 5 min and 1 min, respectively. The yield of vertical NWs is high and their diameter is in the range of 50 nm with a mean length of about 1.5–2 µm. The 1 min reoxidized sample is superior to the 5 min one due to a higher density of vertical NWs and less tilted NWs. The NW density is in the range of 7 NWs/µm^2, being comparable to VS grown InAs NWs on GaAs substrates. A further decrease to about 30 s reoxidation time does not improve the growth quality. Contrary, the NW density decreases drastically, though almost all NWs are vertical. The crystallite density increases as well (Fig. 4.8f).

These results demonstrate that a simple chemical treatment using H_2O_2 can be used to obtain the silicon oxide thickness required for the growth of VS InAs NWs. The growth of the VS NWs is believed to depend strongly on the substrate area being covered with an oxide. This means that short reoxidation times or no reoxidation at all result in very narrow oxide covered areas and, consequently, not much growth selectivity. An optimal reoxidation procedure provides an oxide layer with small pinholes which then enable the NW growth. An even longer reoxidation will form almost compact oxide layers. On these layers, the NWs cannot or only hardly nucleate. NWs obtained via this optimized substrate preparation represent the basis for several structures discussed in the following chapters.

4.2.2. Ga droplet induced etching of Si substrates for the vapor liquid solid growth of InAs nanowires[2]

The crystal structure of VS grown InAs NWs is rather poor, meaning that they contain a high density of stacking faults. Contrary, it was shown in Ref. [109] that VLS InAs NWs have a twinning superlattice with a periodicity of 5 – 6 nm. The growth of these VLS InAs NWs has been reported only rarely and, in each case, only on III-V substrates (GaAs, InAs, InP) covered by a thin layer of SiO_x [109, 205]. Applying the same growth conditions to Si substrates covered by a native oxide, large In droplets form on the surface but no NWs or crystallites are obtained (Fig. 4.10a). Similar results are achieved when the substrate is cleaned with HF prior to the growth (oxide-free surface) or reoxidizied in H_2O_2 as in the previous section. Also a change of the growth parameters does not result in the growth of NWs. Accordingly, the substrate itself is believed to play an important role in the initiation of InAs NW growth, not only the fluxes and the oxide layer. The major difference between Si and III-V substrates is the presence of atomic species with low melting points, such as Ga and In. Additionally, As or P evaporating from the substrate may also play a role. It is believed that pinholes in the oxide are required to act as nucleation site for the NW growth [90, 177]. A native oxide covering the Si substrate does not have such pinholes and the solubility of Si in liquid In is too low to etch these pinholes at the beginning of the growth [166]. Since the solubility of Si in liquid Ga is significantly higher, here, a Ga predeposition technique is applied to create pinholes. The basic principle is depicted in Fig. 4.11. The substrate is heated to a temperature T_{sub}^{Ga} for the deposition of liquid Ga. At this temperature Ga is deposited with a rate R for a duration t_{dep}. Subsequently, the substrate is kept for 5 min at the same temperature in absence of any flux. This process is repeated N times. At the end of the entire Ga pretreatment, the sample is kept another 15 min at the same temperature. During this time, the Ga desorbs completely from the substrate. In the absence of an As flux, Ga forms droplets which completely evaporate at high temperatures if no additional Ga is supplied [129]. Accordingly, the As shutter and valve are closed during the entire Ga pretreatment. After the Ga pretreatment, the substrate temperature is decreased to 530°C and an As flux and an In rate of $1.6 \cdot 10^{-6}$ Torr and 0.05 µm/h, respectively, are provided to grow the NWs. Grap *et al.* have determined these fluxes and temperatures to be ideal for the VLS growth of InAs NWs on GaAs substrates [109].

Standard values for T_{sub}^{Ga}, R, t_{dep} and N during the Ga pretreatment of the surface were chosen to 600°C, 0.08 µm/h, 90s and 5, respectively. A substrate temperature T_{sub}^{Ga} of 600°C in combination with a Ga rate R of 0.08 µm/h is known to promote the growth of GaAs NWs on Si substrates and therefore to be suitable to etch pinholes into silicon oxide. In Fig. 4.10b, a SEM micrograph of a sample using this pretreatment and the above given growth conditions is shown. The InAs growth time was 3 h. NWs and crystallites have formed on the substrate. The NWs are catalyzed by an In droplet, as seen in the close up in Fig. 4.10c. The presence of the droplet is a clear demonstration for a droplet-assisted growth mechanism. This is further supported by the low V/III flux ratio ($\sim$ 7). Figure 4.10h shows InAs NWs and crystallites grown for 1 h after the substrate underwent the above described pretreatment. A high density of crystallites and short NWs is observed. In order to distinguish them, the NWs are colored in blue and are additionally identified by the presence of the In droplet. The NW density is around 2 – 3 NWs/µm^2. They have a mean length of about 150 nm and a diameter of $\sim$ 80 nm. After a growth time of 3 h, their length and diameter increased to $\sim$ 2 µm and $\sim$ 200 nm, respectively. It is expected that both length and diameter increase linearly in time as in the case

[2]Most of the results of this section have been published in T. Rieger, D. Grützmacher, and M. I. Lepsa. *Si substrate preparation for the VS and VLS growth of InAs nanowires.* physica status solidi (RRL) - Rapid Research Letters, 7(10):840-844, 2013. Ref. [256]

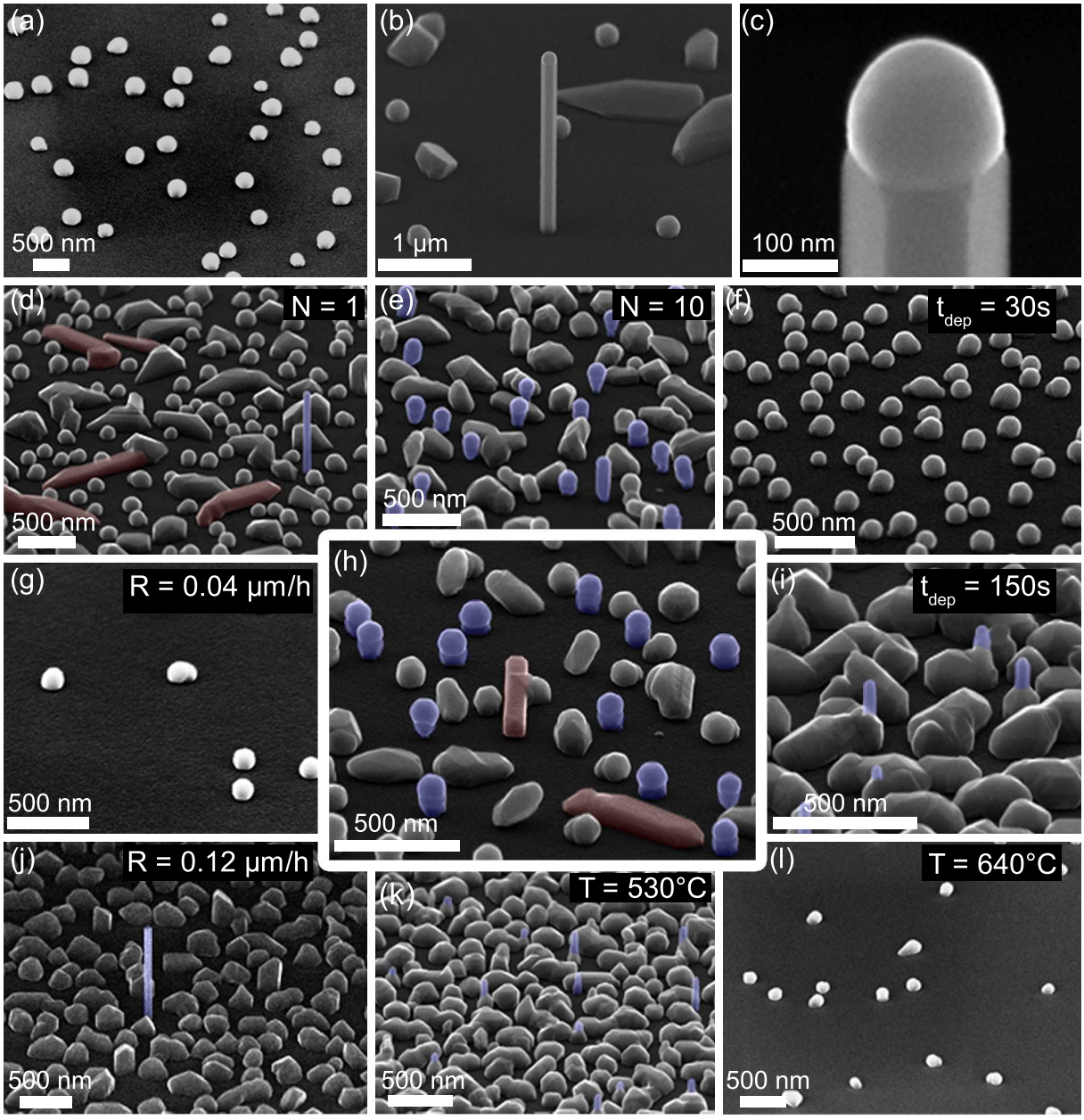

Figure 4.10.: *VLS grown InAs NWs using different Ga predeposition techniques. (a) Si substrate without any pretreatment. (b) Standard Ga predeposition as described in the text and a growth time of 3 h. (c) A zoom-in to the NW top. (d)-(l) SEM images of samples with different predeposition conditions and for 1 h growth time; the central image (h) shows the standard conditions. (d) $N = 1$, (e) $N = 10$, (f) $t_{dep} = 30s$, (i) $t_{dep} = 150s$, (g) $R = 0.04\mu m/h$, (j) $R = 0.12\mu m/h$, (k) $T = 530°C$ and (l) $T = 640°C$. Blue color in (d)-(k) highlights NWs (identified by their length or the droplet on top), while the red color in (d) and (h) marks planar structures with rectangular cross sections. The samples were tilted by 60° relative to the substrate normal. Published in [256].*

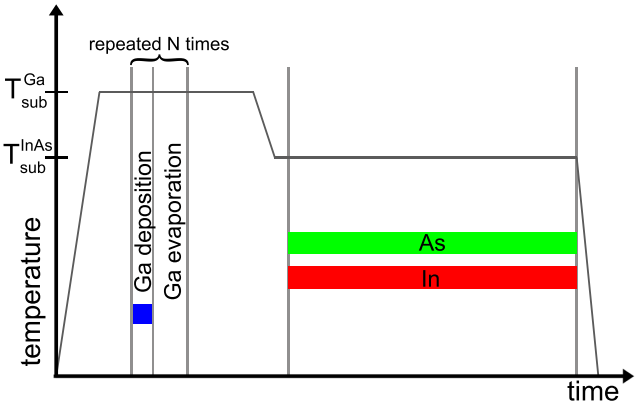

Figure 4.11: *Schematic diagram showing the Ga pretreatment of Si substrates for the VLS growth of InAs NWs. T_{sub}^{Ga} is the substrate temperature during the pretreatment, T_{sub}^{InAs} the substrate temperature during the NW growth. The blue area represents the time Ga is supplied, green and red areas indicate the supply of As and In, respectively.*

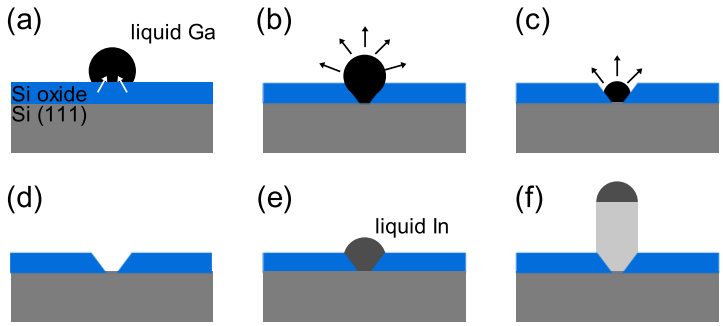

Figure 4.12: *Schematic model of the VLS growth of InAs NWs on Si substrates induced by Ga predeposition. (a) Ga droplet formation and subsequent alloying with Si oxide. (b) Pinhole formation. (c) Ga re-evaporation. (d) Pinhole in the oxide. (e) In droplet formed over the pinhole. (f) NW growth from the In droplet. Published in [256].*

of the VLS growth of GaAs and InAs NWs on GaAs substrates [109, 259]. Similarly, also in this case, a certain incubation time is required until the In droplet forms at a pinhole. To evaluate the impact of the Ga predeposition, each predeposition parameter is varied individually keeping the other parameters constant. Figures 4.10d and e show SEM images where the number of Ga deposition cycles N are 1 and 10, respectively. A small N (Fig. 4.10d) results in a low density of NWs and crystallites. Additionally, many In droplets not catalyzing NWs are seen. Higher N (Fig. 4.10e) give almost the same NW density as shown in Fig. 4.10h but with an increase of the the amount of crystallites. The Ga predeposition time t_{dep} influences the NW growth: a reduction of t_{dep} to 30 s does not promote any NW growth (Fig. 4.10f) while an increase to 150 s enhances the growth of crystallites with only few short NWs in-between (see Fig. 4.10i). Most of these NWs are already partially connected to crystallites. By varying the Ga rate R, similar dependencies are found: a low Ga rate of around 0.04 µm/h does not promote the growth of any crystalline material while a higher Ga rate (0.12 µm/h) results in many crystallites and only few NWs (Fig. 4.10j). Finally, by changing the Ga predeposition temperature to either 530°C or 640°C, as shown in Fig. 4.10k and l, respectively, mainly crystallites or no growth at all is observed.

Taking the above described results into consideration, it is clear that all predeposition parameters strongly influence the subsequent NW growth. Consequently, it is essential to chose the correct set of parameters. A simple picture of the predeposition process and resulting NW growth is described as follows. First, Ga droplets form on the surface (Fig. 4.12a). Subsequently, these droplets alloy with Si from the oxide and the droplets penetrate through the oxide (Fig. 4.12b). Parts of the Si surface are then in direct connection to the Ga droplet. When the Ga supply is switched off, the high substrate temperature causes a re-evaporation of Ga from the droplet (Fig. 4.12c) forming pinholes in the oxide layer (Fig. 4.12d). A subsequent supply of In results in the formation of In droplets in these pinholes (Fig. 4.12e). The supersaturation of the In

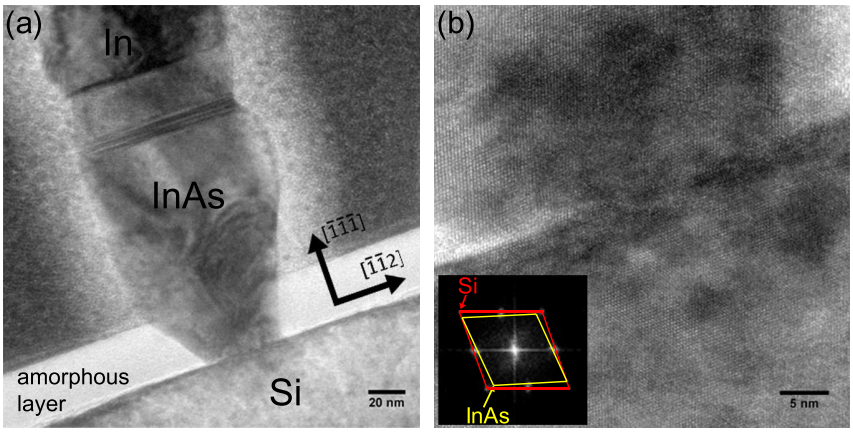

Figure 4.13: *TEM micrographs of a FIB-prepared lamella with VLS grown InAs NWs on Si substrates. (a) TEM cross-section of a NW similar to those in Fig. 4.10h. (b) High resolution image of the InAs/Si interface. The inset shows the FFT of the interface. Dr. Elmar Neumann prepared the FIB lamella. Published in [256].*

droplets with As gives rise in the growth of InAs between the droplet and the Si surface, forming a NW (Fig. 4.12f).

The formation of the crystallites formation may be described in a similar way; having also an epitaxial relation to the Si substrate. Two different kinds of parasitic growth in-between the NWs are observed: irregular shaped crystallites and elongated structures with a rectangular cross-section (see Fig. 4.10d and h). Both are observed only when the Ga pretreatment took place. Therefore, the formation of the parasitic growth should also take place in openings in the oxide, i.e. pinholes or larger exposed areas. The number of crystallites increases as the amount of predeposited Ga is increased. The Ga etches the Si oxide, as described above, and not only pinholes but also larger areas may be exposed, e.g. due to a coalescence of Ga droplets or the existence of several droplets in close vicinity. Crystallites may grow preferentially on these larger areas while NWs are grown from pinholes in the oxide.

To obtain more information on the nucleation process of the NWs, cross-sectional TEM micrographs were acquired. For this purpose, the as-grown sample was first covered by an amorphous material and subsequently, focused ion beam (FIB) was used to prepare a TEM lamella. Figure 4.13 displays TEM micrographs from this lamella. The NW has a conical shape at the bottom indicating that it emerges from a significantly smaller nucleation site (see Fig. 4.13a). The In droplet on top is clearly seen and proves the VLS growth mechanism. The NW itself has only few stacking faults close to the droplet, being in agreement with previous reports about the existence of a pure ZB phase at the bottom [109]. This pure ZB phase at the NW bottom is seen in the HRTEM image of the Si-InAs interfacial region depicted in Fig. 4.13b. The InAs NW exactly adopts the stacking sequence of the Si substrate, no stacking fault or twin is formed at the interface. The inset in Fig. 4.13b shows a FFT of the interfacial region. Two groups of spots corresponding to the Si substrate and the InAs NWs are observed. The spots from the InAs belong to a ZB crystal structure and are rotated by a small angle with respect to the Si lattice. This indicates a slight tilt of the NW with respect to the substrate. This tilt is not necessarily present in all NWs. The difference between the diffraction spots belonging to Si and InAs agrees well with the expected value, reflecting the lattice mismatch and indicating a complete strain relaxation. Due to the Ga pretreatment of the substrate, residual Ga on the surface may influence the NW growth and nucleation. In principle, residual Ga can be located at two different positions within the NW: either it is stored in the droplet (i.e. not incorporated into the NW) or it is incorporated at the NW base during the nucleation process (with a gradual decrease of the Ga concentration along the growth axis). Figure 4.14a shows a TEM micrograph with superimposed EDX line scan of the tip of a long NW including the In droplet. The droplet

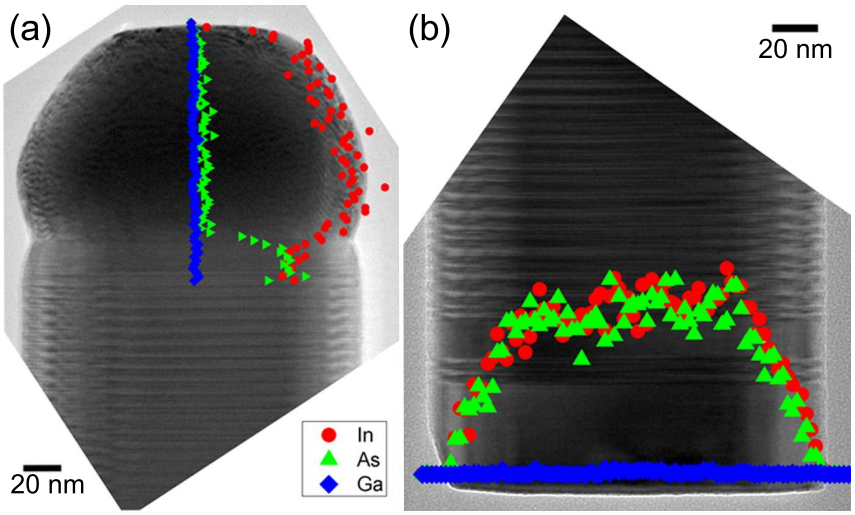

Figure 4.14: *EDX profiles of As ▲, In ● and Ga ♦ superimposed onto TEM images of VLS grown InAs NWs grown on Si substrates. (a) NW top with In droplet. (b) NW bottom. Published in [256].*

is pure In and the Ga and As signals are below the detection limit. The NW base and the corresponding EDX line scan are shown in Fig. 4.14b. Also there, the Ga signal is below the detection limit. Thus, no evidence of Ga participating in the NW growth or nucleation is found.

HRTEM images of a VLS grown InAs NW are depicted in Fig. 4.15. The NW has a uniform diameter with no evidence of tapering, as seen in the overview image in Fig. 4.15a. The droplet on top of the NW is clearly identified. In Fig. 4.15b, the upper part of the NW including the interface to the In droplet is depicted. Immediately below the droplet, the NW diameter slightly shrinks and the crystal structure is WZ. This WZ segment has a length of about 15 nm. Beneath the WZ phase, the crystal structure switches into ZB phase with twins. These twins have a very uniform spacing of about 3 nm ($\sim 8-9$ atomic layers), thus a periodicity of 6 nm. In fact, this twinning superlattice is found almost along the entire length of the NW (see Fig. 4.15c). Only at the bottom and at the top the crystal structure changes. At the bottom, it is typically ZB with only few twins. The identical crystal structure of VLS grown InAs NWs was also found previously when grown on GaAs substrates [109]. Consequently, this reflects that by applying the Ga pretreatment, the growth of In catalyzed III-V NWs can be transferred from GaAs to Si substrates without affecting the properties of the NWs.

At this point, the remaining question is why VLS grown InAs NWs on Si substrates are achieved only via the Ga predeposition technique while they are grown on III-V substrates without a surface pretreatment. In the case of III-V substrates, a Ga oxide or In oxide layer is present between the substrate and the SiO_x layer. Existing pinholes in this SiO_x layer (obtained by etching or due to the porosity of annealed HSQ films) can reach the substrate and the Ga oxide or In oxide can be thermally removed. On Si substrates, on the other hand, pinholes have to be etched into the oxide layer *in situ* since they would reoxidize in air. This *in situ* pinhole etching is achieved more easily by Ga than by In since the solubility of Si is significantly larger in liquid Ga than in liquid In [166].

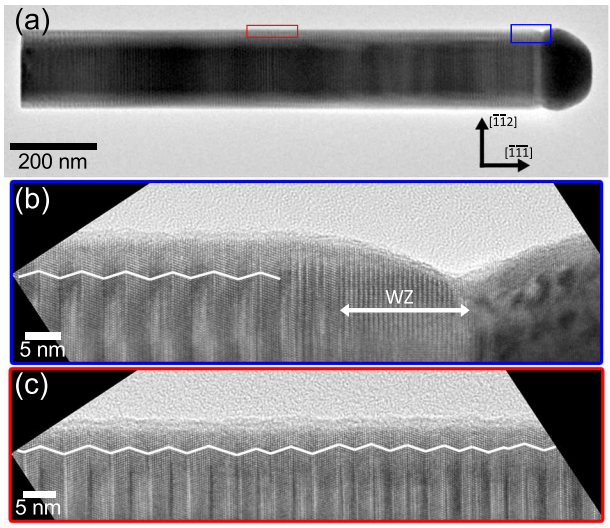

Figure 4.15: *(HR)TEM images of an InAs NW grown on Si substrates. (a) overview image of the entire NW with two marked regions from which HRTEM images are shown in (b) and (c). (b) Crystal structure at the interface NW/droplet. Immediately below the droplet, the crystal structure is WZ whereas it is regularly twinned ZB for the rest of the NW. (c) Twinning superlattice observed along the main part of the NW. The white lines in (b) and (c) indicate the stacking sequence.*

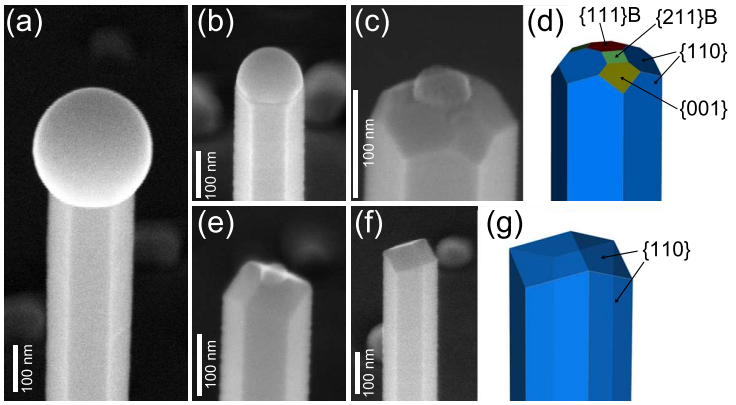

Figure 4.16: *SEM micrographs showing the Ga droplet at different consumption stages (a-c) and (e-f). (a) represents the unintentionally consumed Ga droplet after the NW growth. Consumption durations are (b) 15 min, (c) 20 min, (e) 22.5 min and (f) 25 min. Models in (d) and (g) illustrate the different facets in (c) and (f), respectively. Published in [261].*

4.3. Wurtzite inclusions in vapor-liquid-solid grown III-V nanowires[3]

In III-V NWs, polytypism with the coexistence of the ZB and WZ crystal phases within the same NW is often observed [3, 73, 106, 134, 204, 235]. Usually, investigations are aiming for pure crystal phases e.g. in order to increase the conductivity by decreasing the amount of scattering centers [300]. Having control of the crystal structure also includes to study NWs with pure WZ crystal structures and therefore working e.g. with effects that are not observed in bulk materials such as the direct band gap of WZ GaP [10]. On the other hand, controlling the crystal structure also includes the control of defects such as twins and stacking faults, thus including these defects at a certain position or even switching in a controlled manner between both possible crystal structures. Using the latter, crystal phase quantum dots can be created [4, 292]. This possibility of crystal phase control is discussed and described in the following sections.

As it was shown e.g. in Refs. [259] and [54] as well as Sec. 4.2.2, self-catalyzed III-V NWs have the WZ crystal structure just below the droplet while the main part has the ZB structure. This WZ structure is related to the partial consumption of the droplet at the end of the

[3] Most of the results of this section have been published in T. Rieger, M. I. Lepsa, T. Schäpers, and D. Grützmacher. *Controlled wurtzite inclusions in self-catalyzed zinc blende III-V semiconductor nanowires.* Journal of Crystal Growth, 378:506-510, 2013. Ref. [261] and T. Rieger, T. Schäpers, D. Grützmacher, and M. I. Lepsa. *Crystal Phase Selective Growth in GaAs/InAs Core-Shell Nanowires.* Crystal Growth & Design, 14(3):1167-1174, 2014. Ref. [264]

growth when the group III supply is stopped while the As supply is still maintained. Here, consumption refers to the decreasing size of the Ga (In) droplet due to the growth of GaAs (InAs) while the supply of Ga (In) is interrupted. In order to use this consumption to include short WZ segments in the NWs, the consumption mechanism has to be investigated i.e. the vanishing of the droplet when no group III element is supplied. Exemplary, the consumption mechanism is studied using GaAs NWs. Figure 4.16 shows SEM micrographs of the GaAs NW top at different stages of the droplet consumption. For this analyzes, GaAs NWs were grown for 2h at 600°C with a Ga rate of 0.1 µm/h and an As_4 flux of 10^{-6} Torr. Subsequently, the Ga supply was stopped for a certain duration while the As supply was maintained. During this stage, the droplet is (partially) consumed by the As: the droplet volume decreases due to the growth of GaAs. The times for the exclusive supply of As, i.e. the droplet consumption times, were varied between 2.5 and 25 min. In Fig. 4.16a, the initial stage is shown, thus without an intentional droplet consumption. The contact angle β is $\sim 137°$. The consumption duration in b, c, e and f are 15 min, 20 min, 22.5 min and 25 min, respectively. The droplet consumption can be divided into two stages. In the first stage, the droplet diameter and the contact angle decrease while the NW diameter just beneath the droplet is constant (Fig. 4.16b). This stage is usually present when the substrate is cooled down after the growth. The crystal structure is WZ as confirmed by post-growth TEM analyzes [259]. When the contact angle reaches 90°, the situation changes. The contact angle remains constant and both the droplet diameter and the NW diameter decrease (Fig. 4.16c). In this second stage, new facets are created. These are $\{110\}$, $\{001\}$ and $\{211\}$B facets as schematically shown in Fig. 4.16d. The latter two facets disappear again during further droplet consumption (Fig. 4.16e,f). Only the stable $\{110\}$ facets remain (see Fig. 4.16g). The top pyramidal part has a threefold symmetry which is clear proof that it has a ZB crystal structure. The consumption stages shown in Fig. 4.16c-e are observed only within a short interval of time. During this time, the complete consumption is no longer determined by the material incorporation from the Ga droplet into the NW but by the growth of the most stable $\{110\}$ facets resulting in a much faster vanishing of the droplet than expected from a consumption by incorporation from the Ga droplet. The Ga from the droplet evaporates, it is incorporated below the droplet or on the $\{211\}$B and $\{001\}$ facets. These then change into the stable $\{110\}$ facets due to adatom migration from the droplet to the side facets [130].

Summarizing, the evolution of the crystal structure of GaAs NWs can be described by three stages:

1. NW growth: Ga and As are supplied and the contact angle β is constant at about 137°, $\beta = 137°$. The droplet radius is either constant or slightly increases in time ($\frac{dr_{droplet}}{dt} \geq 0$). Similarly, also the NW diameter increases in time ($\frac{dr_{NW}}{dt} \geq 0$). The crystal structure is ZB with twins.

2. First stage of droplet consumption: Only As is supplied and the contact angle decreases ($\frac{d\beta}{dt} < 0 \wedge \beta > 90°$) while the NW diameter remains constant ($\frac{dr_{NW}}{dt} = 0$). The crystal structure switches to WZ.

3. Second stage of droplet consumption: Only As is supplied, the contact angle remains at 90° and the top diameter of the NW shrinks ($\frac{dr_{NW}}{dt} \leq 0$). At this stage, the crystal structure again switches to ZB.

Especially the last stage seems to depend strongly on the growth conditions since both $\{110\}$ faceted top regions as well as flat surfaces with a $\{111\}$B type top were observed in the literature [82, 248]. Only the first stage of droplet consumption is required to include WZ segments

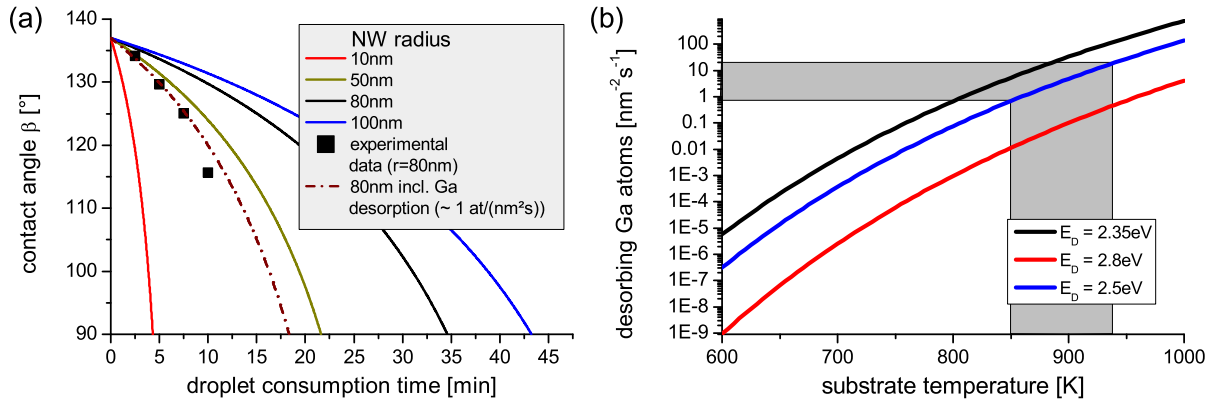

Figure 4.17.: *(a) Calculated contact angle of the Ga droplet as a function of the consumption time for different NW radii and the experimental data (NW radius 80 nm). The As_4 flux is 10^{-6} Torr. (b) Calculated flux of desorbing Ga atoms from the droplet as a function of the temperature. The grey area shows the temperature range for the growth of GaAs NWs and the corresponding desorbing Ga flux considering 2.35 eV$\leq E_D \leq$2.5eV. Published in [261].*

into GaAs NWs. To fully understand the droplet consumption as well as the limitations in the formation of WZ segments, a kinetic model was developed.

4.3.1. Theoretical description and limitations

The first stage of droplet consumption can be modeled as follows: A droplet of given radius r_d is on top of a NW with radius r_{NW}, the contact angle is β. For Ga droplets catalyzing GaAs NWs, this contact angle is 137°. The droplet volume is defined by

$$V_{droplet} = \frac{\pi \cdot r_{NW}^3}{3} \cdot (1 - \cos\beta)^2 \cdot \frac{2 + \cos\beta}{\sin^3\beta} \tag{4.1}$$

and its relevant surface area by

$$A_{droplet} = A_{\perp} \cdot \cos(32°) + A_{||} \cdot \sin(32°) \tag{4.2}$$

Here, $A_{droplet}$ already takes into account that the adatom fluxes impinge under an angle $\alpha = 32°$ on the substrate, i.e. it is subdivided into one component parallel ($A_{||} \cdot \sin(32°)$) and another one perpendicular ($A_{\perp} \cdot \cos(32°)$) to the surface of the substrate. Consumption of Ga from the droplet proceeds via impinging As atoms on the droplet. Diffusion of As on the NW side facets is negligible [250, 185, 102, 103]. Thus, the droplet consumption rate and, consequently, the WZ growth rate are proportional to the directly impinging As flux F_{As}. The proportionality factor depends on the shape of the droplet and the geometry of the MBE system. The total number of As atoms impinging on the droplet is given by

$$N_{As} = F_{As} \cdot A_{droplet} \tag{4.3}$$

The growth rate R is then given by N_{As} and r_{NW} via $R = \frac{N_{As} \cdot \Omega_{GaAs}}{\pi r_{NW}^2}$. Ω_{GaAs} refers to the volume occupied by one GaAs molecule in the crystal. Consequently, the droplet diameter and contact angle are decreased with each impinging As atom and therefore also $A_{droplet}$ and N_{As} decrease. Figure 4.17a shows calculated contact angles as a function of the consumption time for different NW radii. The As_4 flux was set to $1 \cdot 10^{-6}$ Torr, which results in a GaAs NW

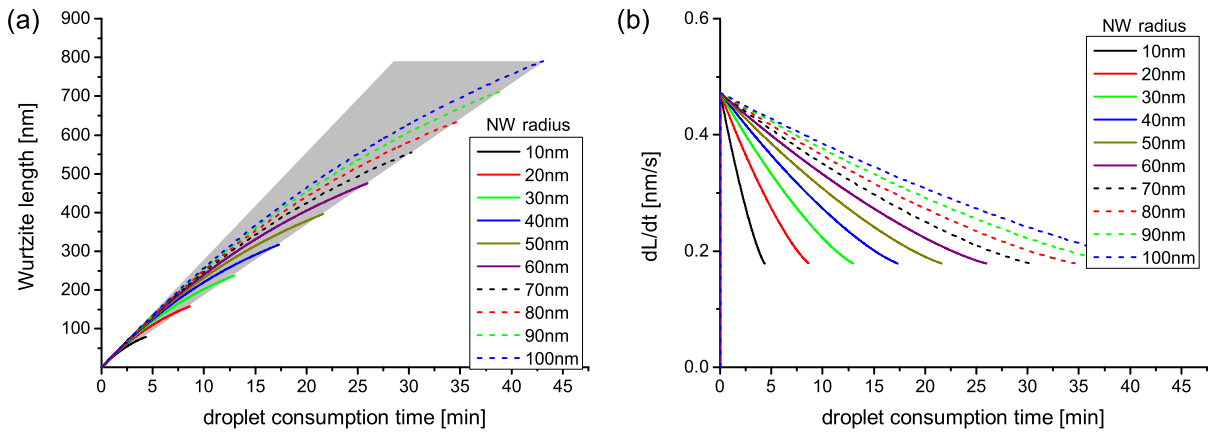

Figure 4.18.: *Expected length (a) and growth rate (b) of the WZ segment as a function of the droplet consumption duration for different initial NW radii. The initial contact angle is 137° and the As_4 flux 10^{-6} Torr. The grey area in (a) indicates the WZ lengths that can be obtained.*

growth rate of about 1.7 µm/h. Experimentally determined contact angles for different droplet consumption times are shown in the same graph. There, the NW radius was 80 nm and the As_4 flux was $1 \cdot 10^{-6}$ Torr. A strong disagreement between the calculated curve for 80 nm radius and the experimental data is present. However, the general shape of the curve is identical. The difference between the experimental and calculated data is explained by an additional Ga consumption mechanism which was not taken into account above, i.e. Ga desorption. According to Heyn [129] the Ga desorption rate R_d can be calculated using

$$R_d = \nu \cdot exp\left(-\frac{E_d}{k_B T}\right) \tag{4.4}$$

where $\nu = \frac{2k_b T}{h}$ is the vibrational frequency of the Ga atoms. Reported values of the activation energy E_d for the desorption of Ga from a Ga droplet vary between 2.35 and 2.8 eV [129, 326, 352]. Using these values, the Ga desorption rate is calculated and plotted as a function of the temperature in Fig. 4.17b. Assuming E_d in the range of 2.35 to 2.5 eV, a desorption rate in the range of 1 to 20 atoms $nm^{-2}s^{-1}$ at a temperature of about 600°C is expected. Using even the lower boundary, i.e. 1 atom $nm^{-2}s^{-1}$, as an additional Ga consumption mechanism, the experimental data can be well fitted as seen in Fig. 4.17a. Here, Ga desorption occurs via the total surface area of the droplet, which is given by

$$A_{des} = 2\pi \frac{{r_{NW}}^2}{\beta}(1 + |\cos\beta|) \tag{4.5}$$

Thus, Ga desorption from the droplet represents a non-negligible mechanism of Ga consumption.

Based on these calculations, the WZ length that is grown when only As is supplied can be estimated. The results are plotted in Fig. 4.18a showing that the length increases sublinear with the growth time, being caused by the continuously decreasing contact angle. This becomes clearer when the first derivative, i.e. the growth rate, is calculated: The growth rate decreases in time and is significantly steeper for thin NWs. Thus, the actual length grown during the As-only supply depends on both the consumption time and the initial NW diameter. The NW diameter typically varies slightly on the sample. However, as shown by the shaded area in Fig. 4.18a, the length can be estimated within a certain window even without knowledge of the NW diameter.

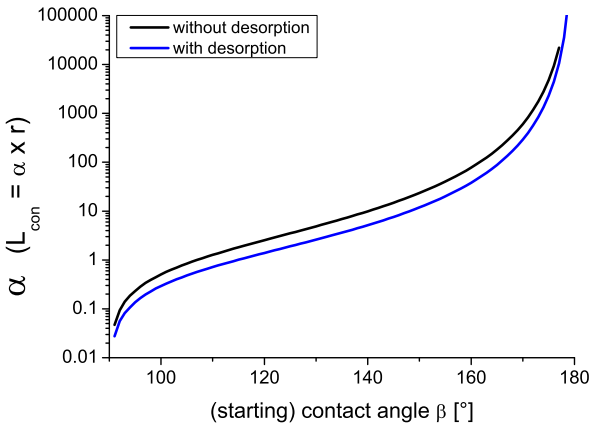

Figure 4.19: *Maximal WZ length as a function of the initial contact angle. The maximal WZ length is given by the factor α being the length normalized to the NW radius.*

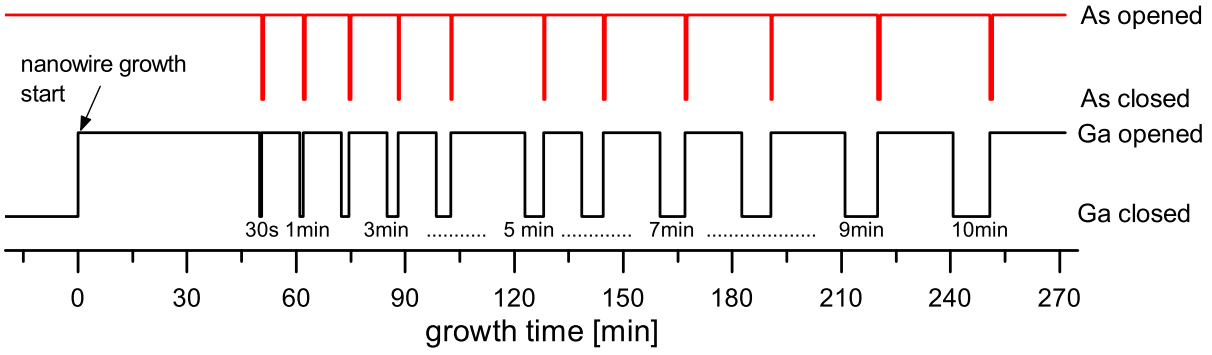

Figure 4.20.: *Schematic illustration of the program to include WZ segments into GaAs NWs using a partial droplet consumption. Published in [261]*

For future structures, several of these WZ segments need to be placed inside a NW either as barriers for crystal phase quantum dots or to modify the electronic transport. In this case, the crystal structure needs to switch back from WZ to ZB and the entire process needs to be repeated several times. For the latter, the droplet contact angle first has to increase again. However, especially for a short supply of both Ga and As the contact angle will not increase back to 137°. The maximal WZ length of the subsequent Ga supply interruption depends on the initial contact angle and not the equilibrium one. Consequently, similar calculations have been repeated for various contact angles between 90° and 180°. The overall conclusion is that the maximal length grown during the consumption L_{con} is proportional to the NW radius r via a factor α ($L_{con} = \alpha \cdot r$). α depends on the (initial) contact angle. Figure 4.19 shows the maximal WZ length (normalized to the NW radius), i.e. the factor α, as a function of the initial contact angle. For an initial contact angle of 137°, the maximal WZ length is roughly 10 times the NW radius. Since Ga desorption occurs, α depends on the actual NW growth rate, i.e. the As flux. Increasing the supplied As flux moves the real curve (with Ga desorption) towards the ideal one (without Ga desorption) due to the decreased contribution of Ga desorption, thus a faster droplet consumption results in less desorption. The switching back from WZ to ZB has to be demonstrated experimentally.

4.3.2. Wurtzite inclusions in GaAs nanowires

In order to experimentally confirm the above shown calculations, GaAs NWs with several Ga supply interruptions were grown. First, GaAs was grown for 50 minutes followed by eleven

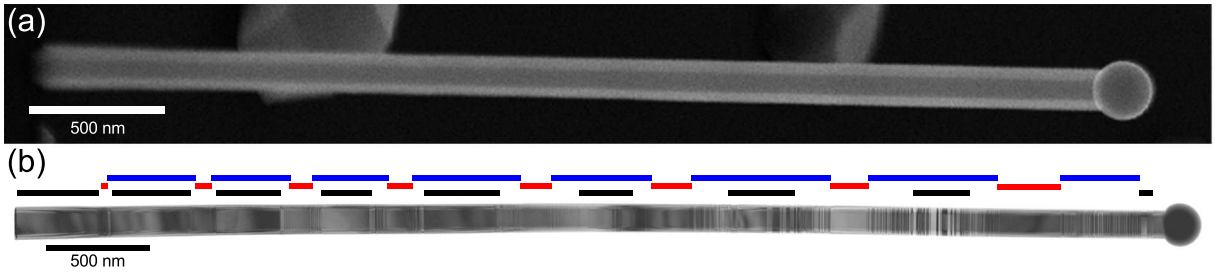

Figure 4.21.: *SEM (a) and TEM (b) micrographs of GaAs NWs with WZ inclusions as given by the growth sequence in Fig. 4.20. Red lines indicate the position of WZ segments, black those of long ZB segments. The blue lines show the length between two WZ neighboring segments.*

Ga supply interruptions increasing from 30s to 10 minutes. Each interruption ended with a short supply of Ga in order to refill the droplet. Subsequently, GaAs was grown again for 15-20 minutes. During the interruption, the contact angle of the Ga droplet decreases due to consumption of Ga by the As whereas the pure Ga pulse is used to increase the droplet fast. The decrease of the contact angle gives rise to a nucleation at the triple phase line between the vapor phase, the liquid droplet and the solid NW [345]. The growth sequence is schematically depicted in Fig. 4.20. Different durations of GaAs growth between two subsequent Ga supply interruptions act as markers for the further analyses. A SEM micrograph of a complete NW is shown in Fig. 4.21a. As obvious, the droplet is present on top of the wire, being an indication for a successful growth sequence maintaining the droplet. The corresponding TEM micrograph is shown in Fig. 4.21b. Several contrast changes along the NW indicate changes in the crystal structure. By means of HRTEM these changes in the crystalline structure can be identified, thus the WZ and ZB crystal phases can be clearly distinguished. Black rectangles next to the TEM micrograph mark long pure ZB parts while red rectangles mark WZ regions. The blue rectangles mark the regions between two adjacent WZ segments. In between the long ZB and WZ regions, the density of stacking faults and twins is high. The lengths of the WZ segments (red rectangles) increase along the NW axis, being in agreement with the growth sequence from Fig. 4.20. Correlating each individual WZ segment with the corresponding duration of the Ga supply interruptions reveals a growth rate of about 1.8-2 µm/h. Similarly, the lengths of the ZB segments in between two adjacent WZ segments correspond to growth rates of $\sim$ 2 µm/h. Both growth rates agree well with previously determined growth rates using similar growth conditions [259]. Interestingly, in general we have observed only eight WZ segments embedded between two ZB parts while the growth sequence has eleven Ga supply interruptions. Consequently, the three shortest Ga supply interruptions being 30 s, 1 min and 2 min were not found to have an impact on the crystal structure of the NWs. Nonetheless, it can be concluded that the Ga supply interruptions longer than 2 min lead to WZ segments and by supplying again both elements, the crystal structure changes back to the ZB phase. However, as seen in the TEM image, the transitions from the long ZB segments to the WZ segments are not abrupt but characterized by a transition region. The length of the transition region is different when switching from ZB to WZ than reverse, additional it depends on the growth history. This means that the transition length is short for an early interruption and considerably longer for a later one. In Tab. 4.2, the lengths of the transition regions as well as the corresponding WZ segment length are listed for several interruption.

HRTEM micrographs of several WZ segments including the transition regions from the NW displayed in Fig. 4.21b are shown in Fig. 4.22, exemplary the interruptions corresponding to a

interruption duration	WZ segment length	length transition region ZB-WZ	length transition region WZ-ZB	number of WZ segments in transition region ZB-WZ	number of WZ segments in transition region ZB-WZ
30 s	-	-	-	-	-
1 min	-	-	-	-	-
2 min	-	-	-	-	-
3 min	15-20 nm	25 nm	10 nm	0	0
4 min	50 nm	20 nm	40 nm	3	4
5 min	70 nm	25 nm	45 nm	4	5
6 min	90 nm	40 nm	60 nm	4	6
7 min	180 nm	80 nm	150 nm	6	11
8 min	250 nm	100 nm	200 nm	7	13
9 min	350 nm	200 nm	$\geq$350 nm	many	many
10 min	400 nm	250 nm	$\geq$400 nm	many	many

Table 4.2.: *Lengths of the WZ segments depending of the Ga supply interruption duration.*

Ga supply interruptions of 3 min, 4 min, 6 min and 8 min are chosen. As obvious for all images, the crystal structure changes from ZB to WZ and backwards and the length of the WZ segment increases with the Ga supply interruption duration. The interface contains mostly twinned ZB with a high density of twins. Some thin WZ segments are found in the transition regions, being indicated by either arrows or blue overlays. Similar as the length of the transition region, also the number of WZ segments within it depends on the growth history. The later the interruption occurs in the growth sequence, the more WZ segments are present in the transition region. In general, more WZ segments are present in the transition regions from WZ to ZB than from ZB to WZ. The number of WZ segments in the transition regions is also given in Tab. 4.2.

The shortest WZ segment found has a length of about 15 – 20 nm and is depicted in Fig. 4.22a. The crystal structure changes from ZB to WZ within $\sim$ 25nm, while it changes back within only $\sim$ 10 nm. A longer Ga supply interruption is shown in Fig. 4.22b. Here, the behavior at the interface changes: The switching from ZB to WZ is more abrupt than vice versa. This is also the case for all further supply interruptions. Both interfaces have only small amounts of the WZ phase. A further increase of the Ga supply interruption duration results in even longer WZ segments (Fig. 4.22c). The interfaces have significant amounts of the WZ phase but more WZ segments are found in the interface from WZ to ZB than reverse. For the longest WZ segment depicted in Fig. 4.22d (Ga supply interruption of 8 min), the interface from ZB to WZ has a length of about 100 nm while it is twice as high when the crystal structure switches back from WZ to ZB. The high resolution images in Fig. 4.22e and f display the interface regions from ZB to WZ and from WZ to ZB, respectively. Black arrows point to WZ segments within these interface regions. Here, it is clearly seen that the interface from WZ to ZB has substantially more short WZ segments than the interface ZB to WZ. The different lengths of the transition regions along the growth axis may be attributed to the size of the droplet. Both the NW diameter and the droplet diameter increase almost linearly with the growth time [55, 259]. Since the volume of the droplet is $\propto r^3_{droplet}$ while its surface is only $\propto r^2_{droplet}$, a larger droplet needs longer to reach the conditions leading to the formation of the WZ phase.

Certainly, it is important to choose the correct Ga supply interruptions since too short times

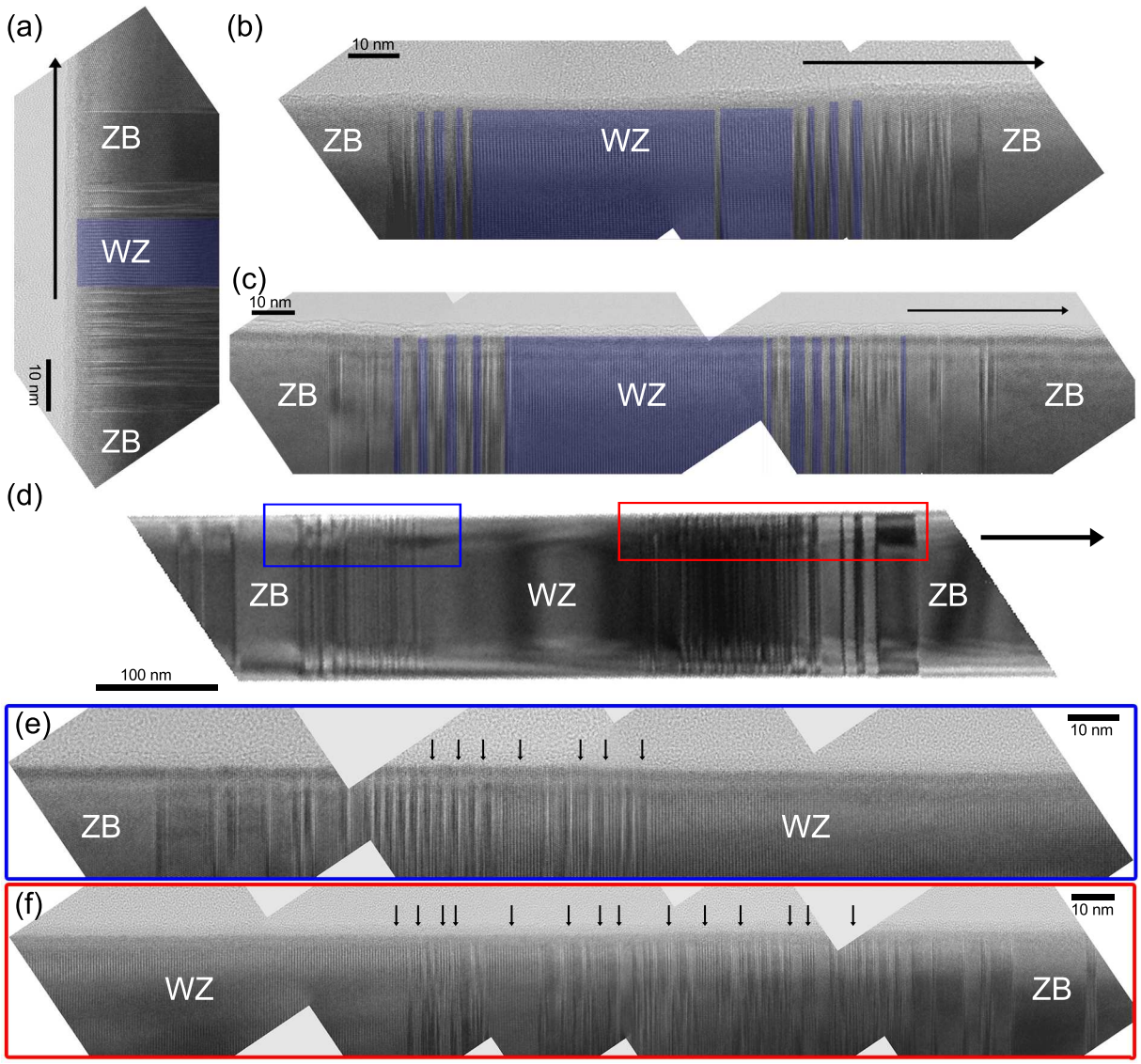

Figure 4.22.: *HRTEM micrographs of WZ inclusions in ZB GaAs NWs. The Ga supply interruption times were (a) 3 min, (b) 4 min, (c) 6 min and (d) 8 min. (e) and (f) show HRTEM images of the interfaces from (e) ZB to WZ and (f) WZ to ZB of the interruption shown in (d). Blue overlays in (a)-(c) mark WZ segments whereas they are highlighted by small arrows in (e) and (f). Arrows in (a)-(d) indicate the NW growth direction. Published in [264].*

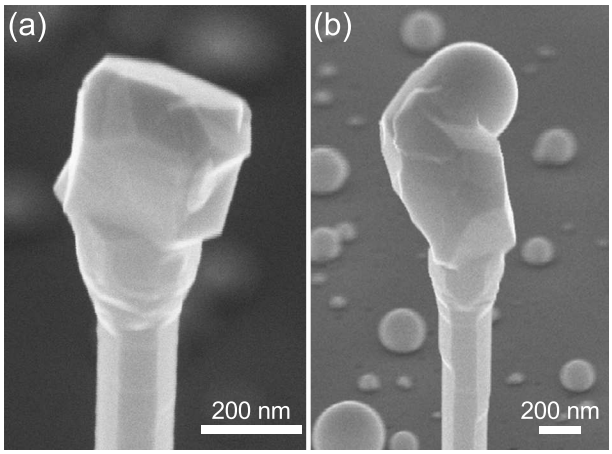

Figure 4.23: *(a) Bulge on top of GaAs NWs. (b) Ga droplet instability after refilling. Published in [261]*

do not modify the crystal structures and too long supply interruptions consume the droplet either completely or result in the formation of a bulge. Such a bulge is shown in Fig. 4.23a and is believed to occur when the consumption leads to a contact of 90° and a decrease of the top diameter. The subsequent refilling of the droplet then results in the formation of the bulge as already pointed out by Krogstrup *et al.* [183]. A similar effect is observed when the Ga refilling pulse is too strong, thus the diameter of the droplet increases rapidly. In this situation, the Ga droplet becomes unstable and starts to move on the NW top facet. This is evident by the SEM image shown in Fig. 4.23b where the Ga droplet is located on a tilted facet and the top part of the GaAs NW has a non-hexagonal shape with several facets.

To summarize, WZ segments with lengths ranging from a few tens of nanometers to several hundreds of nanometers can be inserted in normally ZB GaAs NWs by partially consuming and restoring the Ga droplet. The switching of the crystal structures is not abrupt but characterized by a transition region. This transition region mostly contains the ZB crystal structure with twins but also short WZ segments.

4.3.3. Wurtzite inclusions in InAs nanowires

As shown by Grap *et al.* [109] and in Sec. 4.2.2, also VLS InAs NWs have a short WZ segment beneath the In droplet whereas the main part of the NWs have a twinning ZB superlattice (see Section 4.2.2). The contact angle between the In droplet and the InAs NW is close to 90°, i.e. much smaller than for GaAs NWs. According to Fig. 4.19 such low contact angles allow only rather short WZ segments. Consequently, only three short In supply interruptions of 1, 2 and 3 minutes were applied. To avoid any droplet instability or droplet movement, In refilling pulses after the supply interruptions were not used. The InAs NWs were grown on GaAs (111)B substrates covered by a thin layer of SiO_x. The substrate temperature, In rate and As flux were 530°C, 0.05 µm/h and $1.8 \cdot 10^{-6}$ Torr, respectively. First, InAs was grown for 1.5h followed by the three interruptions. Between two adjacent interruptions, InAs was grown for 20 min. After the last interruption, InAs was grown for 15 min and subsequently the substrate temperature was ramped down.

Figure 4.24a displays a SEM micrograph of the InAs NW with three growth interruptions. Unlike GaAs NWs, the InAs NWs show a direct morphological change due to the interruptions, i.e. a reduction in NW diameter. These morphological changes are caused by the In supply interruption of (b) 2 and (c) 3 min. The In supply interruption of 1 min was not found to have an impact on the crystal structure. In the upper part of the NW, a bulge formed. This bulge is

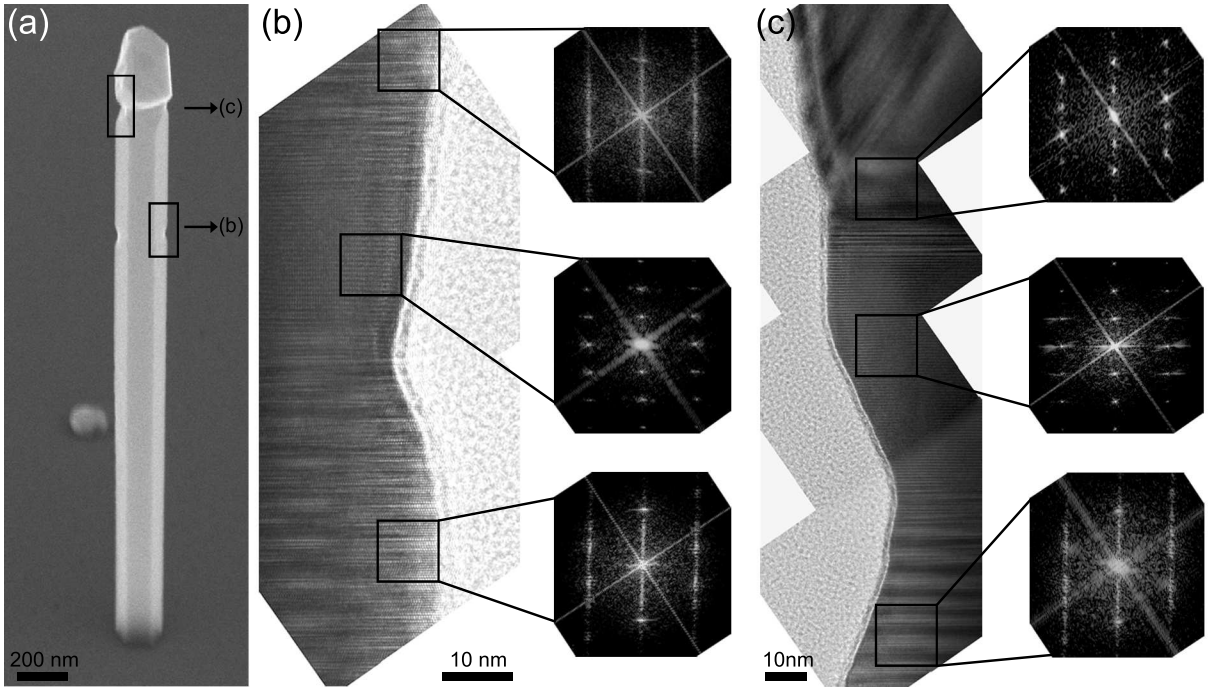

Figure 4.24.: *InAs NW with two WZ segments. (a) SEM micrograph. (b) TEM micrograph of the first WZ segment together with FFTs of the marked areas. (c) TEM micrograph of the second WZ segment together with FFTs of the marked areas. Rectangles in (a) denote the position of the TEM micrographs in (b) and (c).*

similar to observations on GaAs NWs when the Ga supply interruption duration was too long (see Fig. 4.23a). Below the bulge, the diameter of the NW decreases as well.

The TEM micrograph and three corresponding FFTs shown in Fig. 4.24b clearly prove that the crystal structure at the position of the reduced diameter is WZ, being embedded in the twinned ZB superlattice. The transition region from the twinned ZB superlattice to the WZ segment is narrow. The WZ segment has a length of about 25 nm being caused by the In supply interruption of 2 min. As described in the previous section, GaAs NWs do not show a reduction of the NW diameter when the crystal structure switches from ZB to WZ. The reduced diameter for the InAs NWs may have two reasons. Firstly, during the partial consumption of the droplet, the diameter of the droplet might decrease while the contact angle remains constant. The diameter of the NW will decrease as well. Once the In is reintroduced, the droplet recovers and the NW diameter is the same as before.

The second possibility is that the radial growth rate on the WZ phase is slower than on the ZB phase. Several groups have already observed that the radial growth rates on the ZB and the WZ phases in core-shell NWs differ strongly, mostly with a reduced growth rate on the WZ phase [101, 107]. In general, this was attributed to the lower surface energy of the WZ phase compared to the ZB phase [97, 338]. However, the surface energy of the WZ crystal phase is lower for both materials GaAs and InAs than the energy of the ZB phase, only the absolute value for InAs is lower than for GaAs [97].

In Fig. 4.24c the upper part of the NW with the bulge is shown. The crystal structure changes from twinned ZB to WZ to ZB at the top. The switching from twinned ZB to WZ is again associated with a reduction of the NW diameter. Here, the WZ segment has a length of about 60 nm, being longer than the expected length for an In supply interruption of 3 min. The crystal structure of the bulge is ZB without a twinning superlattice (see Fig. 4.24c), being different than

the usual crystal structure of VLS grown InAs NWs. Similar as for the GaAs NWs, the bulge is expected to be formed after the group III supply interruption, i.e. when the group III element is reintroduced and the droplet becomes unstable resulting in a movement of the droplet. In fact, in some cases the bulges have twins perpendicular to ⟨111⟩ directions not being the NW growth direction (not shown).

4.4. Conclusions

In this chapter, a thorough investigation of the growth of InAs and GaAs NWs was performed. The growth conditions for the vapor solid growth of InAs NWs on GaAs (111)B substrates were evaluated, demonstrating that the NW density and dimensions can be tailored over a wide range. The crystal structure of the vapor solid InAs NWs was found to contain a high number of stacking faults. These were correlated with the significantly smaller dimensions of the NW tip than of the mean NW diameter. Subsequently, this InAs NW growth method was adapted for the growth on Si substrates. The necessity of a thin silicon oxide covering the substrate was proven. A chemical reoxidation by hydrogen peroxide was evaluated to be an optimal procedure to obtain the required silicon oxide thickness.
For the following investigations, the focus was set to the vapor liquid solid growth of InAs and GaAs NWs. Pinholes in the silicon oxide were found to be essential for the vapor liquid solid growth of InAs NWs on Si substrates. These pinholes were created via an *in situ* etching of the silicon oxide using Ga droplets. The vapor liquid solid InAs NWs exhibit a twinning superlattice with a short WZ region beneath the droplet. The latter was correlated with the partial consumption of the droplet during the cool down process resulting in a nucleation at the triple phase line. GaAs NWs showed a rather comparable crystal structure having a WZ segment at the top. The occurrence of this WZ segment was described theoretically and a model to estimate the maximal length of it was developed. This model gave evidence that Ga desorption from the droplet limits the maximal WZ length. Making use of the model, it was shown that the crystal structure of vapor liquid solid grown GaAs and InAs NWs can be switched from the ZB to the WZ phase and vice versa.

5 Chapter 5. Lattice mismatched group III-Arsenide heterostructure nanowires

Semiconductor heterostructures are of particular interest due to the different band alignments introduced in Chapter 1. A straddling gap band alignment in core-shell NWs results in an increased electron mobility in InAs/InP core-shell NWs [151, 319] or enhanced photoluminescence intensity in GaAs/AlGaAs core-shell NWs [68, 210]. In these structures, the semiconductor with the smaller band gap is located in the core, the shell passivates the surface of the core. In the reverse arrangement with the small band gap semiconductor as the shell, the carriers are located in the shell and radial quantum heterostructures are obtained [28, 91, 122]. A combination of different III-V semiconductors is not straightforward since they usually differ in lattice constants. In this chapter, lattice mismatched GaAs/InAs core-shell NWs and associated structured are investigated. The lattice constants between GaAs and InAs differ by $\sim 7\%$, which results in considerable strain as well as the formation of misfit dislocations.
Results presented in this chapter have been published in Refs. [25, 262, 264, 329].

5.1. GaAs/InAs core-shell nanowires

GaAs/InAs core-shell NWs benefit from a type I (straddling gap) band alignment with an insulating GaAs core and a highly conductive InAs shell. This confines the electrons into the shell and consequently, tubular conductor are produced [28]. To obtain these structures, GaAs NW cores are grown at a temperature of about 600°C using the self-catalyzed growth mechanism followed by the complete consumption of the Ga droplet. The growth of the InAs shell takes place at 490°C with an In rate of 0.1 µm/h and As_4 flux of 10^{-6} Torr. The growth of the shell is initiated by the formation of separated islands which coalesce during growth of the shell. An extensive discussion of the growth of these core-shell NWs can be found in [255] and [262].

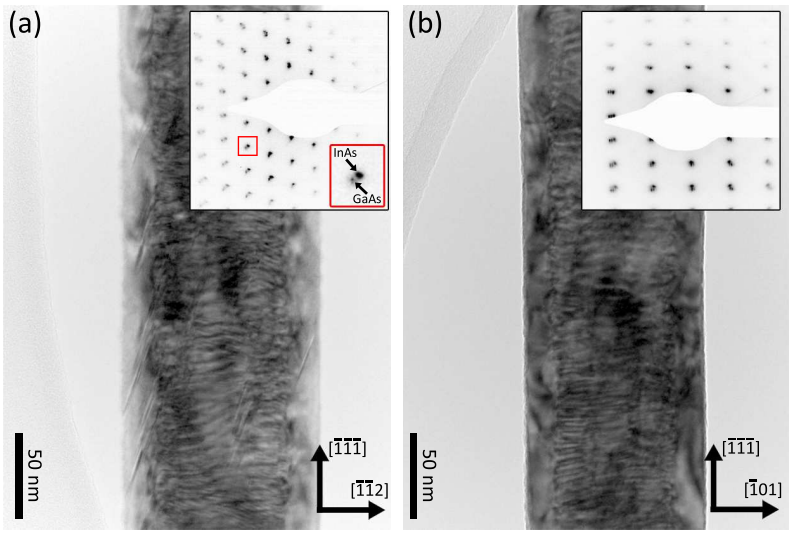

Figure 5.1: *TEM micrographs of a GaAs/InAs core-shell NW from the ⟨110⟩ (a) and the ⟨211⟩ (b) zone axes. The insets show the corresponding electron diffraction patterns (inverted colors) exhibiting a splitting of the diffraction spots.*

5.1.1. Dislocations and strain relaxation[1]

The lattice mismatch of about 7% between GaAs and InAs typically either results in the formation of islands via the Stranski-Krastanov mechanism or dislocations are formed almost immediately to relax the strain. The type of strain relaxation depends on the orientation of the substrate with a (100) orientation favoring the formation of three dimensional islands [324] and (110) and (111) substrate orientations resulting in misfit dislocations [53, 328, 348]. The GaAs NWs are bound by six {110} facets. Consequently, the formation of misfit dislocations is expected. Considering the core-shell NW model developed by Raychaudhuri and Yu [252, 253] being introduced in Section 3.3, dislocations in GaAs/InAs core-shell NWs should occur for almost all dimensions.

Figure 5.1a,b show low resolution TEM micrographs of GaAs/InAs core-shell NWs from the ⟨110⟩ and the ⟨211⟩ zone axes, respectively. From both zone axes Moiré fringes are seen, being an indication for strain relaxation. Certainly, the fringes are observed only within the inner part of the core-shell NW while the outer part is free of a Moiré pattern. In the inner part, the electron beam travels though both the InAs shell and the GaAs core. The presence of the Moiré pattern demonstrates that two lattices with different lattice constants are present, i.e. that strain relaxation takes place. In the outer part of the NW, only the InAs shell is present. The absence of the Moiré pattern proves that the shell has a homogeneous lattice constant. The relaxed strain is further evidenced by the diffraction patterns depicted as insets in Fig. 5.1. All diffraction spots show a splitting, i.e. discrete spots from GaAs and InAs are observed. The lattices are not rotated with respect to each other, i.e. the InAs shell is grown epitaxially on the GaAs NW. Since the spot splitting is observed for all of the diffraction spots, the strain is relaxed both axially and radially. For InAs/GaAs core-shell NWs it was shown that the (residual) strain in the axial and radial direction differ [164]. Axial strain relaxation was found to take place earlier than the radial one. The axial strain relaxation increased with the shell thickness while the radial strain relaxation was either zero (for thin shells) or above 90% [164].

[1] Results of this section have been published in A. Biermanns, T. Rieger, G. Bussone, U. Pietsch, D. Grützmacher, and M. Ion Lepsa. *Axial strain in GaAs/InAs core-shell nanowires.* Applied Physics Letters, 102(4):043109, 2013. Ref. [25] and T. Rieger, M. Luysberg, T. Schäpers, D. Grützmacher, and M. I. Lepsa. *Molecular beam epitaxy growth of GaAs/InAs core-shell nanowires and fabrication of InAs nanotubes.* Nano letters, 12(11):5559-64, 2012. Ref. [262]. XRD measurements and FEM simulations were performed by Dr. Andreas Biermanns in the group of Prof. Pietsch at the University of Siegen.

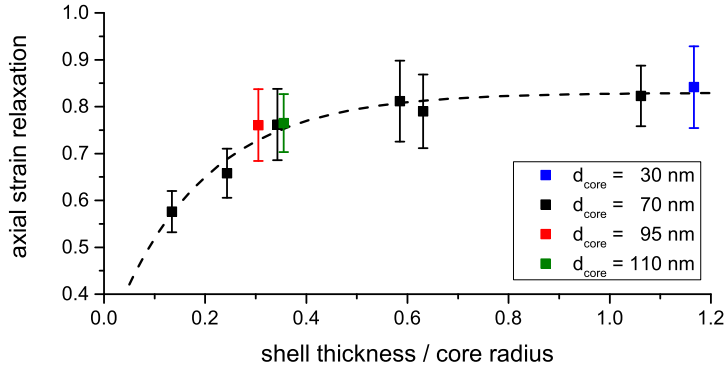

Figure 5.2: *Degree of axial strain relaxation in GaAs/InAs core-shell NWs determined from the Moiré fringes. The GaAs NW cores have diameters of ■ 30 nm, ■ 70 nm, ■ 95 nm and ■ 110 nm. The dashed line is a guide to the eye. Published in [262].*

Since the lattices of the core and the shell are not rotated with respect to each other, the degree of axial strain relaxation can be estimated from the Moiré fringes, where its period D depends on the lattice constants of the two layers. D is given by $D = d_2 d_1/(d_2 - d_1)$. d_1 and d_2 are the distances of the (111) planes of GaAs and InAs, respectively. Assuming an unstrained GaAs core, i.e. d_1 being the value for bulk GaAs, and therefore d_2 being the lattice plane distance of the InAs, the strain relaxation in the InAs shell can be calculated. The degree of axial strain relaxation as a function of the ratio of shell thickness over core radius is depicted in Fig. 5.2. As seen, the InAs shell is strongly strained for thin shells while it relaxes more when the shell thickness increases. The strain relaxation is found to saturate at about 80%, being comparable to findings in InAs/GaAs core-shell NWs [164] as well as InAs layers grown on (111)A oriented GaAs [336]. However, it suggests that the InAs shells are always strained, independent on their thickness. When calculating the spacing of the (111) planes of the InAs shell from the Moiré fringes, it was assumed that the GaAs core is unstrained. Since the dimensions of the core and the shell are in a similar range, this assumption is not reasonable. Rather, the strain is expected to be shared between the core and the shell. This can only hardly be included in the analyses of the Moiré fringes. Consequently, an alternative technique is required to probe the lattice parameters of the core and the shell individually. This can be achieved by XRD measurements with synchrotron radiation[2]. In Fig. 5.3a-d the reciprocal space maps around the GaAs (111) (upper row) and InAs (111) (lower row) reflections are shown. The grey lines indicate the q_z values of unstrained ZB GaAs and InAs. For each shell thickness, a sharp Bragg peak corresponding to unstrained GaAs is observed. This is due to the GaAs (111)B substrate used for the NW growth. Apart from the sharp Bragg peak, an elongated peak in the q_x direction changing its position in the q_z direction is observed. This is attributed to the GaAs core NWs with small lateral dimensions as well as a small random tilt. In Fig. 5.3a, an additional weak peak shifted -0.5% along q_z is found. It belongs to the WZ phase of GaAs which has a larger lattice parameter along the NW growth direction than the ZB phase [23, 178, 235].

An increase of the InAs shell thickness results in a shift of the signal from the GaAs core towards smaller q_z values, i.e. larger lattice parameters. For the thickest shell of about 35 nm, the GaAs core signal is no longer observed, possibly due to the high coverage of the sample surface by parasitic crystallites. Regarding the InAs signal, two distinct peaks at different q_z values are found. The first peak is located at the position of bulk ZB InAs whereas the second peak is shifted to larger q_z values and moves towards the bulk ZB value with increasing the InAs shell thickness. The first peak has its origin in parasitic InAs crystallites grown in-between the

[2]Performed by Dr. Andreas Biermanns at the P08 beamline of the PETRA III synchrotron source at the DESY Hamburg.

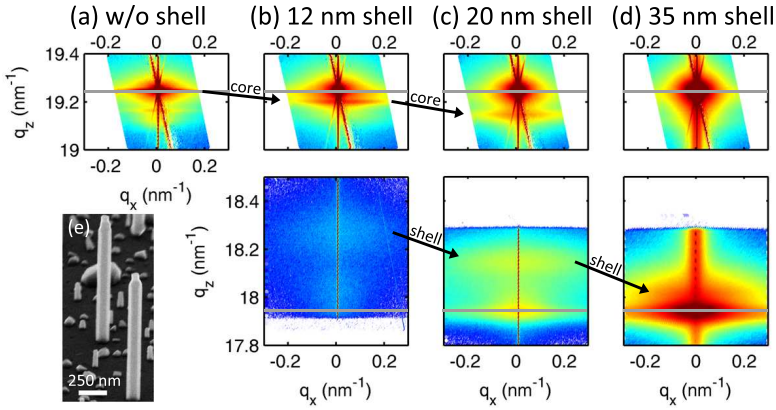

Figure 5.3: *XRD reciprocal space maps around the GaAs and InAs (111) reflections for GaAs/InAs core-shell NWs with different shell thicknesses: (a) bare GaAs NWs, (b) 12 nm InAs shell thickness, (c) 20 nm InAs shell thickness, (d) 35 nm InAs shell thickness. (e) SEM micrograph displaying the GaAs/InAs core-shell NW and the InAs crystallites. [Data courtesy of Dr. Andreas Biermanns] Published in [25].*

NWs. These crystallites are seen in the SEM micrograph displayed in Fig. 5.3e.
Compared to the previous investigation using the Moiré fringes, it is evident that not only the lattice parameters of the InAs shell change with increasing shell thickness, but also the GaAs core changes its lattice parameter. Thus, while the InAs shell relaxes with increasing shell thickness, the strain in the GaAs core is enhanced. In consequence of this, calculating the strain relaxation via the Moiré fringes assuming a constant lattice parameter within the GaAs core does not give the correct value. The analyses by means of XRD results in a more precise measurement of the strain in the core and shell. This is depicted in Fig. 5.4. The strain in the core increases while the strain in the shell decreases with the shell thickness. In order to understand the strain in core and shell with varying shell thickness, two different models were used. A finite element method (FEM) with a constant residual mismatch of 1.5% was used as the first model, details can be found in Refs. [22] and [25]. Especially for thick shells, the absolute values of the strain in the core and shell obtained from the FEM simulation are in a good agreement with the XRD measurements. For thin shells, the deviation between the FEM simulation and the XRD measurement increases and also the general shape of the curve of the experimental data is not well fitted. These differences may be caused by the assumption of a constant residual mismatch at the interface and the fact that only axial strain relaxation was considered. Apart from this, elastic constants can vary for small dimensions [5, 46, 195, 238, 327]. The second model to estimate the strain in the core and in the shell is based on the critical thickness model developed by Raychaudhuri and Yu [252, 253], see Section 3.3 and Appendix A.2. The results are displayed in Fig. 5.4 by the solid lines. The residual strain in the shell is well fitted while the curve representing the strain in core is shifted upwards about 0.8% with respect to the experimental data points. The deviation between the experimental and calculated data may be caused by the same uncertainties as for the FEM-based simulations. Additionally, the model by Raychaudhuri and Yu considers cylindrical NWs while the real cross-section of the NWs is hexagonal.

The presence of Moiré fringes as well as distinct diffraction spots of InAs and GaAs in both the diffraction pattern and the XRD measurement implies the necessity of dislocations relaxing the strain. The large lattice mismatch of about 7% between GaAs and InAs should result in the formation of misfit dislocations already for very thin layers (see Sec. 3.3). Different types of dislocations will have a different impact on the NW, e.g. the strain relaxation and scattering centers for the electronic transport. Accordingly, Fig. 5.5a shows a HRTEM image of a GaAs/InAs core-shell NW with a shell growth time of only 1 min: the shell did not form a complete layer but consists of separated InAs islands. Three dislocations are found in the image, as highlighted by the red lines. The FFT-filtered image in Fig. 5.5b, depicting only the (111) planes of the

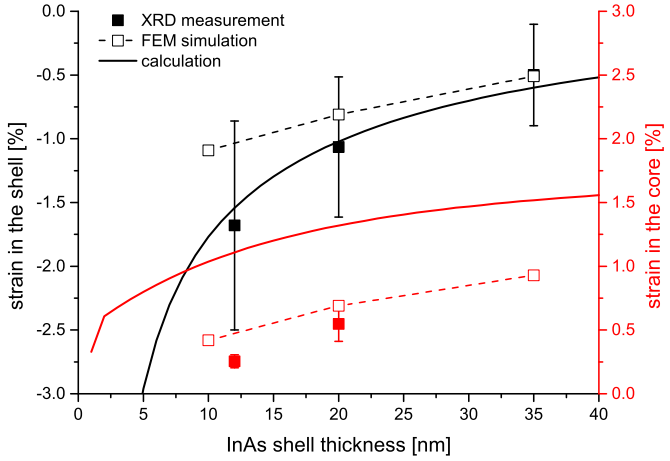

Figure 5.4: *Residual strain in GaAs/InAs core-shell NWs measured by XRD as a function of the shell thickness (■ strain in the core, ■ strain in the shell). Open symbols represent the residual strain obtained from FEM simulations (□ strain in the core, □ strain in the shell), solid lines are obtained by the core-shell model developed by Raychaudhuri and Yu [252, 253], presented in Sec. 3.3 and Appendix A.2. FEM simulations were performed by Dr. Andreas Biermanns.*

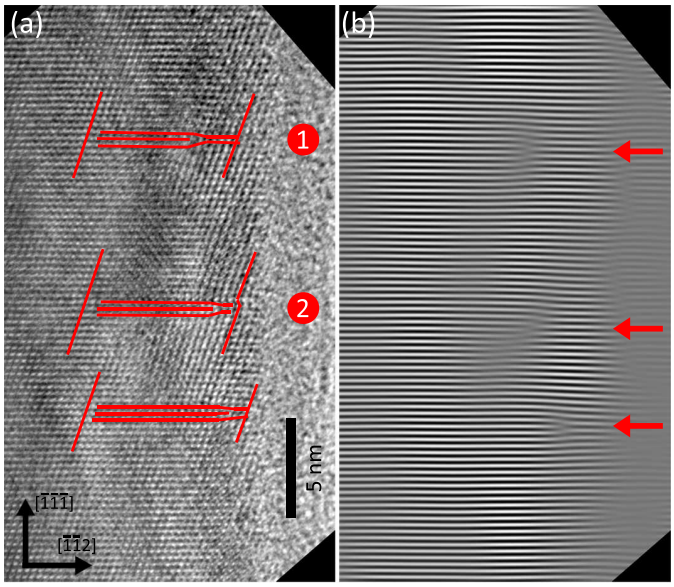

Figure 5.5: *(a) HRTEM image of a GaAs/InAs core-shell NW with a shell growth time of 1 min. Three dislocation of two different types can be identified: the dislocation labeled 1 is a perfect dislocation with Burgers vector $b = a/2\langle 110\rangle$, the dislocation labeled 2 is a Frank partial dislocation with $b = a/3\langle 111\rangle$ and is evident by the formation of a stacking fault in the shell. Published in [262]. (b) FFT-filtered image of (a) evidencing the three misfit dislocations as terminating lattice planes (red arrows).*

crystal, clearly demonstrates the misfit dislocations by terminating (111) planes (see arrows). The dislocations can be assigned to two different types: (1) perfect dislocation and (2) Frank partial dislocation. Both types have been verified by Burgers circuits. The perfect dislocation (upper dislocation, label (1)) has a Burgers vector of $b = a/2\langle 110\rangle$ and leaves a perfect crystal around the dislocation. Only the dislocation core as well as the associated strain field are expected to influence the electronic transport. This type of dislocation can glide, which means that its position can change according to the increasing shell thickness during growth. The dislocation labeled (2) is a Frank partial dislocation which has a Burgers vector of $b = a/3\langle 111\rangle$, thus it purely relaxes the axial strain. The partial dislocation forms a stacking fault in the shell which can, in addition to the dislocation itself, act as a scattering center. According to the model by Raychaudhuri and Yu [252, 253] where its results have been shown in Sec. 3.3, the Frank partial dislocation is the energetically favorable dislocation.

Assuming a uniform spacing between dislocations, the average distance s between them is given by $s = \frac{b}{f-|e|}$ with b being the magnitude of the Burgers vector, the lattice mismatch f and the residual strain e. The highest dislocation density is achieved when the strain is entirely relaxed, i.e. $e = 0$. With $b = a/3\langle 111\rangle$ the distance between dislocation is in the

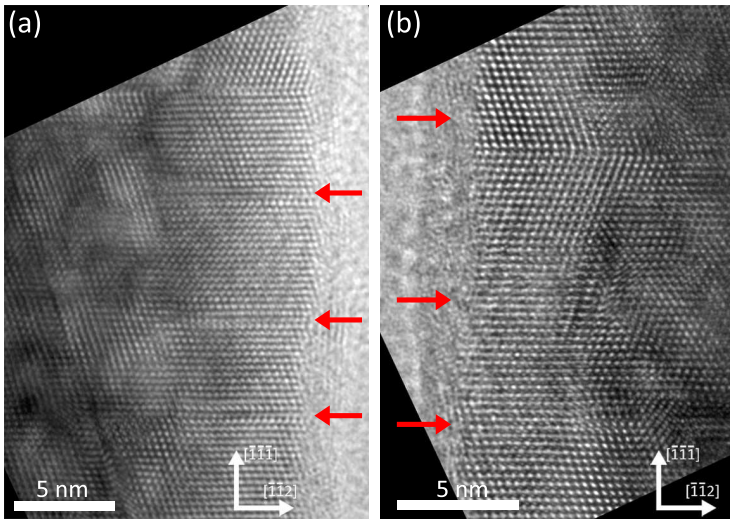

Figure 5.6: *HRTEM images showing arrays of dislocations in GaAs/InAs core-shell NWs. (a) Array of Frank partial dislocations, (b) array of perfect dislocations. The arrows are pointing to the dislocations.*

range of 4.6 – 5 nm. For a residual strain in the core or shell, the average spacing between adjacent dislocation increases. Similarly, the spacing is slightly larger when perfect dislocations relax the strain. The dislocations visible in Fig. 5.5a have a distance of $\sim$ 5 nm and $\sim$ 8 nm, which means that the measured distances are above the calculated ones. This agrees with the incomplete strain relaxation observed by XRD and Moiré fringes. However, the shell thickness is rather small and no uniform shell is formed. Such small shell thicknesses and incomplete shells are technological not relevant since the resistivity is too high [27]. Consequently, the average distance between adjacent dislocations was investigated in NW with thicker shells. This allows to estimate the number of dislocations and therefore the number of scattering centers in a device. Figure 5.6a,b show HRTEM micrographs of a GaAs/InAs core-shell NW with $\sim$ 10 nm shell thickness. An array of Frank partial dislocations is seen in Fig. 5.6a while Fig. 5.6b shows an array of perfect dislocations. In general, the different dislocation types are distributed equally along the NW. The distance between adjacent dislocations is not uniform, thus the residual strain can vary locally. In agreement with the above presented discussion of the strain in the core and shell, the distance between dislocations is typically larger than 5 nm meaning that the strain induced by the 7% lattice mismatch is not completely relaxed.

A close look to Fig. 5.1a already reveals the presence of additional defects. These defects are seen as lines not being perpendicular to the growth direction, thus these are neither twins nor stacking faults arising from the growth of the NW core nor Frank partial dislocation associated stacking faults. Figure 5.7a depicts another low resolution TEM image with these defects (red arrows), but here they are aligned in two different directions separated by a twin boundary (blue arrows). The angle between the defects marked by the red arrows and the twin boundary is $\sim$ 70°, being the angle between two {111} planes. This is seen more clearly in the HRTEM micrograph in Fig. 5.7b. A stacking fault drawing an angle of 20° with the NW growth direction is found. This stacking fault is bounded by Shockley partial dislocations with $b = a/6\langle 211\rangle$ and may be created by a splitting of a perfect dislocation into two partial dislocation. The initial splitting of a perfect dislocation into two Shockley partial dislocations is associated with a gain in energy and creates the observed stacking fault [139]. Strain can increase the distance between the partial dislocations and the length of the stacking fault.

Although the diffraction pattern in Fig. 5.1 already indicated radial strain relaxation, the HRTEM micrographs certainly only revealed dislocations relaxing the axial strain. In order to analyze whether radial strain relaxation occurs, the NW cross section has to be examined. For

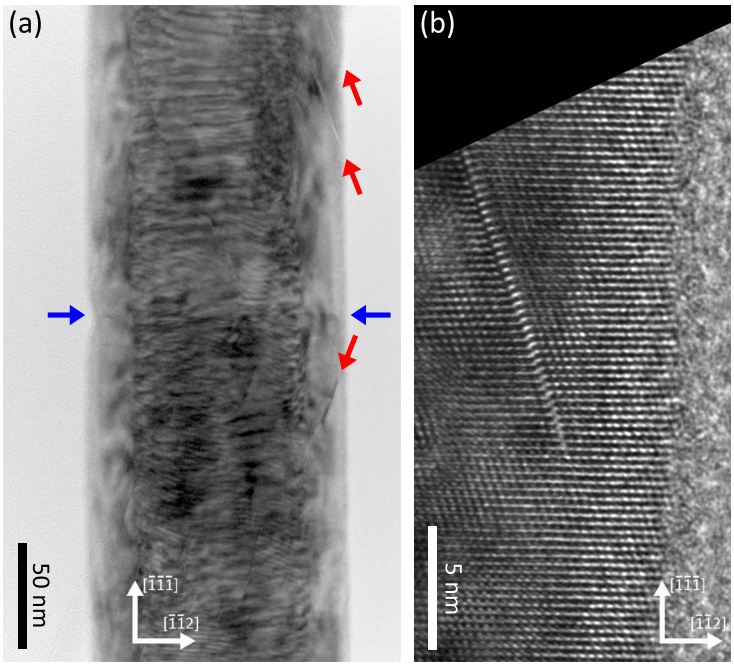

Figure 5.7: *Shockley partial dislocations in GaAs/InAs core-shell NWs. (a) Overview TEM micrograph with three Shockley partial dislocations (red arrows) and a twin boundary (blue arrows), (b) HRTEM micrograph of a single Shockley partial dislocation.*

this purpose, GaAs/InAs core-shell NWs were transferred on Si/SiO_2 substrates and a protective layer of Al_2O_3 was deposited. FIB was used to cut a lamella out of this structure. This lamella contains the NW cross section. Figure 5.8a shows the HAADF STEM image of the cross section; a clear contrast from the core and the shell as well as the hexagonal morphology is seen. The EDX maps of As, Ga and In shown in Fig. 5.8a further prove the core-shell structure with a low interdiffusion.

Figure 5.8b depicts a bright field TEM micrograph which again has a clear contrast between the GaAs core (bright) and the InAs shell (dark). Additionally, the SiO_2 substrate, the Al_2O_3 protection layer as well as Pt from the FIB are seen. A higher magnified image is shown in Fig. 5.8c. The interface between GaAs and InAs is not smooth but has a roughness in the range of $\sim$ 1 nm. This roughness is visible by the dark clouds at the interface between the core and the shell. Similar observations were made on coherent GaAs/InGaAs core-shell NWs [108]. The FFT of this image is displayed in Fig. 5.8d and has distinct reflections for GaAs and InAs, demonstrating the presence of lattices with two different lattice constants. The reflections are belonging to the {220} lattice planes and its separation as well as reciprocal lengths agree well with the expected values for GaAs and InAs. This means that unlike the axial strain relaxation, the radial strain relaxation is very efficient with almost bulk GaAs and InAs lattice constants. Similar observations were made for InAs/GaAs core-shell NWs [164].

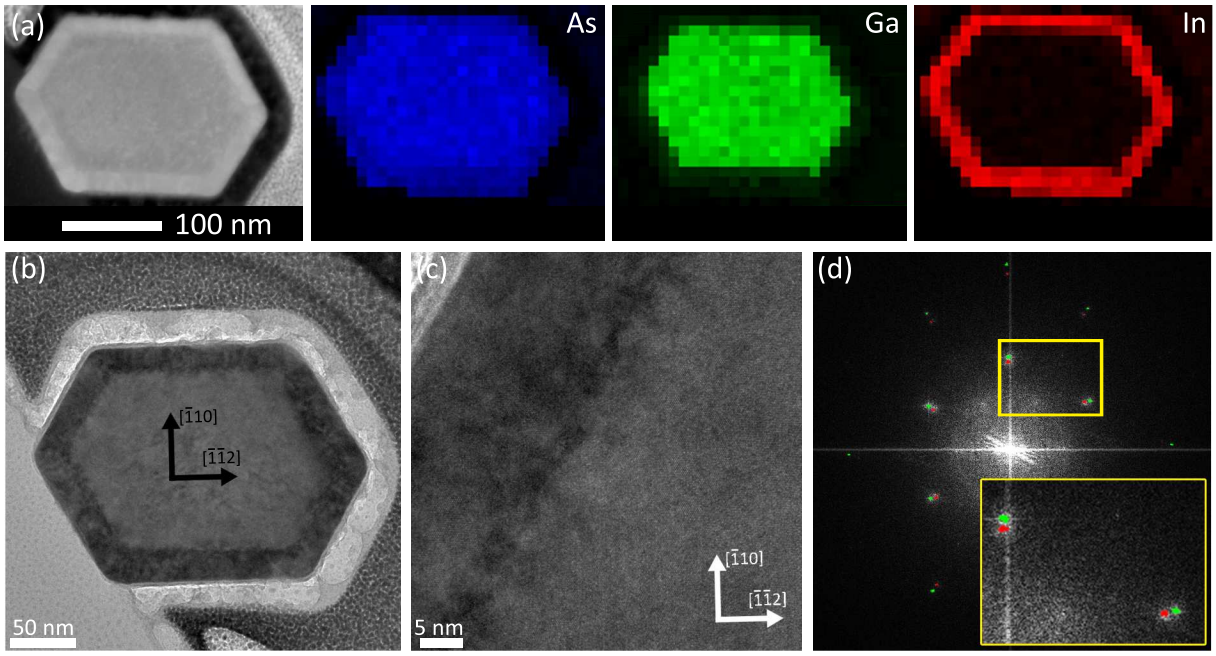

Figure 5.8.: *GaAs/InAs core-shell NW cross section. (a) HAADF STEM image and As (blue), Ga (green) and In (red) EDX maps confirming the core-shell morphology and hexagonal cross section of the core and the shell. (b) Bright field TEM micrograph with clear contrast from the core and the shell. (c) HRTEM image evidencing interfacial roughness due to the presence of dark clouds. (d) FFT of (c) with a splitting of the diffraction spots. The inset shows a detailed part of the FFT, clearly proving the splitted spots belonging to InAs (red) and GaAs (green). The FIB lamella was prepared by Dr. Elmar Neumann.*

5.2. Crystal phase selective growth in GaAs/InAs core-shell nanowires[3]

The GaAs/InAs core-shell NWs typically show a prominent morphological characteristic close to the top. There, the diameter of the NW decreases towards that of the bare GaAs core [262]. This is displayed in Fig. 5.9a,b showing an overview SEM image as well as a detailed micrograph of the top region. The exact shape of the upper part strongly depends on the growth conditions of the core and the growth time of the shell, indicating that adatom diffusion does not influence this shape. Therefore a different mechanism has to be the origin. A possible reason is displayed in Fig. 5.9, depicting a stitched TEM micrograph of the GaAs core. The catalyzing Ga droplet was consumed completely. As seen in the HRTEM micrographs and the corresponding FFTs, the crystal structure at the lower part is ZB with a low density of twins. Moving further towards the top, the density of twins increases and subsequently becomes WZ. Finally, the small triangular top has again ZB crystal structure. This structure of the GaAs NW was already proposed in Sec. 4.3 and can cause the inhomogeneous growth of the InAs shell: growth of the InAs shell takes place on the ZB phase of GaAs while the growth is hindered on the WZ phase.

In order to prove this assumption, several WZ segments were placed in the GaAs core as it was demonstrated in Section 4.3.2. Different durations of GaAs growth between two subsequent Ga supply interruptions act as markers for the further analyses by SEM and TEM. To grow the InAs shell, the Ga droplet was consumed completely and the substrate temperature was ramped down to 490°C. The InAs shell was grown for 10 min with an In rate of 0.1 µm/h and the same As_4 flux as the GaAs core, i.e. 10^{-6} Torr. The complete growth sequence with the substrate temperature as well as the state of the As, Ga and In shutters is depicted in Fig. 5.10. Grey colored regions correspond to WZ segments grown intentionally during the Ga supply interruption.

After the InAs has been grown, the NWs do not exhibit a conformal shell as displayed in Fig. 5.11. Rather, the NW contains several regions where the diameter is reduced, being evident from the overview image in Fig. 5.11a. At these constrictions, it seems that the shell did not grow at all or it grew with a significant smaller growth rate. With the marker technique described above (different durations of GaAs growth between two Ga supply interruptions), a clear correlation between the constrictions and the growth sequence is given. The distance between two adjacent constrictions reflects the GaAs NW growth rate, i.e. 1.8 – 2 µm/h. The length of the constrictions increases along the NW axis. This is once again in agreement with the growth sequence and the investigation of the pure GaAs NW shown in Sec. 4.3.2. Overall, based on the SEM images and the marker technique it is concluded that the constrictions have the WZ crystal structure while InAs shells are grown over the GaAs core having the ZB phase. Figure 5.11 shows that the lengths of the constrictions vary from few to several hundred nanometers.

The SEM micrographs taken at larger magnification are displayed in Fig. 5.11b-f. Apparently, the InAs coverage does not end abruptly but forms tongue-like shapes, indicating that the shell thickness slowly decreases. Also the lateral dimensions of the InAs shell on the side facets, i.e. the size in the ⟨211⟩ directions, decrease. The tongues are more pronounced in the NW growth direction than in the reverse direction. To study the correlation between the growth sequence

[3]Most of the results of this section have been published in T. Rieger, T. Schäpers, D. Grützmacher, and M. I. Lepsa. *Crystal Phase Selective Growth in GaAs/InAs Core-Shell Nanowires.* Crystal Growth & Design, 14(3):1167-1174, 2014. Ref. [264]

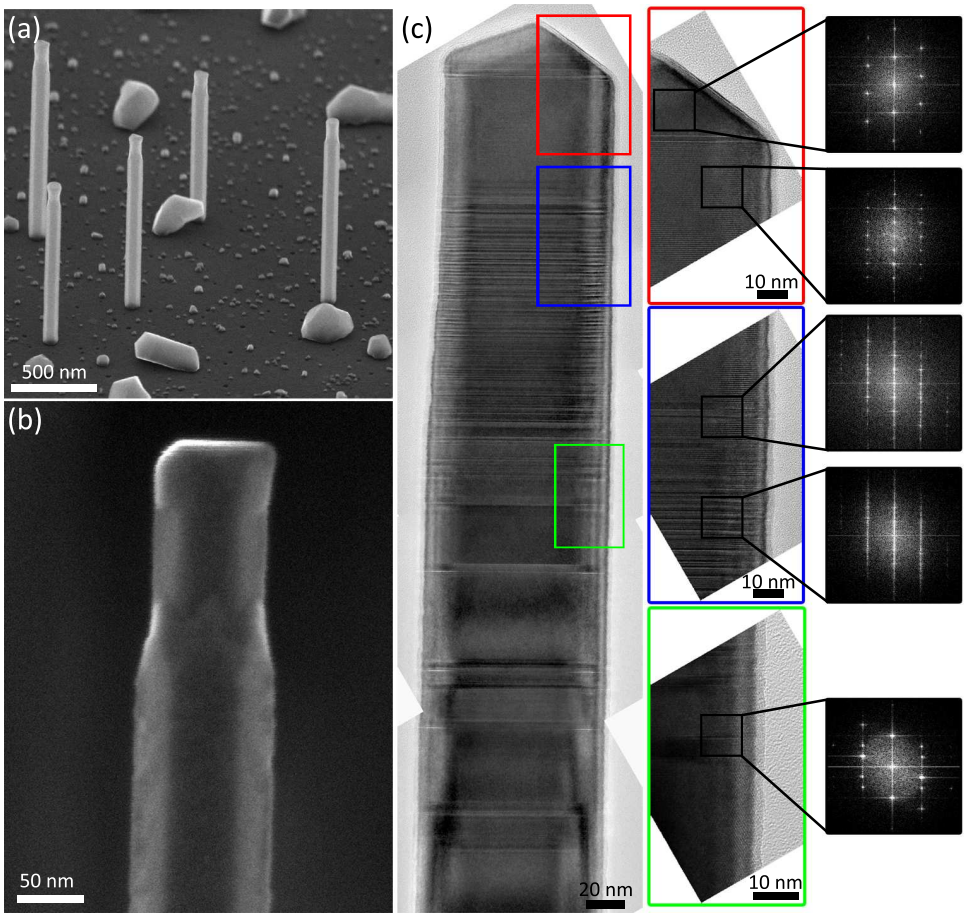

Figure 5.9.: *(a) SEM overview image of GaAs/InAs core-shell NWs evidencing a reduced diameter at the top of all NWs. (b) Higher magnification image of the upper part. (c) TEM micrograph of a GaAs NW after complete Ga droplet consumption. HRTEM and FFTs are acquired from the marked regions.*

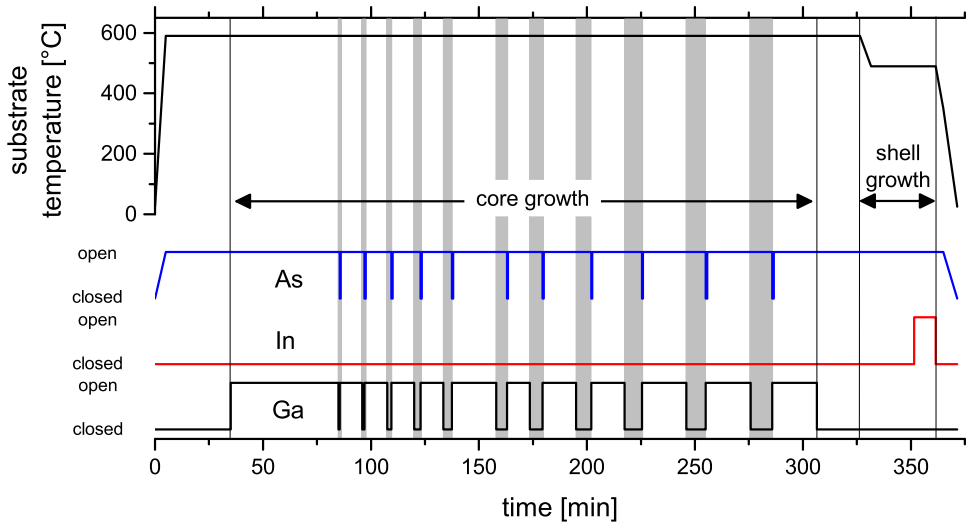

Figure 5.10.: *Growth sequence showing the Ga supply interruptions and the temperature curve for core and shell growth. Grey colored areas indicate intentionally placed WZ segment in the GaAs core. Published in [264].*

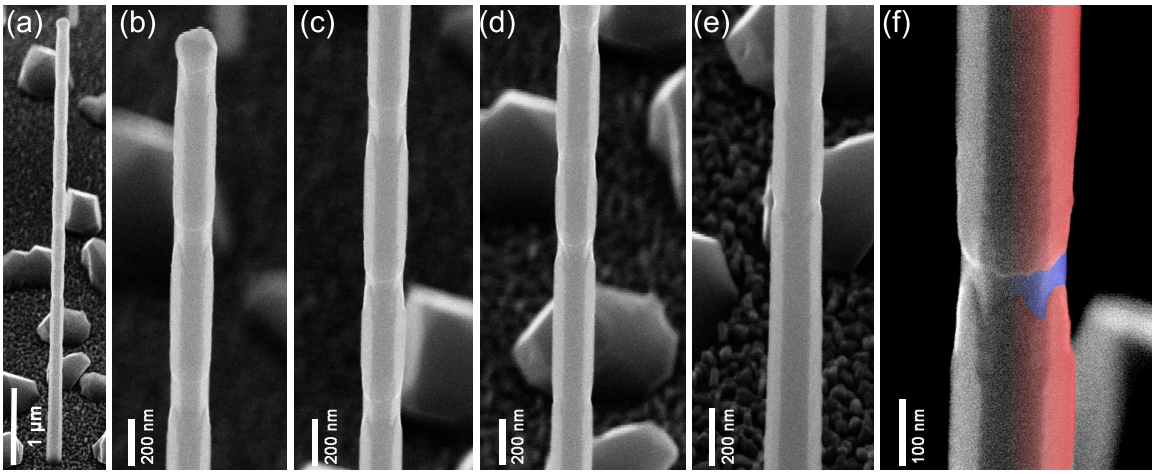

Figure 5.11.: *SEM micrographs of a core-shell NW with the core having several WZ segments as given by the growth sequence shown in Fig. 5.10. (a) Overview of the NW, (b)-(e) higher magnifications depicting all visible interruptions from the top to the bottom of the NW. (f) High magnification image of a single interruption; on the right side, the different materials are color-coded (red: InAs; blue: GaAs). The materials and the shape are identified by the contrast of the SEM micrograph. Published in [264].*

and the appearance of the constrictions in detail, the NWs were examined by TEM. The analyzes clearly show that the crystal structure of the GaAs core corresponding to the constrictions is WZ, being embedded in stacking fault-rich parts. Exemplary TEM micrographs are presented in Fig. 5.12. The complete NW from Fig. 5.12a has several constrictions of different lengths. These are observed by changes of the contrast of the NW as well as changes of the NW diameter. Verification of the suppression of InAs growth on the WZ segments is achieved by EDX line scans. In Fig. 5.12b, four EDX line scans acquired on or near a constriction are superimposed over a HAADF image. The green and red dots denote Ga and In species, respectively. The horizontal scans show that a GaAs/InAs core-shell structure is present in the upper and lower profile, while no In was found in the middle profile. This situation has been confirmed by an additional scan in the vertical direction. In is detected only in the upper and lower part of the constriction while the middle is free of In. Consequently, the constriction clearly represents a gap in the InAs shell. It has a length of about 100 nm. A shorter gap of only $\sim$ 50 nm length is displayed in Fig. 5.12c. Again, EDX is used to confirm the absence of In. In order to detect the shape of the In profile more clearly the In signal is multiplied by a factor of 5, displayed by the blue triangles. The slope of the line is steeper at the upper than at the lower end of the gap. This demonstrates that the shell profile is more abrupt when changing from WZ to ZB than vice versa. This is inverse than the switching of the crystal structure in the core, where it was already shown in Sec. 4.3.2 that the change from pure ZB to pure WZ is more abrupt than from WZ to ZB. Most important for the transition regions presented here shall be the exact crystal structure, especially any WZ segments. This is described in detail later. The information about the shell abruptness at the gap obtained using the EDX profiles is in qualitative agreement with the results obtained from the SEM micrographs shown in Fig. 5.11. Different shapes are observed at the lower and upper end of the gap (see Fig. 5.11f). A simple sketch of the shell gap based on the results obtained from TEM, EDX and SEM is displayed in Fig. 5.12d. Figure 5.12e depicts the gap shown in c by a low resolution TEM micrograph. The presence of the gap is obviously demonstrated by the absence of Moiré fringes and the decrease of the diameter. At the upper and lower end of the gap, stacking faults and twins are seen in the InAs shell. These are correlated with a similar crystal structure of the GaAs core. As already observed in Fig. 5.11f and shown schematically

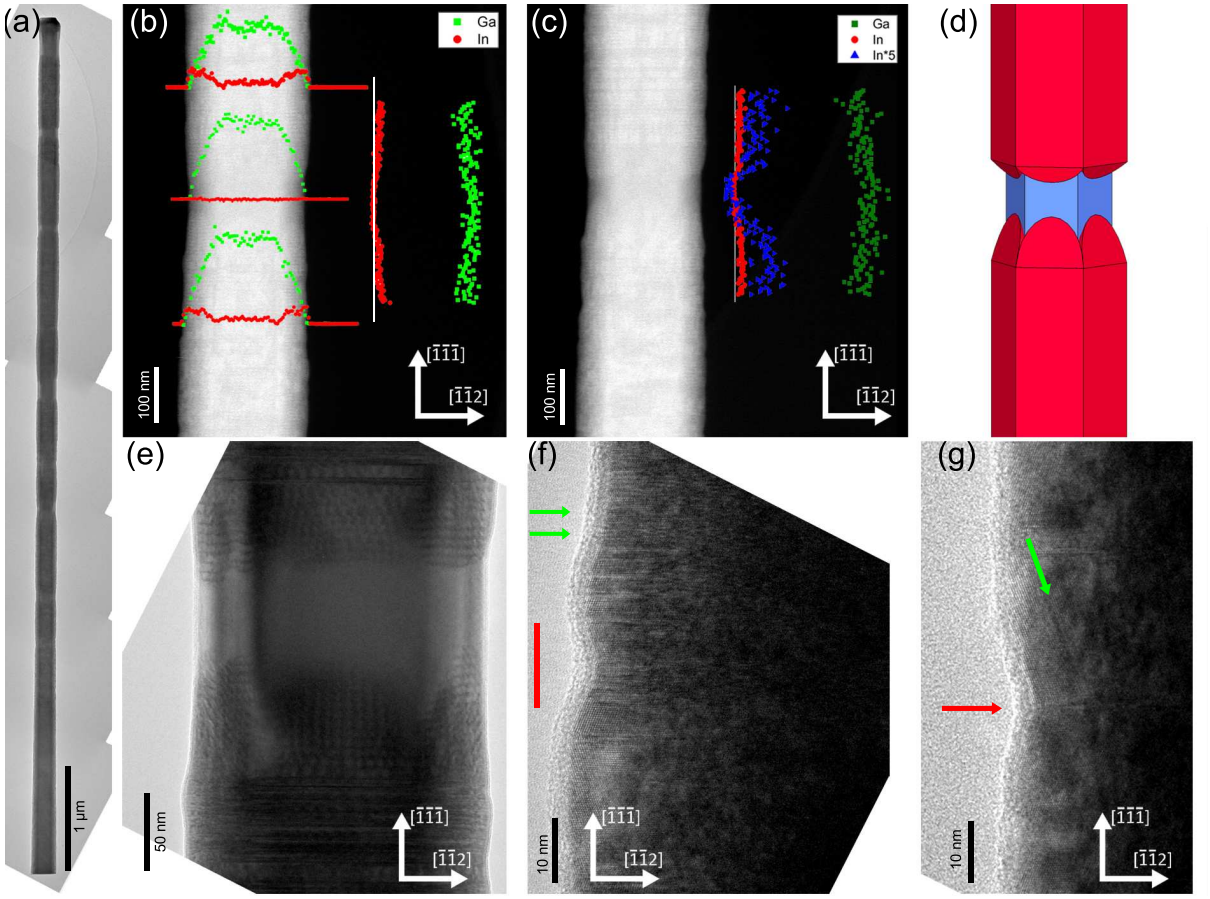

Figure 5.12.: *TEM micrographs demonstrating the growth of InAs on GaAs NWs with WZ segments. (a) Bright field TEM micrograph of a complete NW, in which several gaps in the shell are observed. (b,c) HAADF images with superimposed EDX line scans showing ■ Ga, ● In and ▲ the In signal multiplied by 5. (d) Schematic illustration of a shell gap. (e) Low resolution TEM micrograph of a single shell gap, similar as in (c). (f,g) HRTEM images demonstrating that the shell growth is also affected by the presence of stacking faults or twins. The red bar in (f) indicates a region with high twinning density while the green arrows point to WZ segments. The red arrow in (g) points at the twin boundary and the associated reduction of the shell thickness, while the green arrow points at the (inclined) stacking fault in the shell. Growth direction is from the bottom to the top. Published in [264].*

in Fig. 5.12d, the InAs originating from the upper boundary of the gap covers less of the WZ GaAs core than that one starting from the lower boundary.

The results presented show that the growth of InAs on the WZ phase of the GaAs core is hindered. However, the presence of the tongue-like profile demonstrates that the growth is not suppressed completely. For the entire investigated shell growth durations, no direct nucleation of InAs on WZ GaAs takes place. In fact, InAs does not grow directly on the WZ GaAs core but it advances from the ZB regions. The tongues grow slowly on the WZ $\{\bar{2}110\}$ facets in $[0001]/[000\bar{1}]$ direction. The growth on the WZ $\{\bar{2}110\}$ facets in $\langle 1\bar{1}00\rangle$ direction is even slower which explains the tongue like profiles of the InAs shell at the gaps. This situation is illustrated in Fig. 5.13 by SEM micrographs for short Ga supply interruption, i.e. small gaps in the shell. The length of the gap decreases from left to right. Accordingly, the gap between the two InAs shells is the highest on (a) and vanished on (c). To approximate the shell growth on the WZ

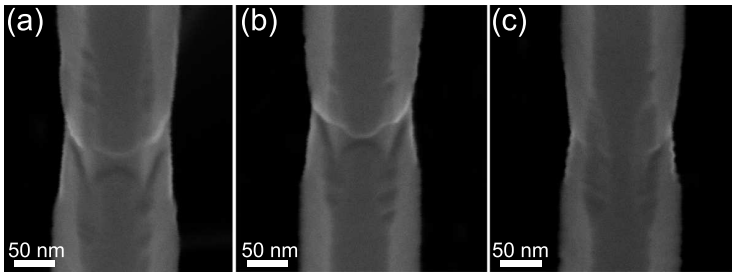

Figure 5.13: *SEM micrographs of interruptions with different lengths. The lengths decrease from (a) to (c). This series also reflects the time-dependent coalescence of InAs grown on WZ GaAs (see the text), with the shell growth time increasing from left to right.*

phase, the different gap lengths can be interpreted as different shell growth times. These indicate the growth kinetics and the coalescence of the InAs tongues. In Fig. 5.13a, a gap between the two InAs segments is obvious. The bottom segment has a tongue-like profile while the top segment ends relative abrupt. At the edges of the hexagonal cross-section of the NW, the InAs shell is rough and/or incomplete. Continuing the InAs growth or decreasing the WZ length in the GaAs core (see Fig. 5.13b), the InAs tongues almost touch each other on the center of the side facets of the NW. The edges are still rough or free of grown InAs. In an even shorter WZ segment, Fig. 5.13c, the InAs tongues coalesced on the NW side facets while InAs growth at the edges of the NW is still incomplete. Rather $\langle 1\bar{1}00 \rangle$ facets are formed at the edges which then vanish after further growth due to the lateral growth of the $\{\bar{2}110\}$ facets.

The shape of the InAs shell on the WZ segments of the GaAs core described above can be correlated with the crystal structure of the transition regions in the GaAs core. The most dominant impact on the growth is due to the WZ phase but stacking faults and twins from these regions may also have an influence. Consequently, twins and stacking faults are analyzed in detail by HRTEM. Figure 5.12f and g show HRTEM micrographs from regions exhibiting a slight roughness of the shell. This uneven shell is associated with stacking defects in the core. In Fig. 5.12f, a reduction of the shell thickness is observed at two positions. In the first case (indicated by the red bar), this is due to a high density of twin planes. The second reduction of the shell thickness (green arrows) is due to the occurrence of WZ segments in the core. However, not only high defect densities or long WZ segments can have an impact on the shell growth, but even a single twin boundary, as shown in Fig. 5.12g. The thickness reduction at this point is correlated with a single twin separating two ZB regions (red arrow). The GaAs NW core always has smooth side facets, independent on twin boundaries or stacking faults (see TEM images in Sec. 4.3.2). No twin-induced roughening of the GaAs side facets is observed. The thickness reduction is therefore not due to morphological changes in the core but due to growth dynamics induced by crystallographic defects. Apart from the thickness reduction, an inclined stacking fault is found in the shell (green arrow in Fig. 5.12g). This inclined stacking fault is only present in the shell and not in the core. Most likely, it occurs due to Shockley partial dislocations at the GaAs/InAs interface. These have already been observed in Sec. 5.1.1.

Although even single or few crystal defects such as twins influence the growth of the InAs shell slightly, longer WZ segments have the strongest impact. Accordingly, the growth of the InAs shell in the vicinity of a long WZ segment in the GaAs core is analyzed in detail in Fig. 5.14. Figure 5.14a displays the growth of InAs on the transition region from the ZB to the WZ phase. FFTs were calculated on different parts along the transition, indicated by the colored frames. The FFTs are plotted as insets. The crystal structure on the left side is twinned ZB (Inset I) and a core-shell structure with smooth side facets is formed. On the right side, the crystal structure is WZ (Inset VI) without a grown shell. In-between, both crystal structures are observed (Insets II - V), but it is mostly ZB with a high density of twins. The shell thickness is found to decrease

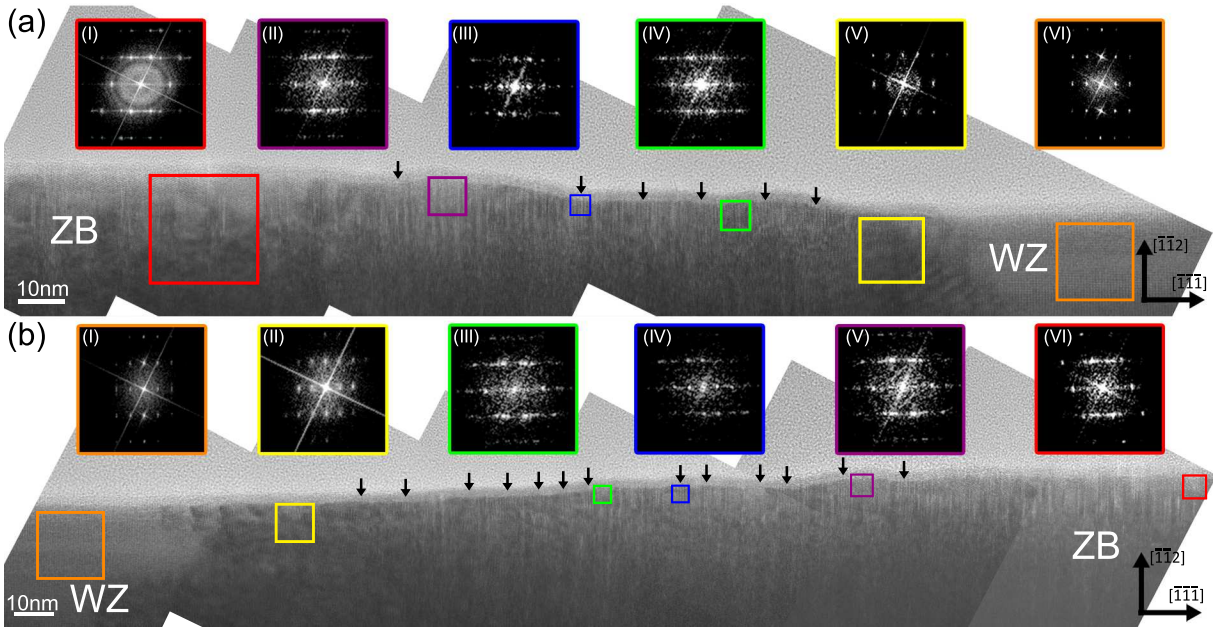

Figure 5.14.: *(a) HRTEM image of the InAs shell grown on the transition region from ZB to WZ of the GaAs core. Insets are FFTs taken from the framed areas. (b) HRTEM image of the InAs shell grown on the opposite transition region from WZ to ZB. Again, FFTs shown in the insets correspond to the framed areas. Published in [264].*

stepwise, each step ends with a WZ segment (Insets III and V). The short WZ segments within the transition region are pointed out by black arrows. As described in Sec. 4.3.2, the number of WZ segments is small when switching from ZB to WZ. This means that the growth is hindered only in few positions. Due to this small number of barriers, the growth front reaches the long WZ segment relatively fast. Once it does, InAs continues to grow slowly on the WZ phase (Inset V). The reverse situation, i.e. when changing from WZ to ZB, is shown in Fig. 5.14b. Again, several FFTs were calculated and are marked by colored frames. The structure changes from a pure WZ core without an InAs shell (Inset I) to a ZB core-shell structure (Inset VI). In-between, both crystal phases are found (Insets II - V). The transition region is characterized by several steps, each ends (in the direction towards the long WZ regions) with a thin WZ segment (Inset IV). The number of WZ segments within the transition region is higher when changing from WZ to ZB than vice versa, identical as in the GaAs core (see Sec. 4.3.2). Since each WZ segment acts as a barrier for the growth of the InAs, the shell grows slower towards the NW bottom than towards the top. The corresponding transition region in the shell (WZ to ZB) is more abrupt than that from ZB to WZ, having a smaller extension of the InAs shell on the WZ GaAs. The same was observed also in the EDX line scans from Fig. 5.12c. This is attributed to the different amounts of WZ segments in the transition region. Comparing the results from GaAs/InAs core-shell NWs (Fig. 5.14) and pure GaAs NW (see Sec. 4.3.2), it is evident that the crystal structure of the shell repeats that one of the core, including all stacking faults, twins and WZ segments.
Several growth conditions for the InAs shell were investigated. A direct growth of the InAs on the WZ GaAs was never observed. Even a decrease of the substrate temperature for the shell growth by 100°C which decreases the adatom mobility did not change the growth behavior.

In the following, the fact that InAs grows on ZB GaAs but growth on WZ GaAs is hindered

	a_c	a_{ZB}	c_{ZB}	a_{WZ}	c_{WZ}
GaAs	5.6536	3.9977	9.7923	3.988	6.562
InAs	6.0583	4.2839	10.4933	4.2742	7.0252
lattice mismatch Δa_i, Δc_i		0.0715	0.0715	0.0718	0.0705

Table 5.1.: *Experimental ZB and WZ lattice parameters for GaAs [201, 298] and InAs [180, 201] and the corresponding lattice mismatch. The ZB lattice parameters are converted into a hexagonal system using $a_{ZB} = a_c/\sqrt{2}$ and $c_{ZB} = a_c\sqrt{3}$. All values are in Å.*

is named "crystal phase selective growth" and an explanation is presented.
The WZ side facets ($\{\overline{2}110\}$) have a lower surface energy than the cubic ones ($\{110\}$) [97, 338] and in general the facet energies of InAs are lower than those of GaAs. Taking this into consideration, growth of InAs on both facets ($\{110\}$ and $\{\overline{2}110\}$) is expected since it leads to a gain in energy compared to the GaAs side facets. However, the bulk energy is lower for the cubic phase [3]. This lower bulk energy of the ZB phase can act as an explanation for the observed crystal phase selective growth: the growth of InAs occurs on the crystal phase where the total energy of the nanoscale system, i.e. the core-shell NW, will be the lowest. The total energy will be dominated by the bulk energy of the GaAs core, due to the relatively large NW diameters, as well as the energy associated with the dislocations formed at the interface. The energy of the side facets plays a minor role. However, the difference in bulk energy between ZB and WZ InAs is small [3], making the observed strong discrepancy in the growth hard to understand. Additionally, a pure explanation in terms of bulk energies does not explain why existing stacking faults and twins in the core have an impact on the growth of the shell.

A more likely possibility is related to different lattice mismatches in the ZB and WZ crystal structures. The cubic ZB lattice with the lattice constant a_c can be converted into an equivalent hexagonal structure with the lattice constants $a_{ZB} = a_c/\sqrt{2}$ and $c_{ZB} = a_c\sqrt{3}$ along the cubic [110] and [111] directions, respectively. Table 5.1 shows experimentally determined values of the hexagonal ZB and WZ lattice parameters for GaAs and InAs. As seen, $c_{ZB}/p_{ZB} < c_{WZ}/p_{WZ}$ (with $p_{ZB} = 3$ and $p_{WZ} = 2$, the number of bilayers along the c-axis within the unit cell) and $a_{ZB} > a_{WZ}$. The distance of the (111) planes in the ZB lattice is shorter than the distance between the (0002) planes in the WZ lattice. Along the a-axis, the atoms are more close in the WZ structure. Calculating the lattice mismatches between GaAs and InAs along the a- and c-directions for both crystal structures, $\Delta a_i = (a_{InAs,i} - a_{GaAs,i})/a_{GaAs,i}$ and $\Delta c_i = (c_{InAs,i} - c_{GaAs,i})/c_{GaAs,i}$, where i stands for ZB or WZ, reveals that the lattice mismatch along the a-direction is slightly smaller in the ZB lattice than in the WZ one while along the c-direction this is larger in the ZB structure than in the WZ structure (see Table 5.1). Certainly, there is a large uncertainty in the exact lattice mismatch caused by variations in the reported values for WZ GaAs and InAs [23, 59, 178, 180, 298, 347]. Nonetheless, the general tendency is clear: in the cubic lattice the mismatch is identical in all directions while in the WZ lattice this differs being smaller in the c- than in the a-direction. As shown before by SEM and TEM micrographs, the growth of InAs on WZ GaAs occurs, but it grows much slower than on ZB GaAs and it always develops from the ZB phases. The InAs shell adopts the crystal structure of the GaAs core, i.e. WZ InAs grows on the WZ phase of the GaAs core. The growth of the InAs on the WZ phase proceeds via "tongues", having a small growth front and being laterally confined. This demonstrates that the growth rate along the c-direction is higher than along the a-direction. This was also shown in Fig. 5.13 displaying almost closed shells on WZ core segments, only the edges being still uncovered. Consequently, the growth along the a-direction is the restricting

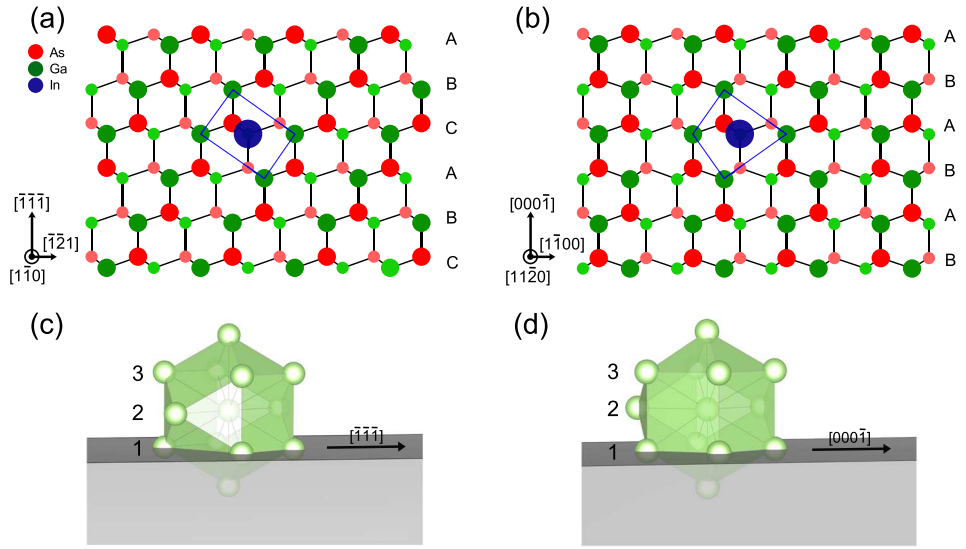

Figure 5.15.: *(a) and (b) show models of the non-reconstructed NW side facets for ZB and WZ GaAs phases, respectively. Large circles denote atoms at the most outer position, while small circles are for the layer behind. The blue circle shows the next incorporated In atom. Blue lines around the In atom indicate the second nearest neighbor atoms. (c) and (d): NW surface with the complete coordination polyhedron (second nearest neighbors) for ZB and WZ structures, respectively. A cut along the grey plan gives the same nearest neighbors as in (a) and (b). Labels next to the coordination polyhedron refer to the layers within it. The central atom (in layer 2) corresponds to the blue In atom in (a) and (b). (c) and (d) were created using VESTA [215]. Published in [264].*

factor, hindering the growth on the WZ phase. This is further supported by the fact that the lattice mismatch along the a-direction is larger in the WZ phase than in the ZB one (see Table 5.1).

The impact of the lattice mismatch in the a-direction is even enhanced by taking into account the local environment for each new incorporated atom. Figures 5.15a and b display non-reconstructed {110} and {$\bar{2}$110} GaAs surfaces corresponding to the ZB and WZ phases, respectively. A reconstruction of the {110} surface changes the positions of As and Ga in the upper layer only slightly: As is shifted upwards while Ga atoms are shifted downwards [156, 305]. The general shape of the surface (viewed along the [1$\bar{1}$0] direction) is not modified. In fact, recent publications have demonstrated that the ZB {110} and WZ {$\bar{2}$110} surfaces of MBE and MOVPE grown GaAs NWs do not exhibit a reconstruction [40, 135]. Consequently, non-reconstructed surface are assumed for both cases. In the bulk, each group III atom is surrounded by 4 group V atoms forming a tetrahedron. The second nearest neighbors are again of group III with a coordination number of 12. They form a cuboctahedron and anti-cuboctahedron in ZB and WZ crystal lattices, respectively. The cuboctahedron (see Fig. 5.15c) is characterized by the inversion symmetry. This is not the case for the anti-cuboctahedron (see Fig. 5.15d). These different symmetries become important when lattice mismatched materials are grown onto each other. The blue circles in Fig. 5.15a and b indicate a new In atom, being incorporated on the side facets to form a nucleus for a new layer. Each surrounding Ga atom (located on layer 1 in the polyhedron) acts with a repulsive force on this new In atom. In the ZB case, these forces cancel each other out along the [$\overline{111}$] and the [$\overline{121}$] directions, regardless of the placement of the In atom (see Fig. 5.15a). In the WZ arrangement, the distribution of existing Ga atoms around a new In atom is not homogeneous. As seen in the drawing shown in Fig. 5.15b, an In atom (blue) placed on an A-layer of the stacking sequence (layer 2 in the polyhedron) has three neighboring

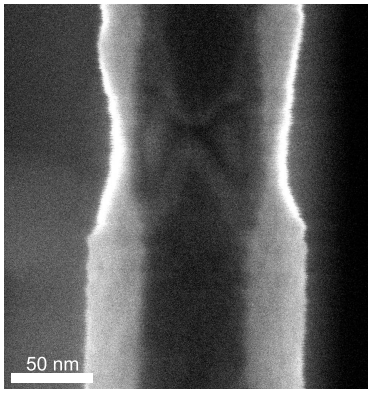

Figure 5.16: *SEM micrograph of an interruption where the two InAs shells are almost coalesced.*

Ga atoms located on the left side (in layer 1 of the polyhedron) while only one is on the right side of the In atom. This arrangement shifts the new In atom slightly to the right in order to minimize its energy and balance the repulsive forces. On the B-layer the situation is inverted and the new In atom is shifted to the left. Consequently, the distance between neighboring In atoms is decreased which, in turn, increases the strain in the InAs. This makes the nucleation and growth of InAs on WZ GaAs non-preferred. The increased strain is not only present in the first layer (labeled number 2 in the polyhedron) of InAs on WZ GaAs but also in the subsequent ones since the overall strain relaxation occurs gradually. Accordingly, the growth of InAs on the initially strained InAs shell is hindered as well which then decreases the growth rate. An In atom on the A-layer also adds a force on surrounding In atoms on the B-layers. Certainly, this force can partially compensate that one induced by the Ga atoms underneath. On edges the forces will always be unbalanced, hindering the lateral growth of a nucleus.
This model does not only give a rough explanation for the the suppressed direct nucleation of InAs on WZ GaAs, but also provides an explanation for the influence of stacking faults and twins on the growth of InAs: each stacking fault or twin is a single layer of WZ, making growth unfavorable at this position.
Differences in the growth of core-shell structures depending on the crystal structure have already been reported in literature, for example when growing InP shells around InAs NWs [107] or GaAsSb shells around GaAs NWs [101]. In each case, the growth rate on the WZ phase was found to be lower than on the ZB phase and even differences in the growth rate along different ZB directions were observed. This difference has been explained by a higher nucleation probability on the ZB phase compared to the WZ one. Nonetheless, direct growth on both crystal structures was observed in both cases. This is the most dominant difference to the situation discussed here. Although the nucleation probability on the ZB and WZ phase may also be strongly different in our case (due to the above mentioned reasons of the local environment and strain), a model only based on the nucleation probability and growth rate cannot explain the observed impact of twins and WZ segments. Further investigation in pure WZ NWs shall contribute to a deep understanding of the crystal phase selective growth.

The presented growth mechanism provides new insights in understanding the differences between the crystal structures and can represent the base for novel devices. For example, the position of InAs quantum dots on GaAs NWs [313, 339] may be controlled by controlling the crystal structure of the core. Several devices can be stacked onto each other, being separated by the insulating GaAs core. Additionally, InAs shell segments forming constrictions or having point contacts to neighboring segments can be fabricated. For the latter, Fig. 5.16 shows a SEM micrograph with two almost coalesced “tongues“, which are be considered as a specific

point contact. Their dimensions can then be controlled by the NW diameter and the InAs shell growth time.

5.3. InAs nanotubes[4]

It was described in the previous section that the WZ segment at the top of the GaAs NW core results in an absence of InAs shell growth. Thus, the GaAs core is exposed and can be removed from the GaAs/InAs core-shell NWs using a wet chemical etchant based on NH_3(aq) and H_2O_2. The etch selectivity between GaAs and InAs using this etchant is high [131, 232, 337], resulting in the formation of InAs nanotubes. This process is displayed in Fig. 5.17a-d showing the GaAs/InAs core-shell NWs before the wet chemical etching (a,b) as well as after the etching (c,d). The NH_3(aq):H_2O_2 based etchant attacks the GaAs core at the exposed part and etches it completely. The InAs shell is not affected by the etchant as visible in the corresponding SEM micrographs (Fig. 5.17c,d). Figure 5.18 shows a HAADF image of an etched GaAs/InAs core-shell NW, an EDX line scan is superimposed. Strong signals originating from As and In are observed whereas the Ga signal is weak. As seen by the brightness of the HAADF micrograph, the In and As EDX signals follow the HAADF intensity and therefore reproduce the local thickness. This means that a hollow ring, i.e. a nanotube, is formed. The presence of the weak Ga signal, observed only in the inner part of the nanotube, may either result from an incomplete etching or an interfacial alloying/roughness. The latter was already assumed in the GaAs/InAs core-shell NW cross section depicted in Fig. 5.8. The etch selectivity between GaAs and $In_xGa_{1-x}As$ is high already for low amounts x of In [131]. Therefore, even an alloyed interface acts as an etch stop. As it is seen in the cross sectional TEM micrograph depicted in Fig. 5.8, the interfacial area between the GaAs and InAs has a thickness of a few nanometers only.

InAs nanotubes obtained from GaAs/InAs core-shell NWs are interesting structures due to two reasons: (1) the removal of the GaAs core allows to investigate the crystalline properties of the InAs shell only and (2) the increased surface area of the nanotube compared to the core-shell NW should significantly affect the transport properties.
Regarding the first opportunity, Fig. 5.17e-g displays (HR)TEM micrographs of an InAs nanotube. Figure 5.17e shows a low resolution image evidencing contrast changes along the NW. The contrast arises from the twins and stacking faults as well as residual strain in the nanotube. The etching certainly may affect the strain in the shell, since it removes the GaAs core which strains the shell compressively. Nonetheless, strain in the InAs can still be present after the removal of the GaAs core. For example, the strain can be induced by the remaining InGaAs at the inner part of the tube as well as residual dislocations. An increase of the magnification clearly proves the existence of stacking faults and twins in the shell (see Fig. 5.17f). These are not only arranged perpendicular to the growth axis of the NW, as it is normal during NW growth, but also perpendicular to other ⟨111⟩ directions. Such stacking faults have already been observed in GaAs/InAs core-shell NWs (see Fig. 5.7g) and are seen even better in the HRTEM image shown in Fig. 5.17g. The white lines indicate the stacking sequences. The image displays a twin perpendicular to the growth direction and some stacking faults perpendicular to other ⟨111⟩ directions. The blue circle and inset highlights a Shockley partial dislocation being the origin of the stacking fault. A similar Shockley partial dislocation is found at the other end of

[4]Results presented in this section have been published in T. Wenz, M. Rosien, F. Haas, T. Rieger, N. Demarina, M. I. Lepsa, H. Lüth, D. Grützmacher, and T. Schäpers. *Phase coherent transport in hollow InAs nanowires.* Applied Physics Letters, 105(11):113111, 2014. Ref. [329]. Electrical measurements were performed by Marion Rosien, analyzes of the data by Tobias Wenz and Marion Rosien.

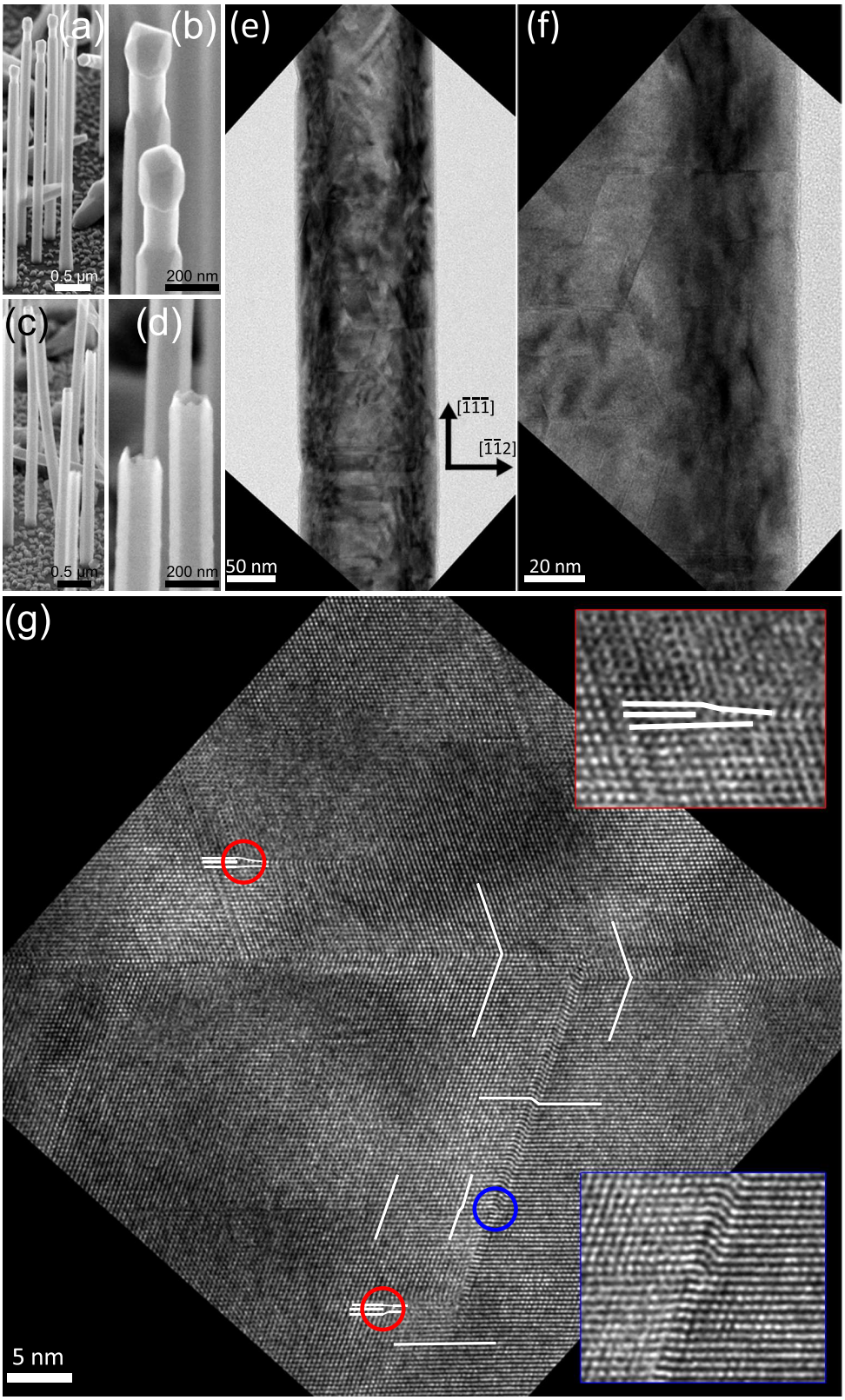

Figure 5.17.: *SEM and (HR)TEM micrographs of InAs nanotubes. (a,b) SEM micrographs of GaAs/InAs core-shell NWs prior to wet chemical etching of the GaAs core and (c,d) SEM micrographs of etched GaAs/InAs core-shell NWs forming InAs nanotubes. (e) Low resolution TEM image. (f) TEM image evidencing twin planes and stacking faults in several* ⟨111⟩ *directions. (g) HRTEM image showing several defects in the InAs nanotube. The insets show threading dislocations (red) as well as a Shockley partial dislocations (blue).*

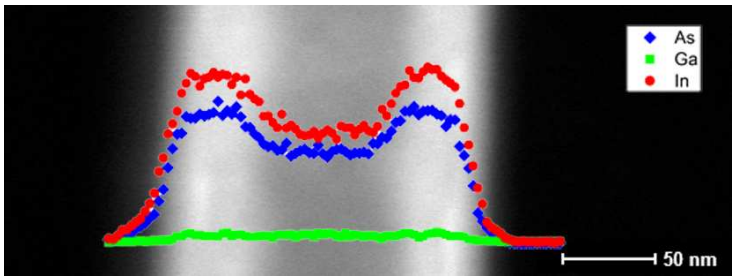

Figure 5.18: *HAADF image of an InAs nanotube with superimposed EDX linescan showing the presence of As ♦, Ga ■ and In ●. Published in [262].*

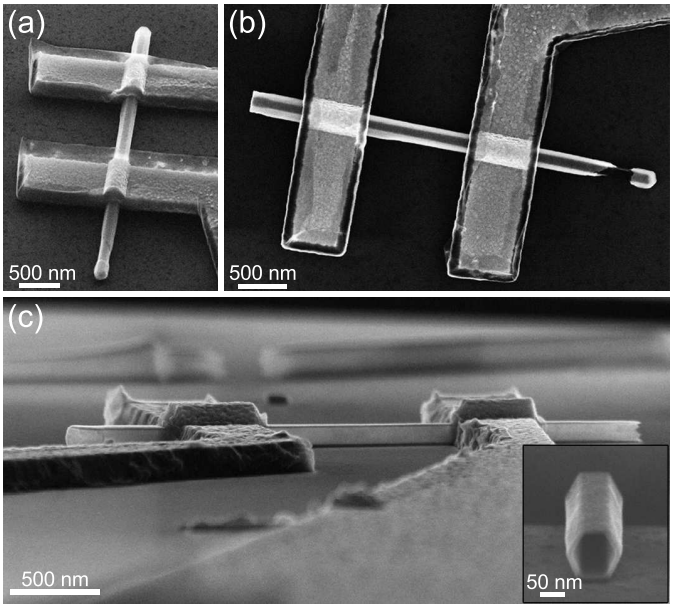

Figure 5.19: *SEM micrographs of a contacted GaAs/InAs core-shell NW (a) and contacted InAs nanotubes (b,c). The inset in (c) clearly proves the hexagonal morphology of the inner and outer part of the nanotube.*

the stacking fault. The red circles and the red inset point to dislocations in the InAs nanotube. These dislocations are not at the (former) interface. Rather, the TEM micrograph represents a plan-view image of the grown InAs surface with a {110} growth front. The dislocations seen in the red circles are consequently threading dislocations which originate from the high lattice mismatch between GaAs and InAs or the initial growth mechanism based on islands and their coalescence.
To conclude, the InAs nanotubes allow to investigate the crystalline structure of the InAs shell in detail without any impact from the GaAs core. In GaAs/InAs core-shell NWs, the different lattice constants in combination with the fast strain relaxation result in Moiré fringes making a detailed investigation difficult.

Concerning the transport properties of InAs nanotubes in comparison to GaAs/InAs core-shell NWs, Fig. 5.19 displays SEM micrographs of a contacted GaAs/InAs core-shell NW (a) and contacted InAs nanotubes (b,c). Contacts to the NWs were made in a similar way as described for earlier studies of NWs [289] employing Ar^+ sputtering before evaporating Ti and Au. The nanotubes were obtained by selectively etching the GaAs out of contacted core-shell NWs using a NH_3(aq):H_2O_2:H_2O 1:1:30 etchant for 3 min. This is necessary since the nanotubes are rather fragile and do not withstand the processing during contacting. As seen in the SEM micrographs in Fig. 5.19b,c the GaAs core is etched completely and the hexagonal morphology of the inner and the outer surface are maintained, further demonstrating the high etch selectivity between GaAs and InAs. Etching the core after contacting the NW also allows to compare the electrical properties of core-shell NWs and nanotubes directly, thus on the very same device.

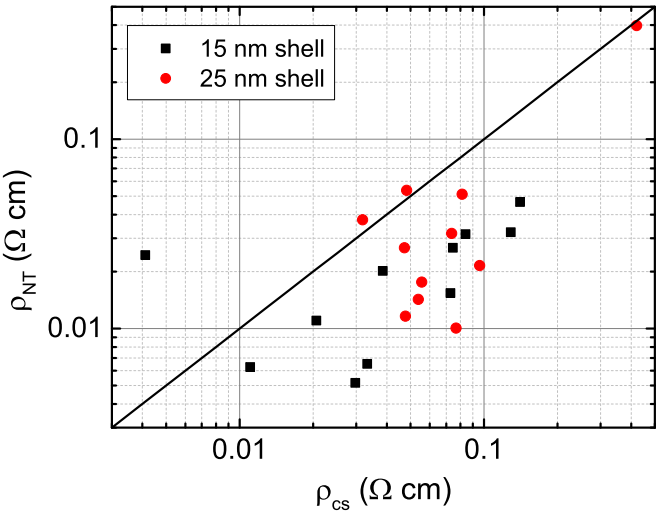

Figure 5.20: *Resistivity map of GaAs/InAs core-shell NWs and InAs nanotubes. The resistivity of GaAs/InAs core-shell NWs ρ_{cs} is obtained before wet chemical etching, the resistivity of the nanotubes ρ_{NT} is measured on the same devices after etching. InAs shells have thicknesses of ■ 15 nm and ● 25 nm. Published in [329]. [Data courtesy of Marion Rosien and Tobias Wenz]*

I-V curves were measured before and after etching the GaAs core and were found to be linear for both systems. The contact resistance can be neglected due to the use of Ar^+ sputtering [289]. In Fig. 5.20 the resistivities before and after etching, i.e. of the GaAs/InAs core-shell NWs and of the InAs nanotubes, are plotted. NWs with shell thicknesses of 15 nm and 25 nm were used for the study, the core diameters are $\sim$ 50 nm and $\sim$ 100 nm, respectively. On average, the resistivity decreases by a factor of about two (2.8 for 15 nm shell thickness and 2.3 for 25 nm shell thickness) after etching, agreeing with the expected increase in electron concentration. Only in three cases an increase of the resistivity is found which may be attributed to damaging the InAs shell during the etching process.

The enhancement of the conductivity can be explained by the increase of the surface to volume ratio. In a rough estimation the surface area is doubled after etching the core. InAs has a surface accumulation layer, i.e. a high density of donor states at the surface [200]. Electrons contributing to the transport are either bulk carriers or are present due to the surface accumulation layer. For thin structures, the average electron concentration is dominated by the surface area, the bulk carriers have a minor contribution. The surface area of the nanotubes is almost doubled with respect to the core-shell NWs and therefore also the average electron concentration is roughly twice as high as for core-shell NWs. The wet chemical etching may also influence the mobility, e.g. by a removal of dislocations (increase of the mobility) or the formation of the additional surface (surface scattering, decrease of the mobility). A precise measurement of the electron concentration and mobility in NWs is difficult due to surface states [26] which may change during the etching process.

5.4. Conclusions

This chapter was devoted to GaAs/InAs core-shell NWs. The axial strain relaxation in these core-shell NWs was monitored *ex situ* using Moiré fringes and X-ray diffraction. It was demonstrated that the lattice mismatch results in strain in both the GaAs core and the InAs shell. While the strain in the shell was found to decrease with increasing shell thickness, the strain in the GaAs core was simultaneously enhanced. HRTEM investigations revealed that the strain was released by perfect dislocations, Frank partial dislocations and Shockley partial dislocations. An overgrowth of GaAs NWs containing both crystal phases, which are ZB and WZ, with InAs gave evidence that the growth on the ZB phase is preferred compared to the growth on the WZ phase. A detailed analyses was conducted demonstrating that the growth of InAs on the

WZ phase of GaAs originates from neighboring ZB regions. Each WZ segment in the core was found to have an impact on the growth of the shell. A model taking into account the effective lattice mismatches on the NW side facets was developed and served as an explanation for the crystal phase selective growth. The absence of the growth of the InAs shell on the WZ phase of the GaAs core allowed to fabricate and analyze InAs nanotubes. The nanotubes were obtained by a wet chemical etching of the core. Structural analyzes of the nanotubes confirmed the defect rich structure of the InAs, even proving the existence of threading dislocations. Electrical measurements demonstrated that the resistivity decreases for the nanotubes compared to the core-shell counterparts. This was explained by an increase of the electron concentration due to the enhanced surface to volume ratio.

6 Chapter 6. Antimony containing heterostructure nanowires

Sb-based semiconductors and semiconductor heterostructures are promising for studies of fundamental physics [218] as well as devices suitable to extend Moore's law, e.g. TFETs [61, 146]. InAs, GaSb and AlSb belong to the "6.1 Å family", i.e. they have lattice constants in the range of 6.1 Å [181]. Consequently, the lattice mismatch between these semiconductors is small. Core-shell NWs containing InAs and GaSb benefit from a broken gap band alignment where the conduction band of the InAs is below the valence band of the GaSb. This band alignment gives rise to band-to-band tunneling allowing subthreshold slopes below 60 mV/dec. AlSb shells covering InAs NWs may be used to prevent electron scattering at the surface of the InAs resulting in InAs NW devices with high mobilities. InSb has the highest electron mobility among the III-V semiconductors and gains from a high spin-orbit coupling [145, 221] making it of high interest for spin-based devices.
The use of antimony during the growth requires significantly reduced growth temperatures, e.g. InSb is often grown at temperatures between 340°C and 420°C [227, 285, 306]. Low substrate temperatures reduce the adatom mobility and enhance the sticking coefficient.
This chapter aims to evaluate the growth of Sb-based NW heterostructures. Some results presented in this chapter have been published in Refs. [258] and [257].

6.1. InAs/$Al_xGa_{1-x}Sb$ core-shell nanowires

A core-shell system consisting of InAs and GaSb is of particular interest due to its unique type III band alignment [173]. This allows the fabrication of TFETs with high on/off ratios and sub-threshold slopes below the thermodynamic limit of 60 mV/dec [61, 146]. In core-shell NWs, the interface area between an InAs core and a GaSb shell is very high while the NW volume is small, as displayed in Fig. 6.1, with an abrupt interface not suffering from graded compositions typically observed in axial heterostructure NWs [74, 233]. The graded compositions in axial heterostructures are ascribed to the "reservoir effect" of the droplet [74] while no droplet is involved in the radial growth. The large interface area being present in core-shell NWs can carry high tunneling currents. NW (T)FETs with a GaSb core and an InAs(Sb) shell have already been investigated and show promising characteristics [72, 99]. By adding Al to the GaSb shell, the band alignment changes from the broken gap (type III) to the staggered gap

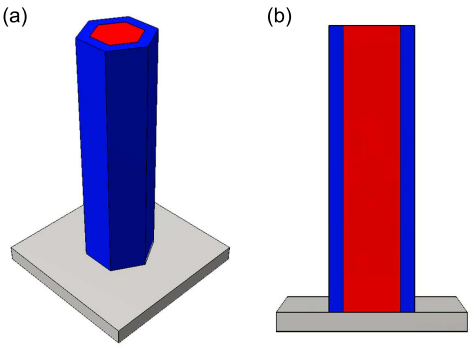

Figure 6.1: *Sketch of a core-shell NW demonstrating the high interfacial area.*

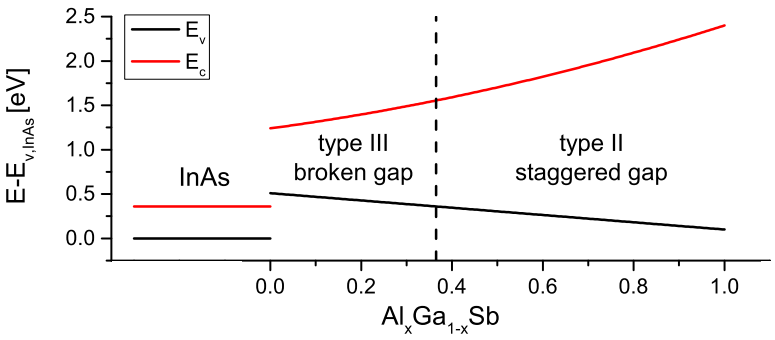

Figure 6.2: *Band alignment of InAs/$Al_xGa_{1-x}Sb$ heterostructures as a function of the Al content x. E_v is the valence band, E_c the conduction band. A transition from type III to type II is seen.*

(type II). The band alignment as a function of the Al content in the $Al_xGa_{1-x}Sb$ is depicted in Fig. 6.2. The band gap of $Al_xGa_{1-x}Sb$ at 300 K is given by $E_g(x) = 0.73+1.57x+0.47x(x-1)$ [6], the conduction band offset varies linearly from GaSb to AlSb [8]. The change from the broken to the staggered gap occurs at Al contents of about 36%. So far, staggered gap InAs/AlGaSb TFETs have been limited to planar structures [196, 197]. However, Knoch and Appenzeller showed that the staggered band alignment with an Al content of about 60% should result in an optimal performance [176]. Considering InAs NWs embedded in shell with high Al contents, the large electron barrier of up to 1.35 eV can significantly enhance the electron mobility due to reduced surface scattering [71, 181, 310]. Consequently, an *in situ* passivation of InAs NWs with an almost defect-free shell is of particular interest for high-mobility devices. Apart from this, a core-shell system with a broken gap band alignment can be used to transfer recently observed phenomena in two dimensional topological insulators [175] into the NW geometry.

The lattice constants of InAs, GaSb and AlSb are 6.0583 Å, 6.09593 Å and 6.1355 Å, respectively [201]. Considering these lattice constants, the lattice mismatches vary between 0.6 and 1.2%. As already introduced in Chapter 3, the critical thicknesses in planar InAs/GaSb and InAs/AlSb heterostructures are in the range of 20 and 10 nm, respectively. Transforming the structure into a core-shell NW system significantly increases the critical thickness [252, 253]. Accordingly, an InAs NW core with a radius of about 40 nm is expected to be misfit dislocation free despite of the thickness of the GaSb shell. For a GaSb shell thickness of about 40 nm the InAs NW core can have a radius of more than 200 nm (see Fig. 3.4 in Sec. 3.4).

6.1.1. GaSb shells[1]

InAs/GaSb core-shell NWs were grown on Si (111) substrates with both As and Sb valved crackers. The substrate preparation and InAs core NW growth was as described in Sec. 4.2.1 with an

[1] Most results of this section have been published in T. Rieger, D. Grützmacher, and M. I. Lepsa. *Misfit dislocation free InAs/GaSb core-shell nanowires grown by molecular beam epitaxy.* Nanoscale, 7(1):356-64, 2015. Ref. [258]. Wet chemical etching of the core-shell NWs was performed by Franz Josef Hackemüller [118].

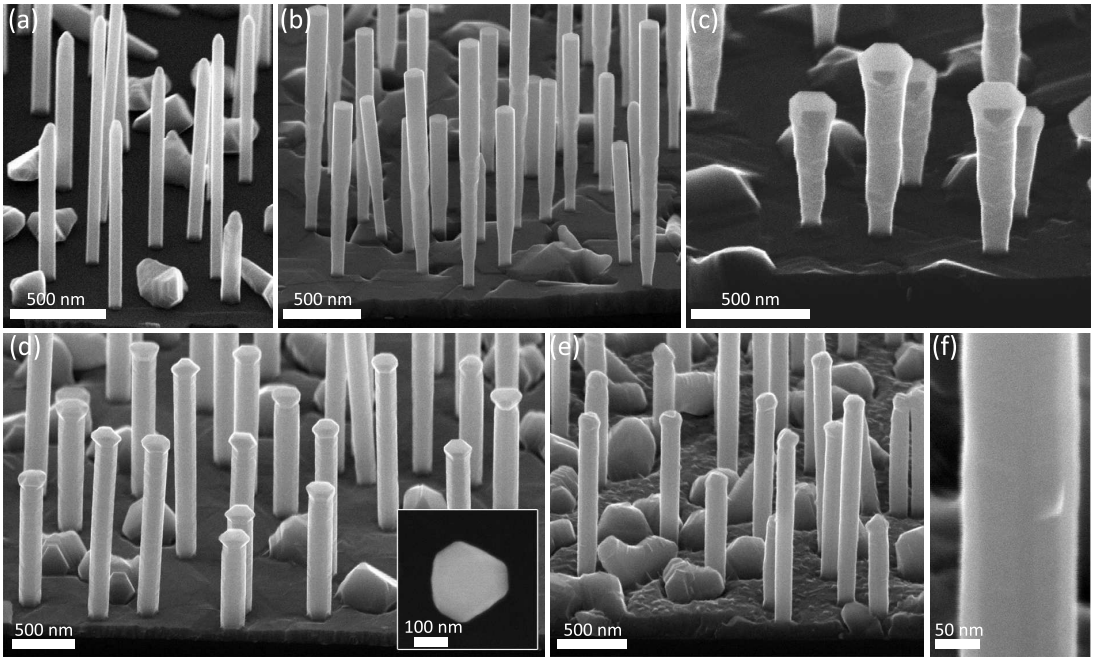

Figure 6.3.: *Bird's eye view SEM micrographs of InAs and InAs/GaSb core-shell NWs: (a) bare InAs NWs, (b)-(e) InAs/GaSb core-shell NWs with shell growth temperatures T^{sub}_{GaSb} of 490° C (b), 400° C (c), 360° C (d) and 300° C (e). (f) Higher magnification image of a NW with GaSb shell growth temperature of 300° C showing a sidewall roughness. The inset in (d) shows a top-view image of a single core-shell NW clearly exhibiting a three-fold symmetry. Published in [258].*

In rate of 0.035 µm/h and an As_4 flux of $1 \cdot 10^{-5}$ mbar. Subsequently, the substrate temperature was lowered to T^{sub}_{GaSb} and the GaSb shell was grown with a Ga rate of 0.1 µm/h and a Sb flux F_{Sb} varying between $2 \cdot 10^{-7}$ and $2 \cdot 10^{-6}$ mbar. The growth of the GaSb shell was initiated by providing Sb for 2 min before opening the Ga shutter. This shutter sequence should create an InSb-like interface and remove As from the chamber before the GaSb is grown. The GaSb shell growth time t_{GaSb} was varied between 5 and 90 minutes.

A typical SEM micrograph of bare InAs NWs is shown in Fig. 6.3a. The NWs have a length of about 1.5 µm and a mean diameter of $\sim$ 100 nm. They do not show any tapering except for the upper $\sim$ 100 nm where the diameter decreases. The NW density is in the range of 1 NW/µm^2, thus relatively low. Low density NWs are ideal for core-shell structures since shadowing effects of neighboring NWs [269] as well as competition for adatoms between them [127] are reduced. As described in Sec. 4.1 the InAs NWs have a hexagonal prism morphology with side facets belonging to the $\langle 110 \rangle$ family. The InAs NWs contain a high density of stacking faults which have been shown in Sec. 4.1.3.
The growth of planar GaSb layers on InAs substrates is carried out at temperatures of about $\sim$ 400°C [15, 120, 226, 266], whereas GaSb is grown on GaAs substrates at about 500°C [138, 148, 225]. Accordingly, GaSb shells were grown in the temperature range T^{sub}_{GaSb} from 300°C to 490°C with a Sb flux of $8 \cdot 10^{-7}$ mbar. Representative SEM images after a shell growth time t_{GaSb} of 90 min are displayed in Fig. 6.3b-e. A parasitic GaSb layer is grown on the Si (111) substrate in-between the NWs under all growth conditions, it is rather smooth but it roughens for the lowest growth temperature. The parasitic layer indicates a low diffusion and high sticking coefficient of the adatoms. The NW morphology is strongly influenced by the growth temperature of the GaSb. Substrate temperatures of 400°C and above result in a strong tapering of the GaSb

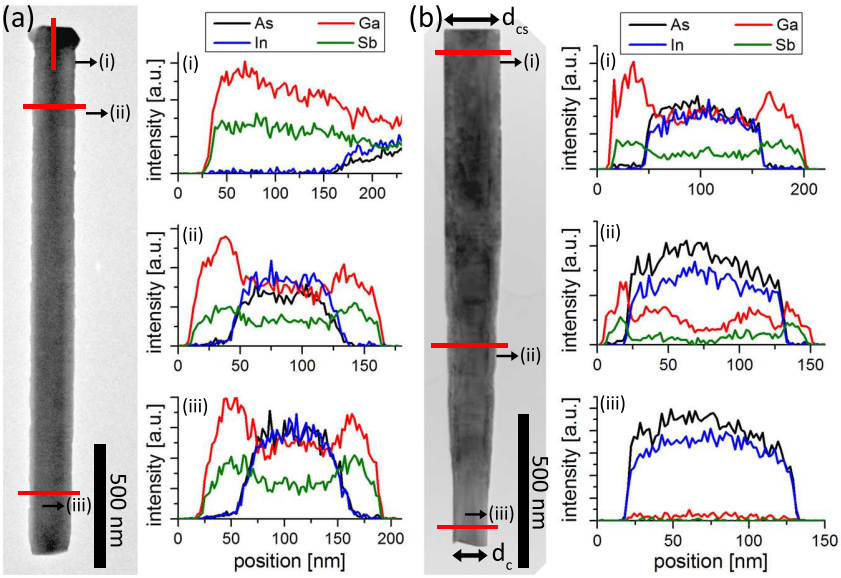

Figure 6.4: *TEM micrographs of InAs/GaSb core-shell NWs with shell growth at 360° C (a) and 490° C (b). EDX profiles are plotted right next to the TEM images, red lines on the images indicate the positions of the profiles. d_c is the core diameter, d_{cs} the diameter of the core-shell NW. Published in [258].*

shell with a thinner shell at the bottom than at the top, i.e. an inverse tapering (Fig. 6.3b and c). A reduction of the substrate temperature to 360°C results in NWs with uniform diameters as well as smooth facets (Fig. 6.3d). Further decreasing the substrate temperature increases the roughness of the GaSb shell as displayed in the higher magnified image in Fig. 6.3f. After the growth of the GaSb shell, the NWs typically exhibit a flat top facet. This is in contrast to the faceted tip of the bare InAs NWs. For temperatures around 350 – 400°C and long shell growth times, this flat top is in conjunction with a radial growth at the top forming a platform (see Fig. 6.3c and d). This platform is described later.

To confirm the core-shell structure, NWs with shells grown at 360°C and 490°C were examined by TEM and EDX. The corresponding TEM images and EDX profiles are depicted in Fig. 6.4a and b, respectively. The low shell growth temperature of 360°C gives rise to a uniform and conformal GaSb shell as seen by the EDX profiles taken at the upper and lower part of the NW displayed in Fig. 6.4a. The shell has a thickness of about 35 nm, being in good agreement with the expected thickness considering the Ga rate, growth time as well as geometry of the MBE system. At these low growth temperatures, the majority of Ga adatoms contributing to radial growth are due to direct impingement, diffusion from or to the substrate has a minor effect. Apart from the GaSb shell, axial growth of GaSb on the NW takes place which develops the platform at the top. The height of the axially grown GaSb is $\sim$ 140 nm, being in good agreement with the expected thickness of a GaSb layer grown on a planar substrate. This once more indicates the low diffusivity of Ga adatoms on the NW facets.

When the substrate temperature is increased, the diffusivity of the adatoms is changed. At 490°C, the InAs/GaSb NWs exhibit a strong inverse tapering with a larger diameter d_{cs} at the top than at the bottom d_c (see Figs. 6.3b,c and Fig. 6.4b). EDX profiles acquired at different positions along the NW axis demonstrate the absence of a GaSb shell at the lower part of the NW while a 40 nm thick GaSb shell is found at the upper part of the NW (see Fig. 6.4b). The shell thickness gradually decreases from the top to the bottom. Here, shadowing effects do not play a role since the NW density is low, i.e. $\sim$ 1 NW/µm^2, and comparable for both samples grown at 490°C and 360°. Rather adatom diffusion along the NW leads to the evolution of the tapered shells. Dimakis *et al.* showed for Si-doped GaAs shells grown around GaAs NWs

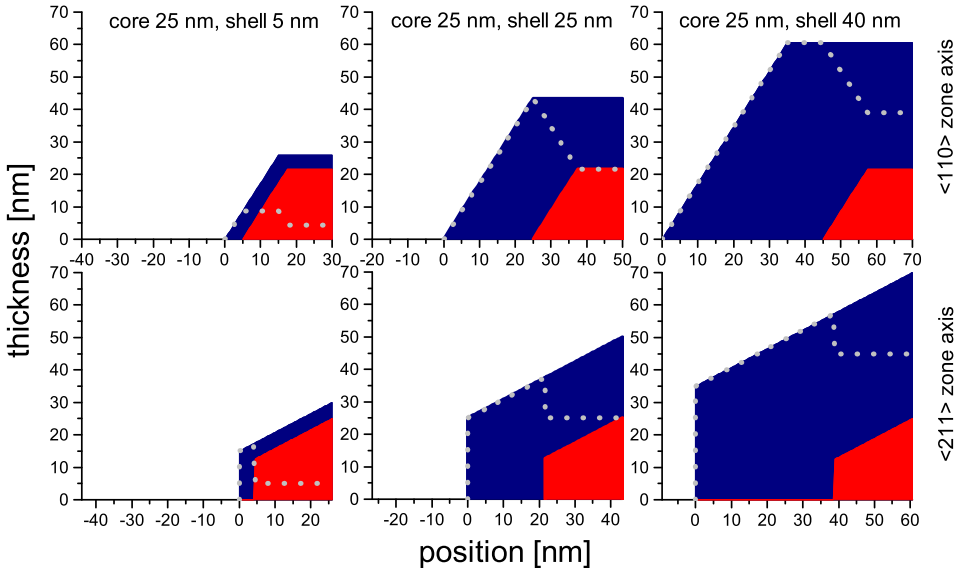

Figure 6.5.: *Schematic cross-sections of core-shell NWs with three different shell thicknesses. The core is colored red, the shell blue. The grey dotted line represents the difference in thickness between shell and core. Published in the Supporting Information of [258].*

that low substrate temperatures and a corresponding low diffusivity of adatoms are required to grow homogeneous shells [82]. Similar to the results shown here, higher temperatures resulted in tapered shells. Temperature differences along the NW [105, 186], different facets at the top part and the main part of the NW, smaller facets at the top (cf Sec. 4.1.3) as well as changes in the effective V/III ratio can be explanations for such a preferred migration of adatoms to the top. All of them may have an effect on the local chemical potential [84, 239, 299, 309, 324]. In general, a homogeneous, non-tapered shell is required but a tapered shell is advantageous for some applications. For example, in a radial TFET, the tapered core-shell morphology allows contacting the InAs as well as the GaSb parts individually without an etching of the GaSb. For the further discussion, a substrate temperature of 360°C is regarded as the optimal temperature for the shell growth since it provides smooth surfaces as well as a uniform shell thickness along the entire NW.

To contact the core and shell of the conformal InAs/GaSb core-shell NWs individually, a selective etching is required. The typical etchant for InAs is citric acid [70, 78] but preliminary investigations[2] showed that the GaSb shell is also strongly affected. The etch rate of the InAs core was surprisingly low, possibly due to the (111) lattice planes being the effective plane being etched. The GaSb shell can be etched using developers based on TMAH (tetramethylammonium hydroxide), e.g. MF™319 and AZ®326MIF [344, 203]. The InAs core was not affected by the etchants.

Typically, the ⟨110⟩ zone axis is used for the analyses of the crystal structure and defects in NWs. This zone axis has the advantage that the crystal structure and especially potential defects such as twins and stacking faults can be identified. The hexagonal shape of the NW with {110} side facets results in a gradual decrease of the local NW thickness towards its edges. This is displayed in the upper row of Fig. 6.5. This gradual decrease of the thickness prohibits an abrupt change of the contrast between the core and the shell in TEM images. Performing EDX

[2] performed by Franz Josef Hackemüller [118]

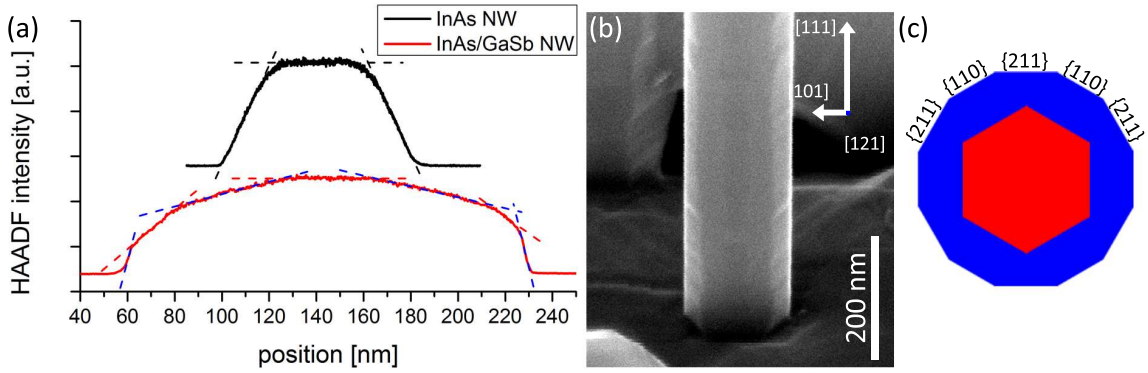

Figure 6.6.: *(a) HAADF profiles of InAs and InAs/GaSb core-shell NWs taken from the* ⟨110⟩ *zone axis. The profiles indicate the cross-sectional shape of the NWs. InAs NWs are bound by six* {110} *side facets while InAs/GaSb core-shell NWs are bound by twelve side facets belonging to the* {110} *and* {211} *family. Dashed lines are guides to the eye. (b) SEM image of the lower part of a core-shell NW showing the presence of multiple side facets. (c) Schematic of the cross-section of InAs/GaSb core-shell NWs. Published in [258]*

analyses from the ⟨110⟩ zone axis produces profiles schematically depicted in Fig. 6.5 (upper images, grey dotted lines). Its exact shape depends on the dimensions of the core and the shell and especially thin shell thicknesses are difficult to measure due to the limited spatial resolution of EDX. Consequently, both techniques, TEM and EDX, have a high uncertainty regarding the evaluation of the shell thickness. Rotating the NW by 30° around the $[\overline{111}]$B growth axis, thus towards the ⟨211⟩ zone axis (see Fig. 2.1), the crystal structure and planar defects can no longer be analyzed [63, 152]. ⟨110⟩ side facets are now parallel to the electron beam and therefore, an abrupt change between the core and the shell can be observed. This situation is schematically drawn in Fig. 6.5 (lower images). This abrupt change allows measuring the shell thickness and native oxide thickness precisely. The interface between the core and the shell is observed from the ⟨211⟩ zone axis with less overlapping effects than from the ⟨110⟩ zone axis. In the following both the ⟨211⟩ and the ⟨110⟩ zone axes are used for a detailed analyzes of the crystal structure, shell and oxide thickness as well potential defects at the interface.

Using the optimized shell growth conditions, i.e. a shell growth temperature of 360°C, the growth time t_{GaSb} was varied between 5 and 90 minutes. The shell thickness was measured by aligning the NWs to the ⟨211⟩ zone axis in the TEM. As described above, this zone axis provides a strong contrast between the core and the shell. The shell thickness plotted against the shell growth time is shown in Fig. 6.7. A linear dependence with a shell growth rate of about ∼23 nm/h is observed. This corresponds well with the supplied Ga rate of 100 nm/h considering the NW and MBE geometry as well as the substrate rotation. Within the studied regime, the Sb flux F_{Sb} does not have an impact on the growth rate of the GaSb shell.

During the overgrowth of the InAs core with GaSb, the morphology of the NW is modified. The morphology of NWs can be monitored by HAADF profiles, demonstrated already in Sec 4.1.3 and Ref. [194]. The InAs core has six side facets belonging to the {110} family as seen by the HAADF signal from the ⟨110⟩ zone axis plotted in Fig. 6.6a and already described in Sec. 4.1. The intensity of the HAADF signal depends on the thickness t as well as on the atomic number Z. In a first approximation, the intensity I scales linearly with t and with Z to the power of γ ($I \propto Z^{\gamma}$). Certainly, usually HAADF profiles cannot be used to determine the facets in core-shell structures since both Z and t vary across the NW diameter. In the case of InAs and

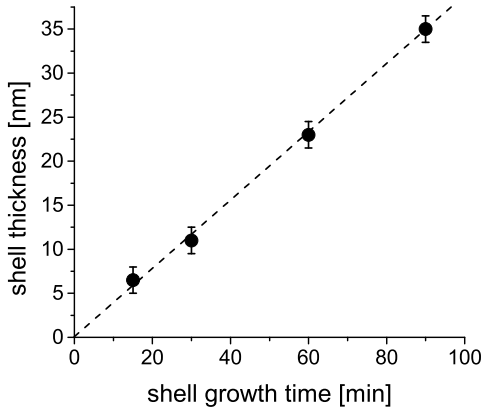

Figure 6.7: *GaSb shell thickness versus shell growth time. The dashed line is a guide to eye. The shell thickness has been measured by TEM from the* ⟨211⟩ *zone axis and shows a linear dependence on the growth time with a growth rate of about* ∼ *23 nm/h. Published in [258]*

GaSb which have almost identical lattice constants, masses and average Z (In: 49, As: 33, InAs: 82; Ga: 31, Sb: 51, GaSb: 82), the materials can only hardly be distinguished by HAADF. Only HR-HAADF images resolve the individual atoms. At lower magnifications, the HAADF profiles still give reasonable information about the NW shape. Accordingly, Fig. 6.6a shows a HAADF profile of an InAs/GaSb core-shell NW plotted together with the profile of a pure InAs NW. The profile of the InAs/GaSb core-shell NW does not exhibit clear large facets but several short linear regions are observed (dashed lines) in the profile indicating a faceted cross-section rather than a round one. Figure 6.6b displays a SEM micrograph of the bottom of a core-shell NW with a 40 nm thick GaSb shell. The viewing direction is $[\bar{1}2\bar{1}]$. Facets perpendicular to the viewing direction can be identified, these being of {211} type. Apart from these facets, another set of facets rotated by 30° is seen, these are of {110} type. Consequently, the HAADF profile agrees with the SEM micrograph demonstrating core-shell NWs with multiple facets. This is schematically depicted in Fig. 6.6c: the InAs NW core with six side facets of {110} type is surrounded by a GaSb shell with a dodecagonal outer shape being bound by {110} and {211} side facets. A detailed investigation reveals that the cross sectional shape changes along the NW axis: at the very bottom of the NW it is hexagonal with {211} side facets. A similar cross sectional shape is present just below the GaSb platform at the top. Taking a profile just slightly above the bottom or below the top modifies the cross-sectional shape strongly. It changes to the dodecagonal shape with a combination of {110} and {211} side facets. This dodecagonal shape is maintained along the major part of the NW. It develops already early during the shell growth and is maintained up to the longest investigated shell growth time of 90 min. Treu *et al.* observed a similar change of the cross sectional shape while overgrowing InAs NWs with InP [307]. It can be concluded that the growth rates and therefore the chemical potentials for adatoms at the GaSb {110} and the {211} facets are similar.

6.1.1.1. Crystal structure analyzes

It was shown in Sec. 3.1 that the low lattice mismatch of about 0.6% between InAs and GaSb results in a critical thickness of about 20 nm for layered systems before strain relaxation takes place. In NWs these critical dimensions are significantly enhanced due to the low dimensions and efficient strain accommodation, see Sec. 3.4. Coherent growth of InAs/GaSb core-shell NWs is expected within a wide area. According to Fig. 3.4, InAs/GaSb core-shell NWs with either the core radius or the shell thickness being below 40 nm are coherently strained (dislocation free), independent on the other dimension (shell thickness or core radius). This is almost identical for both crystal structures.

The presence of dislocations and other defects is investigated by means of (HR)TEM and electron diffraction. For TEM analyzes, NWs with different shell thicknesses are aligned to the ⟨110⟩ and ⟨211⟩ zone axes. In GaAs/InAs (refer to Sec. 5.1.1) and InAs/GaAs [247] core-shell NWs with a lattice mismatch of about 7%, dislocations are often identified by the presence of additional stacking faults caused by Frank partial dislocations. The high density of stacking faults in the InAs core NWs makes it difficult to find such partial dislocations within the NW.
Figure 6.8a shows a TEM image acquired from the ⟨110⟩ zone axis exhibiting clear contrast between the core and the shell. The shell thickness is in the range of 10 nm. The gradual decrease of the local thickness of the InAs core in the ⟨211⟩ directions (due to the hexagonal morphology with {110} facets, see Fig. 6.6) makes it difficult to determine the interface and thus to gain information about the shell thickness or the interface abruptness. The high number of twins and stacking faults being typical for VS InAs NWs is seen. Each of these defects penetrates from the InAs core to the shell indicating an epitaxial growth of the GaSb shell. An electron diffraction pattern of this NW is depicted in Fig. 6.8b, neither spots in the axial nor in the radial direction are splitted suggesting coherent growth. The low lattice mismatch should causes only a slight separation of the diffraction spots which is hard to evaluate. As an additional approach to investigate the growth of the shell, FFT-filtered images maintaining only the (111) lattice planes are produced. The inverse FFT displaying only the {111} planes is depicted in Fig. 6.8c. Each of the {111} planes continues perfectly from the core to the shell, no terminating {111} planes at the interface, in the GaSb shell or in the InAs core are found. Thus, no misfit dislocations are seen over a length of ∼100 nm.
The identical NW is shown in Fig. 6.8d from the ⟨211⟩ zone axis. In this orientation the stacking faults and twins cannot be detected [63, 152]. However, as mentioned before, this zone axis typically provides clear contrast between the core and the shell and enables a precise measurement of the shell thickness. The dark line corresponding to the interface is straight and does not exhibit any roughness. Accordingly, an abrupt interface is expected. An analysis of the interface abruptness by means of EDX is difficult since the signals belonging to In and Sb strongly overlap in the region of 3 – 4 keV. Similar as in the case of the ⟨110⟩ zone axis, the diffraction pattern taken from the ⟨211⟩ zone axis shown in Fig. 6.8e does not exhibit any splitting of diffraction spots.
Assuming loop dislocation with Burgers vectors b either being parallel to the growth axis ($b = a/3\langle 111\rangle$, Frank partial dislocation) or $b = a/2\langle 110\rangle$ (perfect dislocation), a TEM analysis from the ⟨211⟩ zone axis resolves these defects as terminating lattice planes. Determining the type of dislocations is not possible from this zone axis. Figure 6.8f depicts the FFT-filtered HRTEM image from Fig. 6.8d. Identically to the former analyses, no dislocations are observed.

A GaSb shell thickness in the range of 10 nm is far below the critical thickness for InAs/GaSb core-shell NWs and therefore expected to be misfit dislocation free. For GaSb layer thicknesses exceeding 20 nm, strain relaxation is known to take place in planar films [12]. Accordingly, TEM analyses of core-shell NWs with shells of about 40 nm thickness are shown in Fig. 6.8g-l. The low resolution micrograph in Fig. 6g clearly demonstrates the conformal core-shell morphology with relatively smooth side facets. Stacking faults are penetrating from the core to the shell. No Moiré fringes are seen in the image, indicating a pseudomorphic growth of the GaSb shell. The smooth side facets are clearly seen in the higher magnified image in Fig. 6.8h. Identical as for thin GaSb shells, the electron diffraction pattern (Fig. 6.8i) does not exhibit a splitting of the diffraction spots, neither in axial nor in radial direction. Figure 6.8j displays a TEM micrograph from the ⟨211⟩ zone axis of a core-shell NW with a 40 nm thick shell. Again, no

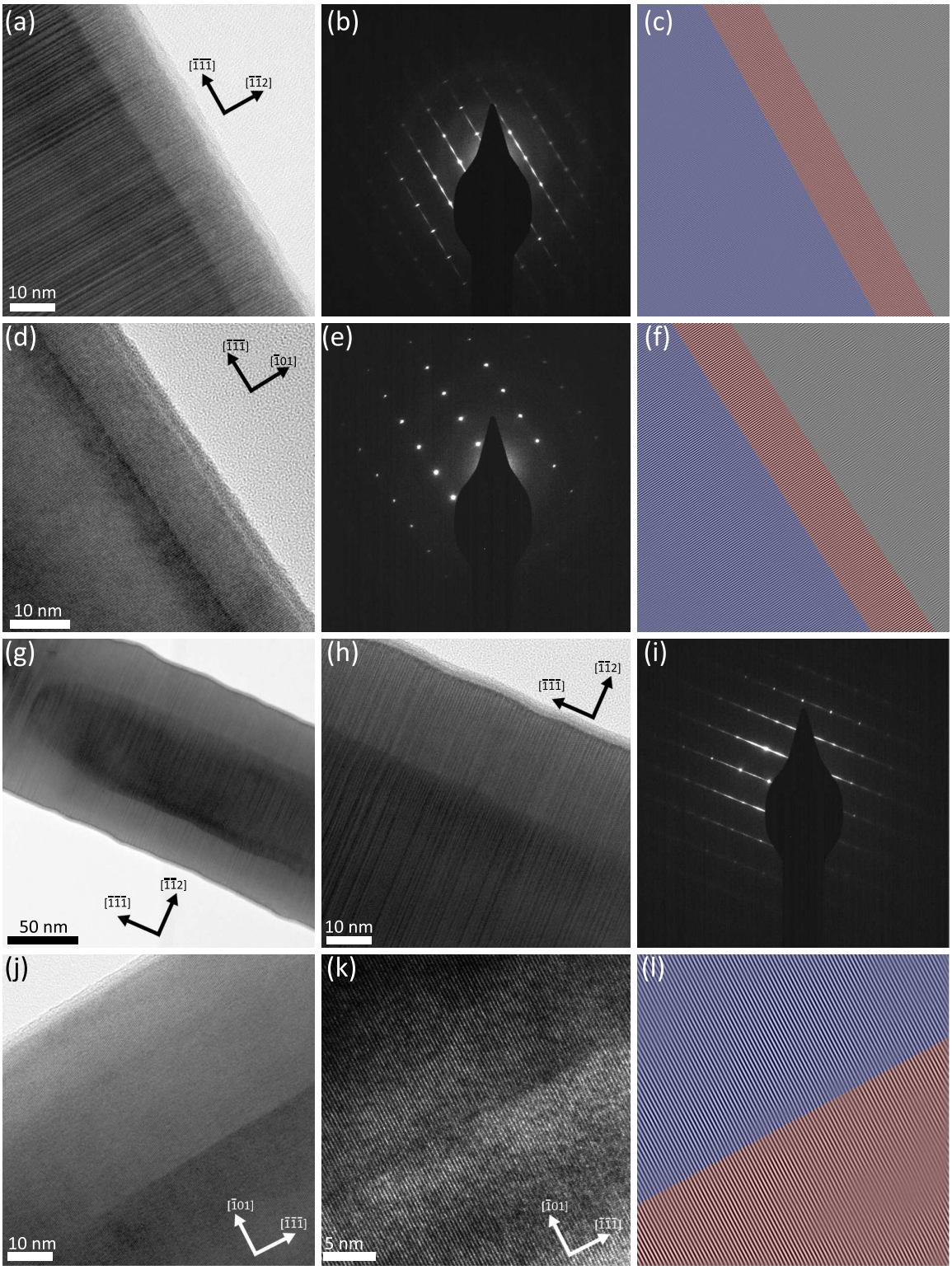

Figure 6.8.: *(HR)TEM and electron diffraction analyses of InAs/GaSb core-shell NWs with (a-f) 10 nm and (g-l) ∼40 nm thick GaSb shells from the* ⟨110⟩ *and* ⟨211⟩ *zone axes. A HRTEM image of a 10 nm thick shell from the* ⟨110⟩ *zone axis is shown in (a), a corresponding electron diffraction pattern and FFT filtered image in (b) and (c), respectively. (d)-(f) show similar images from the* ⟨211⟩ *zone axis. (g) displays a low resolution TEM image of an InAs/GaSb core-shell NW with ∼ 40 nm thick shell from the* ⟨110⟩ *zone axis, (h) HRTEM image from the* ⟨110⟩ *zone axis, (i) electron diffraction pattern. (j)-(l) TEM images and FFT filtered images of a ∼ 40 nm thick shell from the* ⟨211⟩ *zone axis. Colored overlays in (c), (f) and (l) indicate the different materials InAs (blue) and GaSb (red). Published in [258].*

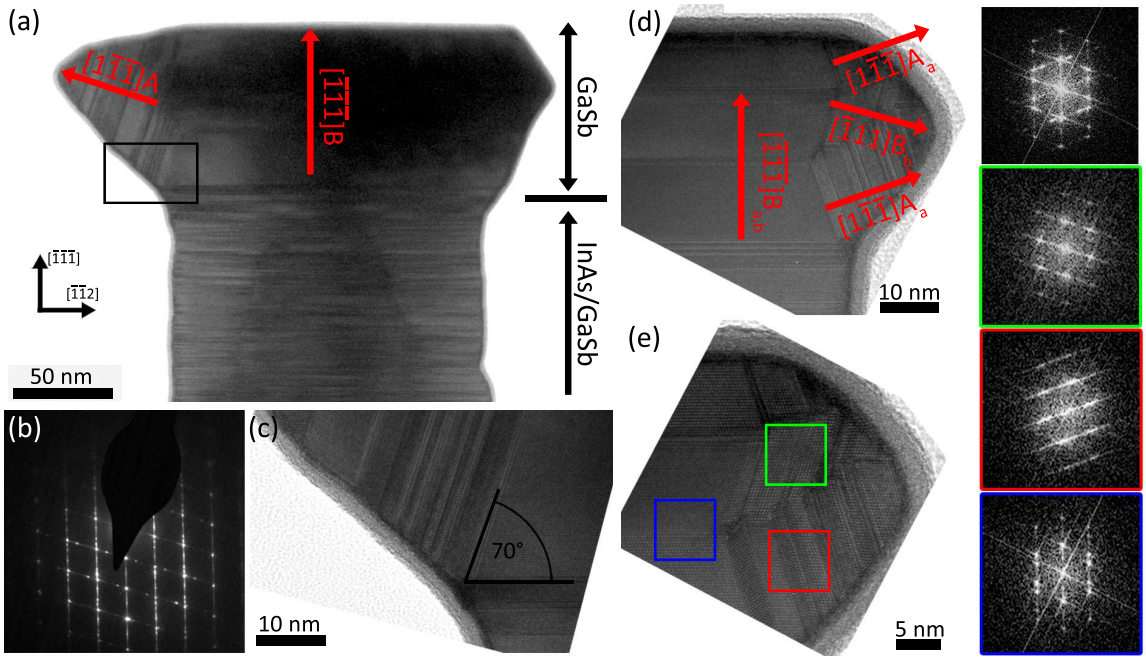

Figure 6.9.: *Origin of the platform formation on top of InAs/GaSb core-shell NWs. (a) TEM micrograph of the upper part of the core/shell NW clearly showing the stacking fault rich part induced by the InAs core as well as an axially grown part with less stacking faults being pure GaSb. In the upper part, additional stacking faults non-perpendicular to the growth direction are found. An electron diffraction pattern of this region is shown in (b), a higher magnification image of the marked region in (a) demonstrating the stacking faults in different directions is displayed in (c). (d) shows a TEM micrograph of a GaSb platform additionally exhibiting twins in the axial direction. The higher resolution image is shown in (e). The lower insets display FFTS of (e) and the colored areas in (e). Published in [258].*

Moiré fringes are visible and smooth side facets are present. The combination of the ⟨110⟩ and ⟨211⟩ zone axes displays both side facets, {211} and {110}, of the core-shell NW, that is a three dimensional view. Both side facets exhibit only a slight roughness.
A HRTEM image of this NW acquired from the ⟨211⟩ zone axis is displayed in Fig. 6.8k, its FFT-filtered image in Fig. 6.8l. The abrupt contrast change from the core to the shell evidences that a high interfacial quality is present even for thick shells and long shell growth durations. Both the HRTEM and the FFT-filtered image demonstrate dislocation free shells of 40 nm thickness, which is above the critical thickness for planar systems. The results perfectly match with the calculations presented in Fig. 3.4: an InAs NW core of 50 nm radius can be covered with a GaSb shell of 40 nm thickness without the formation of misfit dislocations.

The TEM analyzes clearly proves that semiconductors with small lattice mismatches can be combined to core-shell NWs without the formation of misfit dislocations. The critical dimensions exceed those of planar systems. Certainly, if the GaSb shell is grown even thicker, the strain induced by the lattice mismatch may relax by misfit dislocations as also expected by the calculations shown in Sec. 3.
The TEM investigation additionally evidences a rather thick native oxide of the GaSb shell. It has a thickness in the range of $\sim$ 4 nm. For comparison, the native oxides covering the InAs and GaAs NWs presented earlier have a thickness in the range of 2 nm.

6.1.1.2. Structure of the GaSb platform

Finally, the formation and structure of the GaSb platform with larger diameter than the core-shell NW itself is discussed. A TEM micrograph of the upper part of an InAs/GaSb core-shell NW is shown in Fig. 6.9a. The image reveals that the NW tip can be separated into two regions: the lower one being the InAs/GaSb core-shell system and the upper one being pure GaSb. The first one has a high density of stacking faults originating from the InAs core. The InAs core is clearly identified by the change in the contrast. The upper part of the NW exhibits a significantly smaller number of stacking faults in the axial direction. In this upper part, only GaSb is grown (see EDX scan from Fig. 6.4b). The axially grown GaSb (in $[\overline{1}\overline{1}\overline{1}]$B direction) has ZB crystal structure with a low density of stacking faults, WZ segments are not found in this NW section. This is in agreement with the large energy difference between the ZB and WZ crystal structure for GaSb favoring the ZB structure [3]. However, additional stacking faults and twins are present in the radial direction. These occur when the GaSb is grown radially on the ZB GaSb at the top. This radial growth creates the platform at the top of the NWs. The diffraction pattern in Fig. 6.9b reveals two streaky pattern rotated by 70°, representing stacking faults and twins in two $\langle 111 \rangle$ directions. These twins and stacking faults are also observed in the HRTEM image in Fig. 6.9c. Also the radial growth of GaSb at the top has the ZB crystal structure but it exhibits significantly more stacking faults and twins. However, the two discussed $\langle 111 \rangle$ directions are not equivalent. The axial growth takes place in $[\overline{1}\overline{1}\overline{1}]$B direction while the radial growth of GaSb on GaSb with higher stacking fault/twin density is in the $[1\overline{1}\overline{1}]$A direction. Radial growth of GaSb on GaSb in $[\overline{1}11]$B direction takes place as well but is slower than in the $[1\overline{1}\overline{1}]$A direction. It can be concluded that the twin formation probability is higher in the $[1\overline{1}\overline{1}]$A than in the $[\overline{1}\overline{1}\overline{1}]$B direction. Gorji Ghalamestani *et al.* observed similar characteristics when growing InP shells around InAs NWs having twinning superlattices and {111}-type side facets [107]. In that study, a significantly higher growth rate in the $[1\overline{1}\overline{1}]$A than in the in the $[\overline{1}11]$B direction was observed. The same peculiarities are observed for the InAs/GaSb heterostructures shown here. The lengths of the arrows displayed in Fig. 6.9a indicate the average growth rates along the $[\overline{1}\overline{1}\overline{1}]$B (axial) and $[1\overline{1}\overline{1}]$A (radial) directions. Concerning the radial growth in $[11\overline{1}]$B direction, no growth rate could be determined. The growth rate in $[1\overline{1}\overline{1}]$A (radial) direction is larger than in $[11\overline{1}]$B (radial) direction while the growth rate in $[\overline{1}\overline{1}\overline{1}]$B (axial) direction is even higher. However, the adatom impingement differs for the growth in radial and axial direction with a higher rate of impinging adatoms at the top than at the side facet. This explains the higher growth rate in the axial direction. For identical adatom impingement, the growth rate in the $[1\overline{1}\overline{1}]$A direction is higher than in the $[11\overline{1}]$B direction. Fast growing facets typically vanish during the growth while the slowly growing ones remain. In Fig. 6.9a it is observed that the size of the {111}A facet continuously decreases. The {111}B facet remains its dimensions and is flat (refer to the TEM image in Fig. 6.9a as well as in the SEM micrographs in Fig. 6.3). The different growth rates along the $\langle 111 \rangle$A and $\langle 111 \rangle$B directions in conjunction with the different densities of twins also explain the three-fold symmetry seen in the inset of Fig. 6.3d. The four $\langle 111 \rangle$A directions form a tetrahedron and the [111]A direction is directed into the substrate. Accordingly, top view analyzes show that the remaining $\langle 111 \rangle$A directions have a three-fold symmetry.

As mentioned above, the axial growth of GaSb in $[\overline{1}\overline{1}\overline{1}]$B direction does not result in a pure ZB crystal structure but also produces twin boundaries. These are of a lower density than in the $\langle 111 \rangle$A directions. At these twin boundaries, the GaSb crystal is rotated by 180° around the $[\overline{1}\overline{1}\overline{1}]$B direction. Consequently, also the $\langle 111 \rangle$ directions are rotated by 180°. The three-fold symmetry induced by the higher growth rate in the $\langle 111 \rangle$A directions develops into a quasi six-fold symmetry, being also observed experimentally (Fig. 6.3c). In this situation, slowly growing

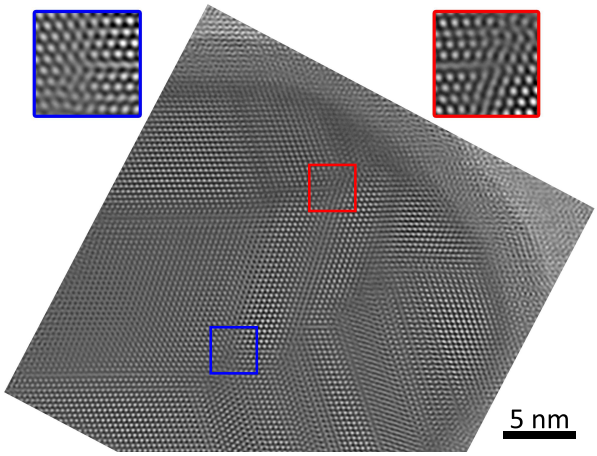

Figure 6.10: *FFT-filtered HRTEM image from Fig. 6.9e showing dislocations located in the GaSb platform not originating from the lattice mismatch between InAs and GaSb. Insets display higher magnification images clearly proving the dislocations. Published in [258].*

⟨111⟩B facets are in close neighborhood to the fast growing ⟨111⟩A facets. These two growth fronts can then coalesce. The corresponding HRTEM image evidences the presence of twins in all ⟨111⟩ directions (Fig. 6.9d,e). The FFT of the image reveals streaks in three orientations. One of the orientations is assigned to the $[\overline{111}]$B direction (blue), another one to the $[1\overline{11}]A_a$ direction (red) and the last one to its twinned counterpart $[\overline{1}11]B_b$ (green). Here, the subscripts a and b denote the two ZB twins. This multiple direction-twinned ZB GaSb may induce defects. These are present only in the upper pure GaSb region with ZB crystal structure. The defects are caused by the growth mechanism of GaSb on twinned ZB GaSb rather than by the lattice mismatch between InAs and GaSb. In order to make the defects visible, Fig. 6.10 displays a FFT-filtered HRTEM image of Fig. 6.9e. Some dislocations are visible, two of them are magnified in the insets. These dislocations are located at the connection point of the ⟨111⟩A and ⟨111⟩B directions.
It should be pointed out that the dislocations in the upper pure GaSb region are observed only for relatively thick shells and are located only in small region at the top. The core-shell region itself, especially the interface between the InAs and the GaSb, is free of dislocations as discussed in detail. Consequently, the defects should not affect the band-to-band tunneling in TFETs. The transport in the GaSb shell itself may be affected e.g. by the strain field of the defects. For NW heterostructures with multiple shells, the formation and structure of the platform affects the growth of additional shells and results in inhomogeneous thicknesses close to the top (see Sec. A.3). Accordingly, the platform represents a morphological characteristic which is not beneficial for NW heterostructures based on multiple shells.

6.1.2. AlGaSb shells[3]

$Al_xGa_{1-x}Sb$ shells are grown around InAs NWs at substrate temperatures of 360°C, being optimal for conformal GaSb shells as described in the previous section. The Sb flux is set to $8 \cdot 10^{-7}$ mbar and the total flux of the group III elements is kept constant at a planer growth rate of 0.1 µm/h. If not mentioned differently, the growth duration of the shell is 60 min resulting in shell thicknesses of ∼ 20-25 nm. Considering planar growth, the critical thickness according to the Matthews-Blakeslee theory is 20 nm for GaSb and decreases to 10 nm for AlSb (see Sec. 3.1).

Figure 6.11 shows overview SEM micrographs of InAs/$Al_xGa_{1-x}Sb$ core-shell NWs with x ranging from 0 to 1 in steps of 0.2. For all Al contents, the NWs have uniform dimensions, no

[3] Most results of this section have been published inT. Rieger, D. Grützmacher, and M. I. Lepsa. *InAs nanowires with $Al_xGa_{1-x}Sb$ shells for band alignment engineering.* Journal of Crystal Growth, 425:80-84, 2015. Ref. [257]

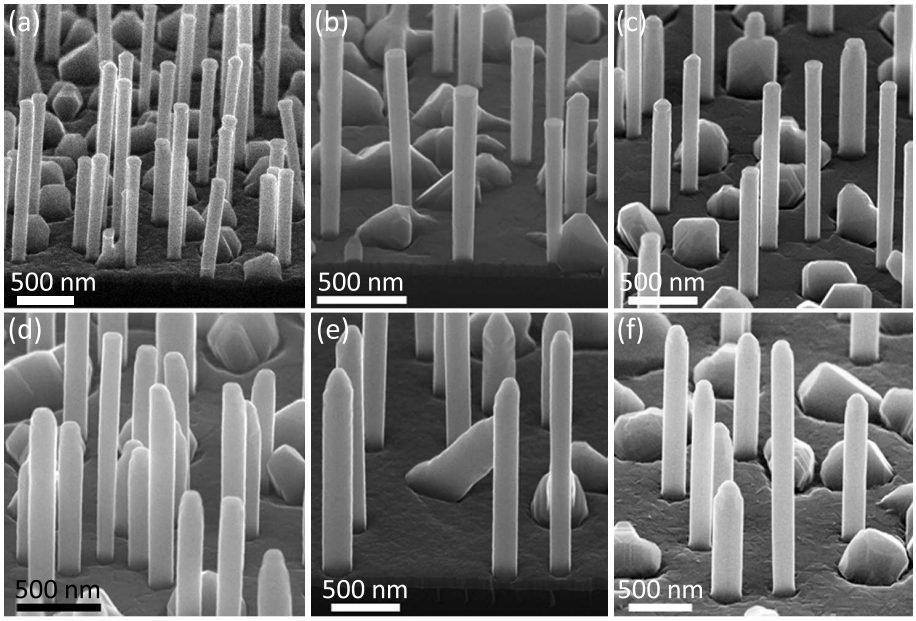

Figure 6.11.: *SEM micrographs of InAs/$Al_xGa_{1-x}Sb$ core-shell NWs with Al contents of (a) 0, (b) 0.2, (c) 0.4, (d) 0.6, (e) 0.8 and (f) 1. Published in [257].*

clustering of the $Al_xGa_{1-x}Sb$ or tapering is observed. The only remarkable difference found is located at the top of the NWs. For pure GaSb shells, a platform develops at the top. This has a flat facet as well as a diameter expansion compared to the rest of the NW as already pointed out in the previous section. By increasing the Al content, the platform slowly vanishes and the flat top facet transforms into a rounded and faceted top similar to that of the pure InAs NW. The transition from a flat to a tapered shell occurs roughly in the region of 40 – 60% Al. It may, however, also depend on the growth time of the shell. The flat top facet of GaSb shells was attributed to a low growth rate of the {111}B facet, the diameter expansion to radial growth occurring on ZB GaSb inducing additional twins (see previous section). When pure AlSb shells are grown, the growth rate of the {111}B facet is higher than that of the {110} and {211} facets. Using TEM micrographs the length of the axially grown GaSb after 60 minutes of growth was measured to be $\sim$ 0 nm while it increased to $\sim$ 50 nm, $\sim$ 80 nm and $\sim$ 95 nm for for $Al_xGa_{1-x}Sb$ shells with $x = 0.2, 0.6$ and 1, respectively. Considering axial growth solely be caused by direct impingement, an axially grown AlGaSb segment of $\sim$ 100 nm is expected, being in good agreement with the length of the AlSb on top of the InAs. Thus, the presence of Al reduces the adatom mobility and therefore favors the axial growth of $Al_xGa_{1-x}Sb$.

The successful and homogeneous incorporation of Al into the shells was confirmed by EDX line scans. Two exemplary scans are shown in Fig. 6.12 together with bright field TEM images. Figures 6.12a and b are taken from a core-shell NW with a nominal Al content of 20 %. The Al signal in the EDX line scan is very weak, but it was clearly identified in the spectra. The TEM image, acquired from the $\langle 211 \rangle$ zone axis, exhibits smooth surfaces and interfaces. No evidences of a phase separation or an inhomogeneous alloy are found. The thickness of the native oxide of the $Al_{0.2}Ga_{0.8}Sb$ shell is in the same range as that of pure GaSb shells, i.e. 3-4 nm. An increase of the Al content in the shell to 60 % significantly increases the thickness of the native oxide. It is then in the range of 8-10 nm (not shown). This is a direct evidence for the incorporation of a higher amount of Al which has a stronger tendency to the formation of a native oxide layer.

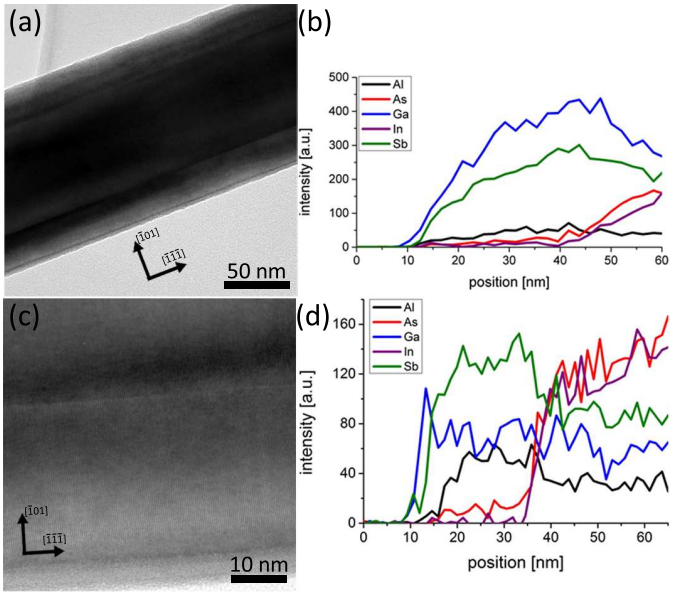

Figure 6.12: *TEM micrographs acquired from the ⟨211⟩ zone axis of (a) $InAs/Al_{0.2}Ga_{0.8}Sb$ and (c) $InAs/Al_{0.6}Ga_{0.4}Sb$ core-shell NWs. EDX profiles shown in (b) and (d) demonstrate the incorporation of Al into the shell as well as a GaSb cap layer on the $InAs/Al_{0.6}Ga_{0.4}Sb$ core-shell NW. Published in [257].*

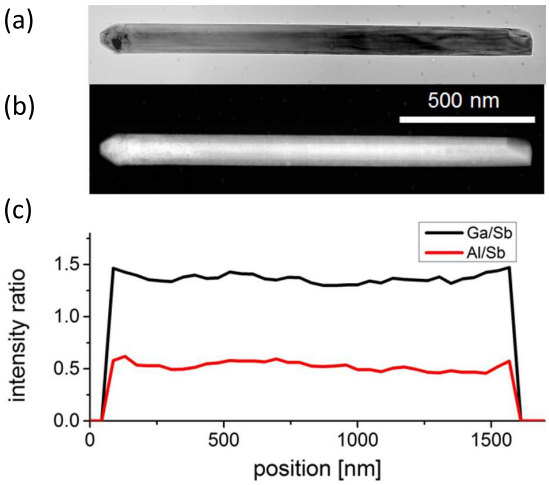

Figure 6.13: *(a) TEM image and (b) HAADF image of an $InAs/Al_{0.6}Ga_{0.4}Sb$ core-shell NW, (c) EDX profile taken along the NW axis with Ga and Al intensity normalized to the Sb intensity. The EDX profile demonstrates a uniform shell composition along the NW. The homogeneous shell thickness is evident from the HAADF image. Published in [257].*

Consequently, an additional thin GaSb cap layer was grown around $InAs/Al_xGa_{1-x}Sb$ core-shell NWs with Al contents above 20 %. Figures 6.12c and d display the TEM micrograph and the corresponding EDX profile of an $InAs/Al_{0.6}Ga_{0.4}Sb/GaSb$ core-shell NW. The thickness of the native oxide is again in the order of ~ 4 nm and a corresponding delayed onset of the Al signal in the EDX profile is observed. The Al to Ga ratio is significantly higher than in Fig. 6.12b. Accordingly, the amount of incorporated Al in the shell increased. The interfaces and surfaces of all layers are found to be smooth. This not only proves that the thin GaSb shell prevents oxidation of the underlying AlGaSb, it is also a first demonstration of a multiple core-shell system based on arsenides and antimonides.

Although the incorporation of Al into the shell is proven, the actual composition of the AlGaSb shell along the growth axis may vary due a temperature gradient along the NW axis [105, 186] or different adatom diffusion lengths for Ga and Al. Consequently, EDX spectra were acquired at different positions along the NW axis of a core-shell NW with an $Al_{0.6}Ga_{0.4}$ shell. In order to compensate for thickness variations and sample drift, the intensities of Ga and Al were normalized to that one of Sb. The TEM micrograph, the HAADF image as well as the corresponding EDX profile displayed in Fig. 6.13 indicate a uniform shell thickness along the NW axis as well

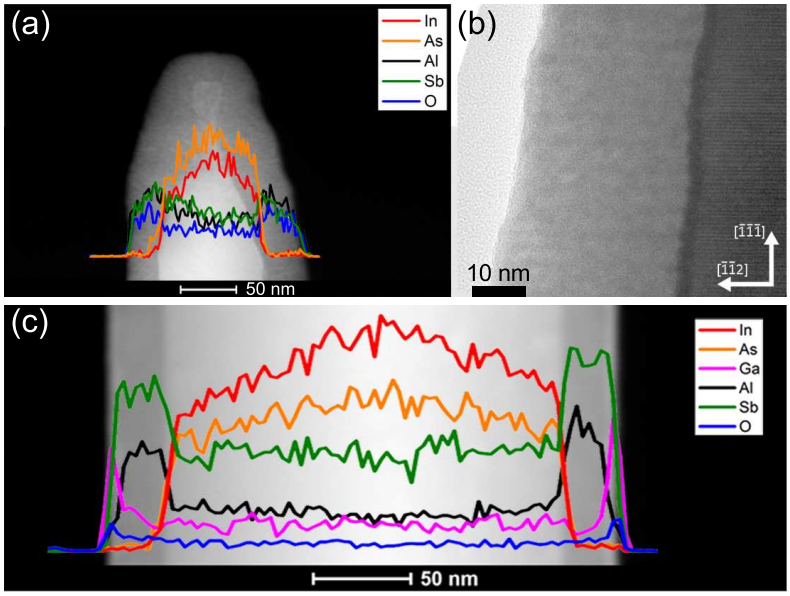

Figure 6.14: *HAADF and TEM images of InAs/AlSb and InAs/AlSb/GaSb core-shell NWs proving the absence of strong oxidation in InAs/AlSb/GaSb core-shell NWs. (a) HAADF image with super imposed EDX linescan of an InAs/AlSb core-shell NW. (b) TEM micrograph of the same NW showing the thick oxidized shell. (c) HAADF image with super imposed EDX linescan of an InAs/AlSb/GaSb core-shell NW. No evidence of oxygen in the AlSb is seen.*

as a relatively uniform composition. Slight variations should rather be caused by the limited time used to acquire the spectra than by a temperature gradient or differences in the adatom mobilities. Accordingly, the substrate temperature of 360°C is low enough that adatom diffusion does not influence the composition of the shell.

When pure AlSb shells are grown, the necessity of a GaSb cap preventing oxidation becomes even more evident. A pure, nominally 20 nm thick AlSb shell oxidizes completely in ambient air if not protected by a GaSb cap. Figure 6.14a displays the HAADF image and superimposed EDX profile of an oxidized AlSb shell covering an InAs NW. A strong signal corresponding to Oxygen is detected in the EDX profile. TEM analyses prove that the shell is entirely amorphous while the InAs core is still crystalline (see Fig. 6.14b). Due to the addition of oxygen, the thickness of the shell increases significantly to around $\sim$ 40 nm. No peel-off of the shell is observed which allows to use the oxidized shell as a passivation of the NW or as a gate dielectric. The addition of thin GaSb shell around the AlSb shell circumvents the oxidation of the AlSb. The HAADF profile and the superimposed EDX profile shown in Fig. 6.14c demonstrate both the absence of Oxygen in the AlSb as well as the absence of a thick amorphous layer. At the NW edges, intensity peaks belonging to Ga and Oxygen are observed, both having similar extents. Hereafter, the Oxygen signal in the EDX spectra decreases drastically, indicating that only a thin oxide is covering the NW. The thickness of the GaSb cap after (partial) oxidation can be approximated both from the EDX profile as well as the HAADF image (bright edges) to about 4-5 nm. The absence of an oxidized AlSb shell is further evidenced by the TEM image depicted in Fig. 6.15a. The crystalline structure of the InAs NW with stacking faults and twins continues into the shell having a thin native oxide layer only. The contrast allows to estimate the AlSb shell thickness to be in the range of 25-30 nm, i.e. more than twice as thick as the critical thickness in planar systems. Due to the high density of stacking faults and twins, the analyses of misfit dislocations becomes difficult when evaluated from the $\langle 110 \rangle$ zone axis. By aligning the NWs to the $\langle 211 \rangle$ zone axis, contrast arising from stacking faults and twins disappears but misfit dislocation, i.e. extra or missing (111) planes, are still visible. Consequently, Fig. 6.15b and c depict HRTEM images from NWs with 10 and 25 nm thick AlSb shells from the $\langle 211 \rangle$ zone axis. Considering planar structures, 10 nm represents the critical thickness for coherent growth of AlSb on InAs. Figure 6.15b displays a TEM micrograph of a NW with a 10 nm thick AlSb shell, contrast arising

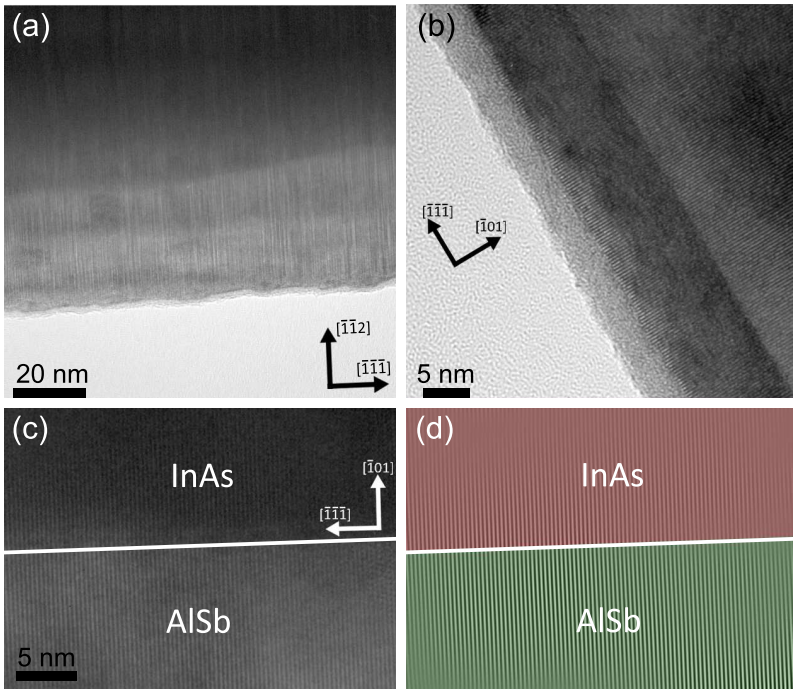

Figure 6.15.: *TEM images of InAs/AlSb/GaSb core-shell NWs. (a) 25 – 30 nm thick AlSb shell with a GaSb cap seen from the* ⟨110⟩ *zone axis. (b) 10 nm thick AlSb shell with a GaSb cap seen from the* ⟨211⟩ *zone axis. (c) Detailed image of an InAs/AlSb/GaSb core-shell NW with a 25 – 30 nm thick AlSb shell with a GaSb cap seen from the* ⟨211⟩ *zone axis. (d) FFT-filtered image of (c). White lines in (c) and (d) indicate the interface InAs-AlSb.*

from the core and shell is clearly observed. The interface appears to be smooth. A native oxide with a thickness of about 4 – 5 nm is present. This is limited to the additional GaSb shell. As expected due to the low lattice mismatch as well as the thin thickness, no misfit dislocation are detected. However, even for an increase of the shell thickness to $\sim$ 25 nm, a thorough analysis of TEM images did not reveal any misfit dislocations. Exemplary, a HRTEM image is shown in Fig. 6.15c, the interface from InAs to AlSb is marked by the white line. Also after long shell growth times, the interface appears to be smooth, indicating only a low temperature-induced intermixing. A FFT-filtered image of Fig. 6.15c showing only the {111} planes is displayed in Fig. 6.15d. Following each of the {111} planes from the InAs core into the AlSb shell and searching for terminating planes allows to identify possible misfit dislocations. Similar as in the image in Fig. 6.15b, no terminating planes and therefore no misfit dislocations were found. In conclusion, coherent growth of InAs/AlSb core-shell NWs is achieved with shell thicknesses exceeding the critical thickness of planar structures significantly. Similar as for the InAs/GaSb core-shell NWs shown in the previous section, the critical thickness in the NW geometry is at least twice as high as for planar systems. It should be mentioned that this is even the case for relatively thick NWs. The core-shell NW depicted in Fig. 6.14c has a core diameter of about 175 – 200 nm and no misfit dislocations are observed in the NW. This further demonstrates the excellent suitability of core-shell NWs of various dimensions for the dislocation-free integration of lattice mismatched material systems.

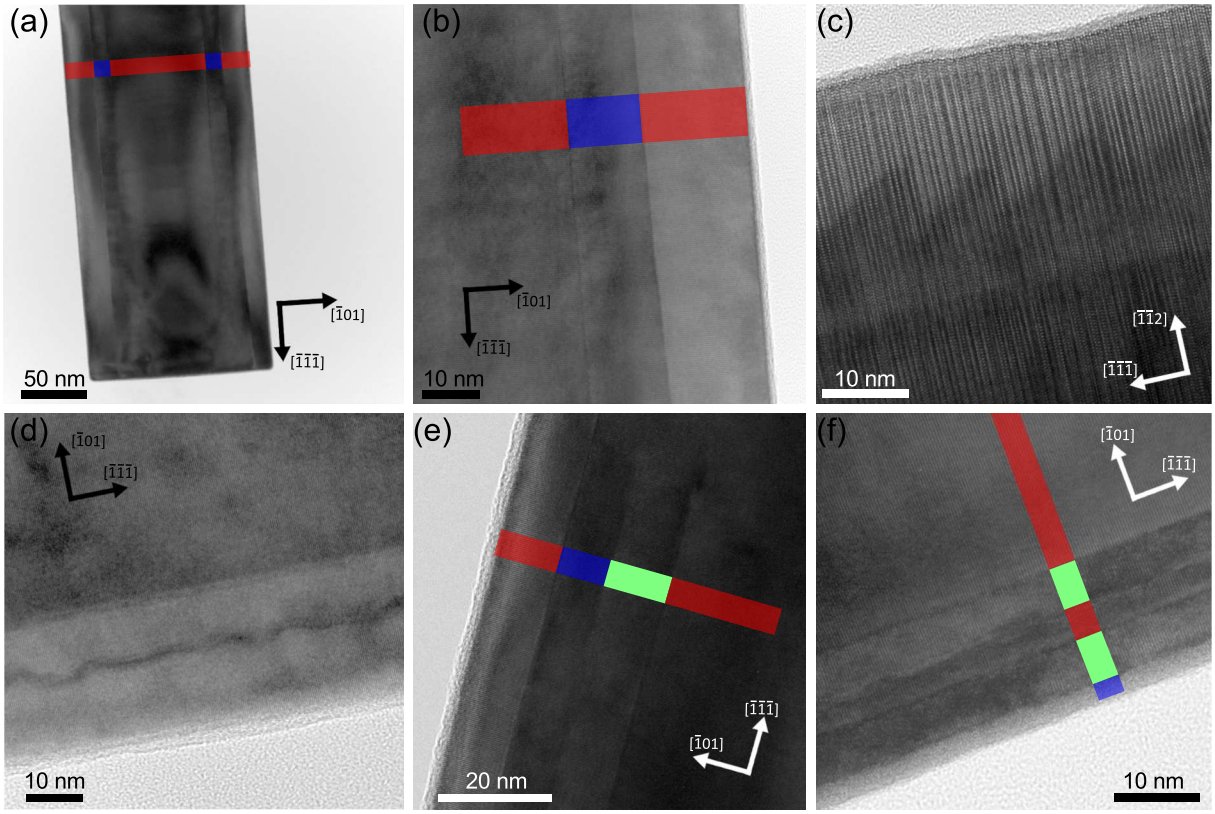

Figure 6.16.: *Preliminary results of InAs/AlGa$_x$Sb$_{1-x}$ core-multiple shell NWs. (a) Low resolution TEM image of an InAs/GaSb/InAs core-shell NW from the ⟨211⟩ zone axis. (b) High resolution TEM image of an InAs/GaSb/InAs core-shell NW from the ⟨211⟩ zone axis. (c) High resolution TEM image of an InAs/AlSb/InAs core-shell NW from the ⟨110⟩ zone axis. (d) High resolution TEM image of an InAs/AlSb/InAs core-shell NW from the ⟨211⟩ zone axis. (e) TEM image of an InAs/AlSb/GaSb/InAs core-shell NW from the ⟨211⟩ zone axis. (f) TEM image of an InAs/AlSb/InAs/AlSb/GaSb core-shell NW forming a radial InAs quantum well from the ⟨211⟩ zone axis. Red overlays indicate InAs, blue and green overlays represent GaSb and AlSb, respectively.*

6.1.3. Future structures based on the InAs/Al$_x$Ga$_{1-x}$Sb core-shell nanowires

The InAs/Al$_x$Ga$_{1-x}$Sb core-shell NWs presented in the previous sections already represent very promising structures for future low power consumption devices (such as TFETs) or high mobility structures (capping of InAs NWs with AlSb). More complex core-shell structures can, however, further enhance the possible applications. In the following, different structures are shortly described and preliminary growth results are discussed. Detailed descriptions including SEM and TEM data are given in the Appendix A.3.

- **InAs/Al$_x$Ga$_{1-x}$Sb/InAs core-shell NWs:** Covering InAs/Al$_x$Ga$_{1-x}$Sb core-shell NWs with an additional shell of InAs can e.g. form two interfaces where band-to-band tunneling takes place (InAs/GaSb/InAs core-shell NWs) or misfit dislocation free InAs tubes (InAs/AlSb/InAs core-shell NWs). In the latter, the InAs shell is separated from the InAs core by the AlSb shell. The InAs core may be doped to high values to act as an "internal" gate having a very uniform influence on the carrier concentration in the InAs shell. InAs/GaSb/InAs core-shell NWs are found to grow with smooth interfaces and free of misfit dislocations, as evident from the TEM micrographs displayed in Fig. 6.16a,b. In

absence of the platform, the NWs exhibit a uniform morphology with smooth side facets and without tapering (Fig. 6.16a,b). A platform at the top of the InAs/GaSb core-shell NW has a strong effect on the growth of the additional InAs shell (see Appendix). If the InAs/GaSb NWs contain the GaSb platform and the associated twinning at the top, the additional InAs shell is found to induce an inverse tapering, i.e. a larger diameter at the top than at the bottom. Correspondingly, the InAs shell is thicker at the top than at the bottom. InAs/AlSb/InAs core-shell NWs exhibit smooth interfaces from the InAs core to the AlSb shell but rough, saw tooth-like interfaces with {111} as well as {001} (ZB notation)/$\{\bar{1}01\bar{1}\}$ (WZ notation) facets from the AlSb shell to the InAs shell (see Fig. 6.16c,d). This roughness is observed from both zone axes used for the NW analysis, i.e. the $\langle 110 \rangle$ zone axis (Fig. 6.16c) and the $\langle 211 \rangle$ zone axis (Fig. 6.16d). The InAs shell was grown at the same temperature as the AlSb and GaSb shells, In and As fluxes were similar to those used for the growth of InAs shells around GaAs cores (see Sec. 5.1). A slight change of the substrate temperature for the growth of the InAs shell does not result in an improvement of the interface. The interface from an AlSb shell to a GaSb shell is smooth (see Sec. 6.1.2). Consequently, the rough interface is attributed to the growth of the InAs shell. Replacing the AlSb shell with an $Al_{0.6}Ga_{0.4}Sb$ shell again results in smooth interfaces.

- **InAs/AlSb/InAs/GaSb and InAs/AlSb/GaSb/InAs core-shell NWs:** In TFET devices, the relatively thick InAs core may result in high parasitic currents and an inefficient gate coupling to the core. Accordingly, the active broken gap heterostructure is placed close to the surface with very thin shells of InAs and GaSb. This is obtained by an InAs/AlSb core. The InAs core solely acts as a host material, AlSb is an isolation layer. InAs/AlSb/GaSb/InAs core-shell NWs have always smooth interfaces (see Fig. 6.16e) while InAs/AlSb/InAs/GaSb core-shell NWs suffer from the rough interfaces observed in InAs/AlSb/InAs core-shell NWs.

- **Radial InAs quantum wells:** Dislocation free tubular conductors based on InAs can be obtained by InAs/AlSb/InAs core-shell NWs as described above. These structures still suffer from scattering of the carriers at the surface of the InAs shell. This scattering may be avoided by an additional AlSb shell as well as a protective GaSb capping layer. This structure forms a radial InAs quantum well. Identical to the previous structures, the interface from the first AlSb shell to the InAs shell is rough while the interfaces from InAs to AlSb are always smooth. Similarly, the GaSb cap has a smooth interface to the AlSb shell. Figure 6.16f displays a TEM micrograph of this particular structure. Also here, a highly doped InAs core may act as an internal gate. Additionally, a modulation doping can be obtained by Te doping in the AlSb [330] or a remote InAs(Si) doping [19].

Certainly, most of these structure still suffer from the rough AlSb/InAs interfaces. Nonetheless, the obtained results already indicate the potential of these heterostructures.

6.2. Temperature induced transition from axial to radial growth in GaAs/InSb heterostructure nanowires

InSb represents a highly interesting semiconductor: the band gap is very small (~ 0.17 eV) with a high electron mobility (~ 77000 cm^2/Vs), small electron mass ($0.014m_0$) and a high g-factor (~ 50) [145, 147]. This combination of semiconductor properties is especially beneficial for high mobility structures [67, 113, 213] and investigations of spin-based devices [13, 221, 224, 316].

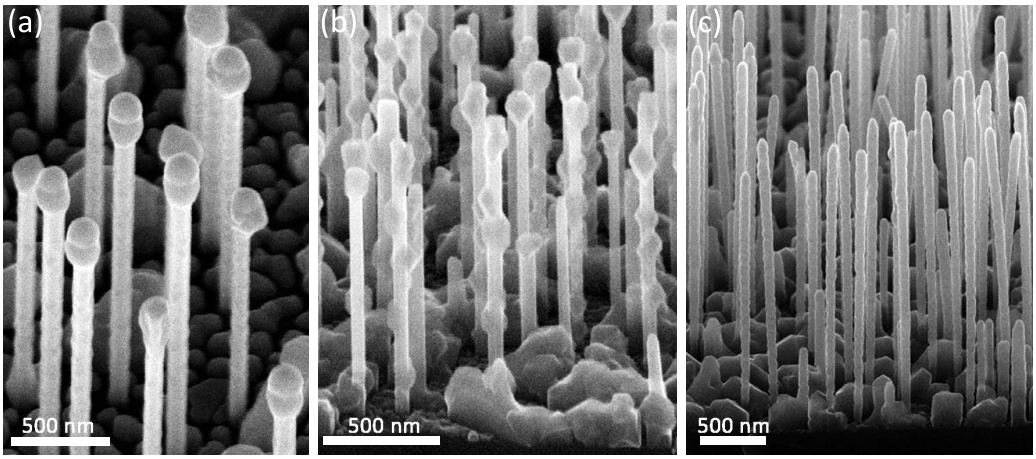

Figure 6.17.: *Temperature dependence of GaAs/InSb heterostructure NWs. Growth temperature of the InSb are (a) 460° C, (b) 380° C and (c) 300° C.*

Additionally, InSb NWs are ideal for the search for Majorana fermions [69, 218]. The growth of InSb NWs without the use of an external catalyst has only been demonstrated by Mandl *et al.* by MOVPE [204]. The obtained NWs were rather short and thick. For Au-catalyzed NWs, typically a stem of InAs or InP is used in order to lift the catalyst particle away from the substrate [42, 43, 86, 245].
In our case, heterostructures based on a combination of GaAs and InSb are used. The lattice mismatch between both semiconductors is $\sim 14\%$, thus very high. Such high lattice mismatches result in critical thicknesses of only few Å. For core-shell NWs this is demonstrated in Sec. 3.4. Considering axial heterostructures, Glas [104] as well as Ye and Yu [342] analyzed the critical dimensions for various lattice mismatches. The results are similar: very thin bottom segments or short axially grown parts are required to achieve dislocation free structures. The band alignment between GaAs and InSb was yet not well investigated, possibly due to the high lattice mismatch and the strong impact of the strain. In planar structures, the alignment should be of type I [209, 280], i.e. similar as for GaAs/InAs. In heterostructure NWs, the alignment is expected to depend strongly on the NW dimensions [242, 243]. A short InSb segment placed axially between GaAs should be a semimetal while the conventional type I alignment is expected be present for longer InSb segments [243]. In a core-shell NW, the GaAs core has to have a negative band gap for thick InSb shells whereas for thinner InSb shells a broken gap heterostructure is expected [242]. While GaAs and GaSb [114, 149, 274] as well as InAs and InSb [42, 43, 86, 245] have frequently been combined in NWs, NW heterostructures based on GaAs and InSb have not yet been investigated.

For the GaAs/InSb heterostructures, GaAs NWs were grown using a substrate temperature of ~ 600°C, a Ga rate of 0.1 µm/h and an As_4 flux of $2.5{\cdot}10^{-6}$ mbar. The catalyzing Ga droplet was consumed, identical as for GaAs/InAs core-shell NWs. Using these slightly different growth conditions than in Sec. 4.3, the GaAs NWs exhibit a flat top facet as shown exemplary in the Appendix A.4. After reducing the substrate temperature to the temperature desired for the growth of InSb, the As shutter was closed and after a pause of 2 min, the Sb shutter was opened. Sb was provided for 30s before In was supplied. Both the substrate temperature and the Sb flux were found to have an impact on the growth. Typically, high Sb fluxes resulted in the formation of InSb particles at the top, similar to observations made in Ref. [245], or several InSb nucleation spots along the NW. The most dominant effect arises from the substrate temperature,

which was varied between $\sim$ 260°C and $\sim$ 500°C. Figure 6.17 demonstrates this effect of the substrate temperature by SEM micrographs. At high temperatures of about 460°C, a large diameter "particle" is found at the top of the NWs and a droplet seems to be present at the top (see Fig. 6.17a). A decrease of the substrate temperature to $\sim$ 380°C results in a nucleation of InSb at several spots along the GaAs NW, as seen in Fig. 6.17b. In some cases, even In droplets distributed along the NW axis are found. Rather similar morphological characteristics have been observed in GaAs/InAs core-shell NWs [262] where conformal core-shell NWs were obtained by further decreasing the substrate temperature. Consequently, Fig. 6.17c displays GaAs/InSb heterostructure NWs with InSb growth at $\sim$ 300°C. The NWs have rather smooth surfaces.
This means that two interesting morphologies are observed: (1) GaAs/InSb heterostructure NWs grown at high temperatures and (2) GaAs/InSb heterostructure NWs grown at low temperatures. These two structures are discussed in detail in the following.

6.2.1. Axial nucleation of InSb on GaAs nanowires

As it is shown in Fig. 6.17a, a high growth temperature of the InSb provides an axially increased NW diameter where a droplet seems to be present on top of the NW. A close up of a single NW is displayed in Fig. 6.18a, clearly demonstrating two sections with different diameters. The lower part has a diameter in the range of $\sim$ 100 nm while it is roughly doubled in the upper short segment. The lower part is GaAs. The transition to the upper region is abrupt and is shown in higher magnification in Fig 6.18b. This proves that the upper part can be further separated into two regions, the lower being crystalline as obvious by the faceted shape. These facets are mainly of {110} type, similar as the long and thin GaAs stem, but two smaller facets are observed as well (see colored areas in Fig. 6.18b). On top of the large diameter section, a hemispherical shape is found, indicating the presence of a droplet. This large diameter section exactly follows the growth direction of the GaAs stem. This situation is observed in most cases, but also other orientations are found. Three of them are depicted in Fig. 6.18c-e. These images show that also upper segments tilted with respect to the stem (Fig. 6.18c,e) or even segments growing downwards the stem (Fig. 6.18d) are found. A detailed analyses reveals that the InSb growth always proceeds in one of the ⟨111⟩ directions, e.g. ⟨111⟩A or ⟨111⟩B. In each situation, a droplet is located at the end of the large diameter section. Interestingly, Au-catalyzed GaAs/GaSb heterostructure NWs showed rather similar morphologies with a preferred growth at the top [274]. In the following, only structures where the large diameter section has the same macroscopic orientation as the GaAs stem are discussed. The GaAs stem typically exhibits a slight roughness induced by the growth of InSb on the side facets of the GaAs (see Fig. 6.18b,c,e).

Pure GaAs NWs are usually straight and do not show any abrupt variation of the diameter (cf. Sec. 4.3.2. Prior to the growth of InSb, the catalyzing Ga droplet was consumed. Accordingly, the large diameter segment on top of the NWs should be InSb and the droplet should be composed of In and, depending on its solubility, Sb. The composition of the entire NW was analyzed by EDX. Figure 6.19a shows the HAADF image and elemental maps of Ga, As, In and Sb. The NW was aligned to the ⟨110⟩ zone axis. The stem is composed of GaAs while the large diameter section at the top contains InSb. No traces of Ga or As are detected within the InSb. The droplet is made up of In. Any statement about the amount of Sb in the droplet is difficult, the corresponding count rates are below the detection limit. The presence of the In droplet in accordance with the absence of traces of Ga or As in the InSb suggests that the Ga droplet was totally consumed before In and Sb were supplied. Therefore, an In droplet was rebuilt on top of an existing GaAs NW, i.e. a GaAs NW serves as the stem for the axial growth. This

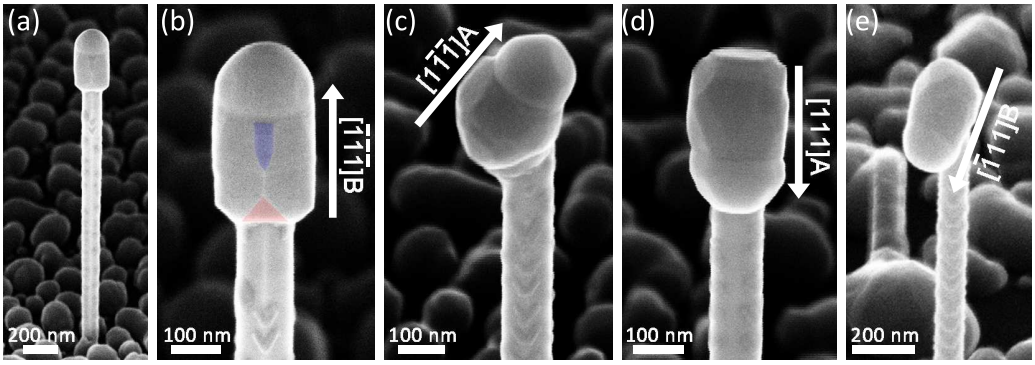

Figure 6.18.: *SEM micrographs of single GaAs/InSb heterostructure NWs focusing on the upper segment. (a) Single NW with InSb growth following the growth direction of the GaAs stem. (b) Close up of the top of (a) The two small facets are colored. (c)-(e) InSb growing in the ⟨111⟩ directions not being the growth direction of the stem. The growth directions of the InSb are written in the corresponding images.*

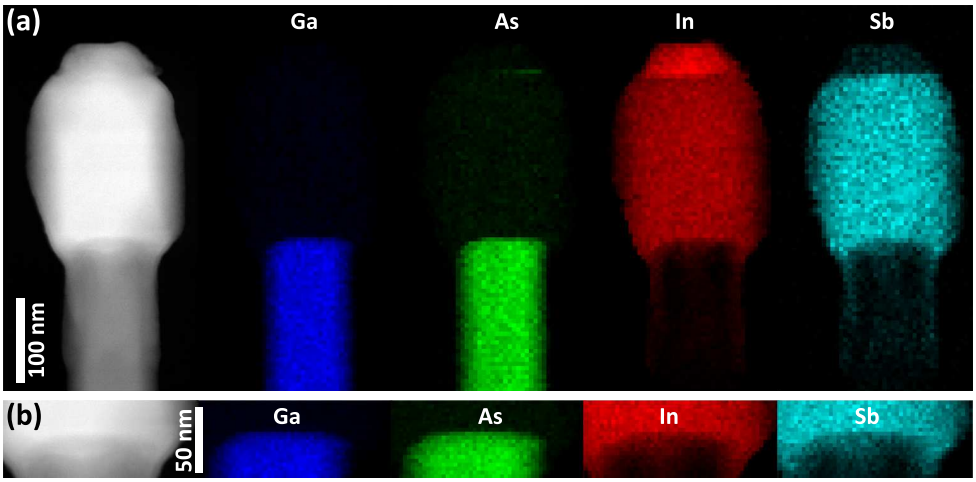

Figure 6.19.: *HAADF images and elemental maps of Ga, As, In and Sb in an axial GaAs/InSb heterostructure. (a) Overview of the upper part including GaAs and the entire InSb. (b) Interface region between both semiconductors.*

growth method may create an abrupt heterostructure between the GaAs and the InSb. A more detailed composition map around the interface GaAs/InSb is plotted in Fig. 6.19b. It evidences a very abrupt transition from the GaAs to the InSb with only slight radial overgrowth of the InSb covering the GaAs stem. This overgrowth takes place at the upper $\sim 20 - 30$ nm of the GaAs stem and forms a short parasitic core-shell segment.

A more detailed picture about the interfacial abruptness and composition of the droplet is gained from Fig. 6.20. Figure 6.20a shows a TEM micrograph of a GaAs/InSb heterostructure NW with about ~ 300 nm InSb grown axially on the GaAs. An EDX line scan superimposed on the image demonstrates that Sb is absent in the droplet, being different than observations made by Mandl *et al.* for MOVPE grown self-seeded InSb NWs [204]. They found Sb concentrations ranging from a few up to 20 % in the In droplet, being dependent on the growth time. Here, careful investigations of GaAs/InSb heterostructure NWs grown for different durations and with slightly different Sb fluxes do not exhibit any conditions where Sb was found to be present in the droplet after the growth. According to the In-Sb phase diagram the solubility of Sb in solid In is very low at room temperature [279]. At the growth temperature of ~ 460°C, the situation is different. There, the solubility of Sb in liquid In is between 20 and 30 %. Due to the large

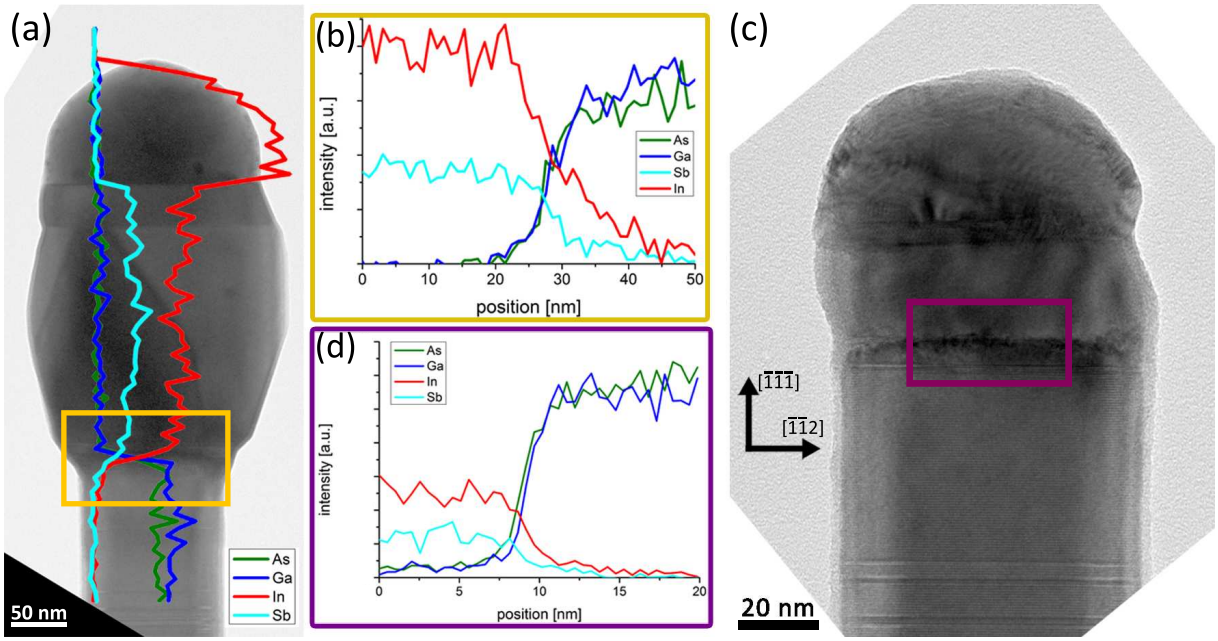

Figure 6.20.: *TEM images and EDX line scans of axial GaAs/InSb heterostructures. (a) TEM image of 300 nm InSb grown on a GaAs stem with a superimposed EDX line scan. (b) Detailed EDX line scan of the region marked in (a). (c) TEM image showing a short InSb segment. (d) EDX line scan of the region marked in (c). The interfacial abruptness is a few nm.*

difference in solubility at room temperature and growth temperature, the post-growth analyses of the droplet does not provide reasonable information about the state of the droplet during the growth. The slow cool down from the growth temperature to room temperature may result in a continuous growth of InSb below the droplet. This growth reduces the concentration of Sb in the droplet. Certainly, the decreasing Sb concentration during the cool down may also affect the crystal structure of the InSb, as it will be discussed later. The high solubility of Sb in liquid In around temperatures of $\sim 460°C$ also serves as an explanation for the increased diameter of the axially grown InSb compared to the GaAs stem. The In droplet nucleated at the top facet of the GaAs stem may have initially the diameter of the stem. During the growth, it becomes saturated with Sb which increases the size of the droplet, i.e. the diameter of the InSb.

The second interesting region is the interface between the GaAs and InSb. Figure 6.20b shows the EDX line scan across the interface. A continuous decrease of the In and Sb signals and an increase of the Ga and As signals in the region between 20 and 40 nm are observed. In the remaining areas, the signals are constant. Consequently, the chemical composition is changed over a distance of about 20 nm. This does not imply than an InGaAsSb alloy is formed in this region, rather a core-shell system, that is a radial growth of InSb on the GaAs, is developed as it is also evident from the EDX maps in Fig. 6.19b. The abruptness of the interface is still high but two different interfaces are formed: one interface in the axial direction where the switching occurs in the [$\bar{1}\bar{1}\bar{1}$]B direction and another interface in the radial $\langle 110 \rangle$ directions. The abruptness along the [$\bar{1}\bar{1}\bar{1}$]B direction is analyzed in a sample with a short InSb growth time of about 5 min shown in Fig. 6.20c. Contrast arising from the interface between GaAs and InSb is clearly evident. The In droplet crystallized during cool down as obvious by the faceted shape and Moiré fringes. An EDX line scan displaying the transition from the GaAs stem to the axially grown InSb is depicted in Fig. 6.20d. Here, the interfacial abruptness is measured to $\sim 2 - 5$ nm, which is mainly limited by the resolution of the EDX analyses. Additionally,

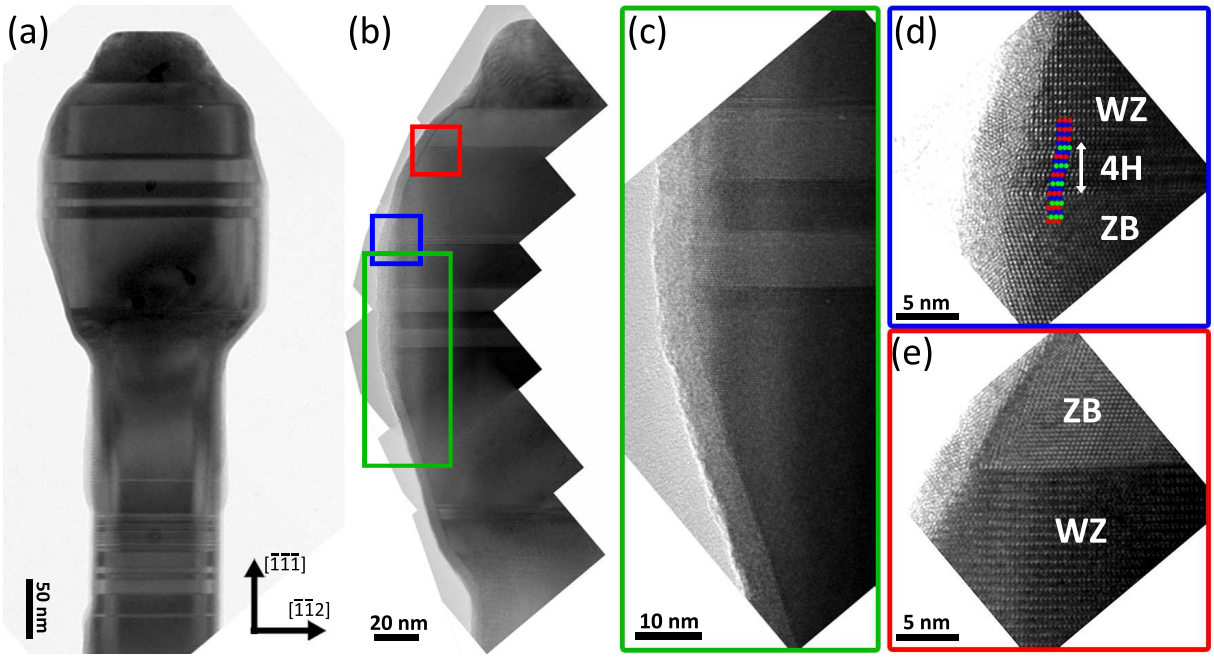

Figure 6.21.: *(HR)TEM images of an axial GaAs/InSb heterostructure NW. (a) Overview image. (b) Axial InSb section. (c) Lower part of the InSb with twinned ZB crystal structure. (d) Transition from ZB to 4H to WZ. The stacking sequence is indicated by colored dots representing the ● A, ● B and ● C layers. (e) Transition from WZ to ZB immediately below the droplet.*

little radial overgrowth of the GaAs stem with the axially nucleated InAs may still occur. This analyzes indicates that the interface between both semiconductors is rather abrupt, despite the fact that both are grown with a droplet and the InSb growth takes place at a temperature close to its melting point ($\sim 525°C$). This is even more surprising by considering that both the group III and the group V elements are exchanged across the junction.

The group III droplet assisted growth of semiconductor NWs typically results in a crystal structure containing only few stacking defects [109, 259]. Concerning the GaAs/InSb axial heterostructure, Fig. 6.21 depicts bright field TEM images of the upper region of the NW displaying the entire InSb part including the droplet as well as parts of the GaAs stem. The low resolution image (Fig. 6.21a) proves that only few stacking defects are present in the InSb section. The GaAs NW stem exhibits the commonly observed crystal structure containing twin defects as well as the WZ phase close to the top (see Sec. 4.3). Figure 6.21b depicts the InSb part in higher resolution. After nucleation of the InSb on the GaAs stem, the crystal structure is uniform for about 150 nm, followed by some twin defects. The crystal structure is ZB as evident from Fig. 6.21c. This crystal structure changes in the upper third of the InSb section. When the diameter of the InSb starts to decrease, the crystal structure changes from ZB to the 4H polytype (see Fig. 6.21d). This 4H polytype is characterized by a stacking sequence of *... ABCBABCBABCB ....* The 4H structure represents a rather unusual crystal structure but was already observed in NWs [73, 132] and also by Mandl *et al.* in self-seeded InSb NWs [204]. Similar as in the study by Mandl *et al.* [204], the 4H polytype is observed only in a small region before it switches into the WZ crystal structure. The WZ structure is present over a length of about 40 nm. Hereafter, it switches back into the ZB crystal structure just beneath the droplet. By means of the hexagonality, the 4H structure is described as an intermediate state between the ZB and the WZ structure [235]. The hexagonality represents the number of hexagonal layers in the unit cell: ZB has a hexagonality of 0%, 4H 50% and WZ has a hexagonality of 100%.

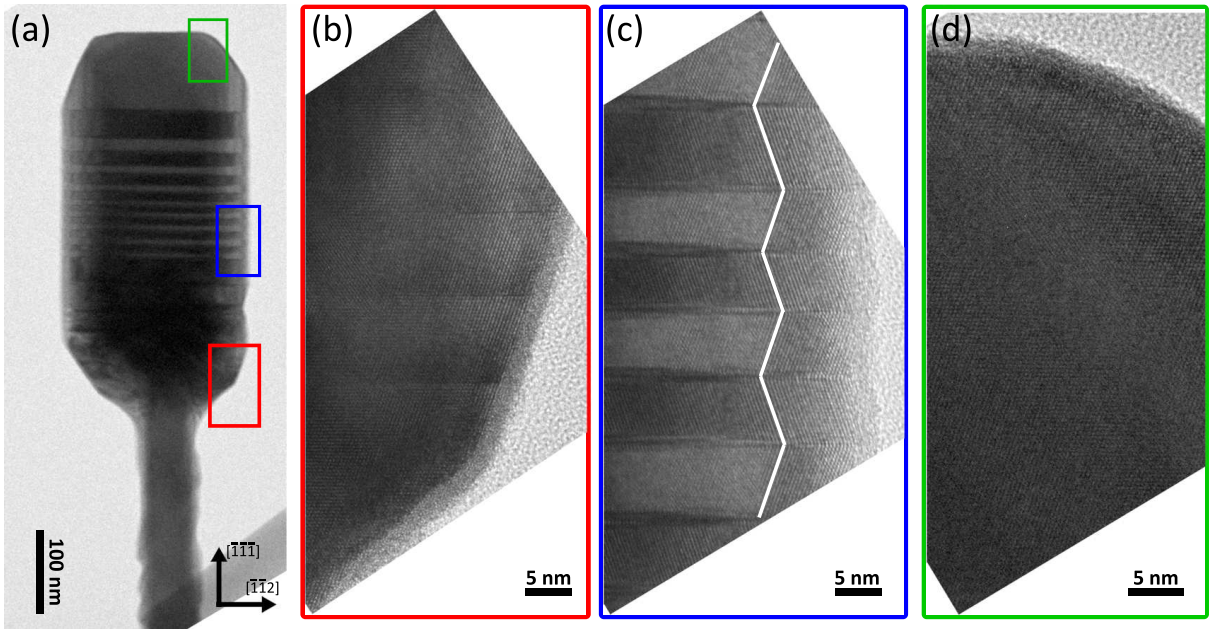

Figure 6.22.: *(HR)TEM images of a long axially grown InSb segment on top of a GaAs stem. (a) Overview image and (b-d) HRTEM images along different positions along the InSb. White lines in (c) indicate the ZB stacking sequence with twins.*

The small ionicity of InSb and the large energy difference between the ZB and the WZ favor the the crystallization in the ZB phase [3, 235]. Mandl *et al.* correlated the change in crystal structure of the InSb with a continuous increase of the Sb concentration in the droplet [204]. In our case, the Sb concentration in the droplet could not be measured *ex situ*. The upper short ZB segment may be caused by the partial consumption of the In droplet during the cool down from the growth temperature.
Interestingly, the crystal structure is not identical on all NWs from the same growth run. In some case,s a (twinned) ZB structure without the WZ or 4H phase is observed. This difference in crystal structure suggests that the crystal structure of the In-assisted growth of InSb, i.e. the presence of twins or other crystal phases except the ZB phase, is very sensitive to the actual growth conditions, which may vary from NW to NW due to variations in the local environment.

This is evidenced by Fig. 6.22 displaying TEM micrographs of a GaAs/InSb heterostructure NW with a rather long InSb growth time of $\sim$ 120 min. The droplet is consumed unintentionally and the InSb segment is the longest obtained. It has a length l of about 700 nm and a diameter d of $\sim$ 250 nm, the aspect ratio $a = l/d$ is 2.8. Considering the long growth time, the InSb section is rather short. In conjunction with the absence of the droplet, this suggests that the droplet was consumed during the growth due to changes in the adatom migration. This reduces the amount of In adatoms arriving at the droplet which leads to a consumption of the droplet during the growth. Nonetheless, the NW displays a good representation of the crystal structure of the InSb, since it has the longest growth time. The crystal structure starts with a long pure ZB segment as seen in Fig. 6.22b. Subsequently, a section with twins in the InSb occurs. The spacing between the twins is not constant but increases along the growth direction (Fig. 6.22c). The upper 100 nm are again of pure ZB crystal structure (Fig. 6.22d), possibly being caused by the consumption of the In droplet during the growth or the cool down. Vapor liquid solid grown InAs NWs actually exhibit an analogous crystal structure of twinned ZB but with periodically spaced twin planes [109]. The vapor liquid solid InAs NWs had a flat top facet, identical to the

axially grown InSb in this study (see Fig. 6.22a,d).

The bulk lattice mismatch between the GaAs in the stem and the InSb grown axially is $\sim 14\%$. Axial heterostructures are usually regarded to be optimal for an efficient combination of mismatched materials, since the interfacial area is small and strain can be relaxed in the radial direction. Glas [104] as well as Ye and Yu [342] calculated the dimensions where pure elastic strain relaxation takes place. For extremely high lattice mismatched such as in the GaAs/InSb system, coherent growth is only possible for very thin NWs and/or very thin epitaxial layers. Previous studies e.g. on GaAs/GaSb and InAs/InSb axial heterostructures, both having a nominal lattice mismatch of about 7%, showed the presence of misfit dislocations [65, 160]. Accordingly, strain relaxation via dislocations is also expected for the present study. Figure 6.23a displays the interface between the GaAs stem and the axially grown InSb of the sample shown in Fig. 6.20c. The NW is oriented along the $\langle 110 \rangle$ zone axis. The GaAs stem is characterized by a long WZ segment at the top, followed by a short ZB region having an almost flat top facet. A slight rounding towards the edges is observed, which is also observed in the EDX maps in Fig. 6.19. The InSb adopts the ZB crystal structure and the stacking sequence of the GaAs, no twins or stacking faults in the InSb near the interface are observed. A higher magnified image of the interface is shown in Fig. 6.23b, the inset displays the corresponding FFT. The splitting of the Bragg spots indicates that plastic relaxation takes place, both axially and radially. Applying a mask to the $(11\overline{1})$ reflections (encircled in red in the FFT) and calculating the inverse FFT, produces the FFT-filtered image shown in Fig. 6.23c. It solely displays the $(11\overline{1})$ lattice planes. Terminating lattice planes are frequently observed at the interface (indicated by the purple arrows), proving the presence of misfit dislocations. No stacking faults associated with the dislocations are observed, thus the dislocations are perfect dislocations. The presence of perfect dislocations was further confirmed by Burgers circuits. The average distance between the dislocation is measured to 2.8 nm. Assuming complete strain relaxation, the expected distance d between two dislocations is given by $d = b/f$, where b is the Burgers vector of the perfect dislocation, $b = a/2 \cdot [110]$, and f is the lattice mismatch. The expected distance between the dislocations is then in the range of 2.7 – 3 nm. Accordingly, the measured distance between neighboring dislocations indicates that the axially grown InSb is completely relaxed.

Figure 6.23d displays the same interface from the $\langle 211 \rangle$ zone axis, thus the NW was rotated by 30° around the growth axis. Both materials and the interface between them are clearly distinguished. The FFT of the image is displayed as an inset. Identical to the FFT shown in Fig. 6.23b, the FFT of the image from the $\langle 211 \rangle$ zone axis exhibits splitted Bragg spots for all lattice planes. The inverse FFT calculated by applying a mask to the (022) spots (x-direction in the FFT) is depicted in Fig. 6.23e. Similar to the inverse FFT of Fig. 6.23c, misfit dislocations are found. They form a regular array with a distance between two adjacent dislocations of ~ 1.4 nm, corresponding to ~ 7 (022) planes. This agrees with the 14% lattice mismatch between both semiconductors. The distance between the (022) planes in the GaAs and InSb regions is measured to ~ 1.97 Å and ~ 2.27 Å, respectively. In bulk GaAs and InSb, these distances are 2 Å and 2.29 Å. Comparing the measured and theoretical values, it is concluded that both semiconductors are completely relaxed in the radial direction. The efficiency and abruptness of the strain relaxation is further analyzed by means of geometric phase analyses (GPA), which provides strain maps from HRTEM images (see Sec. 2.3 and Refs. [142, 143]). Figures 6.23f and g display the ϵ_{xx} and ϵ_{yy} strain maps, respectively. In both strain maps it is seen that the strain is relaxed immediately when the dislocations occur, no gradient is observed. The dislocations are found within a sharp transition region from the GaAs to InSb.

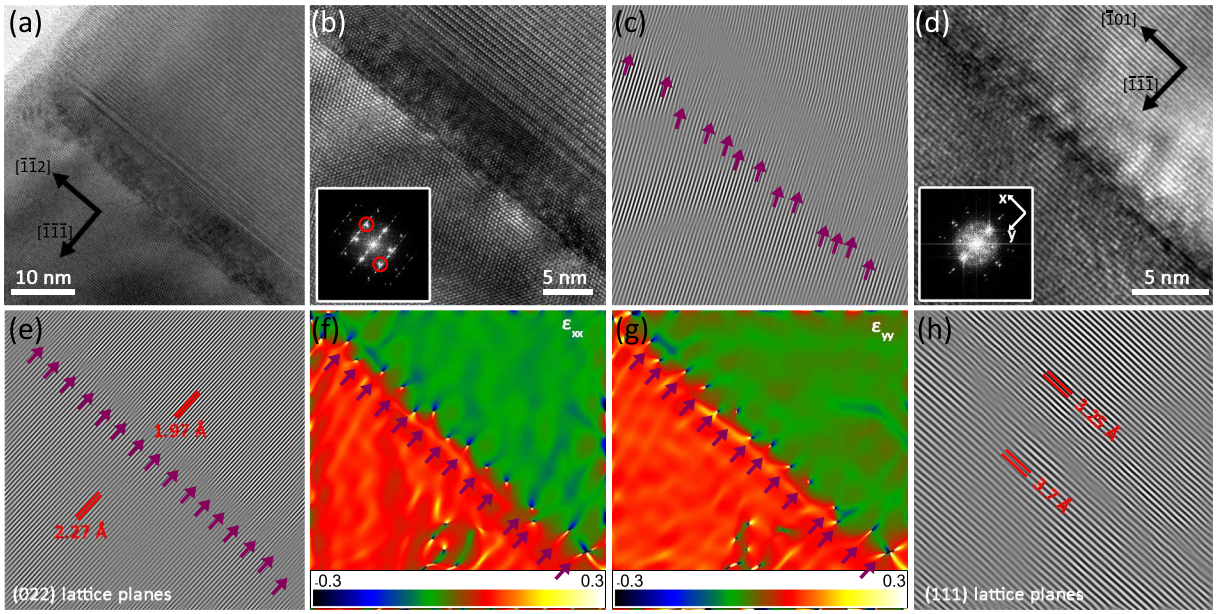

Figure 6.23.: *HRTEM images, dislocations and strain relaxation at the interface between GaAs and axially grown InSb. (a,b) Interfacial region (from the ⟨110⟩ zone axis) exhibiting clear contrast between the semiconductors. Inset in (b) shows the FFT with a splitting of the spots. (c) Inverse FFT calculated by masking the spots marked in the inset in (b). Terminating planes indicate misfit dislocations. (d) HRTEM image of the interface acquired from the ⟨211⟩ zone axis. The inset shows the FFT. (e) Inverse FFT showing the (022) lattice planes. (f,g) ϵ_{xx} and ϵ_{yy} strain maps of (d). (h) Inverse FFT showing the (111) lattice planes. Purple arrows in (c), (e), (f) and (g) point at dislocations.*

This indicates that the interface between GaAs and InSb is not alloyed and further evidences the high abruptness of the heterostructure. The strain maps allow to measure the experimental lattice mismatch in both directions, namely the radial ⟨110⟩ (ϵ_{xx} strain map) and the axial ⟨111⟩ (ϵ_{yy} strain map) directions. This experimental lattice mismatch is evaluated to 13.5 – 15 % for both directions, that is a similar value as the lattice mismatch between the GaAs and InSb. The inverse FFT obtained by considering only the (111) lattice planes of Fig. 6.23d is depicted in Fig. 6.23h. The distance between the (111) planes in the GaAs is measured to ∼ 3.25 Å, which agrees with the distance of 3.26 Å in bulk GaAs. For the InSb section in the NWs, the distance between equivalent (111) lattice planes is ∼ 3.7 Å, matching well with the value of 3.74 Å in bulk InSb. Together with the strain maps and the inverse FFT from Fig. 6.23e, this indicates that the strain is completely relaxed by the misfit dislocations at the interface. Defects are found only at the interface, no extended defects such as threading dislocations are observed.

This study demonstrates the growth of self-assisted axial heterostructure NWs via a droplet-renucleation at the top facet. Such a formation of a droplet on an existing NW was previously described by Somaschini *et al.* [287] and Priante *et al.* [248]. In both investigations, a Ga droplet was created at the flat top facet of a GaAs NW [248] or a GaAs island [287]. In 2014, Somaschini *et al.* further presented axial GaAs/InAs heterostructure NWs based on GaAs islands [286]. No In droplet was involved in the axial growth. The length of the axially grown InAs was very short and typically, substantial radial growth of InAs on the GaAs occurred. Axial GaAs/GaAsSb heterostructure NWs, i.e. heterostructures achieved by the addition of a second group V element, strongly affected the crystal structure of the NWs: the GaAsSb sections had ZB crystal structure and WZ GaAs was observed after the GaAsSb growth took place [162, 220, 244]. Conesa-Boj *et al.* observed pure ZB GaAsSb NWs [56]. The highest Sb content was found to be

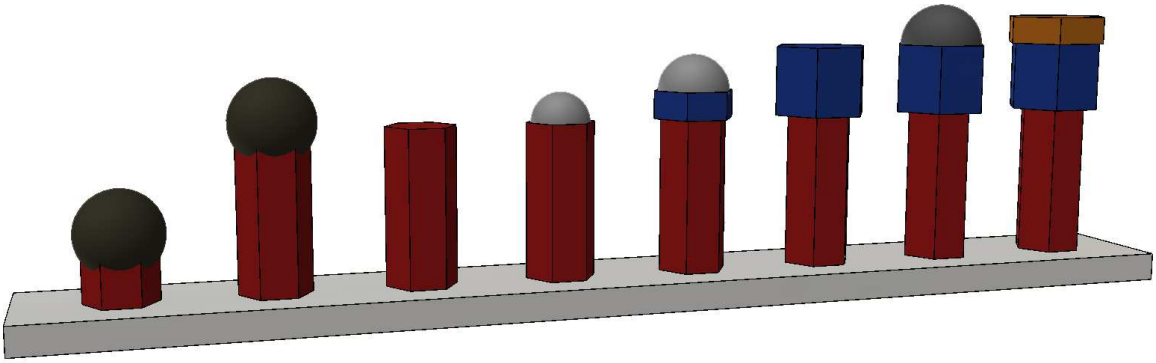

Figure 6.24.: *Schematic of the growth of axial heterostructures in self-catalyzed NWs.*

$\sim$ 30 %. Axial heterostructures of self-catalyzed GaAs/InGaAs NWs had a maximal In content of only $\sim$ 5% [125]. Apparently, the GaAs/InSb axial heterostructure NW presented here is the first demonstration of an axial heterostructure in self-assisted NWs with a change of both the group III and the group V components. The change in composition is very abrupt.
It should be mentioned that even Au-catalyzed InSb NWs are usually grown on top of stems. Most often these are InAs stems [43, 42, 86, 245]. Accordingly, the self-catalyzed growth of InSb NWs via a stem demonstrates a promising way towards Au-free InSb NW structures.

The growth mechanism presented here represents a suitable way to obtain abrupt axial heterostructures in self-assisted NWs. This method is schematically depicted in Fig. 6.24: The NW growth is initiated with the growth of a self-assisted NW stem having a flat top facet after droplet consumption. Using suitable growth conditions, a droplet is recreated on this facet. The droplet catalyzes the growth of a NW on top of the existing one. Since the InSb section used here provides a flat top facet after droplet consumption (see Fig. 6.22), a second axial segment may be grown on top. This enables significantly more complex NW heterostructures.

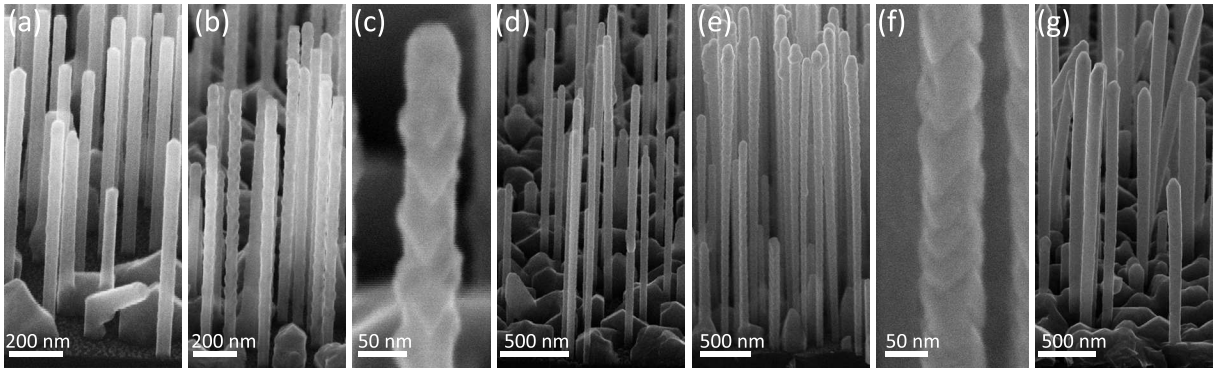

Figure 6.25.: *SEM images of radial GaAs/InSb core-shell NWs with different growth times of the InSb shells. Growth times of the InSb are (a) 2 min, (b,c) 5 min, (d) 15 min, (e,f) 45 min and (g) 90 min.*

6.2.2. Radial growth of InSb

A significant decrease of the substrate temperature for the growth of the InSb from $\sim 460°C$ used for the axial growth down to 280°C – 300°C results in NWs with a rather uniform diameter as it was shown in Fig. 6.17c. Figure 6.25 displays GaAs/InSb heterostructure NWs with varying growth durations of the InSb. The growth durations of the InSb are varied between 2 and 90 min and increase from left to right. For the shortest growth time of the InSb, the roughness of the NW side facets is low due to the low amount of deposited material. An increase of the growth time of the InSb to 5 min roughens the NW (Fig. 6.25b,c), indicating growth of InSb on the side facets of the GaAs NWs. At this stage, separated InSb islands are found on the NW. By further increasing the growth time, the NW surface first remains rather rough (Fig. 6.25d-f) before it becomes relatively smooth (Fig. 6.25g). Consequently, radial growth of InSb on GaAs takes place forming a core-shell NW. Similar growth characteristics were observed in GaAs/InAs core-shell NWs [262] where a nucleation of InAs islands on the side facets of GaAs NWs was followed by a coalescence of the islands. In case of the GaAs/InSb core-shell NWs investigated here, the islands have a preferred orientation and shape as seen in Fig. 6.25c. The islands have a V-shape which is also evident from the SEM images displaying the axial growth of GaAs/InSb heterostructure NWs (see Fig. 6.18). No large nuclei on the WZ phase close to the top of the GaAs core are observed. When coalescence of these V-shaped islands takes place, the surface of the NWs has some similarity to overlapping roof tiles (see Fig. 6.25f). This morphology of overlapping and not separated roof tiles is obtained after a growth time of about 30 – 45 min, which corresponds to a shell thickness of about 10 – 15 nm. The (average) shell thickness increases linearly with the growth time with a growth rate of about $\sim 20 – 25$ nm/h. This agrees with the supplied In flux (100 nm/h) after considering the NW alignment with respect to the effusion cell and the substrate rotation. The good agreement between the supplied flux and the shell growth rate indicates that diffusion from or to the substrate is marginal and also secondary absorption processes can be neglected. The absence of both is caused by the very low growth temperature of about 280°C – 300°C which is significantly lower than the growth temperature used for InSb layers ($\sim 340 – 420°C$) [227, 285, 306].

The core-shell morphology of the GaAs/InSb NWs is confirmed by the EDX map displayed in Fig. 6.26. The InSb shell was grown for 2h. The figure shows the HAADF image of the top segment (a) and roughly at the middle of the NW (b) together with the EDX maps of Ga, As, In and Sb. The EDX analyses clearly proves the existence of the core-shell structure along the entire NW. The shell thickness is ~ 50 nm and is uniform along the NW axis. Apart

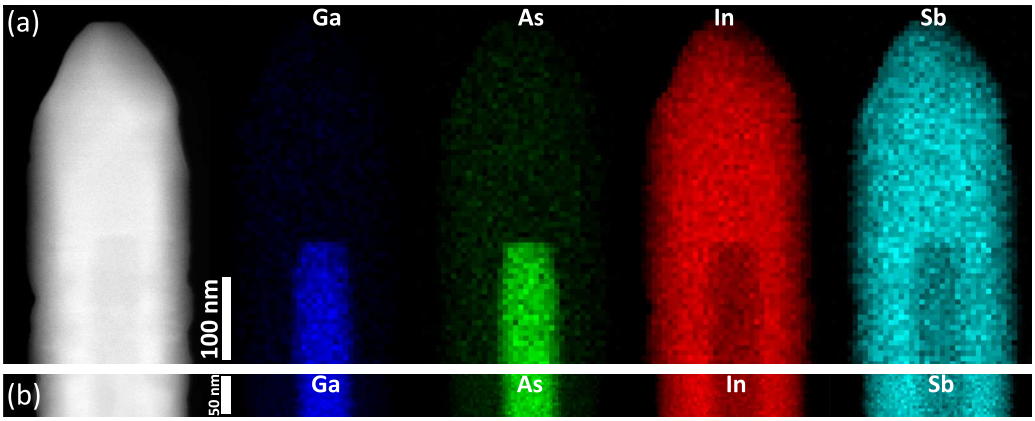

Figure 6.26.: *HAADF image and elemental maps of Ga, As, In and Sb in GaAs/InSb core-shell NWs acquired at (a) the upper part and (b) the middle of the NW.*

from the radial growth, substantial axial growth of InSb is observed. In contrast to the results from the previous section, the axial growth of the InSb is due to a vapor solid growth where no droplet is involved. The EDX maps do not indicate any alloying at the interface, neither in the axial nor in the radial direction. This is in agreement with the study of axial GaAs/InSb NW heterostructures shown in the previous section. The growth temperature used for the axial GaAs/InSb heterostructures was significantly higher which should enhance any diffusion process. Thus, it is concluded that core-shell heterostructures with rather abrupt interfaces are formed.

A bright field TEM image of a GaAs/InSb core-shell NW is shown in Fig. 6.27a. The image can be divided into two sections. In the lower part, a slight contrast arising from the core-shell structure is observed. This region contains only few stacking faults or twins, being in agreement with the crystal structure of GaAs NWs [259]. These GaAs NWs typically have an almost pure ZB crystal structure. The core-shell segment is shown in higher magnification in Fig. 6.27b, evidencing a slight roughness of the shell. Interestingly, the roughness is higher on the left side of the NW. This is discussed in detail later. The upper region, which is pure InSb according to the EDX analyses shown in Fig. 6.26a, contains several planar defects. The diffraction pattern of this region is shown in Fig. 6.27c. Diffraction spots from both ZB twins as well as streaks are observed. A streaky pattern is characteristic for a high density of planar defects such as twins and stacking faults. One ZB twin is dominant in the diffraction pattern, indicating that both ZB orientations are not distributed equally in the axially grown InSb but a preferred orientation is present. The HRTEM micrograph of the axially grown InSb is depicted in Fig. 6.27e. It confirms the high density of stacking faults/twins also observed in the diffraction pattern. Twin-free ZB segments with lengths in the range of 5 – 10 nm are present, the WZ structure is typically not found. Apparently, the vapor solid growth of InSb in $[\overline{1}11]$ direction favors the twinned ZB crystal structure with a high density of twins. The crystal structure is different compared to the vapor liquid solid growth of InSb from an In droplet described in the previous section. There, the crystal structure was typically ZB with long sections of one orientation before a twin occurred.

The GaAs/InSb core-shell region seen in the lower part of Fig. 6.27a and in Fig. 6.27b has the ZB crystal structure, as described above. The diffraction pattern of such a region is displayed in Fig. 6.27d. It evidences a ZB diffraction pattern with streaks. These streaks may arise from twins/stacking faults of the core or stacking faults induced by partial dislocations. No splitting of the diffraction spots is observed. A splitting would be a clear proof of two crystal lattices with different lattice constants as it was observed in the case of axial growth (see Fig. 6.23b,d). Inter-

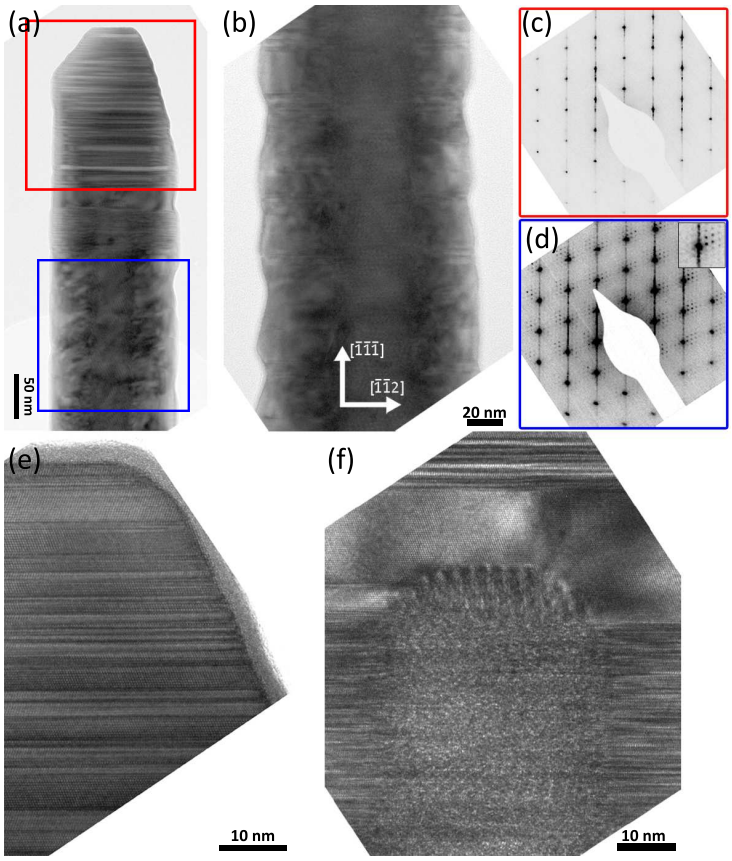

Figure 6.27: *TEM micrographs and diffraction patterns of GaAs/InSb core-shell NWs. (a,b) Low resolution images of the upper segment and the central part. (c,d) Diffraction patterns of the regions marked in (a) (inverted colors). (e) HRTEM images of the axial InSb obtained via VS growth. (f) Interfacial area from the core-shell structure to the axial region.*

estingly, the diffraction pattern of the core-shell NWs reveals an additional diffraction pattern around each diffraction spot. This phenomenon is known as "double diffraction" [332]. Double diffraction occurs when a diffracted beam gets diffracted either in the same crystal or when passing through another crystal. Diffraction in the same crystal is excluded since the thickness is identical as in Fig. 6.27c where double diffraction was not observed. Accordingly, the diffraction in both crystals, the GaAs core and the InSb shell, results in the double diffraction. The second, small diffraction pattern reproduces the ZB pattern of the primary pattern, proving the epitaxial relationship between the core and the shell. The primary diffraction pattern is due to electron diffraction in the InSb shell, scattered electrons are then rediffracted in the GaAs core and produce the small diffraction pattern around the primary diffraction spots. The presence of two lattices with different lattice constants is further confirmed by the TEM micrograph shown in Fig. 6.27f. A central region displaying Moiré fringes is observed, the surrounding does not exhibit these fringes. Moiré fringes are observed when lattices with a different crystal lattice, orientation or lattice constant are superimposed.

The TEM image in Fig. 6.27f further shows that the upper few nanometers are of the GaAs core have ZB crystal structure which are adopted by the InSb shell. Below this ZB section, a high density of stacking faults in the shell is observed. These may originate from Frank partial dislocations occurring at the GaAs/InSb interface when the WZ crystal structure is present. It is described later that only Frank partial dislocations are observed in the WZ core-shell NWs. The WZ crystal structure is usually present close to the top of self-catalyzed GaAs NWs [259]. In contrast to the results obtained for GaAs/InAs core-shell NWs (see Chapter 5.1.1), growth of InSb takes place on both crystal phases of the GaAs core. This may be due to the very low growth temperature of the InSb shell and the corresponding low diffusivity of the InSb adatoms.

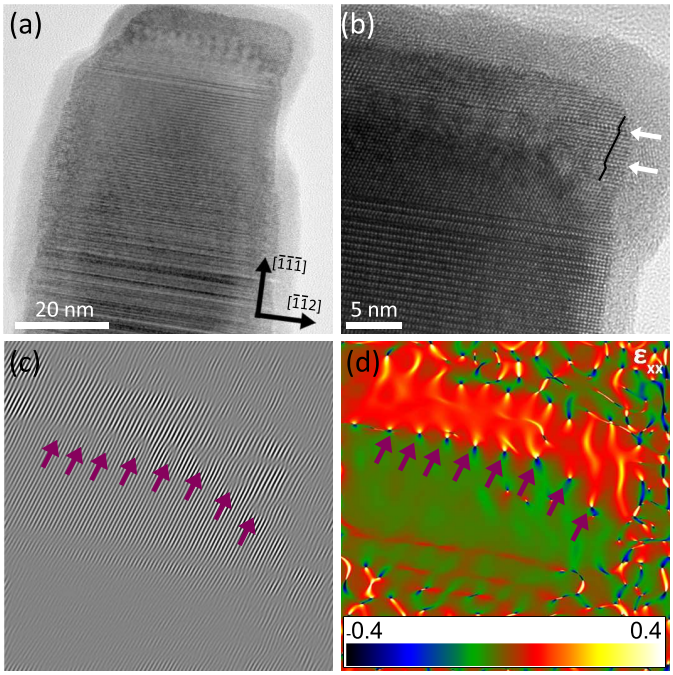

Figure 6.28: *TEM micrographs, inverse FFT image and strain map of InSb grown on top of GaAs via a vapor solid mechanism. (a) Overview image. (b) HRTEM image clearly showing the growth of InSb on top of the GaAs. The natice oxide of the InSb has a thickness of about 5 nm. Arrows are pointing to stacking faults induced by Frank partial dislocations. Black lines indicate the stacking sequence with two stacking faults. (c) Inverse FFT showing the* $(11\bar{1})$ *lattice planes. Misfit dislocations with a regular spacing are seen. (d)* ϵ_{yy} *strain map indicating the abrupt change in the strain, i.e. abrupt strain relaxation. Arrows in (c) and (d) point to dislocations.*

In the following the structural defects present in the GaAs/InSb core-shell NWs are further discussed. Figure 6.28a depicts a TEM micrograph of the upper section of GaAs/InSb core-shell NW with a growth time for the InSb shell of 5 min. It shows the above mentioned WZ structure close to the top of the GaAs core as well as the ZB structure at the top. The short growth time of the InSb shell results in an incomplete shell growth. The native oxide of the InSb shell is about $\sim$ 5 nm in thickness, which is significantly higher than the thickness of the native oxides on GaAs and InAs and in a similar range as for GaSb (see Section 6.1.1.1). Figure 6.28b displays the upper short ZB segment in higher resolution, evidencing axial growth of InSb on GaAs. The InSb adopts the crystal structure and orientation of the underlying GaAs. The large lattice mismatch of around 14 % is relaxed by the formation of misfit dislocations at the interface. These are observed in the FFT-filtered image shown in Fig. 6.28c as well as the ϵ_{yy} strain map in Fig. 6.28d. The FFT-filtered image displays terminating lattice planes, i.e. dislocations. Some of these dislocations create stacking faults being perpendicular to the growth axis (white arrows in Fig. 6.28b) while others are perfect dislocation not affecting the surrounding crystal structure (see Fig. 6.28b). The stacking faults are created by dislocations relaxing the axial strain. Certainly, these dislocations are present only at the rounded edge of the NW. Dislocation mostly relaxing the radial strain component do not result in the formation of stacking faults. The ϵ_{yy} strain map also shows the dislocations and demonstrates the abrupt change in lattice parameters (evidenced by the abrupt change in strain). No gradient at the interface is observed.
It is evident from the presented results that the mechanism of axial growth, either vapor-liquid-solid or vapor-solid, influences the crystal structure but not the defects at the interface between both semiconductors or the strain relaxation.

A HRTEM micrograph displaying the early stage of the growth on the WZ phase is seen in Fig. 6.29a. The inset shows the corresponding FFT. The thick oxide layer being caused by the InSb growth is clearly observed in the HRTEM micrograph. About 2 nm of crystalline InSb are present. The inverse FFT obtained by masking the (0002) reflections shows six terminating (0002) planes, i.e. six misfit dislocations. The distance between two neighboring dislocations

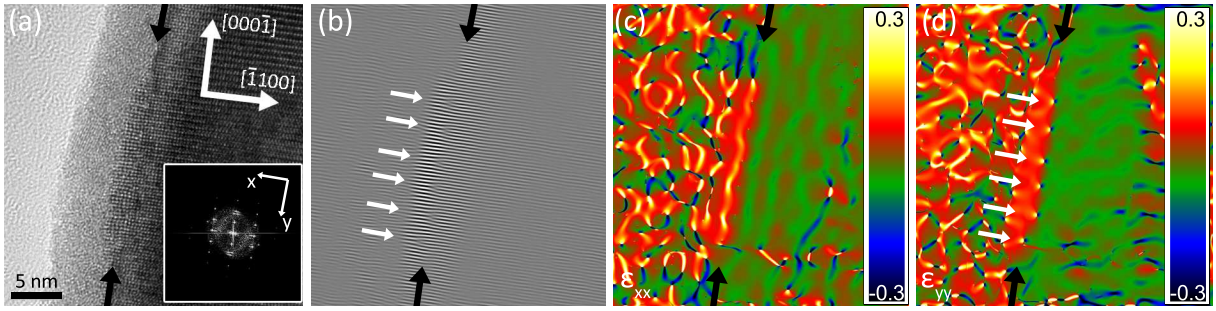

Figure 6.29.: *HRTEM image, inverse FFT and strain maps of InSb grown on WZ GaAs. (a) HRTEM image with the FFT shown in the inset. (b) Inverse FFT showing the (0002) lattice planes with six misfit dislocations (indicated by white arrows). (c) ϵ_{xx} strain map. (d) ϵ_{yy} strain map (white arrows point to dislocations). The black arrows indicate the interface between the GaAs and the InSb.*

varies between 7 and 8 layers, being in good agreement with the expected value of $\sim$ 7 layers[4] Consequently, the axial strain is relaxed almost completely. This is also evident from the ϵ_{yy} strain map displayed in Fig. 6.29d. The ϵ_{yy} strain map displays an abrupt change in the strain as well as the six dislocation mentioned before. No gradient of the strain in the shell or in the core is observed. The entire strain is relaxed at the interface. An interesting feature is observed in the ϵ_{yy} strain map shown in Fig. 6.29c. A line with a high value of the strain is present just at the position of the misfit dislocations. At this position, the strain (compared to the GaAs core) is 14 – 15 % while the strain decreases to $\sim$ 6 % in the thin InSb island. Consequently, the InSb island is relaxed along the $\langle 0001 \rangle$ direction but has a compressive strain in the $\langle 1\bar{1}00 \rangle$ direction. This compressive strain may be caused by the rather thick native oxide covering the small InSb island.
All dislocations in the WZ core-shell section are Frank partial dislocations with Burgers vectors of $b = c/2[0001]$. These dislocations produce stacking faults in the shell which can act as additional scattering centers for the electronic transport. Perfect dislocation are not observed. Similar observation were made in WZ InAs/GaAs core-shell NWs [247].

The nucleation of InSb on the {110} side facets of the ZB GaAs is displayed in Fig. 6.30a. Similarly as for the growth on the WZ phase, the thickness of the InSb is in the range of a few nanometers with a rather thick native oxide shell. The FFT-filtered image and the $(\overline{111})$ strain map are shown in Fig. 6.30b and c, respectively. Four dislocations with a rather uniform distance are found. The distance agrees well with the distance between dislocation in the WZ phase (see above), suggesting again an abrupt change of the lattice constant. This abrupt strain relaxation is also obvious due the change of the color in the strain map (Fig. 6.30c). Contrary to the dislocations observed in the WZ core-shell region, here not only Frank partial dislocations but also perfect dislocations as well as Shockley partial dislocation are seen. All three types are present in Fig. 6.30a: the red arrow points to a perfect dislocation, the blue arrow to a stacking fault having its origin in a Frank partial dislocation and finally, the purple arrows indicate stacking faults coming from a Shockley partial dislocation. These three dislocations have already been observed in GaAs/InAs core-shell NWs with ZB crystal phases (see Chapter 5.1.1). Comparing the results presented in the literature [164, 247] and this thesis for lattice mismatched WZ and ZB core-shell NWs suggests that only Frank partial dislocations relaxing the axial strain are observed in WZ core-shell NWs while three different dislocations are found in ZB core-shell NWs. Most likely this is caused by differences in the magnitude of the Burgers

[4]The lattice mismatch between GaAs and InSb is about 14%, the magnitude of the Burgers vector is $c/2$ which means that the average distance between two dislocations is 2.6 nm which corresponds to $\sim$ 7 layers.

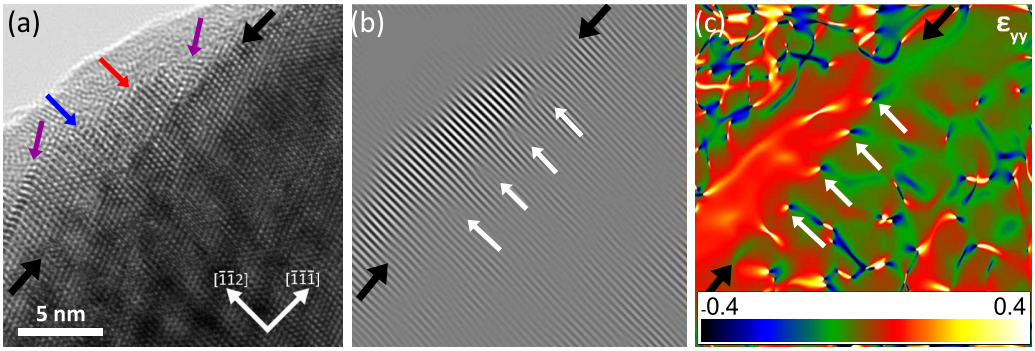

Figure 6.30.: *HRTEM image, inverse FFT and strain maps of InSb grown on ZB GaAs. (a) HRTEM image. The red arrow points to a perfect dislocation, the blue to a Frank partial dislocation and the purple arrows to Shockley partial dislocations. (b) Inverse FFT showing the (111) lattice planes with the misfit dislocations (white arrows). (c) ϵ_{yy} strain map with an abrupt change from the GaAs to the InSb, dislocations are marked by white arrows. The black arrows indicate the interface between the GaAs and the InSb.*

vectors. For the WZ structure, the Burgers vector of the perfect dislocation is $b = c[0001]$ while it is $b = c/2[0001]$ for a Frank partial dislocation. For the perfect dislocation, Frank partial dislocation and Shockley partial dislocation in the ZB lattice, the Burgers vectors are $b = a/2\langle 110\rangle$, $b = a/3\langle 111\rangle$ and $b = a/6\langle 211\rangle$, respectively. Thus, the Burgers vector of the perfect dislocation in the WZ structure is largest. The energy of a dislocation E_{dis} is proportional to the square of the Burgers vector, i.e. $E_{dis} \propto b^2$ [139]. The energy of a perfect dislocation in the WZ lattice is four times the energy of a Frank partial dislocation. This difference in energy favors the formation of Frank partial dislocations in WZ lattices.

Finally, two additional aspects are shortly discussed: (1) the roughness of the NWs and (2) the growth of InSb on WZ GaAs. The roughness of the NWs was already observed in Fig. 6.25c,f as well as in axial GaAs/InSb heterostructure NWs (see Fig. 6.18). In each situation, several V-shaped structures grow on the side facets of the GaAs NW, the morphology is seen most clearly in Fig. 6.18. The V-shapes are aligned in such way that the "arms" are connected at the corner of the hexagonal cross section. Increasing the shell thickness results in a coalescence of the V-shaped structures. However, even for shell thicknesses of 50 nm, a certain roughness of the shell remains (see Fig. 6.27a,b). The origin of the roughness is the nucleation via V-shaped islands. HAADF images of GaAs/InSb core-shell NWs with shell thicknesses in the range of 15 – 20 nm clearly demonstrate the V-shaped nucleation basis. This is displayed in Fig. 6.31a. The red arrow indicates the position of a twin boundary, the blue lines show the V-shapes. The twin boundary changes the alignment of the V-shapes, suggesting an epitaxial relationship as well as crystallographic preferred growth along certain directions. Indeed, the angle between the $[\overline{1}\overline{1}\overline{1}]$ NW growth direction and the arm of the V-shape is $\sim 145°$ which corresponds to the angle between the NW growth direction and the $[0\overline{1}\overline{1}]$ direction. Accordingly, InSb grows in the $\langle 110\rangle$ direction, at least when grown on the $\{110\}$ side facets of GaAs NWs. When the shell thickness increases, the V-shapes are no longer observed. Instead, a high roughness of the shell is observed. Figure 6.31b displays bright field TEM micrograph of a GaAs/InSb core-shell NW with a ~ 50 nm thick InSb shell exhibiting the rough InSb shell. The red arrow again indicates the position of a twin boundary which is clearly observed in the HRTEM image shown as an inset. Interestingly, the roughness is observed only on one side of the NW. Its orientation switches at the twin boundary. The roughness exhibits a saw-tooth profile being bound by (111)B and a mixture of (001) and (211)B type side facets.

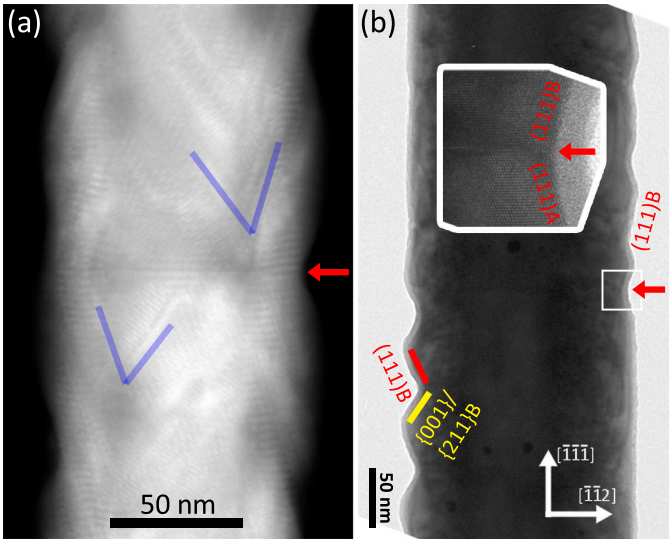

Figure 6.31: *HAADF and TEM images showing the roughness of GaAs/InSb core-shell NWs. (a) HAADF image with a twin boundary (red arrow) and evidence of V-shaped structures (blue lines). (b) Bright field TEM image showing the roughness, changing at the twin boundary (red arrow). The rough side facets are bound by* (111)*B and a mixture of* (001) *and* (211)*B type facets.*

The other aspect deals with the growth of InSb on the WZ phase of GaAs. As it was already demonstrated in Fig. 6.29, the growth of InSb on the WZ phase of GaAs takes place and dislocations are formed at the interface, relaxing the strain induced by the large lattice mismatch. Figure 6.32a displays the upper part of a GaAs/InSb core-shell NW with a shell thickness in the range of $\sim$ 10 nm. The shell thickness is identical on the ZB crystal structure (bottom) and on the WZ structure except for a short region close to the top where the thickness of the shell decreases. Higher magnified images of the WZ region are displayed in Fig. 6.32b,c and evidence a slight tilt of the WZ InSb (0002) planes with respect to the (0002) lattice planes of the GaAs core. The highest tilt angles are around 3° – 5°. No tilt of the ZB (111) lattice planes is observed. The density of stacking faults associated with Frank partial dislocations in the WZ part is less than expected for a complete relaxation of the strain. This may be caused by the tilted lattice planes which conserve the high lattice mismatch at the interface but gradually relax the strain towards the surface as the distance between the (0002) planes increases. Consequently, tilted lattice planes, i.e. a plastic deformation, represent an additional mechanism for strain relaxation, but they can only occur when the structure is not confined in all directions.

6.3. Conclusions

The growth parameters, morphology and structural properties of core-shell heterostructure NWs based on the 6.1 Å family, i.e. InAs, GaSb and AlSb, have been investigated. Two distinct growth regimes for GaSb shells covering InAs NW cores were observed. High growth temperatures of about 490°C resulted in inversely tapered GaSb shells with an exposed InAs core at the bottom of the NWs. The tapered morphology was attributed to the diffusion of Ga adatoms from the lower part of the NWs to the substrate. At substrate temperatures around 360°C, the InAs cores are covered homogeneously with the GaSb shells. Detailed analyses by means of HRTEM revealed the absence of misfit dislocations. This was explained by the small lattice mismatch between InAs and GaSb as well as the reduced dimensions of NWs, being a proof of their efficient strain accommodation.
The replacement of the GaSb shell with $Al_xGa_{1-x}Sb$ influenced the morphology at the upper part of the core-shell NWs. As a consequence of Al in the shell, the thickness of the native oxide was found to increase. Pure AlSb shell were completely oxidized. An additional capping with GaSb

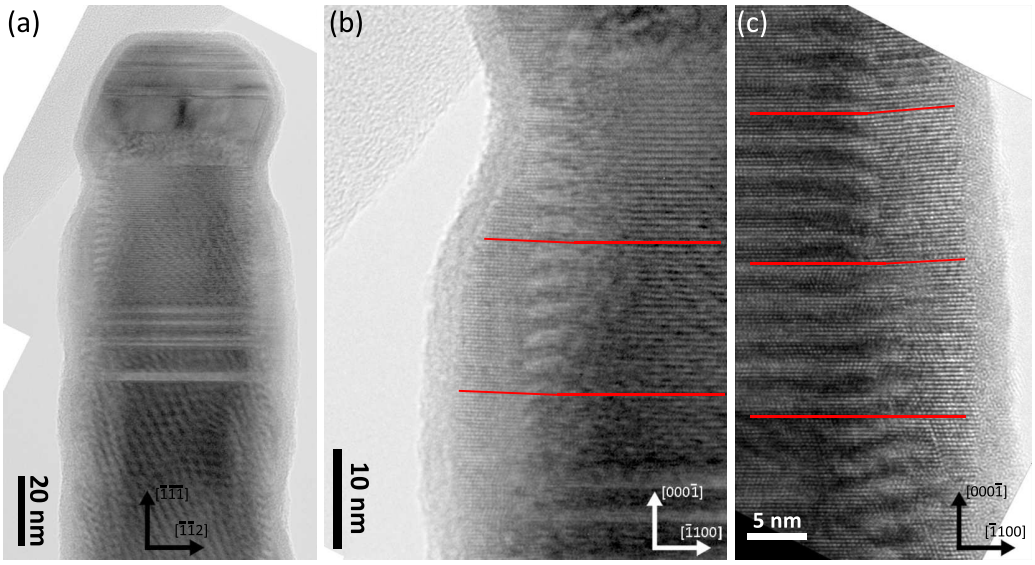

Figure 6.32.: *TEM images showing tilted WZ (0002) lattice planes of the InSb with respect to the GaAs core. (a) Low resolution image. (b,c) high resolution images clearly showing the tilted WZ (0002) lattice planes of the shell. This tilt can reduce the density of misfit dislocations. Red lines in (b) and (c) indicate the alignment of the (0002) planes and clearly demonstrate that the (0002) WZ lattice planes in the InSb are tilted with respect to the GaAs core.*

prevented the oxidation. Identical to the InAs/GaSb core-shell NWs, InAs/AlGa$_x$Sb$_{1-x}$/GaSb core-shell NWs were found to be free of misfit dislocations.

The second part of the chapter was dedicated to GaAs/InSb heterostructures with a lattice mismatch of $\sim$ 14%. SEM and TEM micrographs indicated a temperature dependence of the obtained morphology with an axial heterostructure observed at high growth temperatures while lower growth temperatures resulted in core-shell NWs. The axial GaAs/InSb heterostructure was found to be created by a renucleation of an In droplet on top of a GaAs NW stem. The crystal structure of the axially grown InSb was ZB, partially containing also the 4H polytype and the WZ crystal structure. The strain at the interface was released by perfect dislocations. The core-shell NWs obtained at lower growth temperatures exhibited a significant roughness of the shell. InSb growth took place on both crystal phases of the GaAs core. Strain relaxation on the WZ phase occurred by Frank partial dislocations whereas perfect dislocations, Frank partial dislocations and Shockley partial dislocations have been observed for the growth of InSb on the ZB phase of GaAs. Additionally, plastic relaxation of InSb on WZ GaAs took place, evident as tilted (0002) lattice planes.

Chapter 7.
7 Nanowires on faceted Si (100) substrates

The semiconductor NWs described in the previous chapters represent suitable structures e.g. for FETs, TFETs and high mobility devices. Similarly, LEDs [79] and lasers [210] on the basis of GaAs NWs have already been obtained. The integration of these NWs in semiconductor industry requires that the NWs are grown on Si (100) substrates. Different NWs (composition, doping, dimension etc.) being present on predefined positions and on the same substrate are beneficial in order to engineer the NW properties (e.g. the conductivity) locally or to obtain both electronic and optic components on the same chip. The electronic parts can then e.g. be (T)FETs on the basis of InAs NWs whereas GaAs-based NWs serve as laser for the data transfer via optical fibers.
A connection of NWs to each other further enhances the range of applications e.g. to the investigation of Majorana fermions [7], T-shaped FETs [9] and Hall measurements even on very thin NWs. Such two- or even three-dimensional structures are often grown by a two-step method involving the deposition of Au catalyst particles on existing NWs. This procedure results in "nanotrees" [75, 76, 77, 296]. Recently, the way to produce merged NWs changed. Individual NWs were grown with an angle different from 0° relative to the substrate normal [41, 157, 246]. These individual NW formed junctions during the growth. The growth method was only applied to Au-catalyzed NWs where Au may diffuse into the NW when they form the junction.
In this chapter, we demonstrate the possibility to integrate self-seeded NWs on Si (100) substrates and to form crossed NWs using the Au-free growth method.
Results presented in this chapter have been published in Ref. [263].

7.1. Nanowires on textured Si (100) substrates[1]

To integrate NWs like those presented in the previous chapters as future building blocks for (opto-)electronic devices, several requirements have to be fulfilled. The NW properties, e.g. dimension and crystalline structure, should be controllable and reproducible. Controlling the NW dimensions represents the most simple and most studied requirement, and the dimensions of both InAs and GaAs NWs are controllable over a wide range, see Sec. 4.1 and Refs. [55,

[1]Results of this section have been published in T. Rieger, D. Rosenbach, G. Mussler, T. Schäpers, D. Grützmacher, and M. I. Lepsa. *Simultaneous Integration of Different Nanowires on Single Textured Si (100) Substrates*. Nano Letters, 15(3):1979-1986, 2015. Ref. [263]. XRD pole figures were measured by Dr. Gregor Mussler. Most substrates were prepared by Daniel Rosenbach [267].

109, 127, 259]. The crystalline structure of VLS grown NWs is affected by the shape of the droplet and its supersaturation (see Sec. 4.3 and Refs. [182, 183, 345]). InAs NWs grown via the VS growth mechanism exhibit a change of the crystalline structure from a stacking fault rich structure (refer to Sec. 4.1.3) to twinned ZB due to the addition of Sb [288, 353]. In any case, the NWs should be grown on Si (100) substrates. III-V NWs are typically grown on (111) oriented substrates resulting in NWs being perpendicular to the substrate surface. Recently, a method to integrate NWs on (100) substrates using a SiO_2-nanotube template was demonstrated [33, 160]. This growth requires substantial preprocessing of the substrate. Other approaches to integrate NWs on (100) substrates make use of catalyst particles [89, 323], not being compatible with Si industry. Different semiconductor NWs integrated on the same chip are suitable to obtain both electronic and optic devices with engineered properties, e.g. high electron mobilities as well as optical emission at certain wavelengths. Here, different NWs refers to their dimensions (density, diameter or length), their doping (n- or p-type) or even different compositions, e.g. InAs for the electronic (e.g. FET [297] or TFET [303]) and GaAs for the optic component (e.g. LEDs [79] or lasers [210]). This requirement is in fact difficult to achieve.
In this section, the growth of self-assisted NWs on Si (100) substrates as well as the integration of NWs of different dimensions or composition on the same chip are addressed.

7.1.1. Substrate preparation

N-doped Si (100) substrates are cleaned in piranha solution and hydrofluoric acid [47]. Subsequently, the substrates are etched in solution based on potassium hydroxide (KOH), in order to obtain a textured surface [219, 290]. The KOH solution has a concentration of 1 weight % KOH and 10 vol % isopropanol alcohol. It is heated to 80°C. Etching the sample for 40 minutes in this solution produces pyramidal structures as depicted in Fig. 7.1a. The Si {100} planes are etched about 100 times faster than the {111} planes due to the anisotropic etchant KOH [276]. If the KOH concentration is low, the anisotropic etching produces µm-sized pyramids. The pyramids are bound by four {111} facets with a base width in the order of 5 – 10 µm and they are positioned arbitrary on the substrates. The facets of the pyramids are not atomically flat but exhibit a roughness with surface steps. The substrate can also be prepatterned using a silicon oxide or silicon nitride mask producing regular array of pyramids [88, 282] or grooves (see next section and Ref. [277]).

After the texturing process, the samples are wet chemically cleaned using piranha solution and hydrofluoric acid. A thin silicon oxide layer is obtained by a reoxidation in hydrogen peroxide (see Sec. 4.2.1). Subsequently, the samples are loaded into the MBE system. VLS GaAs and VS InAs NWs are grown at substrate temperatures of 600°C and 480°C, respectively. For GaAs NWs, the Ga rate is set to 0.1 µm/h with an As flux of 10^{-6} Torr. InAs NWs are grown with an In rate and As flux of 0.05 µm/h and 10^{-5} Torr, respectively. The substrates are either rotated or the rotation is stopped and the substrates are aligned to certain effusion cells as described in the corresponding sections. The general geometry is as follows: The angle between the {111} pyramidal side facets and the (100) substrate is 54.7°, thus NWs grown perpendicular on the side facets have an angle of 90°-54.7° = 35.3° with respect to the substrate. In our MBE system, the effusion cells are mounted such that they draw an angle of about 32° with the substrate normal. The entire growth geometry taking into account the geometry of the MBE system as well as the textured substrate is depicted in Fig. 7.1b. The In and As cells are mounted having an angle of 90° between them, while the angles between the Ga effusion cell and the In and As effusion cells are 45°.

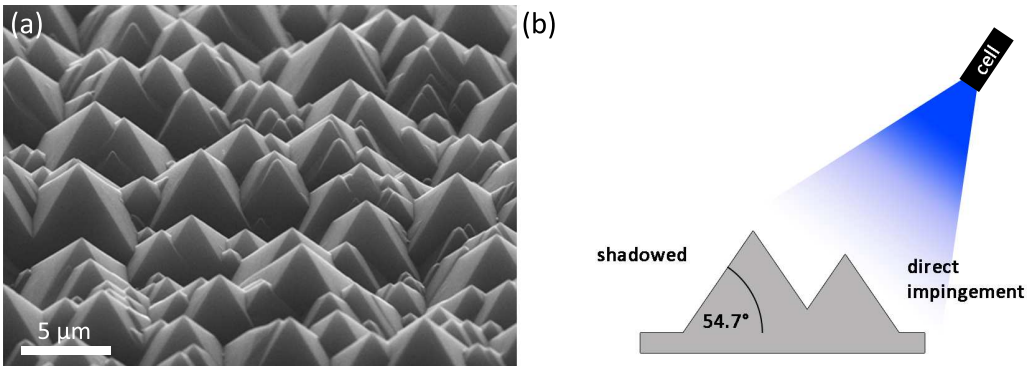

Figure 7.1.: *(a) The substrate surface after texturing a Si (100) sample with a KOH solution of 1 wt% KOH and 10 vol% isopropanol alcohol. (b) Schematic drawing of the MBE system and substrate considering the surface texturing process and the alignment of the effusion cell with respect to the substrate. Without substrate rotation, atoms from the effusion cell impinge directly on one facet while another facet of the pyramid is shadowed. Published in [263].*

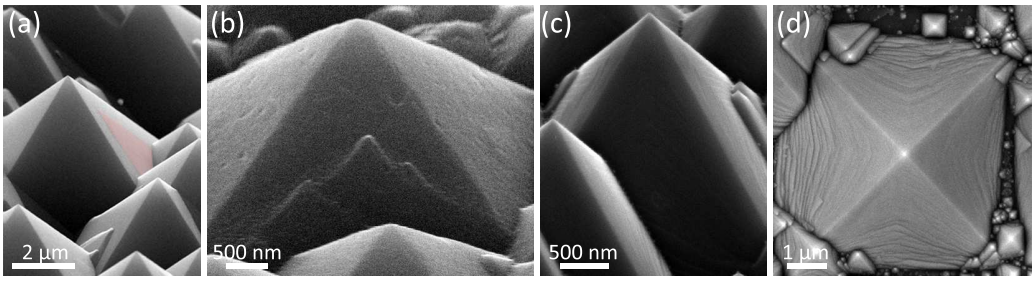

Figure 7.2.: *Surface steps on KOH-etched pyramids (a) Pyramid with a small "double pyramid" (red area). (b) Surface step bound by* {111} *and* {n11} *planes. (c,d) Surface steps bound by* {211} *planes. Published in the Supporting Information of [263].*

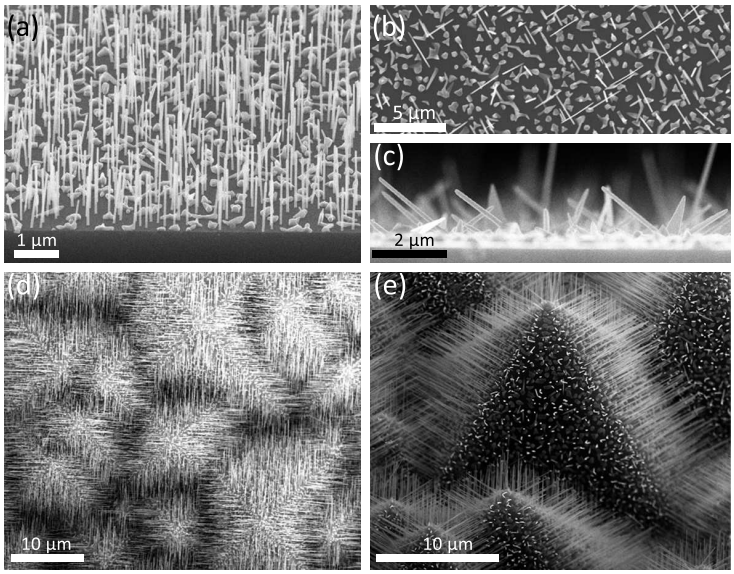

Figure 7.3: *SEM micrographs of InAs NWs grown on (a) Si (111) and (b,c) Si (100) substrates. On Si (111) substrates, NWs grow vertically while they are grown under an angle of 35.3° on (100) substrates. InAs NWs grown on the textured substrate are depicted in (d) and (e). The substrate was rotated during the growth. Published in [263].*

As mentioned above, the KOH etching does not always produce smooth surfaces. The KOH solution contains isopropanol alcohol in order to obtain surfaces as smooth as possible [354], though some roughness cannot be avoided. The roughness is not arbitrary but clear surface steps aligned along defined crystallographic directions are observed. In Fig. 7.2a, a surface step being bound by {111} planes is seen, a "double pyramid" is obtained. Figure 7.2b displays surface steps being bound by {111} as well as {n11} planes. A low concentration of isopropanol alcohol in the KOH solution leads to the formation of surface steps as observed in Fig. 7.2c,d. The surface steps are bound by {211} planes.

The results presented in the following focus on the growth of InAs on the textured substrates. Information about the growth of GaAs NWs are found in the Appendix A.5.

7.1.2. Growth of InAs nanowires on rotating textured substrates

Growing InAs NWs on (111)-oriented Si substrates results in a high density of vertically aligned NWs, as shown by the SEM image in Fig. 7.3a. Replacing the (111) Si substrate with a (100)-oriented one, the NW density is strongly reduced and the NWs are grown non-perpendicular to the substrate (see Fig 7.3b,c). The NW growth direction is still the ⟨111⟩ direction, but the NWs are distributed equally in all four ⟨111⟩ directions without any preferred orientation. When growth takes place on Si (100) substrates patterned with holes, the NW growth vanishes and instead, V-shaped membranes are obtained [57, 272]. Consequently, in order to integrate high density, well aligned self-assisted InAs NWs on (100) substrates, a different substrate preparation scheme is required. At this point, the texturing process described above comes into play. This exposes {111} facets on the (100) substrate.

A top view and a 60° tilted view SEM micrograph of InAs NWs grown on a textured Si substrate are displayed in Fig. 7.3d,e. The NWs are found to grow perpendicular to the side facets of the pyramids, i.e. along the ⟨111⟩ directions of the Si substrate. All facets are covered equally with NWs. As evident from the schematic in Fig. 7.1b, the flux impinges directly on the pyramid facet facing the effusion cell while the opposing facet is shadowed from the flux. The remaining two facets are arranged in such way that the incoming flux has a gracing incidence. A rotation of the sample with 10 rpm results in a homogeneous growth with equal NW densities and dimensions on all pyramidal facets, as visible in Fig. 7.3d,e. This is additionally evidenced

facet	In adatoms	As adatoms	NW density [NWμm^2]
A	direct impingement	grazing incidence	8.1 ± 1.9
B	grazing incidence	shadowed	6.9 ± 1.4
C	shadowed	grazing incidence	~ 0
D	grazing incidence	direct impingement	6.5 ± 0.8

Table 7.1.: *In and As adatom impingement and average NW densities on the different side facets of the pyramids when oriented as in Fig. 7.4a,b.*

by the XRD pole figure depicted in Fig. 7.4d displaying the InAs {111} Bragg peaks. The intensities of all four {111} peaks are identically.

7.1.3. Control of the InAs nanowire growth direction

When the substrate rotation is stopped, the direct flux impinging on one facet and the shadowed flux on another facet strongly affect the NW nucleation and growth. If the substrate is oriented as depicted in Fig. 7.4a,b, direct, shadowed as well as gracing incidence impingement of In and As atoms on the different facets are obtained as listed in Table 7.1. Different angles of adatom impingement as well as four different combinations thereof are present, allowing to study the impact of the adatom fluxes on the NW nucleation and growth within a single growth experiment.

SEM micrographs from the top as well as of all four pyramidal side facets are displayed in Fig. 7.4c. The In effusion cell faced the facet labeled *A* during growth, while the As effusion cell was oriented towards the facet *D*. As mentioned above, here, the substrate was not rotated during the growth. Accordingly, the adatom impingement is not uniform. The top view image already shows that NW growth takes place mainly on the facets *A*, *B* and *D* while growth seems to be absent on the facet labeled *C*. On this facet, the impingement of In atoms is shadowed while As atoms contribute via a grazing incidence. In some cases, single or few NWs are observed on the facet *C*. In that situation, most likely, the NW nucleation took place due to In diffusion on the Si substrate or secondary absorption processes [250, 259]. The adatom impingement is exactly reverse on the facet labeled *B*, i.e. it is shadowed from the As flux while In adatoms impinge with a grazing incidence. This configuration results in a high density of NWs on this pyramid facet. Comparing the results from the two facets B and C gives insights into the role of the adatoms in the nucleation process: a high flux of In atoms is required in order to nucleate NWs while the impact of As atoms on the nucleation rate is low. This is also supported by the pyramid facets *A* and *D*, having direct impingement of either In or As, respectively. The NW density on facet *A* is higher than on facet *D*. Apparently, the increased In flux arising from direct impingement results in an increase of the nucleation probability. Average NW densities measured on the different facets are given in Table 7.1. Interestingly, the different amounts of In and As atoms impinging on the substrate surface mainly influence the NW nucleation but not the growth rate: NWs on all pyramidal facets have almost the same lengths. For NWs nucleated on facets *B* and *D*, In adatom impingement is mainly on the side facets of the NWs while on facet *A* the In adatoms impinge only under a small angle on the NW side facet as well as directly on the top of the NWs. The diffusion length of In adatoms on the NW surface is in the order of 3 – 6 µm. Consequently, all In adatoms impinging on the NW surface can contribute to the axial growth [80, 202]. Due to a low In diffusion length on the silicon oxide [127], In adatoms impinging on the pyramid surface have only a small contribution to the axial growth. Changes arising from an increased shadowing of the silicon oxide surface can be neglected due to the

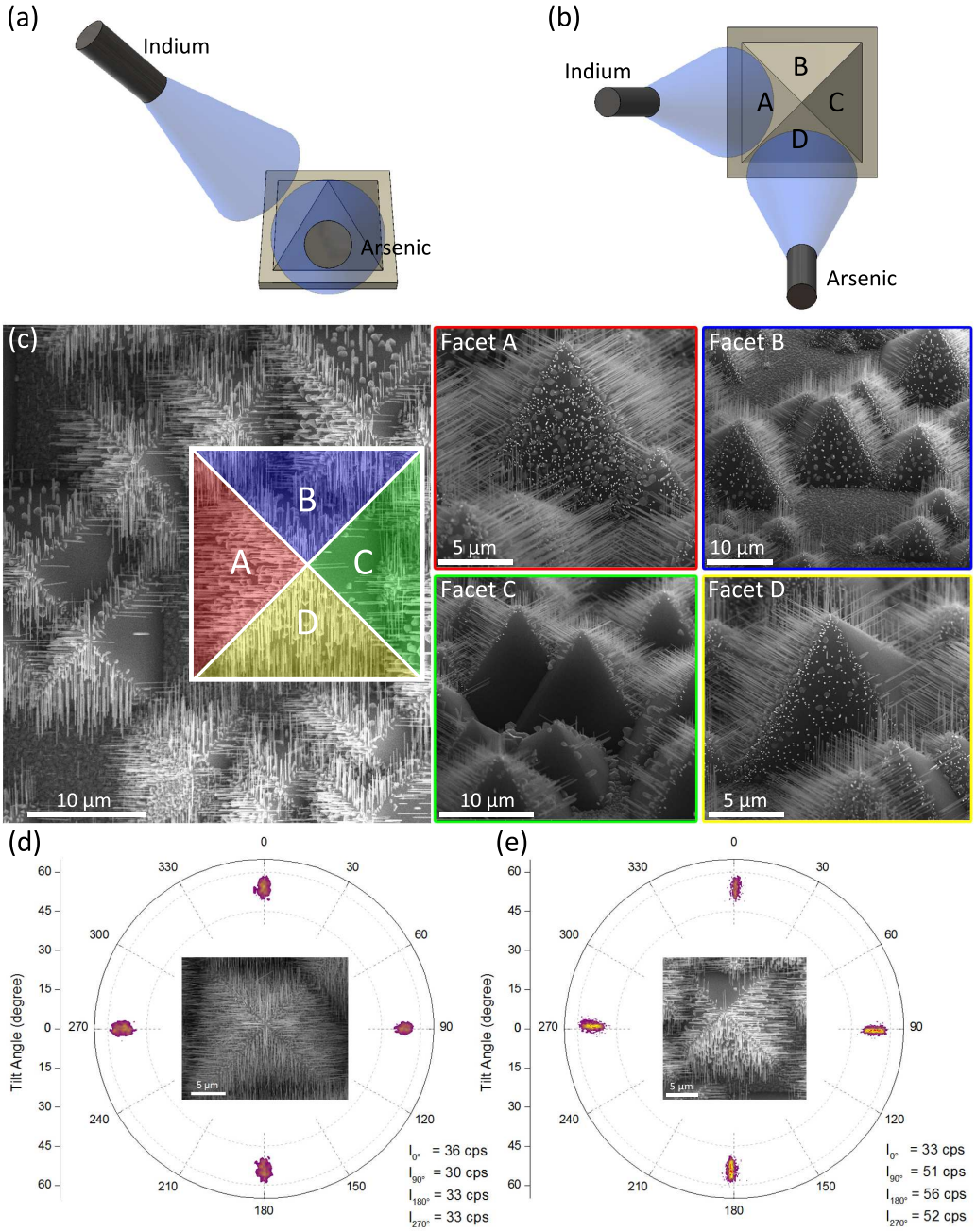

Figure 7.4.: *(a) Tilted view and (b) top-view schematic illustration of the pyramid alignment relative to the effusion cells when a pyramid facet faces an effusion cell. (c) SEM micrographs of InAs NWs grown on textured Si substrates without substrate rotation during growth. The sample was aligned as shown in Fig. 7.4a,b. The top view image includes a schematic overlay with the four different pyramidal side facets being color coded. Tilted view images of each side facets are shown and are framed by the corresponding color. (d,e) XRD pole figures of InAs NWs grown on a rotated substrate (d) and a substrate as aligned in Fig. 7.4a,b (e). Insets show the corresponding top view SEM micrographs. XRD measured were performed by Gregor Mussler. Published in [263].*

facet	In adatoms	As adatoms	NW density [NWμm^2]
A	direct impingement	grazing incidence	5.1 ± 1
B	grazing incidence	grazing incidence	0.4 ± 0.2
C	grazing incidence	direct impingement	1.5 ± 0.4
D	direct impingement	direct impingement	3.7 ± 0.7

Table 7.2.: *In and As adatom impingement and average NW densities on the different side facets of the pyramids when oriented as in Fig. 7.5a,b.*

small diffusion length. Thus, although the In adatom impingement on the NWs differ strongly, the NW lengths are equal.

The selective growth on predefined pyramid facets is further confirmed by a large scale analysis using XRD pole figure measurements depicted in Fig. 7.4d,e. The Bragg peaks corresponding to the InAs {111} reflections have almost the same intensities in three orientations (51 cps for 90°, 56 cps for 180° and 52 cps for 270°) while it is significantly lower in the other direction (33 cps for 0°). These different intensities can be correlated with the SEM micrograph depicted as an inset. The remaining intensity at 0° is mainly caused by parasitic growth on (100) facets in-between the pyramids and short ZB sections in the NWs. Pure ZB NWs would result in uniform intensities for all (111) reflections, but the VS InAs NWs used here have a high density of stacking faults, twin defects and WZ segments and therefore do not exhibit a pure ZB crystal structure (see Sec. 4.1.3). Consequently, mainly reflections from lattice planes perpendicular to the growth direction are observed, which are $(\overline{1}\overline{1}\overline{1})$B planes in the ZB crystal and $(000\overline{2})$B planes in the WZ crystal structure. The symmetry observed in a perfect zinc blende crystal lattice is vanished and the measured intensities indicate the amount of NWs grown on the corresponding facet of the pyramid. Consequently, also the XRD analysis indicates that the NW density on the facet with direct In impingement is higher than on those with grazing incidence.
The InAs NW growth is observed only on the pyramidal side facets and not on remaining Si (100) surfaces. This allows to grow InAs NWs selectively only on the exposed {111} facets of the Si substrate. Possibly, this difference in growth is caused by different Si oxide thicknesses on (111) and (100) surfaces.

The angle of adatom impingement and consequently also the NW growth and nucleation are changed by rotating the substrate by 45° with respect to the former investigation. In this alignment, one edge of the quadratic base of the pyramid is oriented towards the In effusion cell as schematically depicted in Fig. 7.5a,b. An overview of the adatom impingements is given in Table 7.2. A representative SEM micrograph from the top after NW growth is displayed in Fig. 7.5c. The NW density again depends strongly on the initial orientation of the substrate relative to the incoming fluxes and varies on all four pyramid facets. The NW lengths are still equal. The NW density gradually decreases from facet A to D to C to B as evident from Table 7.2. While the In flux impinges directly on the facets A and D, a grazing incidence of In adatoms is observed for the facets B and C. Due to the direct impingement of In adatoms and the corresponding higher In flux, the NW density increases as outlined before. The differences in the NW densities on the facet A and D, both with a direct impingement of As adatoms, are consequently correlated with the impingement of the As atoms: directly impinging As atoms result in a decrease of the NW density (facet D) compared to the grazing incidence of As adatoms (facet A). Thus, a too high As flux hinders the nucleation of NWs, probably due to a decrease of the In adatom diffusion lengths. On the facets B and C, where the In adatoms contribute

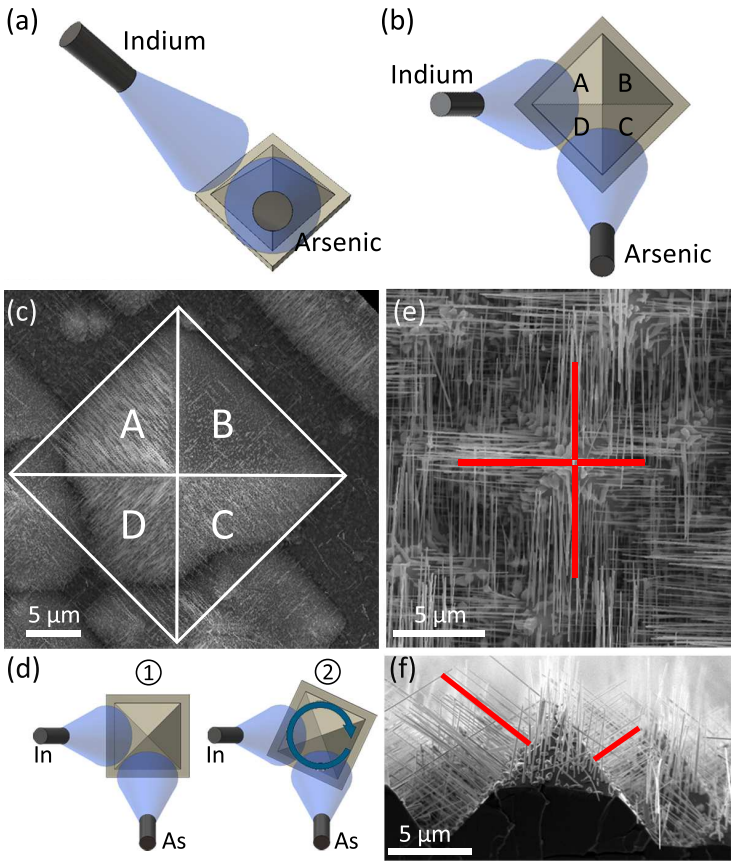

Figure 7.5: *(a) Tilted view and (b) top-view schematic illustration of the pyramid alignment relative to the effusion cells when a pyramid corner faces an effusion cell. (c) SEM micrograph of InAs NWs grown on a sample as aligned in Fig. 7.5a,b. NW growth proceeds mainly on two facets of the pyramid. (d) Schematic of the growth sequence used two obtain NWs of different length: first, one pyramid facet is aligned to the In cell and growth proceeds without substrate rotation. Subsequently, substrate rotation is started and growth continues. (e,f) Top view and side view SEM images of InAs NWs grown using the sequence shown in (d). Red lines indicate the average length of the NW on the side facets. Published in [263].*

via grazing incidence, the situation reverses: the NW density is higher for a direct impingement of As atoms (facet C) than a grazing incidence. Apparently, this indicates a complex interplay between In and As adatoms during the NW nucleation where not only the absolute fluxes but also the V/III influence the NW density.

Using the surface texturing process in combination with the directed fluxes available in the MBE enables the integration of high density InAs NWs on Si (100) substrates and controlling their growth direction as well as their local density as presented above. A combination of the NW growth on non-rotating as well as rotating substrates even allows to obtain NWs with different lengths on the different pyramidal facets. This is demonstrated by the SEM micrograph displayed in Fig. 7.5e,f. The NW growth proceeds as shown schematically in Fig. 7.5d and was initiated by orienting one pyramid side facet towards the In effusion cell. The opposing facet was shadowed from the In flux. InAs was grown for 2.5h without rotating the substrate, resulting in NWs grown on three pyramidal facets. Subsequently, the substrate rotation was started and growth continued for another 2.5h. A rotation of the substrate distributes the In adatoms equally on all pyramid facets and NW nucleation takes place on the previously shadowed facet. The already existing NWs continue growing. Consequently, short NWs are expected on the initially shadowed facet while they should be substantially longer on the other three facets. This is exactly the situation shown in Fig. 7.5e,f as indicated by the red lines denoting the average NW lengths. The NW lengths differ roughly by a factor of two, reflecting exactly the difference in growth time. Varying not only the substrate rotation but also the growth parameters, this technique opens the way to locally control the NW dimensions, i.e. both NW length and diameter.

Similar growth characteristics are also obtained by the VLS growth of self-catalyzed GaAs

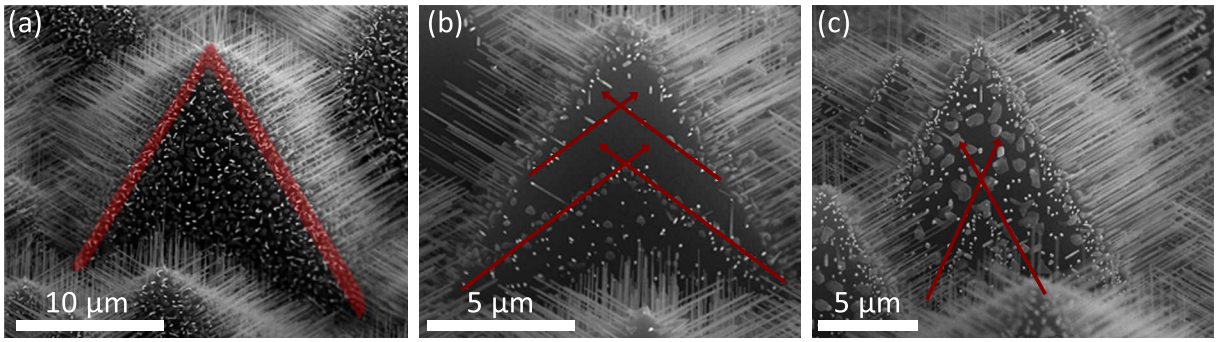

Figure 7.6.: *Self-alignment of InAs NWs on pyramidal side facets. (a) Increased NW density at the pyramid edges. NWs aligned along* ⟨111⟩ *directions/*{211} *planes (b) and* ⟨112⟩ *directions /*{111} *planes (c) of the pyramid side facets. The red region in (a) marks the increased NW density close to the edge of the facets. The red lines in (b) and (c) indicate the preferred alignment of NWs along certain directions on the pyramid side facets. Published in [263].*

NWs on textured Si substrates: Ga droplets and consequently also GaAs NWs are not present when the pyramidal facet is shadowed from the Ga flux. The NW lengths differ on the pyramidal side facets, being dependent on the angle of As impingement. This proves that the As flux controls the GaAs NW growth rate, identical as reported in the literature [55, 250, 259]. The NW diameter as well as the tapering are mainly defined by the Ga flux [55, 259]. When one edge of the pyramid is aligned to the Ga effusion cell, the necessity of high As fluxes to obtain a high yield of vertical GaAs NWs on Si 111 facets is obvious[273]. High Ga fluxes increase the parasitic growth in-between the NWs. GaAs NWs grown with four different growth conditions can be achieved on the very same sample within close vicinity, allowing to study their impact in a single experiment. For the sake of completeness, the analyzes of the growth of GaAs NWs on textured Si substrates is presented in detail in the Appendix A.5.
The presented results prove the capability of textured substrates to investigate the nucleation and growth of nanostructures.

7.1.4. Nanowire self-alignment

The InAs NWs are found to grow at preferential nucleation sites on the pyramidal side facets. The preferential alignment is seen in the SEM images in Fig. 7.6a-c. In Fig. 7.6a, a common feature is observed: the NW density close to the edges of the side facets is higher than in the center. Similar characteristics are also found in Fig. 7.3e and Fig. 7.4c. The increase of the NW density is observed within an area about 1 µm from the edge. A possible explanation for the observation is the diffusion of In adatoms on silicon oxide. Hertenberger *et al.* estimated the diffusion length to be 750 nm at 480°C [127], that is a similar range. Adatom diffusion towards the edges increases the effective amount of In atoms which in turn increases the nucleation probability as already described above. The assumption of In diffusion towards the edges requires that the pyramid edges act as a sink for the In atoms. An alternative explanation is that the surface properties of the pyramid near the edges are different favoring the nucleation of NWs. Such differences may e.g. arise from the texturing or reoxidation process prior to the growth and affect the roughness or oxide thickness. As shown in Secs. 4.1, 4.2.1 and Ref. [202], the oxide thickness has a strong impact on the NW density.
The second type of preferred nucleation site is exemplary displayed in Fig. 7.6b,c. NWs are aligned along certain directions/planes on the side faces of the pyramid. These are either the ⟨112⟩ directions/{111} planes or ⟨111⟩ directions/{211} planes. The alignment of NWs along

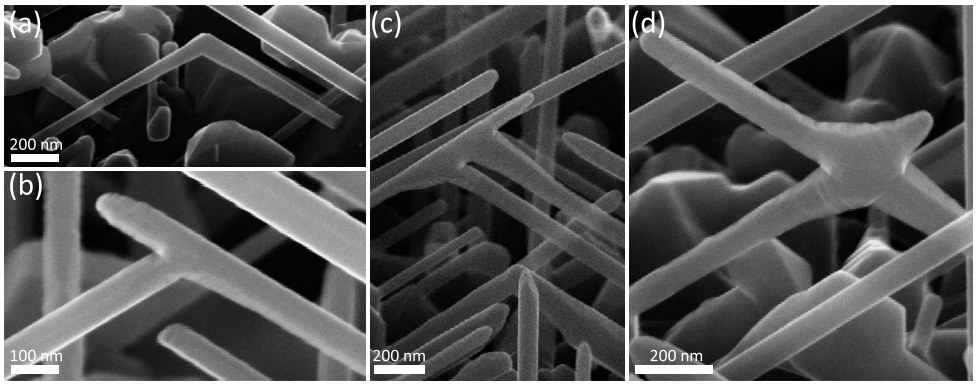

Figure 7.7.: *InAs NW junctions grown on textured Si (100) substrates. (a) L-shaped junction. (b) T-shaped junction. (c)* Π*-shaped junction. (d) X-shaped junction.*

these directions is not observed on all pyramidal facets. Consequently, the preferred nucleation sites are expected to be caused by the texturing process. The KOH etching induces surface steps. Exemplary SEM images showing such surface steps have been presented in Fig. 7.2. "Double pyramids" are easily created during the KOH etching process. These exhibit steps along the {111} planes and result in an alignment similar as depicted in Fig. 7.6a. Steps along the {211} planes are observed especially when only a low amount of isopropyl alcohol was added to the KOH solution. Isopropyl alcohol improves the smoothness of the etched pyramidal facets [354]. Nonetheless, some surface steps may still be present on the pyramids. The preferred nucleation of NWs along the certain directions of the Si pyramids is therefore caused by surface steps which also represent edges. Consequently, the alignment of NWs along the ⟨112⟩ and ⟨111⟩ directions is similar to the increased NW density at the pyramid edges discussed above.
The self-alignment of NWs at surface steps opens the way to an easy alignment procedure for NWs making use of etched steps on the surface rather than any hole pattern in order to predefine the nucleation sites.

7.1.5. Nanowire connections

When two NWs with different growth directions nucleate on opposing or neighboring facets of the pyramids, they can coalesce during the axial or radial growth and form NW junctions. Due to the arbitrary positioned pyramids the density of these junctions is low. A selection of different NW junction geometries is shown in Fig. 7.7. Typically, three different structures are observed, being an L-shaped NW junction (Fig. 7.7a), a T-shaped NW junction (Fig. 7.7b) and an X-shaped NW junction (Fig. 7.7d). In the L-shaped structure, any NW tips are absent resulting in the fact that the NW lengths do not increase anymore, rather the involved NWs grow radially. In the T- and X-shaped junctions, the tips of one or both NWs remain, allowing that the axial NW growth proceeds. Certainly, also more complex structures such as that one shown in Fig. 7.7c develop. It has a Π-like shape where two NWs nucleated on the same pyramid facet hit another NW.
The density of these NW junctions is too low for practical usage and they do not grow in a controlled way. Both are optimized when prepatterned substrates e.g. with V-grooves are used. This procedure is described in Section 7.2.

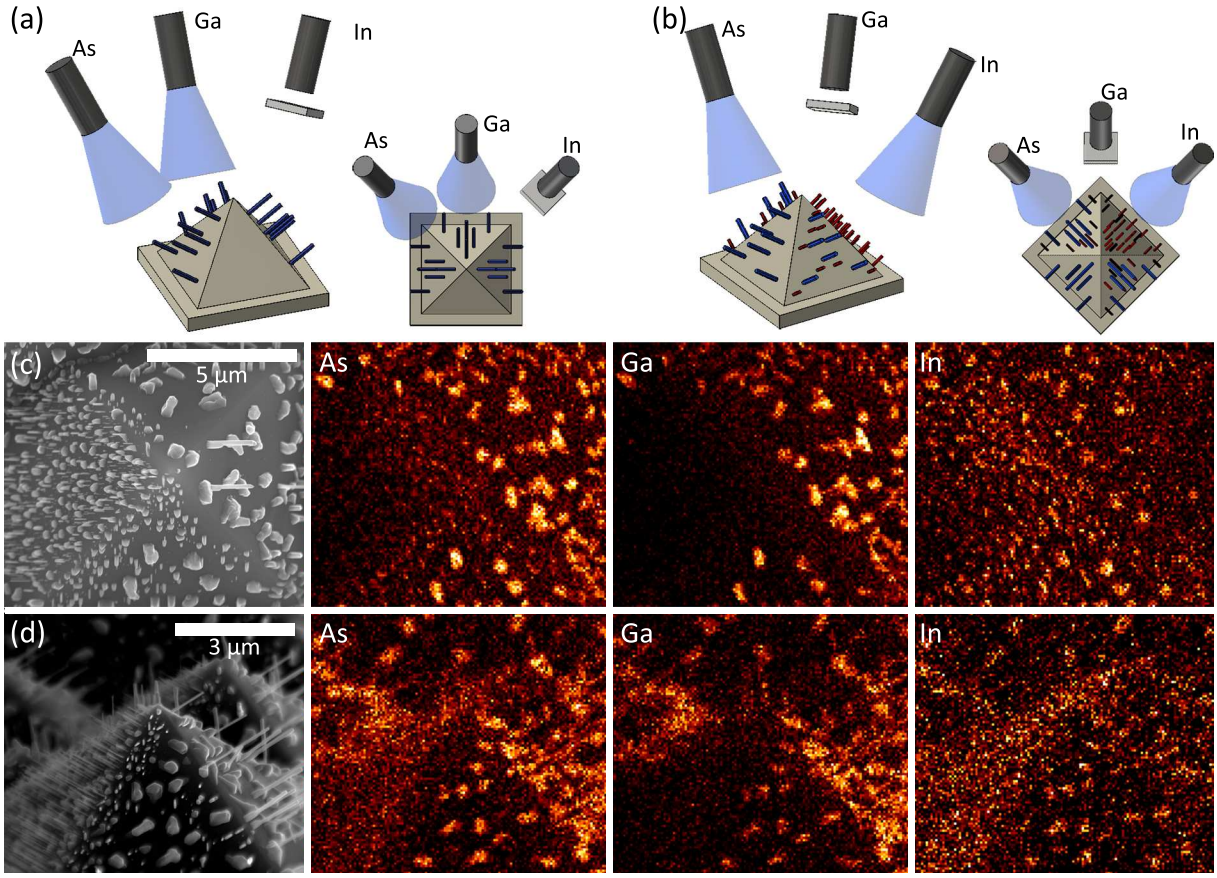

Figure 7.8.: *(a,b) Schematic drawings for the growth of both GaAs (blue) and InAs (red) NWs on the same sample. (a) Alignment of one pyramid facet towards the Ga effusion cell and growth of GaAs NWs. (b) Subsequent rotation of the substrate such that the bare facet of the pyramid is oriented towards the In effusion cell. (c,d) SEM micrographs and EDX maps from the top and from the side of the sample taken after the growth of both GaAs and InAs NWs. Published in [263].*

7.1.6. Simultaneous integration of different nanowires on one substrate

Using textured substrates, it was demonstrated that NW growth takes place preferentially on {111} facets and that the NW growth direction is controlled by the usage of directed fluxes. Furthermore, InAs NWs with different dimensions were grown on the same substrates. This technique not only enables the integration of III-V semiconductor NWs on (100) Si substrates but also provides a basis to study the impact of growth parameters within a single experiment.

The variability and potential of the growth on textured substrates is further demonstrated by an experiment for the integration of different III-V NWs on a single textured sample. For this experiment, a textured Si substrate is aligned with one pyramid facet facing the Ga effusion cell. GaAs NWs are grown in a self-catalyzed manner for 45 min at 600°C without rotating the substrate. Due to the directed flux, GaAs NWs grow only on three facets of the pyramid (see schematic in Fig. 7.8a). Subsequent to the consumption of the catalyzing Ga droplet, the substrate temperature is decreased to 480°C. The bare side of the pyramid is aligned to the In effusion cell (see schematic in Fig. 7.8b) and InAs NW are grown for 30 min without rotating the substrate. The directed flux of the group III atoms results in a growth on selected facets only.

Figure 7.8c,d shows SEM micrographs as well as EDX maps acquired in the SEM. Two different types of NWs are identified: thick and low density GaAs NWs as well as a high density of thin InAs NWs. As evident from the EDX maps, Ga is only found on three pyramid facets, while one facet is entirely free of Ga. Indium is detected on all pyramid facets, but it is mainly present on three facets. The lowest amount of In is found on the pyramid facet being shadowed from the incident In flux. Detailed SEM and EDX analyses of this pyramid facet shows that InAs is grown either in the form of crystallites or at the bottom of existing GaAs NWs. When grown at the bottom of the NWs, associated defects shall hinder the device performance. Most reasonable, the GaAs NWs collect some of the In adatoms. The GaAs NWs are not shadowed from the incoming In flux due to the relatively low angle of the incident fluxes ($\sim 32°$ relative to the substrate normal). A MBE system with a larger angle of the incoming flux shall give rise to shadowed GaAs NWs and allow the defect-free growth of both GaAs and InAs NWs on one and the same sample. In fact, in the Omicron Pro100 MBE installed at the "Nanocluster" the angle of the incoming flux is 42° instead of 32°.
As evident from the EDX maps in Fig. 7.8c,d, the presented growth sequence produces InAs NWs on one pyramid facet as well as GaAs NWs on the opposing facet. On the remaining two facets of the pyramid, both InAs NWs as well as GaAs NWs partially covered with InAs are found. By optimizing the substrate preparation, i.e. producing V-grooves, only two opposing {111} facets remain and therefore the presence of NWs composed of different alloys on the same {111} facet should be avoided.

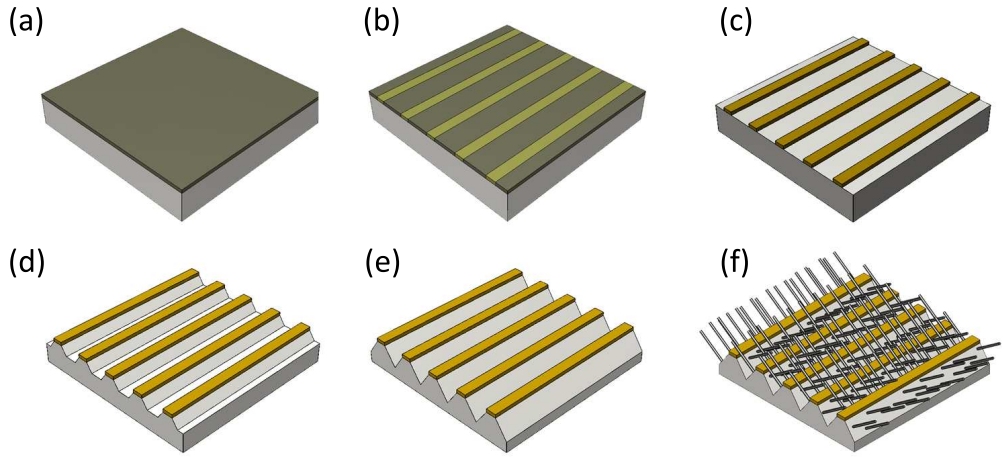

Figure 7.9.: *Schematic of the substrate preparation for V-grooves on silicon (100) substrates including the NW growth. (a) Si substrate covered by HSQ. (b) e-beam lithography. (c) Development and hard bake of HSQ. (d,e) KOH etching. (f) NW growth.*

7.2. Merged nanowires grown on V-grooves[2]

In the previous section, a texturing process of Si substrates was used for the growth of NWs on (100) Si substrates but certainly, the pyramids were positioned arbitrary not allowing to control the NW position on the substrate. Position controlled growth can be achieved by positioning either pyramids or V-grooves in a controlled manner on the substrate [88, 277, 282].
When NWs are grown on such V-grooves, NWs nucleated on opposing facets can merge during the growth forming junctions, similar as it was also shown in Sec. 7.1.5. Merged NWs are required for the braiding of Majorana fermions [7] but can e.g. also be used for T-shaped transistors [9], to determine the carrier concentration via the Hall effect or to form NW networks. Merged NWs make Hall measurements on NWs easier since the required overlay accuracy for lateral contacting decreases [26]. The morphology, growth mechanism and crystal structure of NW junctions represents a very interesting aspect. Merged NWs reported in literature are grown via Au catalyst particles and coalescence of two separate NWs [41, 157, 246]. An alternative way is the growth of NW trees, i.e. the growth of Au cataylzed NWs on already existing NWs [75, 76]. Merged NWs and NW networks obtained without the use of external catalyst have not yet been investigated.

7.2.1. Substrate preparation

The structuring of the Si substrate with V-grooves is schematically depicted in Fig. 7.9. (100) oriented Si substrates are covered by a $\sim$ 200 nm thick hydrogen silsesquioxane (HSQ) layer. The HSQ layer is deposited by spin coating and has two functions: first, it is used as a negative-tone e-beam resist and secondly, as an etch mask. Lines and spaces of various dimensions are written into the HSQ layer by electron beam lithography. Subsequently, the structure is developed using MF^{TM}CD-26. Prior to the KOH etching, the samples are hard baked for 4h at 450°C. This thermal curing significantly enhances the etch resistance of the HSQ [52, 349] and is found to be mandatory. If not hard baked, the HSQ layer is removed within a few seconds when placed in the KOH etch solution. Following the hard bake, the samples are etched in a solution containing

[2]Electrical measurements were performed by Daniel Rosenbach and Sebastian Heedt. Sebastian Heedt and Daniel Rosenbach assisted in the preparation of the V-grooves.

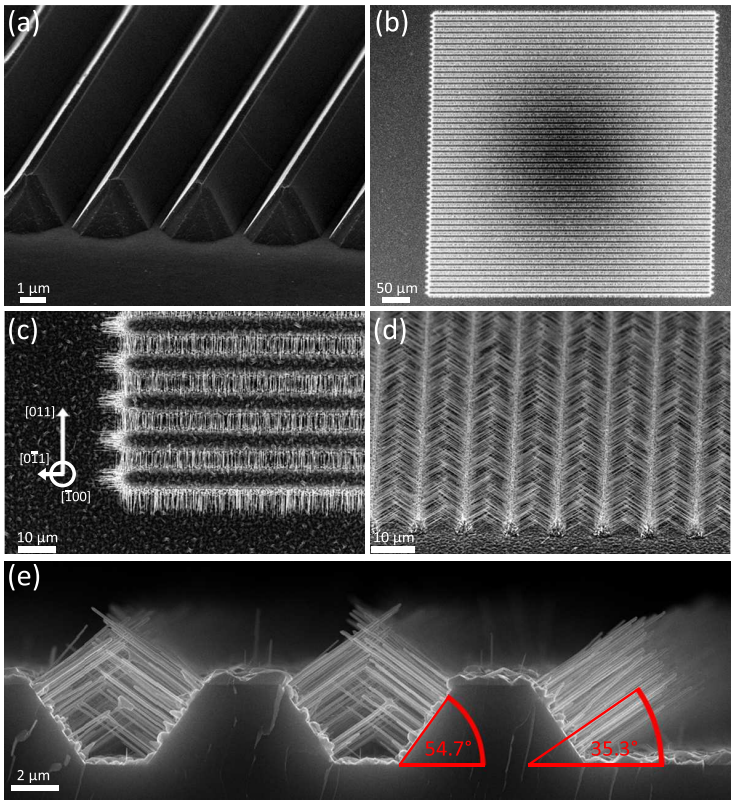

Figure 7.10: *SEM micrographs of the textured substrate (a) prior to and (b-e) after the NW growth. (a) displays a tilted view SEM image o the V-grooves. (b) shows a top view image of a field of lines and spaces, in (c) the lower left corner of the field is shown in higher magnification. NWs are only grown on the V-grooves while NW growth is absent on the remaining (100) facets. A tilted view SEM micrograph is depicted in (d), proving that the NWs grow only perpendicular to the* {111} *side facets of the V-grooves. (e) Cross-sectional view of the V-groove pattern with InAs NWs being grown on the* {111} *side facets of the grooves. The dark area in the center of (b) is an artifact of the image acquisition.*

33 wt % KOH and 7 vol % IPA. The solution is heated to 40°C, the etching time is 40 min. The surface of the substrates after the etching is schematically depicted in Fig. 7.9d,e, a SEM micrograph is shown in Fig. 7.10a. The anisotropic KOH etching produces V-grooves due to a higher etch rate of the Si {100} facets than the Si {111} facets. The {111} side facets of the grooves draw an angle of 54.7° with respect to the substrate. Residuals created during the KOH etching are removed with diluted HCl and piranha solution [223]. For the final substrate preparation before the NW growth, the native oxide is removed by diluted HF and H_2O_2 is used to rebuild a thin silicon oxide.

After loading into the MBE system, InAs NWs are grown at a substrate temperature of 490°C via the VS growth mechanism with an In rate of 0.05 µm/h and an As_4 flux of 10^{-5} Torr. These are the parameters typically used for the vapor solid growth of InAs NWs, see Secs. 4.1 and 4.2.1 .

7.2.2. Nanowire growth on V-grooves

Figure 7.10b displays a top view SEM image of a field of lines and spaces after NW growth, a higher resolution image of a corner of the field is displayed in Fig. 7.10c. A perfect alignment of the NWs at the V-grooves is seen, thus the NWs align only in [011] and [0$\bar{1}\bar{1}$] directions, except for the ends of the lines where the NWs also align in the [0$\bar{1}$1] and [01$\bar{1}$] directions. The tilted view SEM image shown in Fig. 7.10d demonstrates that the InAs NWs grow perpendicular to the {111} side facets of the V-grooves, thus they follow the ⟨111⟩ directions of the Si substrate. The NWs draw an angle of 35.3° with respect to the (100) surface, as evident from the cross sectional image in Fig. 7.10e. NWs are only observed on the {111} facets while they are not found on the remaining (100) facets. The same characteristic was also observed for the growth of InAs NWs on textured substrates presented in the previous section. The NWs have a uniform

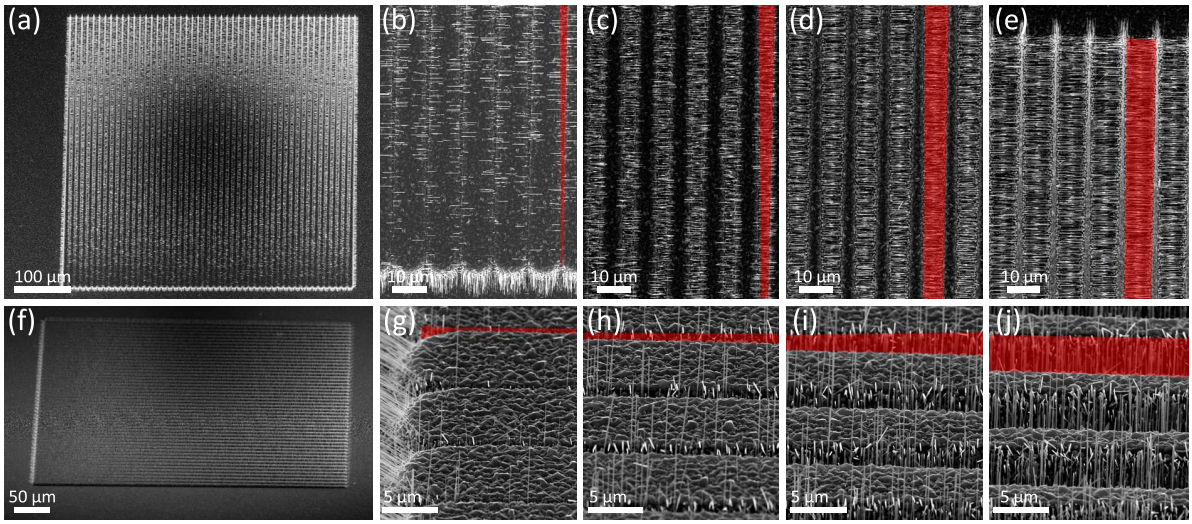

Figure 7.11.: *SEM micrographs of NWs grown in V-grooves with varying pitch. The pitch varies between 200 nm and 10 µm. (a, f) top and tilted view image of the entire structure. (b-e) top view images of higher magnification. (g-j) tilted view images of higher magnification. The pitch increases from b (g) to e (j). The larger the pitch and the size of the* {111} *facets, the higher the NW density. The red overlays indicate the dimensions of the grooves.*

and good alignment, i.e. all NWs grow perpendicular to their particular Si {111} facet. On etched (100) surfaces at the bottom of the grooves or formerly protected (100) surfaces at the top of the V-grooves, only crystallites are observed.
In fact, this demonstrates that the NWs grown on textured substrates presented in the previous section can be grown in a controlled manner on Si substrates by producing V-grooves. This opens the way to a position controlled growth of different semiconductor NWs on Si (100) substrates.

From Fig. 7.10e it is already evident that NWs grown on opposing V-groove facets have a certain probability to touch each other in the center of the groove. Due to the non-polar Si substrate the alignment of the V-grooves is not crucial, thus it does not matter whether they are bound by $(11\overline{1})$ and $(1\overline{1}1)$ facets or by $(1\overline{11})$ and (111) facets. NWs grow on all facets similarly, since only the NW nucleus defines the ⟨111⟩B NW growth direction. This is different for III-V substrates where V-grooves would either be bound by A-facets ($(1\overline{11})$ and (111)) or B-facets ($(11\overline{1})$ and $(1\overline{1}1)$). For a potential future integration of NWs grown on Si substrates, this provides a higher degree of freedom in the growth of NWs and therefore the alignment of devices. Concerning merged III-V NWs it is important that the NWs grow on opposing {111} facets and not on neighboring ones ($(1\overline{11})$ and $(11\overline{1})$, e.g. in inverted pyramids). Growth on opposing facets produces junctions with an angle of 109.47° between their nuclei, being the angle between two ⟨111⟩B directions in a perfect ZB crystal. In the other case (growth on neighboring facets, e.g. $(1\overline{11})$ and $(11\overline{1})$ facets), the angle between the nuclei is 70.53° which is the angle between a ⟨111⟩B and a ⟨111⟩A direction in a perfect ZB lattice. Since the NW growth always proceeds in ⟨111⟩B direction, this certainly produces an anti-phase boundary between the NWs. In order to obtain a high yield of NW junctions, the probability that NWs grown on opposing facets are facing each other needs to be high. This probability is partly influenced by the growth parameters, allowing to tailor the NW density, but much more by the dimensions of the grooves. The impact of the groove pattern is evident from the SEM micrographs depicted in Fig. 7.11. Here, the width of the "spaces" is varied between 200 nm and 10 µm with steps of 200 nm. After the KOH etching, V-grooves are obtained for small "spaces" while larger "spaces" result in incomplete V-grooves with residual (100) facets at the bottom. Accordingly, first the size of

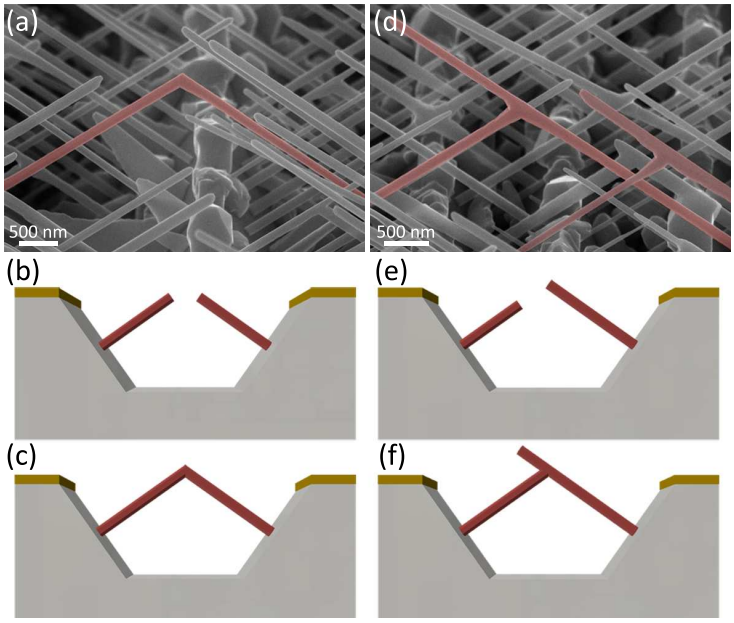

Figure 7.12: *NW junctions with two (a) and three (d) arms. The junction in (a) forms an L-shape and is caused by the coalescence of two NW tips as schematically depicted in (b) and (c). Consequently this junction is a tip-to-tip junction. The junction in (d) is created when a NW tip coalesces with the side facet of another NW, thus a tip-to-side junction. It has a T-shape.*

the {111} facets increases and subsequently, the size of the {111} facets remains constant but their distance increases for fixed etching times. SEM micrographs from the top (a-e) as well as acquired under an angle of 60° (f-j) are shown in Fig. 7.11. The width of the "spaces" increases from b-e and g-j, respectively. As seen, small spaces and corresponding small {111} facets result only in a few NWs having the same lateral position inside the grooves. Accordingly, NW junctions are not obtained. With increasing width of the spaces, the number of NWs obtained per unit length increases. This is associated with the increase of the size of the {111} facets. When the NW density per unit length increases, the probability of two NWs facing each other increases and, apparently, also the number of NW junctions is enhanced. At this point, the number of NW junctions is no longer limited by the number of NWs per unit length but by the distance between the NW nuclei, i.e. the required lengths of the NWs to form a junction. This necessary (mean) NW length depends on the width of the spaces and the etching depth. The larger the width of the spaces and the lower the etching depth, the larger the required NW length.

NWs grown on the opposing facet of the V-groove influence the NW growth due to shadowing and competition. This is seen in the cross sectional image depicted in Fig. 7.10e. The NWs grown on the right-most {111} facet, being the last {111} facet of the pattern, have a uniform length. For the NWs on the other {111} facets this is different: the NWs have the highest length when grown at the upper part of the groove while the length decreases by $\sim 50\%$ for NWs at the bottom of the groove. This non-uniformity is due to the NWs grown on the opposing facet, since the NWs have uniform dimensions when grown without an opposing facet nearby. Actually, not only the NW length decreases towards the bottom of the groove but also the NW diameter.

Consequently, it exists an optimal pattern to obtain a high density of NW junctions. Based on experimental investigations, spaces with a width in the range from 1 – 5 µm and an etching depth of about 2 – 3 µm result in high density NW junctions. V-grooves with a subsequently produced SiO_2 mask with holes shall significantly enhance the yield of NW junctions to about 100 %. However, this requires substantial more processing and NWs grown in such hole patterns typically have a larger diameter, see Ref. [127].

7.2.3. Formation of nanowire junctions

Three NW junctions in different shapes are found: L-shape (Fig. 7.12a), T-shape (Fig. 7.12d) X-shape (Fig. 7.13a,b). Apart from these three basic structures, also more sophisticated structures are observed which represent combinations of the basic structures. The three basic structures are described in the following:

1. **L-shaped junctions:** The first shape of the NW junctions is shown in Fig. 7.12a. It has roughly the shape of an "L". The evolution of the NW junction is depicted schematically in Fig. 7.12b,c. The NWs are nucleated on opposing {111} facets and the coalescence takes place between the tips of both NWs. The growth fronts of both NWs vanish and further growth is only a radial growth. The NWs do not elongate anymore. This junction can also be called "tip-to-tip" junction.

2. **T-shaped junctions:** If the tip of one NW touches the side facets of another NW and coalescence occurs, the NW junction has a T-shape. This situation is depicted in Fig. 7.12e,f. In this configuration, the growth front of one NW vanishes due to the coalescence while the growth front of the second NW remains. Thus, one NW continues growing axially. The junction is a "tip-to-side" junction.

3. **X-shaped junctions:** The last structure is obtained by the coalescence of neighboring NWs due to radial growth. A detailed side view SEM micrograph of the junction is shown in Fig. 7.13b. Its top view image is depicted in Fig. 7.13d. The NWs are slightly displaced and radial growth took place at the connection point. The situation before coalescence is displayed in Fig. 7.13c: two NWs initially grow slightly displaced to each other without coalescence. A schematic model for the formation of X-shaped NW junctions is shown in Fig. 7.13e,f. First, NWs grow slightly displaced on opposing side facets, neither the tips coalesce during growth nor a tip coalesces with a NW side facet. Proceeding growth of the NWs takes place both axially and radially. Subsequently, the two NWs coalesce due to radial growth. As observed in the SEM images from the side and from the top, the interface between both NWs seems to act as a sink for the adatoms, i.e. a preferred place for the radial growth. Since this NW junction is formed by radial growth of the NW side facets, it is called "side-to-side" junction. Both NWs can expand axially after the coalescence. This growth mechanism for X-shaped NW junctions is identical to that one presented by Car *et al.* [41] where InSb-based NWs are grown by MOVPE on prepatterned substrates. There, the pattern is made in such way that the catalyzing Au droplets are slightly misaligned giving rise to two separate NWs in close proximity. Coalescence into one X-shaped NW occurs due to radial growth.

For all three junctions, the angle between the arms are 109.47° which is the angle between the ⟨111⟩B directions. The merged areas often shows an increased roughness or an increase of the diameter, see Fig. 7.12b.
As obvious, the three different junctions can be classified into two groups. The first group contains the L- and T-shaped junctions. For both junctions, at least one NW tip plays an active role during the formation of the junction. The entire structures of the L- and T-shaped junctions are in one plane. The X-shaped junctions form the second group. These NW junctions are not perfectly in one plane, they do not lie absolutely flat on the substrate after transfer. This can make the contacting of the structures difficult. To enhance the number of T-shaped junctions, a growth sequence similar as presented in the previous section can be applied: the NW growth is initiated without a substrate rotation which produces NWs on only one Si {111} facet of the

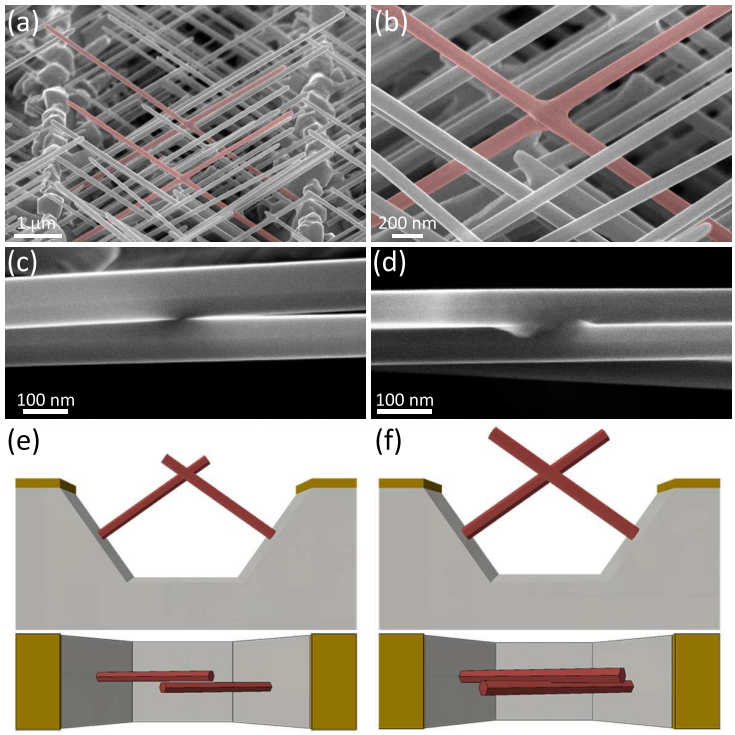

Figure 7.13: *SEM images and model of X-shaped NW junctions. (a,b) Tilted view SEM micrographs demonstrating the three dimensional character. (c) Top view image of two NWs close to each other before coalescence. (d) Top view image of two NWs after coalescence. (e,f) Schematic of the formation mechanism of X-shaped NW junctions. First, two NWs grown on opposing facets of the V-grooves grow close to each other without coalescence of the tips (e). Subsequently, radial growth takes place resulting in coalescence of both NWs (f).*

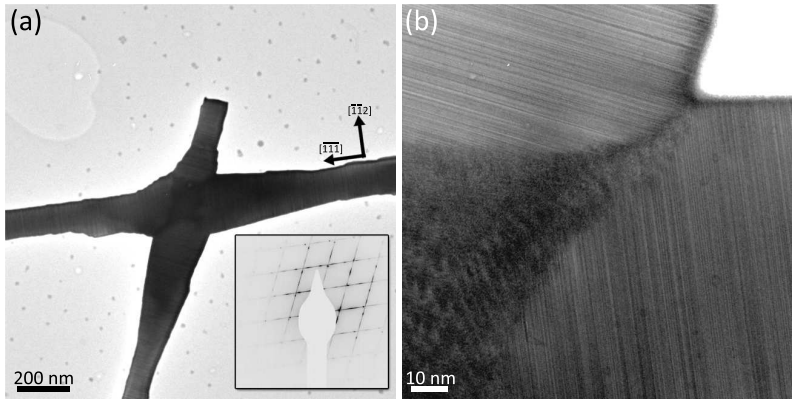

Figure 7.14: *TEM micrographs of an X-shaped NW junction. (a) Low resolution image evidencing an increased thickness around the junction. The inset displays the diffraction pattern of the NW (inverted colors). (b) High resolution TEM image of the X-shaped junction. A Moiré pattern is observed, indicating two crystal structures with different orientations.*

V-groove while the opposing facet of the V-groove is free of NWs. After starting the rotation of the substrate, NWs also start to grow on the opposing facet. The difference in NW length then increases the yield of T-shaped junctions.

7.2.4. Crystal structure of InAs nanowire junctions

The crystal structure of the NW junctions is expected to have an impact on the electrical and optical properties since not only stacking faults and twins are present but also grain boundaries may occur. Single crystalline NW junctions can only be obtained in ZB NWs since the ZB crystal structure contains four equivalent ⟨111⟩B directions. In the WZ phase, the NW growth direction is [0001]B. This direction is present only once in the WZ crystal. Consequently, NW junctions from Au catalyzed WZ InAs NWs have the ZB crystal structure in the junction despite of the WZ phase in the remaining NW [157]. VS grown InAs NWs typically contain a high density of stacking faults and twins, as it was shown in Sec. 4.1.3. The relatively high growth temperature of VS grown InAs NWs together with the completely different growth and formation mechanism of the junctions may have a strong impact on the crystalline structure of NW junctions.

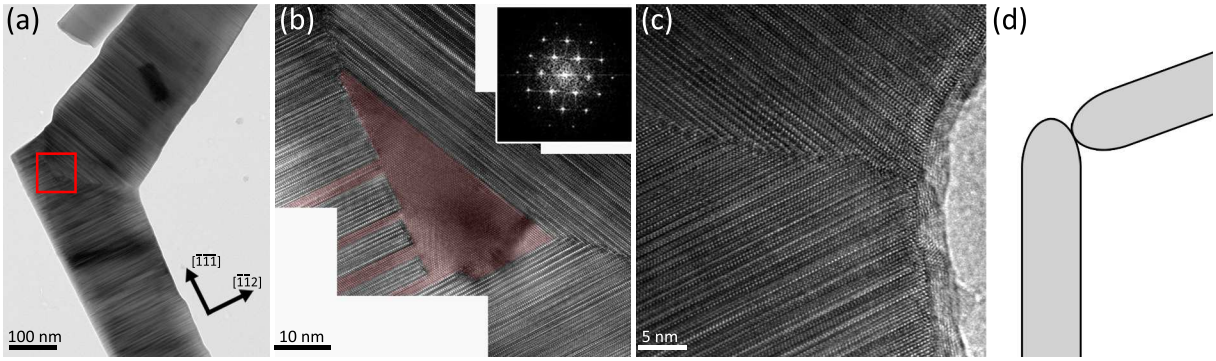

Figure 7.15.: *TEM images of an L-shaped NW junction. (a) Low resolution image. (b) High resolution image of the central part of the junction having ZB crystal structure (red overlay). (c) High resolution image of the outer part of the junction between both NWs. (d) Schematic illustration of the formation of the junction.*

Figure 7.14a depicts a low resolution TEM image of an X-shaped junction and its diffraction pattern as an inset. The NWs exhibit an increased roughness in close proximity to the junction as well as increased NW diameter. The diffraction pattern reveals two streaky patterns rotated by $\sim 110°$, being close to the ideal value of 109.5° between two $\langle 111 \rangle$B directions. The streaky patterns are a clear indication for a high density of stacking faults and twins, being typical for VS growth of InAs NWs but they do not provide information about the crystal structure of the junction. This is caused by the fact that an area of at least 200 nm in diameter is used to obtain the diffraction pattern. The crystal structure of the junction is seen in the higher resolution TEM image shown in Fig. 7.14b. The two arms of the NW junction contain several stacking faults whereas the junction itself, i.e. the connection of both individual wires, is much darker. This, first of all, indicates that this part of the NW junction is thicker, similar as it is expected from the growth model depicted in Fig. 7.13. Secondly, a close look reveals the presence of a Moiré pattern. Such Moiré patterns are an indication for the presence of two crystals with either different lattice constants (e.g. in GaAs/InAs core-shell NWs, see Sec. 5.1.1) or different crystal orientations. The latter is the situation in this case and produces a grain boundary. The grain boundary preserves the polarity although the stacking fault and twin density is high. De la Mata *et al.* demonstrated that the twins in NWs are orthotwins [66], also called rotational twins, where the polarity is conserved and the crystal is only rotated by 180° around the growth axis.

The X-shaped NW junction is grown in a completely different way than the L- and T-shaped junctions, as discussed above. A pure radial growth creates the X-shaped NW junction while the remaining two types are produced by an intersection containing at least one NW tip. It is important to highlight that the InAs NWs used in this study are grown without any droplet, being different to the study of Kang *et al.* who have used Au-catalyzed InAs NWs [157].

Figure 7.15a shows an L-shaped NW junction. At first sight, the junction only seems to contain the high density of stacking faults expected in VS grown InAs NWs. A higher magnified image of the central region of the junction (see red square in Fig. 7.15a) reveals a triangular shaped region with pure ZB crystal structure. The corresponding TEM image is shown in Fig. 7.15b and the FFT of the triangular shaped region is displayed as an inset in the same figure. On two sides the ZB triangle is bound by the {111} planes of the two NWs. These are

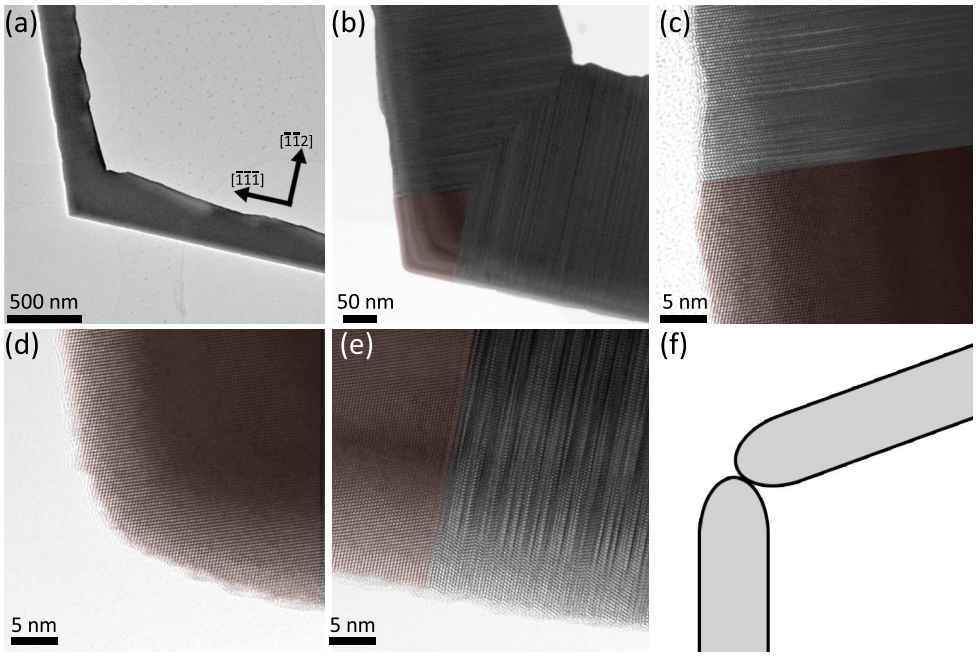

Figure 7.16.: *TEM images of the L-shaped elbow structure. (a) Overview image. (b) Low resolution image of the elbow. (c, e) HRTEM images of different parts of the elbow showing the pure ZB elbow itself (d) and the transition to the stacking fault rich NWs. Red overlays show the ZB crystal structure of the elbow. (f) Schematic illustration of the formation of the junction.*

the {111} planes representing the growth fronts of the NWs. The remaining side of the triangle is bound by a {211} plane. Some of the ZB planes of the triangular region continue into the disordered stacking sequence of the NW, as highlighted by the colored overlay. The outer parts of the junction exhibit the expected border between the stacking fault rich NWs, as seen in Fig. 7.15c. This is similar as for the X-shaped junction. Although the junction between the two NWs is not perfect, the NWs exhibit a crystallographic connection which can be beneficial for the electronic transport.

Another L-shaped NW junction is displayed in Fig. 7.16. Here, the crystal structure differs since also the merging mechanism is slightly different. The NW junction shown in Fig. 7.15 is created by a NW tip penetrating into the segment close to the tip of the other NW A schematic illustration is displayed in Fig. 7.15d. In contrary, the junction depicted in Fig. 7.16 does not show any evidence of a penetrating NW, rather it is a perfect tip-to-tip merging forming an elbow structure (see schematic in Fig. 7.16f). The crystal structure in the elbow is ZB, connecting both NWs (see Fig. 7.16b,d). About 50 – 100 nm away from the elbow, the crystal structure switches back to the stacking fault rich one (see Fig. 7.16c,e). The two observed crystal structures in the L-shape NW junctions (Fig. 7.15 and Fig. 7.16) differ due to the merging mechanism being either a NW penetrating slightly into the tip of another NW or a pure merging of two NW tips.

A TEM analysis of the third possible NW junction, a T-shape, is displayed in Fig. 7.17. During the transfer of the NW junction from the as-grown substrate to the TEM grid, one branch of the junction was broken off. This site of fracture is seen in Fig. 7.17a,b and demonstrates that the junction it self is rather stable. The crystal structure of this particular junction is shown in Fig. 7.17b,c; Fig. 7.17d depicts the diffraction pattern. The latter again exhibits two streaky patterns rotated by about 110°. The (HR)TEM images display the expected stacking fault rich

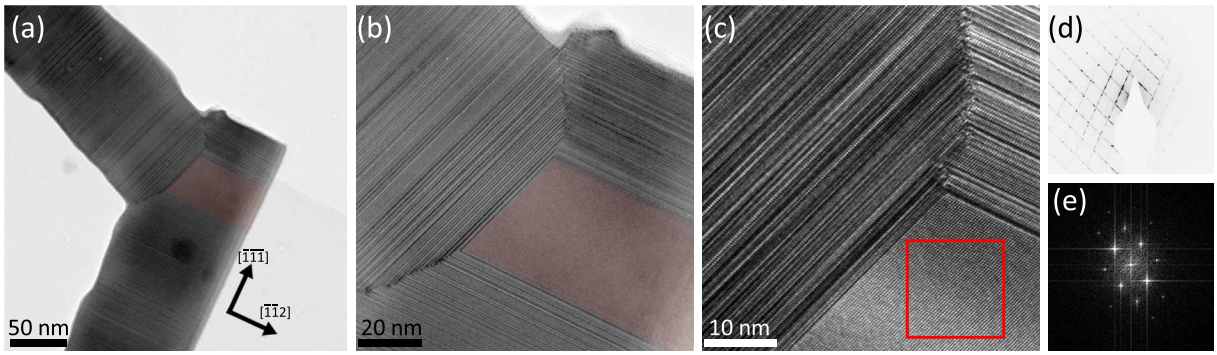

Figure 7.17.: *Low (a, b) and high (c) resolution TEM images of a T-shaped NW junction with pure ZB phase at the junction. One arm of the junction was broken off during NW transfer to the TEM grid. Red overlays in (a, b) denote the ZB phase at the junction. (d) Diffraction pattern of the NW (inverted colors). (e) FFT of the red rectangle in c. The FFT demonstrates the pure ZB crystal structure.*

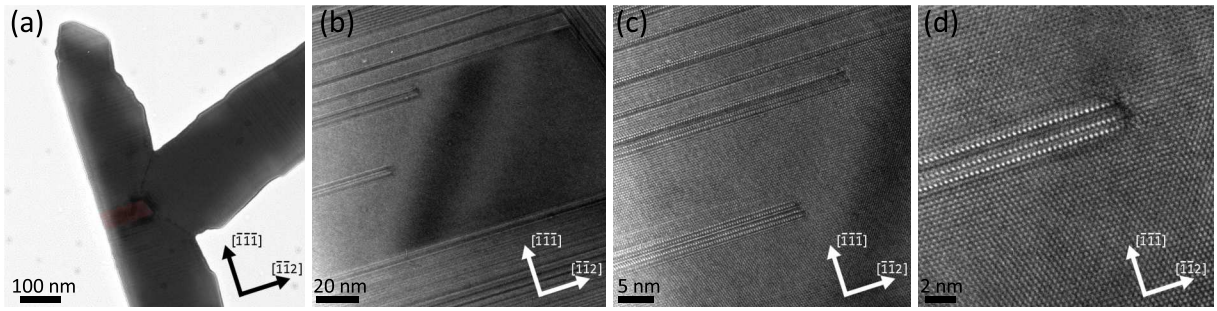

Figure 7.18.: *Low (a, b) and high (c, d) resolution TEM micrographs of a T-shaped NW junction having two stacking defects in the ZB phase of the junction. The red overlay in (a) highlights the ZB crystal structure in the junction.*

InAs NWs and an exceptional large defect free region at the merging point of the NWs. This has ZB crystal structure (see the FFT in Fig. 7.17e) and extends across the entire NW diameter. In contrast to the work by Kang *et al.* [157], this defect free ZB region cannot be created by an etching of a droplet into the NW modifying its crystal structure, since these InAs NWs are grown without any droplets. Accordingly, the transformation of the crystal phase has to take place via a solid phase mechanism. In order to investigate this solid phase transformation of the crystal phase, additional tip-to-side NW junctions are investigated, displaying the transformation at different stages.

Figures 7.18 and 7.20 show tip-to-side junctions with an incomplete ZB segment at the connection point. In Fig. 7.18 a long ZB segment is found at the connection point of both NWs, but at two positions within this ZB segment stacking faults not penetrating the entire NW diameter are found. The lengths (in $\langle 211 \rangle$B direction) of the stacking defects are different while their height (in $[\overline{1}11]$ direction) is almost identical, being 6 – 8 atomic layers (see Fig. 7.18b-d). The varying length of the stacking defects in the ZB region proves that they are caused by a dynamic process rather than by the already existing crystal structure of the NWs. The stacking faults in the ZB region may be bound by three Shockely partial dislocations, similar as in the study by Zhen *et al.* [351]. These three Shockley dislocation would then have a total Burgers vector of zero [351]. The stacking sequence around the defect is illustrated in Fig. 7.19: it shows the FFT-filtered HRTEM image of Fig. 7.18d with superimposed stacking sequence denoted by colored circles. A perfect ZB lattice is present on the right side of the image while some stacking

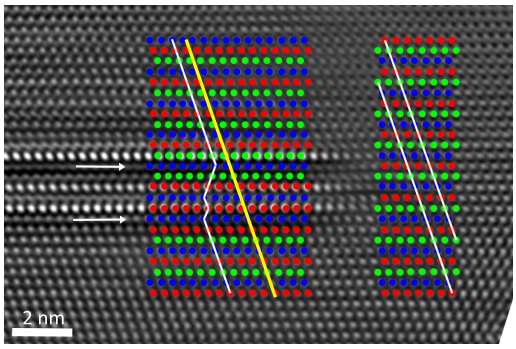

Figure 7.19: *FFT-filtered HRTEM image of the defect shown in Fig. 7.18. Colored circles denote the stacking layers ● A, ● B and ● C. White lines show the stacking sequence, being either ZB or having twins or stacking faults. The yellow line indicates the stacking of a perfect ZB lattice. White arrows show the first and last stacking fault in the defect.*

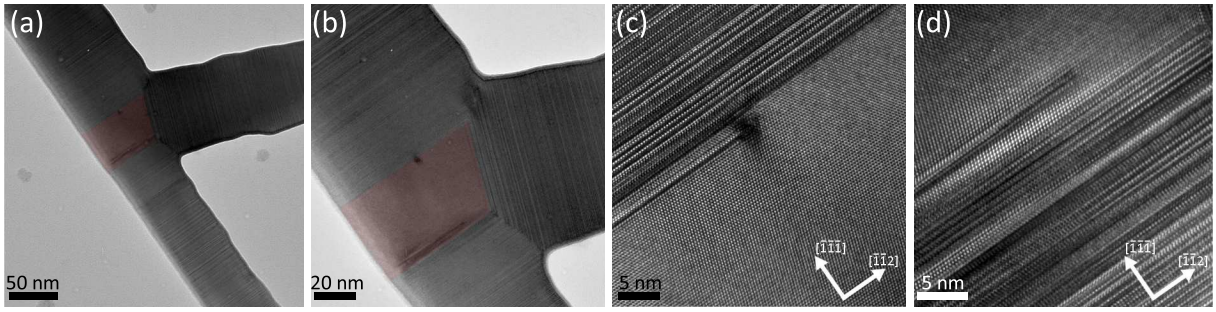

Figure 7.20.: *TEM micrographs of a T-shaped NW junction with a long ZB segment at the junction and one defect at both sides of the pure crystal phase in the junction. (a,b) Low resolution images showing the shape of the junction and the dimensions of the pure phase (red overlay) in the junction. (c) Defect at the upper part of the pure phase. (d) Defect at the lower part of the junction.*

defects are observed on the left side. The defective structure on the left part is not pure WZ but contains stacking faults and twins. Interestingly, the stacking sequences of the perfect ZB regions in the upper part of the image differ slightly. The upper sequence on the left part starts with a stacking *BACBACB* while the stacking on right side begins with *ACBACBA*. Apparently, the stacking sequence is shifted by one atomic layer. Such a shift of atoms in a layer can be caused by Shockley partial dislocations.

Patriarche *et al.* [237] and Zheng *et al.* [351] demonstrated a phase transformation from individual WZ GaAs and InAs NWs into the ZB crystal structure, respectively. In the first case, this was caused by an epitaxial burying of WZ GaAs NWs in a ZB GaAs matrix. The transformation of the crystal structure in the second case occurred due to a remelting of the catalyzing Au droplet at high temperatures, creating a small portion of ZB which then spreads out laterally. For both situations, Shockley partial dislocations are believed to be responsible for the phase transition. These dislocations can also explain the observed crystal structure and the transformation in this investigation. However, it is important to mention that the previous studies by Patriarche *et al.* and Zheng *et al.* discuss the transformation of large, pure WZ segments into ZB while here the original crystal structure is rich of stacking faults and twins.

In the present structure, the transition from the stacking fault rich structure to the ZB is not only created by Shockley partial dislocations. This is seen by the (HR)TEM images in Fig. 7.20, depicting another T-shaped NW junction. Here, the original NW decreased its diameter after the junction. Possibly, the junction acts as a sink for the adatoms or the coalescence of the NWs reduced the size of the NW tip. More importantly, higher resolution images show two regions within the ZB structure that exhibit defects: one region close to the upper boundary

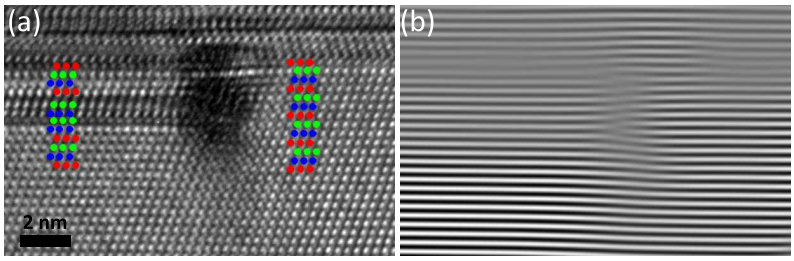

Figure 7.21: *HRTEM (a) and FFT-filtered (b) images of the defect shown in Fig. 7.20c. Colored circles in a denote stacking layers ● A, ● B and ● C and show the existence of a stacking fault. The FFT-filtered image clearly demonstrates a dislocation.*

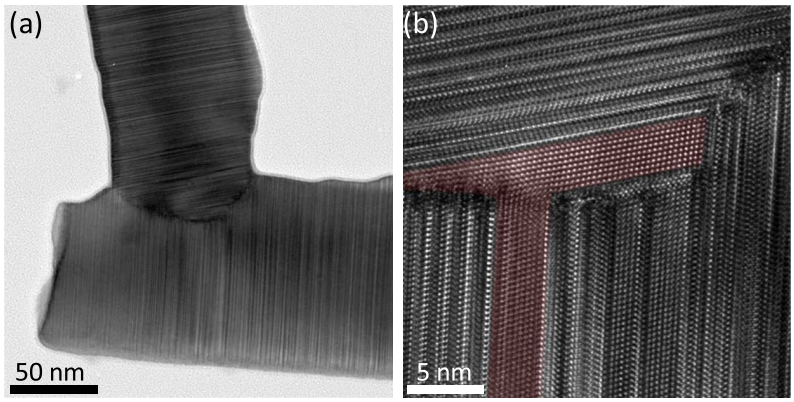

Figure 7.22: *T-shaped NW junction at the beginning of the phase transformation into ZB. (a) Low resolution TEM image. (b) HRTEM micrograph. The red area in (b) shows the ZB segment.*

(see Fig. 7.20c) and the other one close the lower boundary (see Fig. 7.20d) in the image. The latter is described in an identical way as it was done for Fig. 7.18, that is the existence of several Shockley partial dislocations. The other defect shown in Fig. 7.20c is different, which is already seen by the dark contrast around it. Such dark contrast typically arises from the strain field around a dislocation core. The dislocation is displayed more clearly in the HRTEM and FFT-filtered images depicted in Fig. 7.21a,b, respectively. The FFT-filtered image clearly shows the presence of a dislocation, evident by the terminating lattice plane. The HRTEM image with a colored overlay representing the atoms on the different layers shows how the stacking sequence is modified by the dislocation. The perfect ZB stacking sequence *..ABCABC**A**BCABCA..* on the right side of the dislocation is changed into a *..ABCABCBCABCA..* stacking sequence on the left side. Apparently, a stacking fault is created by the removal of an *A* plane. This dislocation is a single Frank partial dislocation, which cannot glide but move by climbing only. Possibly the dislocation is created by the fact that some of the NWs grow with a slight tilt, which means that the growth directions of the two NWs did not match exactly.

The remaining question concerns the initial stage of the phase transformation. The exact mechanism is hard to evaluate since it requires an *in situ* investigation. However, different stages are observed on different NWs, as already pointed out above and in Figs. 7.17, 7.18 and 7.20. An early stage with only a short ZB segment is seen in Fig. 7.22a,b. A ZB segment of about 4 nm thickness is observed close to the top of the hitting NW. This ZB crystal structure already continues in the other NW, having a thickness of the ZB segment of about 3 nm. These are the thinnest ZB segments observed at the NW junctions, but are already longer than the usual thickness of pure crystal phases in VS grown InAs NWs. This suggests that a phase transformation already started. When the tip of one NW hits the side facets of the other NW, the local chemical potential may change, affecting the adatom diffusion and the local V/III ratio. This may have a strong impact on the crystal structure in the upper few nm, favoring the ZB crystal structure of the hitting NW at the junction.

Another interesting fact is given by the shape of the tip of the hitting NW penetrating into the other NW. Figures 7.23a,b show two exemplary SEM images of this region. In both situations,

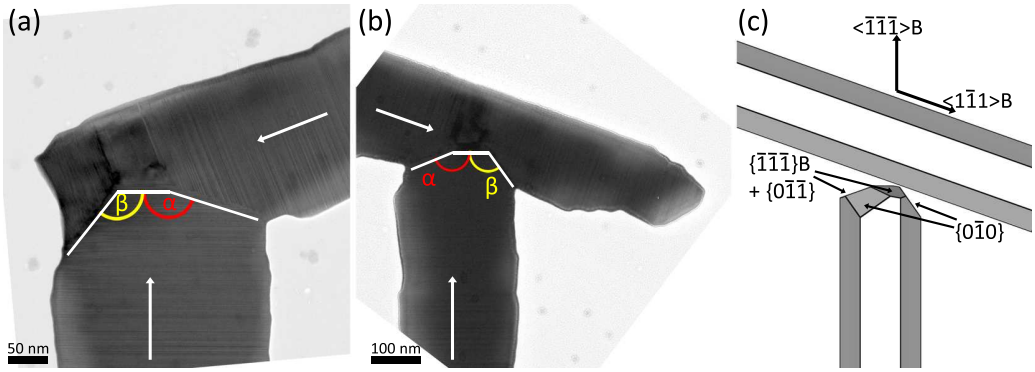

Figure 7.23.: *Morphological shape of the junction in T-type NW junctions. (a,b) TEM micrographs of two exemplary NWs with lines indicating the shape of the interface between both NWs. White arrows show the growth directions. (c) Schematic illustration of the orientation of both NWs and the top facets of the hitting NW.*

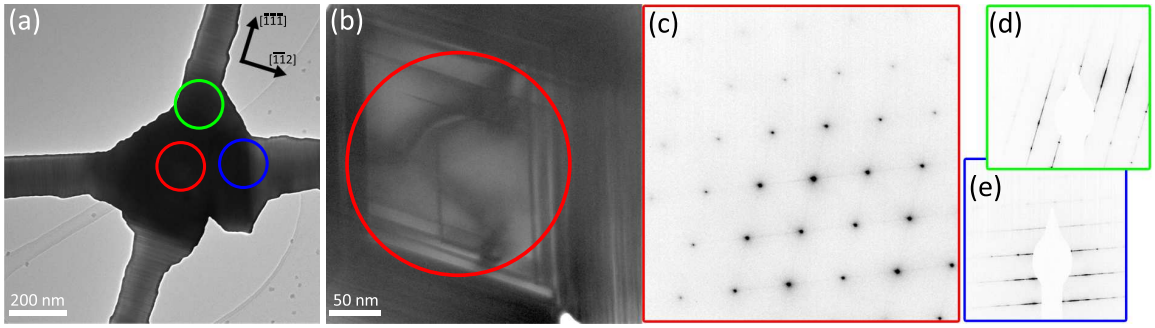

Figure 7.24.: *X-shaped NW junction with ZB structure in the junction. (a) Overview image. (b) Higher magnified image of the central region of the junction. (c-e) Diffraction patterns (inverted colors) of the regions marked in (a,b).*

the shape of the NW tip is not uniform but a faceted, penetrating part is observed with a small flat $(\overline{111})$B top facet and two facets tilted by α =160° and β =125–145°. These angles indicate crystallographically defined facets, which cannot originate from a WZ structure since it would require a sixfold symmetry. Rather the facets belonging to the angles α and β are assigned to the ZB crystal structure with α coming from stepped $\{\overline{111}\}$B and $\{0\overline{11}\}$ facets and β belonging to $\{0\overline{1}0\}$ facets. This is schematically depicted in Fig. 7.23c. Interestingly, these facets show a clear pure ZB characteristic although the surrounding crystal structure contains a very high density of stacking faults and twins. Both stacking faults and twins should result in a more uniform arrangement of the penetrating facets. The orientation of the ZB crystal structure in the junction agrees with the orientation of the facets belonging to the angles α and β. In all investigated NW junctions, the orientation of the angles α and β is identical, which means that the angle α is found in the inner part of the junction. This orientation allows a monocrystalline which is only obtained if the junction has the same crystalline orientation as the substrate, as pointed out by Car *et al.* [41]. Consequently, the growth direction of the NWs ($\{\overline{111}\}$B) defines the orientation of the ZB crystal structure in the junctions, independent of the existing stacking faults and twins.

As it has been mentioned above, the X-shaped NWs exhibit the stacking fault rich structure also in the junction between the two NWs (see Moiré fringes in Fig. 7.14), which is different than for the L- and T-shaped NW junctions. However, in one X-shaped NW junction a different crystal structure is observed. Figure 7.24a shows this X-shaped junction. The circles denote the

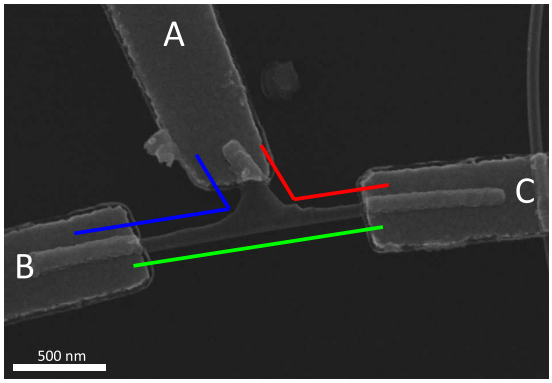

Figure 7.25: *SEM micrograph of a T-shaped InAs NW junction contacted by Ti/Au electrodes. The contacts are labeled A, B and C. [Data courtesy of Daniel Rosenbach and Sebastian Heedt]*

positions where diffraction patters were acquired. A higher magnified image of the central region is displayed in Fig. 7.24b, it does neither show Moiré fringes nor a high density of stacking faults. Rather, a uniform brightness with only very few stacking faults is observed. The diffraction pattern of this region is shown in Fig. 7.24c and exhibits ZB diffraction spots. Light streaks caused by the few stacking faults are present as well. Moving the diffraction aperture slightly out of the junction (see green and blue circles in Fig. 7.24a) shows the streaky pattern being typical for VS grown InAs NWs. This structure was observed only in one out of seven X-shaped NW junctions, the others exhibited the Moiré pattern discussed before. Nonetheless, this crystal structure further demonstrates the surprising crystal phase transformation in the junctions which should be beneficial for the transport due to the absence of grain boundaries or additional stacking defects.

7.2.5. Electronic transport through InAs junctions

As outlined before, the junctions typically exhibit a ZB crystal structure while the NWs itself have a high density of stacking faults. Consequently, the crystal structure of NW junctions is not expected to have an impact on the resistivity. In order prove this assumption, Fig. 7.25 displays a contacted T-shaped InAs NW junction. The NW is placed on a Si/SiO_2 substrate and the Si substrate acts as a global back gate. Ohmic contacts are achieved by Ar^+ sputtering followed by the evaporation of Ti and Au. The angle between the arms is $\sim 110°$, being the angle between two $\langle 111 \rangle$B directions in a ZB crystal.

Figure 7.26a shows the I-V curves for all contact combinations. The contacts are labeled as shown in the SEM micrograph and each current path is additionally marked by a color (A-B: blue, A-C: red, B-C: green). The I-V curves are obtained at room temperature in a two terminal configuration and are linear for all combinations, thus no Schottky-contacts or barriers are present. The slope varies slightly, which is attributed to the contact resistance, small variations in the NW diameter and differences in the contact separation. The transfer characteristics are displayed in Fig. 7.26b. The source drain voltage is set to 500 mV. The source drain current is controlled by the back gate voltage, i.e. the NW is depleted at negative gate bias and electrons are accumulated at positive bias. The curves are rather similar, suggesting that the junction does not influence the transport strongly. The resistivites are approximated to $\rho_{AB} = 6.5 \cdot 10^{-2} \Omega cm$, $\rho_{AC} = 5.5 \cdot 10^{-2} \Omega cm$ and $\rho_{BC} = 4.6 \cdot 10^{-2} \Omega cm$. Based upon the transfer characteristic, the electron concentration and carrier mobility can be approximated and compared to values from single NWs. In each case, the electron concentration is in the range of $\sim 5 \cdot 10^{17}$ cm^{-3} with a mobility of ~ 600 cm^2/Vs. Similar values for the electron concentration and mobility were also observed in InAs NWs grown via selective area MOVPE [334]. This means that the junctions

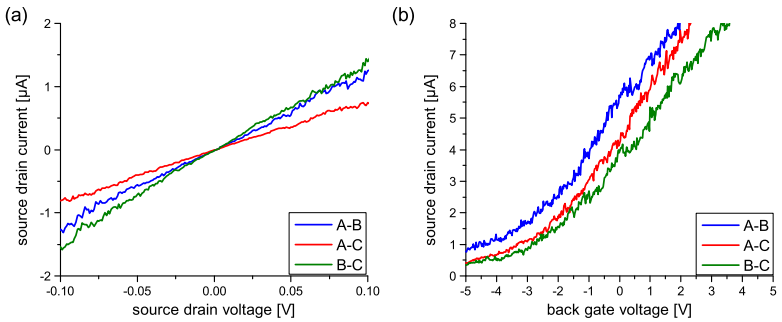

Figure 7.26: *(a) I-V curve and (b) transfer characteristic of a T-shaped InAs NW junction. [Data courtesy of Daniel Rosenbach and Sebastian Heedt]*

do not induce additional scattering centers to the NWs.

7.3. Conclusions

The first section of the chapter was dedicated to the growth of NWs on textured Si (100) substrates, that are substrates containing pyramids bound by {111} facets. It was shown that the growth direction of the NWs is controlled by aligning the pyramids with respect to the effusion cell of the group III element, i.e. growth of NWs on predefined facets of the pyramids was demonstrated. The alignment with respect to the effusion cell was found to give rise to different growth conditions on each of the pyramid facets, leading to different NW densities and dimensions and allowing to study the NW growth by the four growth conditions in close vicinity. Making use of the growth of NWs on predefined pyramidal facets, the simultaneous integration of NWs with different compositions on the very same substrate and within close vicinity was demonstrated.
The application of Si substrates patterned with V-grooves instead of pyramids enabled the fabrication of InAs NW junctions. The optimal dimensions of the V-grooves for the growth of NW junctions have been identified. Three basic shapes of NW junctions were obtained: L-shaped, T-shaped and X-shaped junctions. Detailed TEM analyzes revealed a transformation of the crystal phase via a solid phase mechanism, most probably induced by Shockley partials dislocations. First electrical measurements conducted on T-shaped junctions indicated that the junction does not influence the room temperature transport properties.

8 Chapter 8. III-V/high κ core-shell nanowires

The integration of III-V NWs in future electronic devices requires the use high κ dielectrics as gate oxides or as a passivation of the NW surface. Certainly, these dielectrics need to be of high quality. This is related to the interface from the high κ dielectric to the semiconductor, the roughness of the dielectric as well as the dielectric properties (e.g. leakage current and dielectric constant) itself. The latter can be affected by the stoichiometry of the films, its density as well as the formation of crystalline phases in the amorphous layer. The deposition of dielectric layers may also influence the semiconductor. Strain induced by the thermal mismatch between the semiconductor and the dielectric film can have an impact on the carrier mobility.
High κ dielectrics deposited via an ALD process are ideal for the integration of high aspect ratio structures in semiconductor devices due the highly conformal deposition. Dielectrics of both Al_2O_3 and HfO_2 deposited by ALD on III-V semiconductor surfaces benefit from a self-cleaning effect. This depends on the precursor and oxidation state [49, 133, 191, 295, 301, 302].
In this chapter, the interaction between an amorphous Al_2O_3 shell covering a GaAs NW core and the formation of crystalline HfO_2 phases on InAs NWs are studied by HRTEM and XRD. The high κ dielectric shells are deposited by ALD.
Some of the results presented in this chapter have been published in [260].

8.1. Strain in GaAs/Al_2O_3 core-shell nanowires[1]

In order to study a possible interaction between semiconductor nanostructures and amorphous shells induced by the thermal mismatch, we have chosen GaAs and Al_2O_3 as a model system. Among the III-V semiconductors, GaAs has one of the highest thermal expansion coefficient α_{GaAs}, the thermal expansion coefficient $\alpha_{Al_2O_3}$ of amorphous Al_2O_3 is slightly higher. Con-

[1] XRD measurements were performed by Andreas Biermanns in the group of Prof. Pietsch at the University of Siegen. Torsten Jörres assisted in the preparation of the samples [154].

semiconductor	α [K^{-1}]	high κ	α [K^{-1}]
GaAs	$6.9 \cdot 10^{-6}$	Al_2O_3	$0.9 - 2 \cdot 10^{-5}$
InAs	$4.5 \cdot 10^{-6}$	HfO_2	$2 \cdot 10^{-5}$
GaSb	$7.8 \cdot 10^{-6}$	SiO_2	$5 \cdot 10^{-7}$
InSb	$5.4 \cdot 10^{-6}$	Si_3N_4	$3.2 \cdot 10^{-7}$

Table 8.1.: *Thermal expansion coefficients of several III-V semiconductors and high κ materials at 20° C. [140, 153, 150, 145, 161, 314]*

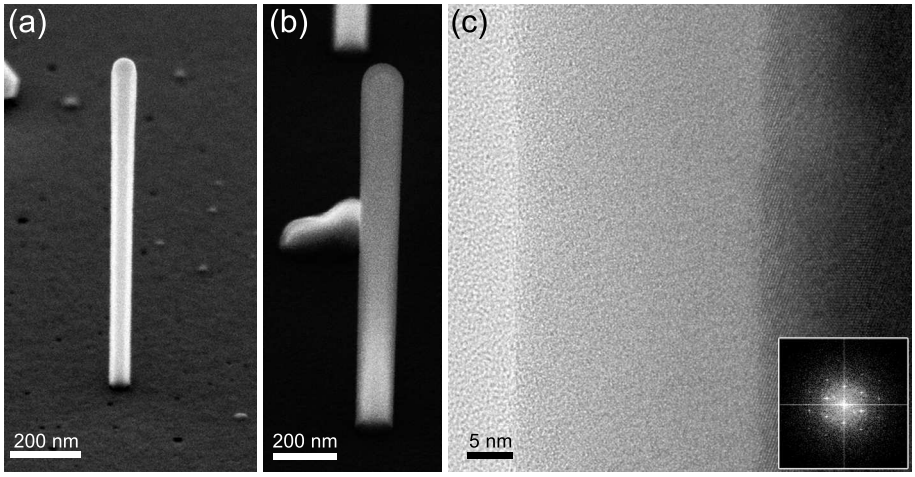

Figure 8.1.: *SEM and TEM micrographs of GaAs NWs without (a) and with (b,c) Al_2O_3 shells. The TEM image clearly demonstrates the 30 nm thick amorphous Al_2O_3 shell, the inset evidences the ZB crystal structure of the GaAs.*

sequently, the difference in thermal expansion coefficients is small. In Tab. 8.1, the linear thermal expansion coefficients of various semiconductors and high κ materials at 20°C are shown. To obtain a measurable strain in the GaAs NW, the temperature difference between the deposition of the Al_2O_3 and the strain measurement taking place at room temperature should be high. Additionally, a high volume ratio of the Al_2O_3 shell to the GaAs core is preferential. Both conditions are in fact also reasonable: a high deposition temperature improves the quality of the oxide layer while the volume ratio is high due to the small NW diameter in future electronic devices.
Accordingly, GaAs NWs having a length of about 1 µm and a diameter of 80 nm were covered by 30 nm Al_2O_3 deposited at a temperature of 315°C. The GaAs NWs were grown on a GaAs (111)B substrate. SEM micrographs before and after the Al_2O_3 deposition are shown in Fig. 8.1a and b, respectively. Contrast changes due to the amorphous shell are clearly seen. Figure 8.1c displays an exemplary HRTEM micrograph confirming the shell thickness to be 30 nm. Similar micrographs taken at different positions along the NW axis confirm the homogeneous coverage. The surface roughness determined from the TEM micrographs is very small. It is similar to the roughness of a bare GaAs NW, indicating that the roughness of the shell only depends on that of the underlying structure. In addition, no evidence of an interfacial layer is found. In any case, the TMA precursor is known to provide a self-cleaning mechanism of the GaAs surface. This partially removes the native Ga and As oxides [49, 133, 191].

In order to measure the elastic interaction between the GaAs core and the Al_2O_3 shell, high resolution XRD measurements have been performed at the P08 beamline of the PETRA III synchrotron source. Using a monochromatic, parallel x-ray beam with a photon energy of 10 keV and a size of 50µm × 100µm (vertical × horizontal), reciprocal space maps around the symmetric (111) as well as the asymmetric (422) reflections of GaAs were recorded.
Figure 8.2 shows a comparison of the intensity distribution in the q_x-q_z plane around the symmetric (111) reflections of an uncovered GaAs NW reference sample (a) as well as the NWs covered by the Al_2O_3 shells (b). The central part of Fig. 8.2a displays the intense Bragg reflection from the GaAs substrate (label: s). In addition, the reciprocal space map exhibits a weaker signal being elongated along the q_x direction (label: NW). This signal is characteristic for NW ensembles. The high aspect ratio and a typically small random tilt along the growth direction

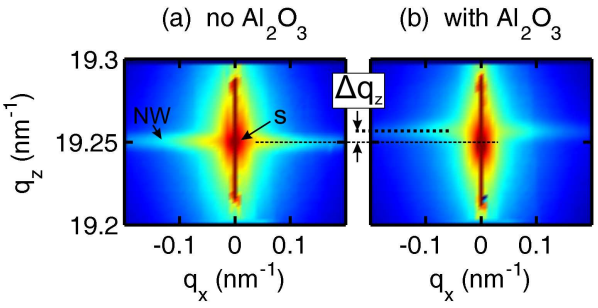

Figure 8.2: *Reciprocal space maps around the GaAs (111) reflection (s) of NWs without (a) and with (b) Al_2O_3 shell. After the deposition of the shell, the Bragg peak of the NWs shifts towards larger values of q_z, showing a compressive strain in the GaAs core. (Logarithmic color scale) [Data courtesy of Dr. Andreas Biermanns]*

leads to the broadening of the signal along q_x. Within the experimental resolution ($1 \cdot 10^{-4}$), the signal from the NWs is at the same q_z as the substrate signal. This evidences that the NWs and the substrate have the same lattice parameter, as expected for ZB type NWs and already seen in Sec. 5.1.1.

The signal of the Al_2O_3 covered NWs is shifted by $\Delta q_z = 8 \pm 2 \cdot 10^{-3}$ nm^{-1} towards larger q_z values. This shift indicates a compressive strain along the growth direction of the NWs with a magnitude of $\Delta c/c = \Delta q_z/q_{z,0} \approx (4 \pm 1) \cdot 10^{-4}$. Asymmetric (422) Bragg reflections displays a compressive strain in the radial direction with the same magnitude. However, a smaller resolution in the corresponding direction in reciprocal space and a significant peak broadening due to the small diameter of the NWs makes a more detailed evaluation of the radial strain component not possible.
The strain present in the GaAs core is expected to be caused by the thermal mismatch between GaAs and Al_2O_3. The linear thermal expansion coefficient of GaAs at room temperature is around $6.9 \cdot 10^{-6} K^{-1}$ [153] while it is higher for amorphous Al_2O_3. Here, linear thermal expansion coefficient of amorphous Al_2O_3 ranging from $0.9 - 2 \cdot 10^{-5} K^{-1}$ have been reported [140, 150, 161]. Crystalline Al_2O_3 has a linear thermal expansion coefficient of about $6.5 \cdot 10^{-6} K^{-1}$ [171]. The difference between GaAs and amorphous Al_2O_3 agree roughly with the measured strain in the core assuming linear elasticity theory.
Certainly, the thickness of the Al_2O_3 is rather high compared to technological relevant ones [343] but in future devices, the NWs will be thinner than in this study, i.e. thinner than 80 nm. The volume ratio between the semiconductor, i.e the NW, and the gate dielectric is then in a similar range as it is here ($V_{NW}/V_{Al_2O_3} \approx 0.5$). Other III-V semiconductors such as InAs, InP and InSb, all being highly interesting for electronic devices, as well as Si have lower thermal expansion coefficients than GaAs [145]. The thermal mismatch between the III-V core and the Al_2O_3 shell and hence the induced strain in the core would be even larger for these semiconductors. When the NWs are embedded in BCB (benzocyclobutene) for the fabrication of future vertical devices, the thermal curing of the BCB results in an additional strain [36]. A metal layer used for contacting the NW or as gate dielectric has an additional impact on the strain in the NW [87]. Consequently, many processing steps after the NW growth influences the strain in the NW.

8.2. Formation of crystalline phases in InAs/HfO_2 core-shell nanowires[2]

The high dielectric constant of HfO_2 together with the large band gap [50] makes it superior to Al_2O_3. The linear thermal expansion coefficient of HfO_2 is in a similar range as that of amorphous Al_2O_3 (see Tab. 8.1). Thick or high-temperature deposited layers of HfO_2 tend to be partially crystalline. This crystallinity is observed for layers above a certain thickness [188, 265] or when deposited above a certain temperature [121, 187]. Post-deposition annealing transforms amorphous HfO_2 to crystalline HfO_2 [29, 136]. However, in most of the investigations, Si wafers were used as substrates, only very few investigations were done on other materials, e.g. Ge [291] or III-V [37, 141, 158, 159, 169], and/or nanostructures [96, 278].
Five different crystal structures apart from the amorphous phase of HfO_2 have been reported: monoclinic (space group $P2_1/c$), two orthorhombic phases (space groups $Pbca$ and $Pnma$), cubic (space group $Fm3m$) and tetragonal (space group $P4_2/nmc$) [193, 350]. Amorphous, monoclinic and orthorhombic HfO_2 are reported to have dielectric constants of about 20 while it is ~ 29 and ~ 70 in the cubic and tetragonal phase, respectively [350]. Consequently, crystalline HfO_2 phases may be advantageous for electronic applications. However, grain boundaries in the polycrystalline HfO_2 are reported to be conductive, promoting leakage currents [20, 144, 211, 241]. Although HfO_2 has already been widely used as a high-k gate dielectric for InAs NWs, its quality has not been investigated. In several studies, the HfO_2 was deposited at about 80-120°C [21, 31, 32, 98]. This is a rather low deposition temperature for HfO_2. In some studies, also aluminum was added and therefore AlHfO was used [304]. The reason for such a low deposition temperature was the usage of a lift-off technique for the dielectric [21, 31, 32, 98]. A low deposition temperature decreases the dielectric constant and increases the carbon content in the HfO_2 [199]. Apparently, a lift-off technique for the high κ dielectric only makes sense when a structuring of the dielectric is not possible in another way.

In this study, the morphological and structural characteristics of HfO_2 shells around InAs NWs are investigated. InAs NWs grown via the vapor-solid mechanism presented in Section 4.2.1 were grown on Si substrates and transferred into the ALD immediately after unloading from the MBE system. In the ALD chamber the substrate was ramped to the deposition temperature T_{dep} under a constant flow of Ar. For the deposition of HfO_2, TDMAH and ozone were used as precursors. Two series were grown: (1) a constant number of 100 deposition cycles at different substrate temperatures T_{dep} and (2) different numbers of deposition cycles (n) at a constant substrate temperature of 250°C. In a third series, also TMA was used for the deposition of thin Al_2O_3 layers within HfO_2: laminate structures have been produced. In these laminates, the following sequence was deposited: 15 cycles HfO_2 / x cycles Al_2O_3 / 30 cycles HfO_2 / x cycles Al_2O_3 / 30 cycles HfO_2 / x cycles Al_2O_3 / 15 cycles HfO_2. The number of Al_2O_3 deposition cycles x was varied from 1 to 10. In each case, the total thickness of the laminate structure is in the order of 10 nm. All samples are in the as-deposited state, they were not annealed after HfO_2 deposition. In separate experiments, HfO_2 and Al_2O_3 deposition rates were determined on Si (100) substrates at a constant temperature of 250°C. Al_2O_3 was found to grow with a rate of 0.85 Å/cycle whereas the deposition rate of HfO_2 was found to be 1 Å/cycle.

[2]Results of this section have been published in T. Rieger, T. Jörres, J. Vogel, A. Biermanns, U. Pietsch, D. Grützmacher, and M. I. Lepsa. *Crystallization of HfO_2 in InAs/HfO_2 core-shell nanowires.* Nanotechnology, 25(40):405701, 2014. Ref. [260]. Parts of the HfO_2 depositions were done by Torsten Jörres. XRD measurements have been performed by Jonas Vogel and Dr. Andreas Biermanns in the group of Prof. Pietsch at the University of Siegen. Processing of the FETs and electrical measurements were done by Marion Rosien.

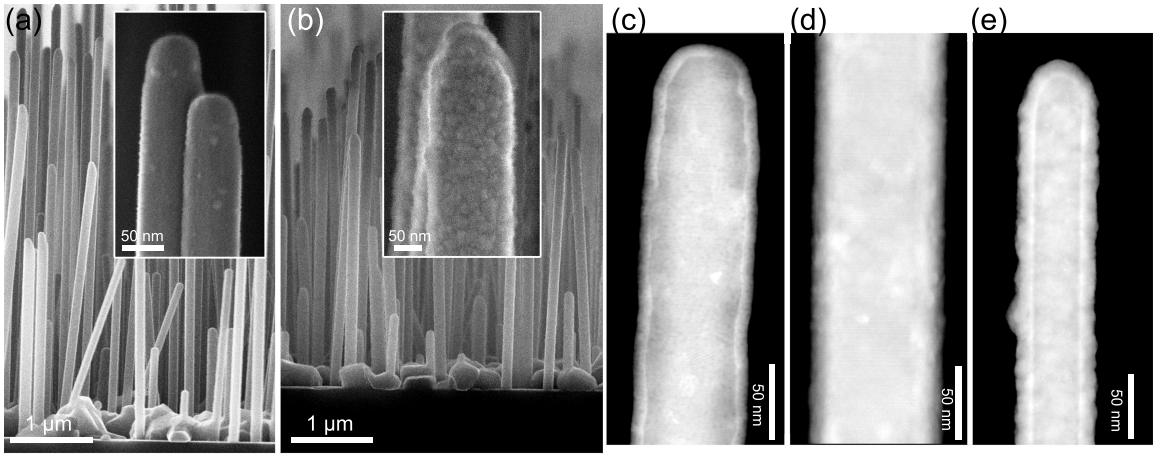

Figure 8.3.: *SEM micrographs of InAs/HfO_2 core-shell NWs with 100 cycles of HfO_2 deposited at 250° C (a) and 320° C (b). Apart from NWs, InAs crystallites are seen on the samples. Insets display higher magnification images of single NWs showing a temperature dependent roughness of the HfO_2 shell. (c)-(e) HAADF images of single InAs/HfO_2 core-shell NWs with 100 cycles of HfO_2 deposited at 175° C (c), 250° C (d) and 320° C (e). Published in [260].*

8.2.1. Morphology of HfO_2 shells

Typical SEM micrographs of as grown InAs/HfO_2 core-shell NWs are depicted in Fig. 8.3 a,b. The NW density is high (5-10 NWs/µm^2, see Sec. 4.2.1) and also InAs crystallites are found. The NWs are covered conformal and homogenously using all deposition conditions despite of the high NW densities as well as the high aspect ratio. This was verified by a detailed TEM analyses. The thicknesses of the HfO_2 at the top and bottom of the NWs are identical, no morphological or structural differences in the HfO_2 layers were found along the wire axis.
In Fig. 8.3 representative SEM and HAADF micrographs of samples from the first series with increasing substrate temperatures for the HfO_2 deposition are shown. The temperature T_{dep} varied from 125°C to 320°C, the number of deposition cycles was constant at 100 corresponding to a nominal thickness of 10 nm. Overview SEM images of samples with HfO_2 shells deposited at 250°C and 320°C are displayed together with higher magnification images of single NWs (insets) in Fig. 8.3a and b. HAADF images of core-shell NWs with shells deposited at 175°C, 250°C and 320°C are shown in Fig. 8.3c-e, respectively. HfO_2 deposited at 125°C results in smooth NW surfaces without any irregularities in SEM images or HAADF images (not shown). When the deposition temperature is increased to 175°C smooth NW surfaces are obtained, but a single bright spot in the HAADF image is seen (see Fig. 8.3c). Changes in the contrast of the HAADF signal are due to a change in Z-contrast, the thickness and/or changes in the crystalline orientation, e.g. a crystalline material in an amorphous matrix. HfO_2 tends to form crystalline phases which can result in an increased thickness of the HfO_2 layer [121]. The InAs NWs have smooth side facets and a single crystal orientation. Consequently, bright areas in HAADF images indicate changes in the HfO_2, namely crystalline phases. A further increase of the deposition temperature to 250°C results in small dot-like structures which are seen in the inset of Fig. 8.3a. Additionally, they are identified by significantly more changes in the contrast in the HAADF images shown in Fig. 8.3d. The dot-like structures on the NW side facets indicate an increase of the surface roughness. This is correlated with the increased amount of crystalline HfO_2 as it is shown later. At the highest deposition temperature being 320°C, the NW surface is rough as obvious in both the SEM and the HAADF images (Fig. 8.3b,e).

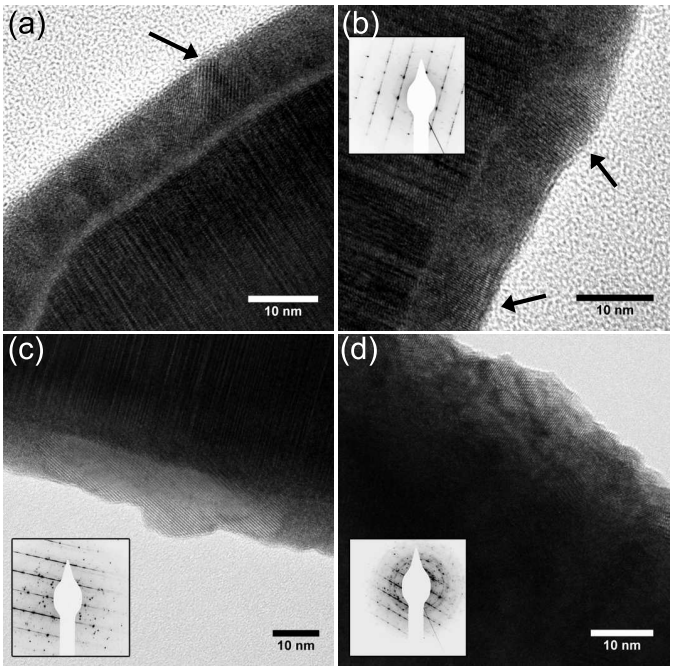

Figure 8.4: *HRTEM micrographs of InAs/HfO_2 core-shell NWs with varying shell deposition temperatures. (a)-(d) HRTEM images with deposition temperatures of 125° C, 175° C, 250° C and 320° C, respectively. Insets in (b)-(d) show selective area electron diffraction patterns (inverted colors), displaying the streaks arising from the InAs NW as well as Debye-Scherrer rings from the crystalline HfO_2. Arrows in (a) and (b) point to small crystalline regions of HfO_2. Published in [260].*

(HR)TEM micrographs of InAs/HfO_2 core-shell NWs with varying deposition temperatures are depicted in Fig. 8.4. As it was already seen in the SEM image in Fig. 8.3a, the HfO_2 shell deposited at 250°C is not smooth: it exhibits some roughness. The corresponding HRTEM image is shown in Fig. 8.4c. Here, the origin of the roughness becomes clear: crystalline HfO_2 formed. This crystalline HfO_2 has a higher growth rate than amorphous HfO_2 [121]. The crystallinity is clearly proven by the presence of lattice fringes. Similarly, TiO_2 films grown by ALD show an increase of the growth rate once the layer crystallizes [170]. The presence of Debye-Scherrer rings in the diffraction pattern (inset in Fig. 8.4) shows that the growth of the HfO_2 is not in an epitaxial relation with the InAs NW. Debye-Scherrer rings are typical for polycrystalline material. The streaks in the diffraction pattern are from the stacking fault rich NWs, typical for the VS growth of InAs NWs as shown in Sec. 4.1.3 and Refs. [217, 288]. Due to conducting grain boundaries [20, 144, 211, 241], polycrystalline HfO_2 is not beneficial for gate dielectrics. Inhomogeneous thicknesses locally modify the gate capacitance resulting in a nonuniform gate influence. Consequently, smooth and amorphous layers are required. Figure 8.4a, b and d show HRTEM images and diffraction patterns from NWs with HfO_2 deposition at 125°C, 175°C and 320°C, respectively. Similar as in the images shown in Fig. 8.3b,e the layer deposited at the highest temperature is rough and seems to be completely crystalline, as evident by the Debye-Scherrer rings. Additionally, EDX line scans acquired on these NWs indicate a thickness larger than the expected 10 nm, namely 20-25 nm. This increased thickness agrees well with the higher growth rate of crystalline HfO_2 compared to amorphous HfO_2 [121]. At low deposition temperatures (125°C and 175°C) the HfO_2 layers are smooth and exhibit only small crystalline regions within the amorphous HfO_2 matrix. In Fig. 8.4a and b, the crystalline HfO_2 regions are pointed out by arrows. Low deposition temperatures, however, are known to reduce the dielectric constant of HfO_2 [199], making a deposition around 250°C preferable. As evident from the correlation of SEM and TEM micrographs, crystalline regions showing an increased thickness compared to the amorphous parts are observed by SEM while small crystalline parts are only identified by TEM.

The different deposition temperatures and crystallinities result also in different wet etching

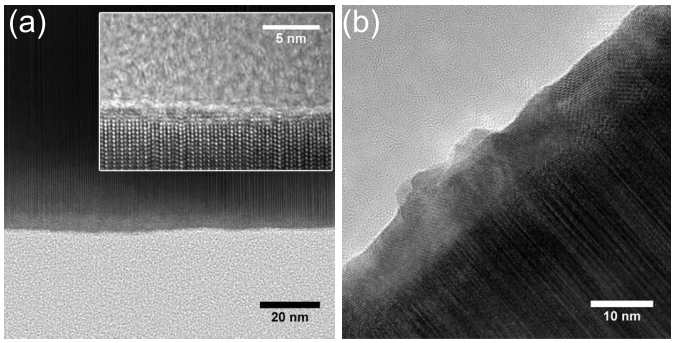

Figure 8.5: *TEM micrographs of InAs/HfO_2 core-shell NWs after wet chemical etching in 0.5% HF for 30s. 100 cycles HfO_2 were deposited at 125° C (a) and 250° C (b). The inset in (a) depicts a close-up showing no evidence of a residual oxide layer on the NW. Published in [260].*

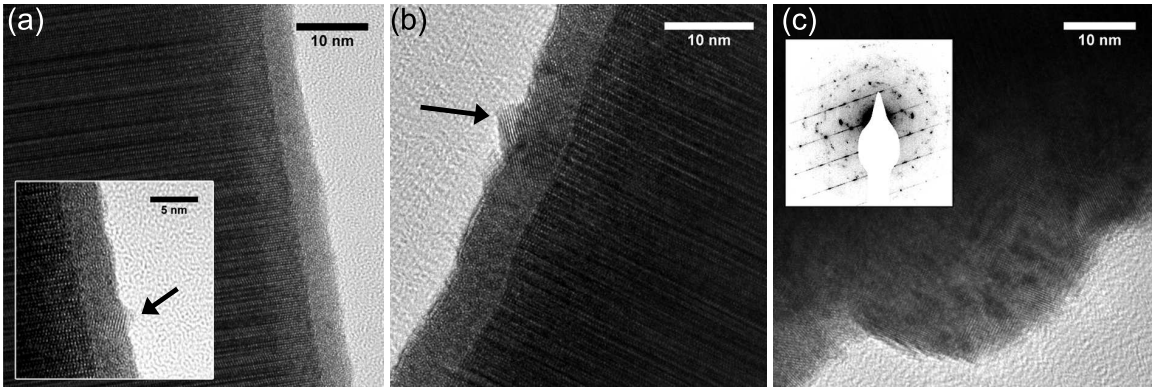

Figure 8.6.: *TEM micrographs of InAs nanowires with HfO_2 shells of different thicknesses. Nominal thicknesses are 3 nm, 5 nm and 20 nm in (a), (b) and (c), respectively. The deposition temperature is 250° C. The inset in (a) depicts a small HfO_2 crystallite (arrow). The inset in (c) displays an electron diffraction pattern with pronounced Debye-Scherrer rings (inverted colors). Arrows in (a) and (b) point to crystalline HfO_2 phases. Published in [260].*

kinetics. This is evident by exemplary TEM images shown in Fig. 8.5. NWs covered with 10 nm HfO_2 deposited at temperatures of 125°C, 250°C and 320°C were etched for 30s in highly diluted HF (0.5%). The HfO_2 layer is completely removed when deposited at the lowest temperature (Fig. 8.5a) whereas its thickness changed only marginally when deposited at 250°C (Fig. 8.5b) or above. For the 250°C sample, the thickness of the amorphous HfO_2 decreased only by about 1 – 2 nm. Due to the roughness of the shell, any information about the etch rate of crystalline HfO_2 cannot be derived. For the sample deposited at the highest deposition temperature, no evidence of an etching is found. HF-based wet chemical etching of HfO_2 strongly depends on the deposition parameters and the post-deposition treatment: the higher the temperature for the deposition or post-deposition annealing, the lower the etch rate [48, 94]. For both cases, this is associated with the degree of crystallization of the HfO_2 layer. However, even the etch rate of amorphous HfO_2 varies strongly with the deposition temperature, as observed on the 125°C and 250°C samples.

To further understand the formation of the crystalline phases, the substrate temperature T_{dep} was set to 250°C and the number of deposition cycles n was varied between 30 and 200 (Series 2). Corresponding TEM images and diffraction pattern are shown in Fig. 8.6. First small crystallites are already seen in the sample with a HfO_2 thickness of only 3 (inset in Fig. 8.6a). However, only few of these crystallites were found on each NW, most of the NW does not contain any crystalline HfO_2 (see Fig. 8.6a). The number and the size of the HfO_2 crystallites increase with increasing the thickness of the dielectric. 50 deposition cycles of HfO_2 result in

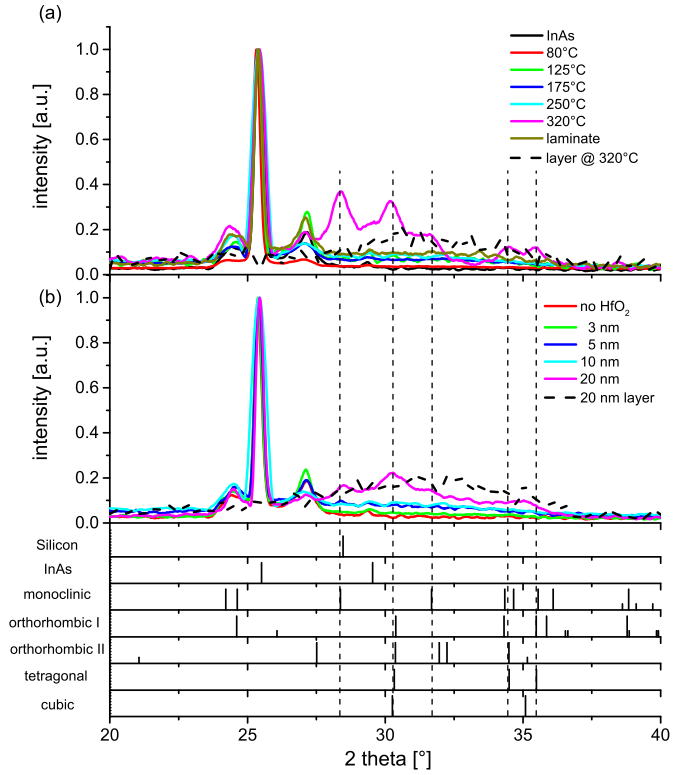

Figure 8.7: *XRD measurements with a constant incidence angle of 5° normalized to the (111) InAs peak. (a) shows the temperature-dependent series, (b) the thickness-dependent series. Dashed curves represent layer systems (Si (001)/HfO_2) for comparison. The bottom shows all possible peak positions for Si, InAs and the five possible crystal structures of HfO_2. [Data courtesy of Jonas Vogel and Dr. Andreas Biermanns.] Published in [260].*

crystallites with diameters up to 5 nm (see Fig. 8.6b). The lateral size increases to $\sim$ 30 nm for 100 deposition cycles (cf. Fig. 2c). The sample with the highest thickness (200 cycles) has a very rough surface and pronounced Debye-Scherrer-rings are obvious (Fig. 8.6c), being similar as the sample grown at the highest temperature in series 1. Apparently, the formation of the HfO_2 crystallites proceeds as follows: the deposition starts with an amorphous structure and turns to a crystalline structure with increasing thickness. Some of the HfO_2 crystallites may even be in contact with the InAs NW without an amorphous interface as seen in Fig. 8.4c.
Similar growth runs were performed on planar samples, i.e. Si/HfO_2 structures were produced. These do not show any evidence of crystalline phases or an increased surface roughening up to a temperature of about 300°C. Additionally, the impact of the crystalline structure of the InAs NWs on the crystallization of the HfO_2 was investigated: 1nm Al_2O_3 was first deposited on the NWs followed by 10 nm HfO_2. The Al_2O_3 is always amorphous when deposited by ALD, thus the subsequent HfO_2 grows on an amorphous layer. Crystalline HfO_2 regions of similar amounts and sizes were still observed, proving that the crystallinity of the substrate does not influence the HfO_2 deposition.
The strong tendency to the formation of crystalline HfO_2 may be caused by the nanoscale dimensions in combination with the faceted shape of the NWs. Alternative explanations like the effective substrate material (InAs) or the high density and high aspect ratio structures (NWs) should mostly affect the first deposition cycles or result in a slower pumping near the sample surface giving rise to a local CVD-like process with higher deposition rate. No evidences for these explanations are observed.

8.2.2. Crystal structure of the HfO_2 crystallites

It has been mentioned above that several crystalline structures of HfO_2 have been reported. Each crystal structure has different dielectric properties. Accordingly, it is important to have

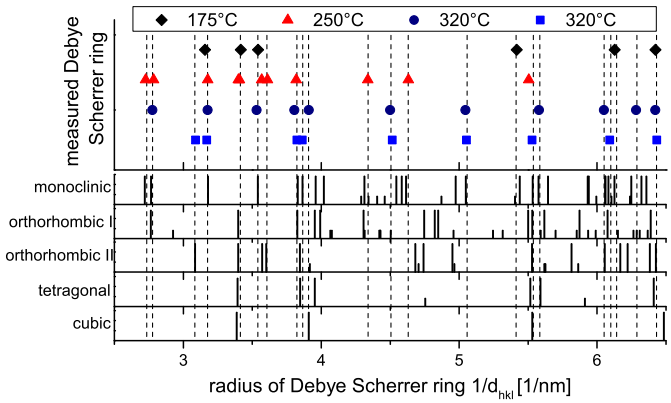

Figure 8.8: *Radii of Debye-Scherrer rings as measured from diffraction pattern of InAs/HfO_2 core-shell NWs with a nominal HfO_2 thickness of 10nm. In the bottom of the figure, the expected radii for the five possible crystal structures are plotted. Published in [260].*

knowledge about the crystal structures present in the HfO_2 shells. The crystal structure of the HfO_2 shells was analyzed using two methods: XRD and electron diffraction in the TEM. Figure 8.7 shows XRD scans of the different deposition series: in (a) the deposition temperature T_{dep} is varied (series 1) while in (b) the deposited thickness (number of deposition cycles n) varies (series 2). Reflections from the Si (111) substrates are not seen due to the constant incidence condition of the x-ray beam. The XRD signal is composed of signals from to polycrystalline HfO_2 and the single crystal InAs NWs. The peak at $\sim 26°$ belongs to the (111) InAs planes. Peaks at $\sim 24°$ and $\sim 27°$ are present for on all samples, even without HfO_2 shells. Consequently, they are attributed to the presence of parasitic InAs, grown in random orientation in between the NWs.
The XRD patterns do not change much below a substrate temperature of 320°C. No clear additional peaks are identified, but a broad peak is present in the region from $\sim 27°$ - $35°$. This broad peak may be attributed to the nanocrystalline regions [136] found in the HRTEM images. Only at the highest temperature, additional peaks are observed. These are ascribed to a combination of the monoclinic phase as well as one additional phase. This is either the orthorhombic or the tetragonal phase.
Similar observations were made for samples with different HfO_2 thicknesses (series 2, see Fig. 8.7b). The broad signal between 27° and 35° increases until peaks occur at a nominal thickness of 20 nm. The peak positions are identical with those of the 320°C sample. Thus, the crystalline structure is a combination of the monoclinic and orthorhombic or tetragonal phase.
Comparable XRD measurements were performed on planar Si(001)/HfO_2 structures, i.e samples without InAs NWs. Si substrates were selected since they represent the best studied substrate for the deposition and crystallization of HfO_2 and therefore allow to compare the results to the literature. XRD measurements from a sample with 10 nm HfO_2 deposited at 320°C and a sample with 20 nm HfO_2 deposited at 250°C on Si substrates are plotted in Fig. 8.7 together with the results from the NWs. The measurements of the planar structures on Si do not show any peaks. Only a broad signal in the range from 25 – 35° is observed. Depositing HfO_2 with similar conditions on InAs NWs gives rise to clear peaks in the XRD measurements (see Fig. 8.7a,b). Consequently, the formation probability of crystalline HfO_2 is strongly enhanced when deposited on InAs NWs compared to the deposition on planar Si samples.

The other method to determine the crystal structure of the HfO_2 is given by the diffraction patterns, i.e. measuring the radii of the Debye-Scherrer rings. This method has some advantages and disadvantages compared to the XRD analyzes. Only crystalline regions on the NW are taken into account when the diffraction patterns are analyzed whereas XRD also probes the substrate. However, in the diffraction patterns only few or single NWs are analyzed and less material contributes to the diffraction signals. This produces only weak diffraction spots or Debye-

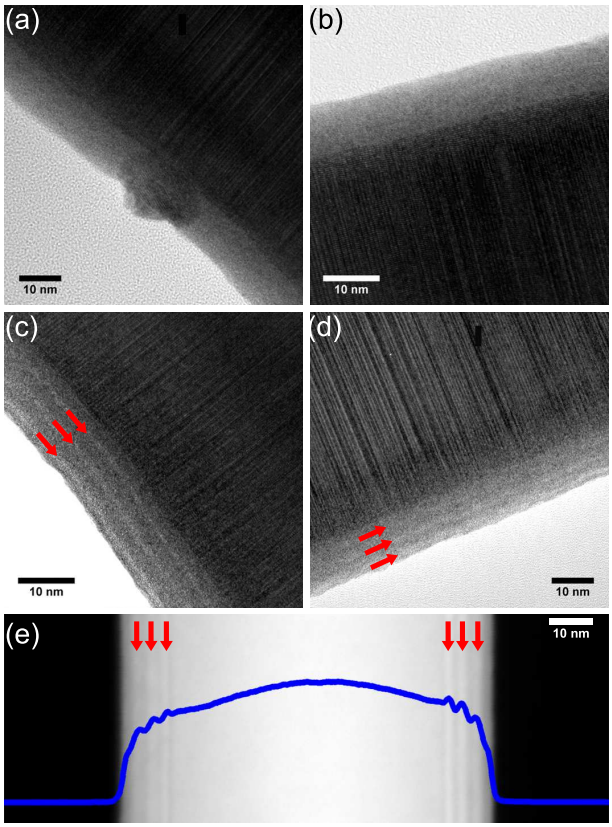

Figure 8.9: *TEM micrographs of laminate structures with $x = 1$ (a), $x = 3$ (b), $x = 6$ (c) and $x = 10$ (d). (e) shows a HAADF image of the laminate structure with $x = 10$. The blue curve plots the HAADF signal. Clear contrast from the Al_2O_3 layers is observed in both TEM and HAADF images (see red arrows). Published in [260].*

Scherrer rings making the identification of the crystal phases difficult. Accordingly, only samples with clear Debye-Scherrer rings were analyzed. Figure 8.8 displays the radii of the Debye-Scherrer rings obtained from the 10 nm thick HfO_2 shells deposited at substrate temperatures of 175°C, 250°C and 320°C. At the bottom of the figure, the radii of Debye-Scherrer rings for all five possible crystal structures of HfO_2 are plotted. Most of the radii of Debye-Scherrer rings can be indexed using the monoclinic phase of HfO_2, being in agreement with the XRD analyses. Some Debye-Scherrer radii (e.g. radii of 3.1nm^{-1}, 3.4nm^{-1}, 4.5nm^{-1}, and 6.4nm^{-1}) cannot be associated with the monoclinic HfO_2 phase, but with the orthorhombic and tetragonal phases. Radii of 3.1nm^{-1} and 4.5nm^{-1} are only possible for the orthorhombic phases. Consequently, HfO_2 is present in the monoclinic phase as well as the orthorhombic phase. The presence of tetragonal HfO_2 cannot be excluded from the analyzes. Similar crystal structures are found to be present in planar Si/HfO_2 structures investigated in the literature, although in general for thicker HfO_2 films or grown at higher deposition temperatures [136, 308].

8.2.3. Laminate HfO_2/Al_2O_3 structures to suppress crystallite formation

A possibility to avoid the formation of crystalline HfO_2 are laminate structures with Al_2O_3 [39, 45, 51, 192, 340]. Such laminate structures increase the crystallization temperature [45, 192] and modify the dielectric constant, leakage currents and hysteresis [39, 51, 340]. The laminate structures investigated here consist of 15 cycles HfO_2 / x cycles Al_2O_3 / 30 cycles HfO_2 / x cycles Al_2O_3 / 30 cycles HfO_2 / x cycles Al_2O_3 / 15 cycles HfO_2. The number x of Al_2O_3 cycles in-between two adjacent HfO_2 depositions was varied between 1 and 10. The thickness of the laminate is in the order of 10 nm. InAs/HfO_2 core-shell NWs with 10 nm thick HfO_2 shells exhibit large crystalline regions in the HfO_2 (see Fig. 8.4c). Figure 8.9a-d show representative TEM micrographs for $x = 1$, 3, 6 and 10, respectively. A single deposition cycle of Al_2O_3

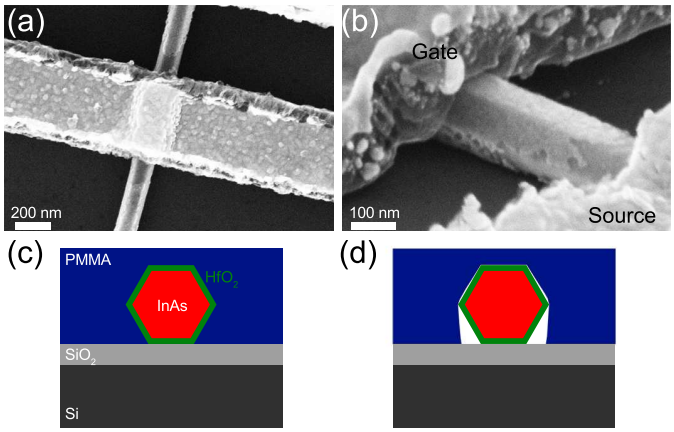

Figure 8.10: *Contacted InAs/HfO_2 core-shell NW with a shell deposited at low temperature. (a) top view SEM micrograph of the source contact, (b) tilted view SEM micrograph of the region between source and gate. Schematic of the ideal (c) and real (d) resist distribution.*

is not sufficient to suppress the crystallization process as seen in Fig. 8.9a. Nonetheless, the number of crystallites along each NW was already reduced significantly. By an increase of the number of Al_2O_3 deposition cycles x to 3, the dielectric layer becomes completely amorphous and also remains amorphous by further increasing the Al_2O_3 thickness (see Figs. 8.9b-d). The Al_2O_3 interlayers provide clear contrast to the HfO_2 layers (see red arrows in Fig. 8.9c,d). This contrast indicates that intermixing between both materials is negligible at temperatures of 250°C. Additionally, the growth rate of the HfO_2 on the NWs can be approximated by the distance between the Al_2O_3 layers. Figure 8.9e shows a HAADF micrograph of the sample with $x = 10$ Al_2O_3 deposition cycles. The blue curve displays the HAADF signal averaged over a vertical distance of 2 nm. Three intensity peaks at both edges are observed, these are attributed to the Al_2O_3 interlayers. The measured HfO_2 deposition rate is equal to that on planar Si substrates, i.e. 1 Å/cycle. To summarize, a single Al_2O_3 deposition cycle is not sufficient to suppress the formation of HfO_2 completely but already three Al_2O_3 deposition cycles, i.e. 2.3 Å, are. It is clearly evident that HfO_2 crystallites are observed only when a certain thickness is exceeded. This method does not only provide the possibility to obtain different thicknesses of the HfO_2-based dielectric layers but also to control its properties.

8.2.4. Structuring HfO_2 shells for source/drain contacts

To use the InAs/HfO_2 core-shell NWs for FETs, the HfO_2 gate dielectric has to be removed locally for the source-drain contacts. As it has been shown above, HfO_2 shells deposited at low temperatures can be etched with diluted HF while high temperature deposited HfO_2 shells are almost not affected at all. Consequently, at first sight, low temperature deposited shells are regarded as the better choice. Figure 8.10 shows a top view (a) as well as a tilted view (b) SEM micrograph of processed InAs/HfO_2 FETs with a HfO_2 shell deposited at a temperature of 120°C. The source contact is shown in Fig. 8.10a. A clear change in brightness along the NW is observed, indicating changes in the surface morphology. The origin is seen in the tilted view SEM micrograph (Fig. 8.10b): the HfO_2 is also etched outside the source region. Interestingly, the HfO_2 is etched inhomogeneously with only slight etching on the upper facet and a much stronger etching at the NW facet close to the substrate. This inhomogeneity indicates that the smallest achievable separation between the source (drain) and the gate is defined by etch mask, that is the PMMA. The etching time (30s) as well as well as the HF concentration (0.5%) are low, thus the PMMA should be stable against the etching. Consequently, the etching inhomogeneity is expected to be mainly caused by the interface between the PMMA and the NW. Figure 8.10c displays the ideal distribution of the PMMA around the NW, while in Fig. 8.10d the expected profile is depicted. In the latter case, the NW is not assumed to be covered completely by the

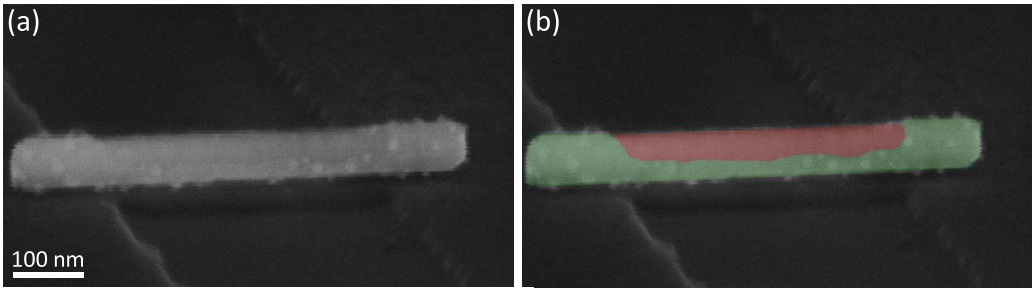

Figure 8.11.: *Etching of the HfO_2 shell around InAs NWs using a combination of Ar^+ bombardment and HF etching. (a) SEM micrograph and (b) false color image (red: etched HfO_2, green: remaining HfO_2). [Data courtesy of Marion Rosien [268]]*

PMMA, rather small voids between the PMMA and some NW side facets are believed to remain. These voids may act as etch channels causing the inhomogeneity of the HfO_2 shell thickness. Therefore, the possible applications of low temperature deposited HfO_2 shells around NWs are limited to structures with rather long distances between the source/drain contacts and the gate metal.

HfO_2 shells deposited at higher temperatures are etched only very slowly by HF (see above) and, certainly, the voids between the PMMA and the NW should form similar structures as in Fig. 8.10a,b. Additionally, PMMA does not withstand a long exposure to HF [119]. The laminate HfO_2/Al_2O_3 shells represent an alternative to pure HfO_2 shells, but the different layers may be etched differently making the etching more complicated. Consequently, the removal of pure HfO_2 deposited at high temperatures is investigated. Chen *et al.* demonstrated a technique to significantly enhance the etch rate of HfO_2 in HF by a bombardment of the HfO_2 *a priori* with Ar^+ [48]. This Ar^+ bombardment was found to induce an amorphization of the crystalline HfO_2 which can then be etched easily with 5% HF.
An Ar^+ bombardment of 15 s performed using a reactive ion etching tool with an Ar gas low of 8 ml/min and a power of 80 W is not sufficient to turn the HfO_2 amorphous. Increasing the bombardment to 60s enables to etch the HfO_2 in 5% HF. Figure 8.11a displays the SEM micrograph of an InAs/HfO_2 core-shell NW with 8 nm HfO_2 shell thickness where the central part was exposed to the Ar^+ bombardment prior to the HF etching. The outer parts were protected by a PMMA mask. After Ar^+ bombardment, the sample was placed in 5 % HF for 60s. The HfO_2 shell is removed only in the region exposed to the Ar^+ ions. Additionally, only the HfO_2 at the upper half is removed (see false color image in Fig. 8.11b), indicating that the lower part is protected from the Ar^+ ions. This clearly demonstrates that the Ar^+ bombardment enhances the HF etch rate and allows a high control of the HfO_2 etching using HF.

The complete removal of the HfO_2 at exposed regions is further confirmed by preliminary electrical measurements with top gates. InAs/HfO_2 core-shell NWs with HfO_2 shell thicknesses of $\sim$ 4 nm and $\sim$ 9 nm are contacted via Ti/Au electrodes and have Ω-shaped top gates. The top gates have a width of about 500 nm, the distance between the source and the drain is 1.5 µm. The Ohmic source-drain contacts are fabricated by a two step process. First, a PMMA layer serves as etch mask. After etching, this PMMA mask is removed since it is damaged due to the Ar^+ bombardment, making a lift-off more complicated. In the second step, a new layer of PMMA is spin coated and a mask for the source-drain contact metallization is written. This mask has openings exactly at the exposed region of the NWs. Figure 8.12 shows the I-V curve (inset) and the transfer characteristic at a source drain bias of 100 mV. The electronic transport is controlled via a Ti/Au top gate. The I-V curves are linear, indicating Ohmic contacts after

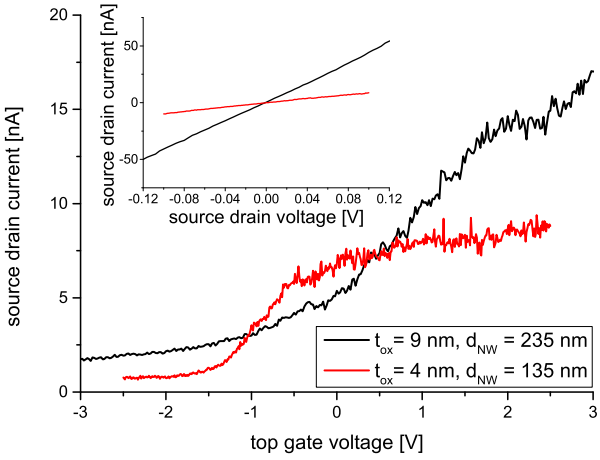

Figure 8.12: *I-V curve (inset) and transfer characteristic of InAs/HfO_2 core-shell NWs with HfO_2 thicknesses of 4 and 9 nm. The source-drain voltage is 100 mV. [Data courtesy of Marion Rosien] [268]*

etching the HfO_2. The transfer characteristics show a clear dependence of the source drain current on the top gate voltage. The thinner NW can be depleted almost completely at negative gate voltages and the current saturates at positive top gate voltages. The thicker NW does not reach the saturation and is not depleted completely at negative gate voltage. Certainly, for both NWs the source drain currents are low being partly attributed to the large contact separation length. Although the I-V characteristics are linear, the contact resistance may still be rather high which increases the overall resistance of the device [289]. This high contact resistance can be caused by residues of HfO_2 or the native oxide of the InAs [289].
To conclude, high temperature deposited HfO_2 layers can be removed from InAs NWs with a high lateral control via a combination of Ar^+ bombardment and wet chemical etching in HF.

8.3. Conclusions

Al_2O_3 dielectrics deposited by ALD on GaAs NWs induced a compressive strain in the semiconductor. This strain was attributed to the different linear thermal expansion coefficients of the III-V semiconductor and the high κ dielectric. HfO_2 shells deposited around InAs NWs were found to contain significant amounts of crystalline phases. The size and number of crystalline HfO_2 grains are a function of the deposited thickness and the substrate temperature. X-ray and electron diffraction revealed that HfO_2 crystallites with the monoclinic and the orthorhombic crystal phases are present. Laminate structures based on Al_2O_3 and HfO_2 avoid the formation of crystalline HfO_2 phases. A two-step process based on an initial Ar^+ bombardment followed by a wet chemical etching in diluted HF was found to be ideal for the structuring of the HfO_2 shells deposited at high temperatures for source drain contacts.

9 Chapter 9. Summary and Outlook

The aims of this thesis were the growth of various III-V NWs and NW heterostructures on GaAs and Si substrates as well as the control over the crystal structure in NWs, focusing on the exploration of the growth parameters, crystal defects, critical dimensions and strain relaxation. The investigated NWs represent candidates for applications in electronic devices (e.g. FETs [297] and TFETs [176]) as well as for the study of fundamental physics, such as the search for Majorana fermions [7, 41] and magneto-conductance oscillations [111, 112]. In particular, the following topics were addressed:

- The growth and crystal structure of InAs NWs on GaAs (111)B, Si (111) and Si (100) substrates: These NWs are the building blocks of some heterostructures investigated in the thesis and represent candidates for electronic devices.
- The growth of NWs with different compositions or dimensions on the very same substrate, which allows to integrate optic and electronic components on the same sample and in the same deposition run.
- The control over the crystal structure of vapor liquid solid grown InAs and GaAs NWs, enabling to integrate barriers in the NWs and to study the conditions leading to the formation of the WZ phase.
- The growth and structural characterization of various heterostructure NWs: These heterostructure NWs allow to investigate the critical dimensions and strain relaxation in low dimensional structures and the possible applications benefit from the different types of band alignments between the semiconductors, e.g. enabling band-to-band tunneling or the formation of tubular conductors.
- The formation of NW junctions, which are 2- or even 3-dimensional structures composed of individual quasi one dimensional NWs.
- The structure and impact of high κ films covering III-V NWs: The high κ shells can act as both dielectrics for the gate electrode and NW passivations preventing the altering of the NW properties.

In order to achieve these goals, MBE and ALD have been used to grow the III-V semiconductors and deposit the high κ films, respectively. Analyzes of the structures were performed by SEM,

TEM and XRD.

First, the growth of InAs NWs on GaAs (111)B and Si (111) substrates was investigated, focusing on the influence of the deposition parameters and of the required substrate preparations on the orientation and dimensions of the NWs. InAs NWs grown via the vapor solid mechanism were found to be rather dense with densities of up to 40 NWs/µm^2. These high NW densities resulted in a subsequent coalescence of neighboring NWs due to radial growth. The NW density could be decreased significantly by a reduction of the supplied In rate, resulting in NW densities being suitable for core-shell NWs. This reduction of the In rate had only a marginal effect on the NW dimensions. NWs as thin as 30 nm in diameter have been observed. An *in situ* doping with Si decreased the aspect ratio of the InAs NW being attributed to the reduction of the In diffusion length. The crystal structure of the vapor solid grown InAs NWs was found to contain numerous stacking faults, only the NW bottom being pure WZ. The latter indicated that conditions leading to the nucleation differ from the axial extension of the NW itself. The nucleation may be caused by an In droplet [24], while the axial growth is droplet free [128]. Indeed, the tip of the NWs, defining the crystal structure during the axial growth, was observed to be faceted with a combination of the {110} and {211} facets. The diameter of the tip was found to be in the range of the expected transition from ZB to WZ, serving as an explanation for the presence of the stacking faults.
The vapor solid growth mechanism of InAs NWs was transferred to Si (111) substrates employing an HF etching of the substrate followed by a reoxidation in hydrogen peroxide. The optimal reoxidation time for a high density of vertical NWs was evaluated to be 1 min. The vapor-liquid-solid growth of InAs NWs on Si substrates via catalyzing In droplets was achieved by applying a Ga predeposition technique. This predeposition enabled the NW growth by etching pinholes into the native silicon oxide. Detailed EDX analyzes revealed the absence of Ga in both the NW and the catalyzing In droplet at the NW tip, confirming a complete reevaporation of the Ga after the pinhole formation. The vapor liquid solid grown InAs NWs exhibited a zinc blende twinning superlattice and short WZ segment below the droplet. The latter was attributed to nucleation at the triple phase line. Apparently, an *ex situ* Si substrate preparation based on a wet chemical treatment for the droplet-free growth of InAs NWs was identified while the necessity of an *in situ* substrate preparation for the droplet assisted InAs NW growth was evaluated.
The vapor solid growth of InAs NWs was adapted to the technological important Si (100) substrate by applying a texturing process exposing pyramids with {111} facets. In the absence of a substrate rotation, the alignment of the pyramids with respect to the effusion cells allowed to grow NWs selectively on predefined facets. In the same time, this technique made it possible to investigate the impact of the growth parameters on the nucleation and subsequent growth in close vicinity and within a single experiment. For example, the influences of the In and As fluxes on the NW density and the role of the As flux on the growth rate of GaAs NWs were proven. Making use of the selective growth on predefined facets, the growth of InAs NWs with different dimensions as well as GaAs and InAs NWs on the very same substrate within close vicinity was demonstrated. Such an integration of different NWs on the same sample allows to obtain the optimal semiconductor for different devices, e.g. FETs and lasers, on the same chip.

A kinetic model was developed explaining the consumption mechanism of the catalyzing Ga droplets on top of GaAs NWs in the presence of As. The model takes into account Ga evaporation from the droplet with a rate of about 1 atom nm^{-2} s^{-1}. This evaporation was found to have a significant contribution to the decrease of the droplet volume. During the droplet consumption the crystal structure switches from ZB to WZ [54, 109, 259]. Making use of the model,

the length of the WZ was predicted. The application of a suitable growth sequence containing group III supply interruptions allowed us to place WZ segments of variable lengths in both ZB GaAs and InAs NWs. Detailed HRTEM investigations demonstrated that the switching from ZB to WZ is not abrupt but an interfacial region between both crystal phases is present. The lengths and structural characteristics of these interfacial regions were found to depend on the growth history, which are any previous supply interruptions as well as the state of the droplet (size, contact angle).

The growth and structural properties of almost lattice matched as well as lattice mismatched NW heterostructures have been investigated. Within the investigated dimensions, core-shell NW heterostructures based on the combination of InAs, GaSb and AlSb were found to be free of misfit dislocations. This was attributed to the lattice mismatch being below 1.2 % as well as the effective strain accommodation in nanostructures. From calculations based on the model developed by Raychaudhuri and Yu [252, 253] it was expected that the critical thickness in core-shell NWs is at least twice the critical thickness in planar systems. The structural characterization performed on InAs/GaSb and InAs/$Al_xGa_{1-x}Sb$ core-shell NWs confirmed this assumption. It was observed that two distinct regimes for the growth of the GaSb shell are present in InAs/GaSb core-shell NWs: the low temperature growth resulted in conformal core-shell NWs while inversely tapered shells were obtained by a growth at higher temperatures. The different morphological characteristics were attributed to a decrease of the adatom diffusion length with a reduction of the growth temperature. $AlGa_xSb_{1-x}$ shells containing more than 20% Al were found to require a GaSb protective cap to prevent strong oxidation.
GaAs cores covered by an InAs shell, forming a conductive tube due to the type I band alignment, relaxed by the formation of misfit dislocations of three different types: perfect dislocations with $b = a/2\langle 110\rangle$ and partial dislocations. These are either Frank partial dislocations ($b = a/3\langle 111\rangle$) producing a stacking fault perpendicular to the growth direction or Shockley partials ($b = a/6\langle 211\rangle$) having stacking faults along other $\langle 111\rangle$ directions. Strain relaxation in the shell was found to occur gradually, inducing simultaneously strain in the GaAs core. The growth of the InAs shell was strongly influenced by the crystal structure of the underlying GaAs core: WZ segments in the core resulted in the absence of InAs shell growth and even twin boundaries were found to result in a roughening of the shell. This was investigated making use of the previously obtained control of the crystal phase in the GaAs core. A phenomenological model based on different lattice mismatches in WZ and ZB core-shell NWs as well as the impact of neighboring group III atoms was developed to explain this crystal phase selective growth. The absence of the InAs shell on the WZ phase allowed us to fabricate InAs nanotubes and to study the electronic transport in these nanotubes. A decrease of the resistivity compared to the core-shell NW counterparts was evaluate, which was attributed to a higher electron concentration in the nanotubes.
Two morphological different GaAs/InSb NW heterostructures have been obtained. The first one is the demonstration of abrupt interfaces between two semiconductors in axial heterostructures grown via the self-catalyzed growth mechanism as well as the first observation of self-catalyzed InSb NW growth by MBE. This was achieved by the nucleation of an In droplet catalyzing the growth of InSb on top of a GaAs NW stem. The interface between both materials was estimated to be more abrupt than 4 nm. The diameter of the InSb was expanded with respect to the GaAs NW stem. This was attributed to the high solubility of Sb in liquid In at temperatures of about 460°C. The axial InSb segments were composed of the ZB crystal phase, partially also containing the WZ phase and the 4H polytype. The occurrence of the 4H and WZ phase was expected to be caused by variations in the droplet supersaturation, possibly during the cool down process

after the growth.
A decrease of the substrate temperature was found to reduce the adatom mobility and increase the sticking coefficient, promoting the radial growth of InSb on GaAs NWs. The radial growth of InSb on GaAs took place on both crystal phases, i.e. ZB and WZ. Identical as for the GaAs/InAs core-shell NWs, the lattice mismatch in the ZB parts in the axial direction was relaxed by perfect, Frank partial and Shockley partial dislocations. Dislocations in the WZ part were observed to be Frank partial dislocations only. The preferred formation of Frank partial dislocations in WZ core-shell NWs was explained by the reduced energy for these dislocations compared to perfect dislocations. As an additional mechanism of strain relaxation, plastic deformation of the InSb shell on the WZ phase of the GaAs core via tilted (0002) lattice planes was identified.

NW junctions, that are NW structures based on the coalescence of two or more individual NWs, have been obtained by the growth of InAs NWs on Si (100) substrates patterned with V-grooves. The optimal dimensions of the V-grooves for a high amount of NW junctions were identified, being lines and spaces with widths in the range of 1 – 5 µm and depths of about 2 µm. Three different shapes of NW junctions were observed and their corresponding formation mechanisms have been described: tip-to-tip (L-shape), tip-to-side (T-shape) and side-to-side (X-shape) junctions. Detailed analyses of the crystal structure of these junctions revealed unexpected ZB phases at the connection point between the NWs. The normally stacking fault rich crystal structure of InAs NWs was transformed into the ZB phase at the tip-to-tip and tip-to-side junctions. The crystal phase transformation was ascribed to a solid phase mechanism involving Shockley partial dislocations. The side-to-side junctions either evidenced Moiré fringes indicating the presence of two separated crystal structures or pure ZB junctions. Preliminary room temperature transport in tip-to-side junctions showed no major difference compared to normal InAs NWs.

Finally, the NWs and NW heterostructures described previously require the passivation of the surface to prevent an altering of the NW properties and to act as a high κ dielectric for electronic application. The deposition of Al_2O_3 around GaAs NWs was found to induce a small compressive strain due to different thermal expansion coefficients of the semiconductor and the high κ dielectric. Concerning HfO_2 shells around InAs NWs, a preferential formation of crystalline phases of the HfO_2 was observed. The amount of crystalline HfO_2 on the NWs was significantly higher than on planar substrates. The tendency of the HfO_2 to crystallize was found to increase with both the thickness and the deposition temperature. Laminate structures based on HfO_2 and Al_2O_3 layers suppressed the crystalline phases. HfO_2 shells deposited at higher temperatures were found to be more resistant to HF-based wet etching than shells deposited at lower temperatures. A combination of Ar^+ bombardment with a subsequent diluted HF etching removed the HfO_2 shells with high lateral control. FET measurements confirmed the successful local etching of the HfO_2.

Certainly, more investigations are required to fully understand some of the aspects discussed in this thesis. To completely reveal the hindered growth of InAs on WZ GaAs, GaAs NWs with pure WZ crystal structure are required since ZB segments in close proximity can affect the nucleation. Using the self-catalyzed growth mechanism, pure WZ GaAs NWs have not been reported, only grown via the Au-assisted growth method [95, 155, 281]. Accordingly, additional work is required to obtain phase pure self-assisted NWs.
The mechanism of the crystal phase transformation in the NW junctions should be studied in more detail. The transformation of the crystal phases may be accelerated by thermal annealing

in As atmosphere. Electronic transport at room as well as at low temperatures is expected to provide further knowledge about the quality of the junctions, i.e. the presence of barriers such as grain boundaries.
NW heterostructures composed of semiconductors belonging to the 6.1 Å family (InAs, GaSb and AlSb) represent another promising structure. InAs/AlSb/InAs core-shell NWs are expected to exhibit a higher electron mobility compared to the GaAs/InAs core-shell NWs due to the absence of misfit dislocations. In both structures, a conductive InAs shell is present. The passivation of InAs with AlSb, either in the form of InAs/AlSb core-shell NWs or as radial InAs quantum wells, should result in rather high electron mobilities due to the conduction band offset of 1.35 eV, similar as for planar layers [181]. Although the growth of some of these InAs-GaSb-AlSb heterostructures has already been addressed in this thesis, a more detailed study of the growth and interfacial quality of InAs on AlSb is required. Additionally, the transport properties of these structures have to be investigated. The passivation of NWs with a high κ dielectric, represents another topic that should be examined thoroughly. Such a passivation is expected to decrease the altering of the NW properties, like mobility and electron concentration, and consequently decrease the spread of the NW resistivity.
The mentioned investigations will strongly benefit from the "nanocluster", where MBE systems, an ALD as well as sputtering tools are connected to each other. This allows the deposition of semiconductors, high κ dielectrics and various metals without breaking the vacuum. The III-V MBEs installed at the "nanocluster"have e.g. a higher angle of the incident flux compared to the GENII system. This higher angle is expected to give rise to a complete shadowing during the simultaneous integration of different NWs on the same sample.

Moreover, additional methods of analysis shall be used to enhance the knowledge e.g. about the impact of stacking defects and dislocation on the electronic transport. Electron holography represents a suitable technique to locate the positions of barriers inside the NWs and to measure the electrostatic potential inside devices [212, 311]. Fabricating devices suitable for such measurements is difficult since the NWs have to be contacted on an electron transparent membrane which is still suitable for room and low temperature measurements. Hackemüller recently developed the technology to obtain such substrates [119].

Acknowledgments

Certainly, many people contributed to this thesis via different ways. Several of these persons should be thanked here explicitly.
First of all, I thank my doctoral advisor Prof. Dr. Detlev Grützmacher for giving me the opportunity and all the support to prepare the thesis at the PGI9. I could not only enter the fascinating world of the growth and properties of nanoscale objects, I was also allowed to present the research at several international conferences.
I am thankful to my academic supervisor Dr. Mihail Ion Lepsa for introducing me to the MBE growth, hundreds of discussions e.g. about the growth, the crystal structure and the substrate preparation but also for giving me the opportunity to try different things. This open-minded atmosphere is perfect for research.
All the TEM-based investigations would not have been possible without the help of Dr. Martina Luysberg. She introduced me to the *Tecnai* microscope at the Ernst Ruska Centre and supported this research with a lot of critical questions.
Some of the most important people are often those who don't receive much public appreciation: the engineers keeping all the systems running! My sincere gratefulness is dedicated to Christoph Krause who took care about the III-V MBEs, the ALD, the metallization system, the DI water in the lab .... All the systems seemed to work at 98% of the time. Werner Pieper is acknowledged for the maintenance of the TEM.
The XRD measurements presented would not have been possible without Dr. Gregor Mussler as well as the group of Prof. Dr. Ullrich Pietsch, namely Dr. Andreas Biermanns and Jonas Vogel, at the University of Siegen. They always shared their knowledge e.g. about x-ray diffraction and the crystal structure with me.
Many students contributed with their internships and their diploma, bachelor or master theses to the results shown here:

- Torsten Jörres assisted with the deposition of Al_2O_3 and HfO_2 layers by ALD during his diploma thesis
- Marion Rosien initiated the electrical measurements on the InAs nanotubes during her internship and subsequently processed the InAs/HfO_2 core-shell NW FETs during her master thesis
- Daniel Rosenbach prepared textured substrates, V-grooves and analyzed the corresponding NWs during his bachelor thesis
- Franz Josef Hackemüller investigated the selective wet chemical etching for InAs/GaSb core-shell NWs and started the challenging substrate preparation for electron holography during his master thesis and associated projects
- Denise Temme, Jordan Occena and Peyton Shi helped analyzing the NWs during their internships

Some students recently started their work on the NWs:

- Daniil Vakulov started to analyze NW junctions electrically and to prepare the V-grooves via optical lithography during his internship at the PGI9
- Naeem Ashraf started to prepare Si substrates for the position controlled growth of NWs, associated with his master thesis

Elmar Neumann (PGI8-PT) and Benedikt Bauer (University of Regensburg) helped with the fabrication of the NW cross-sections for TEM analyzes, either by means of FIB or ultramicrotomy. The latter is fascinating simple and fast method to obtain NW cross section ... but unfortunately not available at the PGI9.
Sebastian Heedt is thanked especially for his support during the fabrication of the V-grooves and for "pushing" me to focus on this exciting growth.
Special thanks are dedicated to Prof. Dr. Thomas Schäpers, Prof. Dr. Hans Lüth and all their "transport guys" for their continues interest in the core-shell NWs and their tries to explain me the transport in detail. Certainly, the almost infinite number of students working on the transport in the NWs, primary the GaAs/InAs core-shell NWs, are acknowledged for discussions, suggestions etc: Dr. Christian Blömers, Dr. Yusuf Günel, Dr. Karl Weis, Fabian Haas, Önder Gül, Sebastian Heedt, Patrick Zellekens, Tobias Wenz, Lukas Jarvers, Sven Dickheuer, Jens Schwenderling, Franz Josef Hackemüller, Marion Rosien, Daniel Rosenbach, Daniil Vakulov, Torsten Jörres ....
The "epitaxy people", Dr. Hilde Hardtdegen, Dr. Kamil Sladek, Jörn Kampmeier, Anna Haab etc are acknowledged for discussions and suggestions for all the epitaxy-related stuff.
During the PhD, I shared the office with Dr. Svetlana Borisova, Jörn Kampmeier, Jan Dauber, Marion Rosien and Daniil Vakulov, who have always supported me with funny and interesting stories and made even long office day passing by.
The work of the clean room team, especially Dr. Jürgen Moers and Dr. Stefan Trellenkamp, helped a lot for achieving the results.
The heart and soul of the institute, Silke Piper, is of course acknowledged for maintaining the good atmosphere and her help with all administrative stuff.

Finally, special acknowledgments are devoted to my family and my girlfriend for all the non-scientific support. Without this, 3 1/2 years of PhD studies would not have been possible.

List of Figures

List of Tables

List Of Abbreviations

ALD	**A**tomic **l**ayer **d**eposition
BCB	**B**enzo**c**yclo**b**utene
EBL	**E**lectron **b**eam **l**ithography
EDX	**E**nergy **d**ispersive **x**-ray spectroscopy
FEM	**F**inite **e**lement **m**ethod
FET	**F**ield **e**ffect **t**ransistor
FFT	**F**ast **F**ourier **t**ransformation
FIB	**F**ocused **i**on **b**eam
GPA	**G**eometric **p**hase **a**nalysis
HAADF	**H**igh **a**ngle **a**nnular **d**ark **f**ield
HRTEM	**H**igh **r**esolution **t**ransmission **e**lectron **m**icroscope
HSQ	**H**ydrogen **s**ilses**q**uioxane
MBE	**M**olecular **b**eam **e**pitaxy
MIBK	**M**ethyl **i**so**b**utyl **k**etone
MOVPE	**M**etal **o**rganic **v**apor **p**hase **e**pitaxy
NW	**N**ano**w**ire
SAED	**S**elective **a**rea **e**lectron **d**iffraction
SEM	**S**canning **e**lectron **m**icroscope
STEM	**S**canning **t**ransmission **e**lectron **m**icroscope
TEM	**T**ransmission **e**lectron **m**icroscope
TFET	**T**unnel **f**ield **e**ffect **t**ransistor
UHV	**U**ltra **h**igh **v**acuum
VLS	**V**apor-**l**iquid-**s**olid
VS	**V**apor-**s**olid
WZ	**W**urt**z**ite
XRD	**X**-**r**ay **d**iffraction
ZB	**Z**inc **b**lende

Bibliography

[1] L. Ahtapodov, J. Todorovic, P. Olk, T. Mjåland, P. Slåttnes, D. L. Dheeraj, A. T. J. van Helvoort, B.-O. Fimland, and H. Weman. A story told by a single nanowire: optical properties of wurtzite GaAs. *Nano letters*, 12(12):6090–5, 2012. doi:10.1021/nl3025714.

[2] K. E. Aifantis, A. L. Kolesnikova, and A. E. Romanov. Nucleation of misfit dislocations and plastic deformation in core/shell nanowires. *Philosophical Magazine*, 87(30):4731–4757, 2007. doi:10.1080/14786430701589350.

[3] T. Akiyama, K. Sano, K. Nakamura, and T. Ito. An Empirical Potential Approach to Wurtzite-Zinc-Blende Polytypism in Group III-V Semiconductor Nanowires. *Japanese Journal of Applied Physics*, 45(No. 9):L275–L278, 2006. doi:10.1143/JJAP.45.L275.

[4] N. Akopian, G. Patriarche, L. Liu, J.-C. Harmand, and V. Zwiller. Crystal phase quantum dots. *Nano letters*, 10(4):1198–201, 2010. doi:10.1021/nl903534n.

[5] P. A. Alekseev, M. S. Dunaevskii, A. V. Stovpyaga, M. Lepsa, and A. N. Titkov. Measurement of Young's modulus of GaAs nanowires growing obliquely on a substrate. *Semiconductors*, 46(5):641–646, 2012. doi:10.1134/S106378261205003X.

[6] C. Alibert, A. Joullié, and C. Ance. Modulation-spectroscopy study of the $Ga_{1-x}Al_xSb$ band structure. *Physical Review B*, 27(8):4946–4954, 1983. doi:10.1103/PhysRevB.27.4946.

[7] J. Alicea, Y. Oreg, G. Refael, F. von Oppen, and M. P. A. Fisher. Non-Abelian statistics and topological quantum information processing in 1D wire networks. *Nature Physics*, 7(5):412–417, 2011. doi:10.1038/nphys1915.

[8] N. G. Anderson and S. D. Jones. Optimized tight-binding valence bands and heterojunction offsets in strained III-V semiconductors. *Journal of Applied Physics*, 70(8):4342, 1991. doi:10.1063/1.349115.

[9] J. Appenzeller, C. Schroer, T. Schäpers, A. Hart, A. Förster, B. Lengeler, and H. Lüth. Electron interference in a T-shaped quantum transistor based on Schottky-gate technology. *Physical Review B*, 53(15):9959–9963, 1996. doi:10.1103/PhysRevB.53.9959.

[10] S. Assali, I. Zardo, S. Plissard, D. Kriegner, M. A. Verheijen, G. Bauer, A. Meijerink, A. Belabbes, F. Bechstedt, J. E. M. Haverkort, and E. P. A. M. Bakkers. Direct band gap wurtzite gallium phosphide nanowires. *Nano letters*, 13(4):1559–63, 2013. doi:10.1021/nl304723c.

[11] J. E. Ayers. *Heteroepitaxy of Semiconductors: Theory, Growth, and Characterization*. CRC Press, 2007.

[12] A. Y. Babkevich, R. A. Cowley, N. J. Mason, S. Sandiford, and A. Stunault. X-ray scattering from epitaxial GaSb/InAs thin films below and above the critical thickness. *Journal of Physics: Condensed Matter*, 14(30):7101–7121, 2002. doi:10.1088/0953-8984/14/30/302.

[13] S. Bandyopadhyay, M. I. Hossain, H. Ahmad, J. Atulasimha, and S. Bandyopadhyay. Coherent spin transport and suppression of spin relaxation in InSb nanowires with single subband occupancy at room temperature. *Small (Weinheim an der Bergstrasse, Germany)*, 10(21):4379–85, 2014. doi:10.1002/smll.201401022.

[14] M. Bar-Sadan, J. Barthel, H. Shtrikman, and L. Houben. Direct imaging of single Au atoms within GaAs nanowires. *Nano letters*, 12(5):2352–6, 2012. doi:10.1021/nl300314k.

[15] A. N. Baranov, N. Bertru, Y. Cuminal, G. Boissier, C. Alibert, and A. Joullié. Observation of room-temperature laser emission from type III InAs/GaSb multiple quantum well structures. *Applied Physics Letters*, 71(6):735, 1997. doi:10.1063/1.119629.

[16] J. Batey and S. L. Wright. Energy band alignment in GaAs:(Al,Ga)As heterostructures: The dependence on alloy composition. *Journal of Applied Physics*, 59(1):200, 1986. doi:10.1063/1.336864.

[17] B. R. Bennett, J. B. Boos, M. G. Ancona, N. A. Papanicolaou, G. A. Cooke, and H. Kheyrandish. InAlSb/InAs/AlGaSb Quantum Well Heterostructures for High-Electron-Mobility Transistors. *Journal of Electronic Materials*, 36(2):99–104, 2007. doi:10.1007/s11664-006-0057-5.

[18] B. R. Bennett, B. P. Tinkham, J. B. Boos, M. D. Lange, and R. Tsai. Materials growth for InAs high electron mobility transistors and circuits. *Journal of Vacuum Science & Technology B: Microelectronics and Nanometer Structures*, 22(2):688, 2004. doi:10.1116/1.1667507.

[19] B. R. Bennett, M. J. Yang, B. V. Shanabrook, J. B. Boos, and D. Park. Modulation doping of InAs/AlSb quantum wells using remote InAs donor layers. *Applied Physics Letters*, 72(10):1193, 1998. doi:10.1063/1.121010.

[20] G. Bersuker, J. Yum, L. Vandelli, A. Padovani, L. Larcher, V. Iglesias, M. Porti, M. Nafría, K. McKenna, A. Shluger, P. Kirsch, and R. Jammy. Grain boundary-driven leakage path formation in HfO_2 dielectrics. *Solid-State Electronics*, 65-66:146–150, 2011. doi:10.1016/j.sse.2011.06.031.

[21] M. J. Biercuk, D. J. Monsma, C. M. Marcus, J. S. Becker, and R. G. Gordon. Low-temperature atomic-layer-deposition lift-off method for microelectronic and nanoelectronic applications. *Applied Physics Letters*, 83(12):2405, 2003. doi:10.1063/1.1612904.

[22] A. Biermanns. *X-ray diffraction from single GaAs nanowires*. PhD thesis, University of Siegen, 2012.

[23] A. Biermanns, S. Breuer, A. Davydok, L. Geelhaar, and U. Pietsch. Structural evolution of self-assisted GaAs nanowires grown on Si(111). *physica status solidi (RRL) - Rapid Research Letters*, 5(4):156–158, 2011. doi:10.1002/pssr.201105055.

[24] A. Biermanns, E. Dimakis, A. Davydok, T. Sasaki, L. Geelhaar, M. Takahasi, and U. Pietsch. Role of liquid indium in the structural purity of wurtzite InAs nanowires that grow on Si(111). *Nano letters*, 14(12):6878–83, 2014. doi:10.1021/nl502878a.

[25] A. Biermanns, T. Rieger, G. Bussone, U. Pietsch, D. Grützmacher, and M. Ion Lepsa. Axial strain in GaAs/InAs core-shell nanowires. *Applied Physics Letters*, 102(4):043109, 2013. doi:10.1063/1.4790185.

[26] C. Blömers, T. Grap, M. I. Lepsa, J. Moers, S. Trellenkamp, D. Grützmacher, H. Lüth, and T. Schäpers. Hall effect measurements on InAs nanowires. *Applied Physics Letters*, 101(15):152106, 2012. doi:10.1063/1.4759124.

[27] C. Blömers, T. Rieger, T. Grap, M. Raux, M. I Lepsa, H. Lüth, D. Grützmacher, and T. Schäpers. Gate-induced transition between metal-type and thermally activated transport in self-catalyzed MBE-grown InAs nanowires. *Nanotechnology*, 24(32):325201, 2013. doi:10.1088/0957-4484/24/32/325201.

[28] C. Blömers, T. Rieger, P. Zellekens, F. Haas, M. I. Lepsa, H. Hardtdegen, O. Gül, N. Demarina, D. Grützmacher, H. Lüth, and T. Schäpers. Realization of nanoscaled tubular conductors by means of GaAs/InAs core/shell nanowires. *Nanotechnology*, 24(3):035203, 2012. doi:10.1088/0957-4484/24/3/035203.

[29] F. Bohra, B. Jiang, and J.-M. Zuo. Textured crystallization of ultrathin hafnium oxide films on silicon substrate. *Applied Physics Letters*, 90(16):161917, 2007. doi:10.1063/1.2724925.

[30] J. L. Boland, S. Conesa-Boj, P. Parkinson, G. Tütüncüoglu, F. Matteini, D. Rüffer, A. Casadei, F. Amaduzzi, F. Jabeen, C. L. Davies, H. J. Joyce, L. M. Herz, A. Fontcuberta I Morral, and M. B. Johnston. Modulation Doping of GaAs/AlGaAs Core-Shell Nanowires With Effective Defect Passivation and High Electron Mobility. *Nano letters*, 2015. doi:10.1021/nl504566t.

[31] B. M. Borg, K. A. Dick, B. Ganjipour, M.-E. Pistol, L.-E. Wernersson, and C. Thelander. InAs/GaSb heterostructure nanowires for tunnel field-effect transistors. *Nano letters*, 10(10):4080–5, 2010. doi:10.1021/nl102145h.

[32] B. M. Borg, M. Ek, B. Ganjipour, A. W. Dey, K. A. Dick, L.-E. Wernersson, and C. Thelander. Influence of doping on the electronic transport in GaSb/InAs(Sb) nanowire tunnel devices. *Applied Physics Letters*, 101(4):043508, 2012. doi:10.1063/1.4739082.

[33] M. Borg, H. Schmid, K. E. Moselund, G. Signorello, L. Gignac, J. Bruley, C. Breslin, P. Das Kanungo, P. Werner, and H. Riel. Vertical III-V nanowire device integration on Si(100). *Nano letters*, 14(4):1914–20, 2014. doi:10.1021/nl404743j.

[34] R. Boukhicha, C. Gardès, L. Vincent, C. Renard, V. Yam, F. Fossard, G. Patriarche, F. Jabeen, and D. Bouchier. Gold anchoring on Si sawtooth faceted nanowires. *EPL (Europhysics Letters)*, 95(1):18004, 2011. doi:10.1209/0295-5075/95/18004.

[35] S. Brotherton and J. Lowther. Electron and Hole Capture at Au and Pt Centers in Silicon. *Physical Review Letters*, 44(9):606–609, 1980. doi:10.1103/PhysRevLett.44.606.

[36] G. Bussone, E. Dimakis, R. Grifone, A. Biermanns, A. Tahraoui, D. Carbone, L. Geelhaar, T. U. Schülli, and U. Pietsch. Impact of strain induced by polymer curing in benzocyclobutene embedded semiconductor nanostructures. *physica status solidi (RRL) - Rapid Research Letters*, 8(12):1007–1010, 2014. doi:10.1002/pssr.201409346.

[37] Y.-C. Byun, C. Mahata, C.-H. An, J. Oh, R. Choi, and H. Kim. Interfacial and electrical properties of HfO_2 gate dielectrics grown on GaAs by atomic layer deposition using different oxidants. *Journal of Physics D: Applied Physics*, 45(43):435305, 2012. doi:10.1088/0022-3727/45/43/435305.

[38] R. Calarco, R. J. Meijers, R. K. Debnath, T. Stoica, E. Sutter, and H. Lüth. Nucleation and growth of GaN nanowires on Si(111) performed by molecular beam epitaxy. *Nano letters*, 7(8):2248–51, 2007. doi:10.1021/nl0707398.

[39] F. Campabadal, J. M. Rafi, M. Zabala, O. Beldarrain, A. Faigon, H. Castan, A. Gomez, H. Garcia, and S. Duenas. Electrical characteristics of metal-insulator-semiconductor structures with atomic layer deposited Al_2O_3, HfO_2, and nanolaminates on different silicon substrates. *Journal of Vacuum Science & Technology B: Microelectronics and Nanometer Structures*, 29(1):01AA07, 2011. doi:10.1116/1.3532544.

[40] P. Capiod, T. Xu, J. P. Nys, M. Berthe, G. Patriarche, L. Lymperakis, J. Neugebauer, P. Caroff, R. E. Dunin-Borkowski, P. Ebert, and B. Grandidier. Band offsets at zincblende-wurtzite GaAs nanowire sidewall surfaces. *Applied Physics Letters*, 103(12):122104, 2013. doi:10.1063/1.4821293.

[41] D. Car, J. Wang, M. A. Verheijen, E. P. A. M. Bakkers, and S. R. Plissard. Rationally designed single-crystalline nanowire networks. *Advanced materials*, 26(28):4875–9, 2014. doi:10.1002/adma.201400924.

[42] P. Caroff, M. E. Messing, B. Mattias Borg, K. A. Dick, K. Deppert, and L.-E. Wernersson. InSb heterostructure nanowires: MOVPE growth under extreme lattice mismatch. *Nanotechnology*, 20(49):495606, 2009. doi:10.1088/0957-4484/20/49/495606.

[43] P. Caroff, J. B. Wagner, K. A. Dick, H. A. Nilsson, M. Jeppsson, K. Deppert, L. Samuelson, L. R. Wallenberg, and L.-E. Wernersson. High-quality InAs/InSb nanowire heterostructures grown by metal-organic vapor-phase epitaxy. *Small*, 4(7):878–82, 2008. doi:10.1002/smll.200700892.

[44] A. Casadei, P. Krogstrup, M. Heiss, J. A. Röhr, C. Colombo, T. Ruelle, S. Upadhyay, C. B. Sorensen, J. Nygard, and A. Fontcuberta i Morral. Doping incorporation paths in catalyst-free Be-doped GaAs nanowires. *Applied Physics Letters*, 102(1):013117, 2013. doi:10.1063/1.4772020.

[45] H. S. Chang, H. Hwang, M.-H. Cho, D. W. Moon, S. J. Doh, J. H. Lee, and N.-I. Lee. Thermal stability and decomposition of the HfO_2-Al_2O_3 laminate system. *Applied Physics Letters*, 84(1):28, 2004. doi:10.1063/1.1637955.

[46] C. Chen, Y. Shi, Y. Zhang, J. Zhu, and Y. Yan. Size Dependence of Young's Modulus in ZnO Nanowires. *Physical Review Letters*, 96(7):075505, 2006. doi:10.1103/PhysRevLett.96.075505.

[47] G. Chen and I. Kashkoush. Effect of Pre-Cleaning on Texturization of c-Si Wafers in a KOH/IPA Mixture. *ECS Transactions*, 25(15):3–10, 2010. doi:10.1149/1.3300415.

[48] J. Chen, W. J. Yoo, D. S. H. Chan, and D.-L. Kwong. Effects of Annealing and Ar Ion Bombardment on the Removal of HfO_2 Gate Dielectric. *Electrochemical and Solid-State Letters*, 7(3):F18, 2004. doi:10.1149/1.1642577.

[49] C.-W. Cheng, J. Hennessy, D. Antoniadis, and E. A. Fitzgerald. Self-cleaning and surface recovery with arsine pretreatment in ex situ atomic-layer-deposition of Al_2O_3 on GaAs. *Applied Physics Letters*, 95(8):082106, 2009. doi:10.1063/1.3213545.

[50] M. C. Cheynet, S. Pokrant, F. D. Tichelaar, and J.-L. Rouvieère. Crystal structure and band gap determination of HfO_2 thin films. *Journal of Applied Physics*, 101(5):054101, 2007. doi:10.1063/1.2697551.

[51] M.-H. Cho, Y. S. Roh, C. N. Whang, K. Jeong, H. J. Choi, S. W. Nam, D.-H. Ko, J. H. Lee, N. I. Lee, and K. Fujihara. Dielectric characteristics of Al_2O_3-HfO_2 nanolaminates on Si(100). *Applied Physics Letters*, 81(6):1071, 2002. doi:10.1063/1.1499223.

[52] S. Choi, M. J. Word, V. Kumar, and I. Adesida. Comparative study of thermally cured and electron-beam-exposed hydrogen silsesquioxane resists. *Journal of Vacuum Science & Technology B: Microelectronics and Nanometer Structures*, 26(5):1654, 2008. doi:10.1116/1.2960565.

[53] R. Choudhury, D. R. Bowler, and M. J. Gillan. Atomic structure of misfit dislocations at InAs/GaAs(110). *Journal of physics. Condensed matter : an Institute of Physics journal*, 20(23):235227, 2008. doi:10.1088/0953-8984/20/23/235227.

[54] G. Cirlin, V. Dubrovskii, Y. Samsonenko, A. Bouravleuv, K. Durose, Y. Proskuryakov, B. Mendes, L. Bowen, M. Kaliteevski, R. Abram, and D. Zeze. Self-catalyzed, pure zincblende GaAs nanowires grown on Si(111) by molecular beam epitaxy. *Physical Review B*, 82(3):1–6, 2010. doi:10.1103/PhysRevB.82.035302.

[55] C. Colombo, D. Spirkoska, M. Frimmer, G. Abstreiter, and A. Fontcuberta i Morral. Ga-assisted catalyst-free growth mechanism of GaAs nanowires by molecular beam epitaxy. *Physical Review B*, 77(15):2–6, 2008. doi:10.1103/PhysRevB.77.155326.

[56] S. Conesa-Boj, D. Kriegner, X.-L. Han, S. Plissard, X. Wallart, J. Stangl, A. Fontcuberta i Morral, and P. Caroff. Gold-free ternary III-V antimonide nanowire arrays on silicon: twin-free down to the first bilayer. *Nano letters*, 14(1):326–32, 2014. doi:10.1021/nl404085a.

[57] S. Conesa-Boj, E. Russo-Averchi, A. Dalmau-Mallorqui, J. Trevino, E. F. Pecora, C. Forestiere, A. Handin, M. Ek, L. Zweifel, L. R. Wallenberg, D. Rüffer, M. Heiss, D. Troadec, L. Dal Negro, P. Caroff, and A. Fontcuberta I Morral. Vertical III-V V-Shaped Nano-Membranes Epitaxially Grown on a Patterned Si[001] Substrate and their Enhanced Light Scattering. *ACS nano*, 6:10982–91, 2012. doi:10.1021/nn304526k.

[58] A. Cullis, A. Pidduck, and M. Emeny. Growth morphology evolution and dislocation introduction in the heteroepitaxial system. *Journal of Crystal Growth*, 158(1-2):15–27, 1996. doi:10.1016/0022-0248(95)00430-0.

[59] L. C. O. Dacal and A. Cantarero. Ab initio calculations of indium arsenide in the wurtzite phase: structural, electronic and optical properties. *Materials Research Express*, 1(1):015702, 2014. doi:10.1088/2053-1591/1/1/015702.

[60] E. Dailey, P. Madras, and J. Drucker. Au on vapor-liquid-solid grown Si nanowires: Spreading of liquid AuSi from the catalytic seed. *Journal of Applied Physics*, 108(6):064320, 2010. doi:10.1063/1.3487971.

[61] S. Datta, H. Liu, and V. Narayanan. Tunnel FET technology: A reliability perspective. *Microelectronics Reliability*, 54(5):861–874, 2014. doi:10.1016/j.microrel.2014.02.002.

[62] A. Davydok, T. Rieger, A. Biermanns, M. Saqib, T. Grap, M. I. Lepsa, and U. Pietsch. Alloy formation during molecular beam epitaxy growth of Si-doped InAs

nanowires on GaAs[111]B. *Journal of Applied Crystallography*, 46(4):893–897, 2013. doi:10.1107/S0021889813010522.

[63] S. A. Dayeh, C. Soci, X.-Y. Bao, and D. Wang. Advances in the synthesis of InAs and GaAs nanowires for electronic applications. *Nano Today*, 4(4):347–358, 2009. doi:10.1016/j.nantod.2009.06.010.

[64] S. A. Dayeh, W. Tang, F. Boioli, K. L. Kavanagh, H. Zheng, J. Wang, N. H. Mack, G. Swadener, J. Y. Huang, L. Miglio, K.-N. Tu, and S. T. Picraux. Direct measurement of coherency limits for strain relaxation in heteroepitaxial core/shell nanowires. *Nano letters*, 13(5):1869–76, 2013. doi:10.1021/nl3022434.

[65] M. de la Mata, C. Magén, P. Caroff, and J. Arbiol. Atomic scale strain relaxation in axial semiconductor III-V nanowire heterostructures. *Nano letters*, 14(11):6614–20, 2014. doi:10.1021/nl503273j.

[66] M. de la Mata, C. Magen, J. Gazquez, M. I. B. Utama, M. Heiss, S. Lopatin, F. Furtmayr, C. J. Fernández-Rojas, B. Peng, J. R. Morante, R. Rurali, M. Eickhoff, A. Fontcuberta i Morral, Q. Xiong, and J. Arbiol. Polarity assignment in ZnTe, GaAs, ZnO, and GaN-AlN nanowires from direct dumbbell analysis. *Nano letters*, 12(5):2579–86, 2012. doi:10.1021/nl300840q.

[67] M. C. Debnath, T. D. Mishima, M. B. Santos, L. C. Phinney, T. D. Golding, and K. Hossain. High electron mobility in InSb epilayers and quantum wells grown with AlSb nucleation on Ge-on-insulator substrates. *Journal of Vacuum Science & Technology B: Microelectronics and Nanometer Structures*, 32(2):02C116, 2014. doi:10.1116/1.4866397.

[68] O. Demichel, M. Heiss, J. Bleuse, H. Mariette, and A. Fontcuberta i Morral. Impact of surfaces on the optical properties of GaAs nanowires. *Applied Physics Letters*, 97(20):201907, 2010. doi:10.1063/1.3519980.

[69] M. T. Deng, C. L. Yu, G. Y. Huang, M. Larsson, P. Caroff, and H. Q. Xu. Anomalous zero-bias conductance peak in a Nb-InSb nanowire-Nb hybrid device. *Nano letters*, 12(12):6414–9, 2012. doi:10.1021/nl303758w.

[70] G. C. DeSalvo. Citric Acid Etching of $GaAs_{1-x}Sb_x$, $Al_{0.5}Ga_{0.5}Sb$, and InAs for Heterostructure Device Fabrication. *Journal of The Electrochemical Society*, 141(12):3526, 1994. doi:10.1149/1.2059365.

[71] L. Desplanque, D. Vignaud, and X. Wallart. High mobility metamorphic AlSb/InAs heterostructures grown on InP substrates. *Journal of Crystal Growth*, 301-302:194–198, 2007. doi:10.1016/j.jcrysgro.2006.11.229.

[72] A. W. Dey, J. Svensson, M. Ek, E. Lind, C. Thelander, and L.-E. Wernersson. Combining axial and radial nanowire heterostructures: radial Esaki diodes and tunnel field-effect transistors. *Nano letters*, 13(12):5919–24, 2013. doi:10.1021/nl4029494.

[73] D. L. Dheeraj, G. Patriarche, H. Zhou, T. B. Hoang, A. F. Moses, S. Grø nsberg, A. T. J. van Helvoort, B.-O. Fimland, and H. Weman. Growth and characterization of wurtzite GaAs nanowires with defect-free zinc blende GaAsSb inserts. *Nano letters*, 8(12):4459–63, 2008. doi:10.1021/nl802406d.

[74] K. A. Dick, J. Bolinsson, B. M. Borg, and J. Johansson. Controlling the abruptness of axial heterojunctions in III-V nanowires: beyond the reservoir effect. *Nano letters*, 12(6):3200–6, 2012. doi:10.1021/nl301185x.

[75] K. A. Dick, K. Deppert, M. W. Larsson, T. Mårtensson, W. Seifert, L. R. Wallenberg, and L. Samuelson. Synthesis of branched "nanotrees" by controlled seeding of multiple branching events. *Nature materials*, 3(6):380–4, 2004. doi:10.1038/nmat1133.

[76] K. A. Dick, K. Deppert, M. W. Larsson, W. Seifert, L. R. Wallenberg, and L. Samuelson. Height-controlled nanowire branches on nanotrees using a polymer mask. *Nanotechnology*, 18(3):035601, 2007. doi:10.1088/0957-4484/18/3/035601.

[77] K. A. Dick, Z. Geretovszky, A. Mikkelsen, L. S. Karlsson, E. Lundgren, J.-O. Malm, J. N. Andersen, L. Samuelson, W. Seifert, B. A. Wacaser, and K. Deppert. Improving InAs nanotree growth with composition-controlled Au-In nanoparticles. *Nanotechnology*, 17(5):1344–1350, 2006. doi:10.1088/0957-4484/17/5/029.

[78] O. Dier, C. Lin, M. Grau, and M.-C. Amann. Selective and non-selective wet-chemical etchants for GaSb-based materials. *Semiconductor Science and Technology*, 19(11):1250–1253, 2004. doi:10.1088/0268-1242/19/11/006.

[79] E. Dimakis, U. Jahn, M. Ramsteiner, A. Tahraoui, J. Grandal, X. Kong, O. Marquardt, A. Trampert, H. Riechert, and L. Geelhaar. Coaxial multishell (In,Ga)As/GaAs nanowires for near-infrared emission on Si substrates. *Nano letters*, 14(5):2604–9, 2014. doi:10.1021/nl500428v.

[80] E. Dimakis, J. Lähnemann, U. Jahn, S. Breuer, M. Hilse, L. Geelhaar, and H. Riechert. Self-Assisted Nucleation and Vapor-Solid Growth of InAs Nanowires on Bare Si(111). *Crystal Growth & Design*, 11(9):4001–4008, 2011. doi:10.1021/cg200568m.

[81] E. Dimakis, M. Ramsteiner, C.-N. Huang, A. Trampert, A. Davydok, A. Biermanns, U. Pietsch, H. Riechert, and L. Geelhaar. In situ doping of catalyst-free InAs nanowires with Si: Growth, polytypism, and local vibrational modes of Si. *Applied Physics Letters*, 103(14):143121, 2013. doi:10.1063/1.4824344.

[82] E. Dimakis, M. Ramsteiner, A. Tahraoui, H. Riechert, and L. Geelhaar. Shell-doping of GaAs nanowires with Si for n-type conductivity. *Nano Research*, 5(11):796–804, 2012. doi:10.1007/s12274-012-0263-9.

[83] V. G. Dubrovskii. *Nucleation Theory and Growth of Nanostructures*. NanoScience and Technology. Springer Berlin Heidelberg, Berlin, Heidelberg, 2014. doi:10.1007/978-3-642-39660-1.

[84] V. G. Dubrovskii, N. V. Sibirev, J. C. Harmand, and F. Glas. Growth kinetics and crystal structure of semiconductor nanowires. *Physical Review B*, 78(23):235301, 2008. doi:10.1103/PhysRevB.78.235301.

[85] J. Dufouleur, C. Colombo, T. Garma, B. Ketterer, E. Uccelli, M. Nicotra, and A. Fontcuberta i Morral. P-doping mechanisms in catalyst-free gallium arsenide nanowires. *Nano letters*, 10(5):1734–40, 2010. doi:10.1021/nl100157w.

[86] D. Ercolani, F. Rossi, A. Li, S. Roddaro, V. Grillo, G. Salviati, F. Beltram, and L. Sorba. InAs/InSb nanowire heterostructures grown by chemical beam epitaxy. *Nanotechnology*, 20(50):505605, 2009. doi:10.1088/0957-4484/20/50/505605.

[87] J. Eymery, V. Favre-Nicolin, L. Froöberg, and L. Samuelson. X-ray measurements of the strain and shape of dielectric/metallic wrap-gated InAs nanowires. *Applied Physics Letters*, 94(13):131911, 2009. doi:10.1063/1.3114369.

[88] Y. Fan, P. Han, P. Liang, Y. Xing, Z. Ye, and S. Hu. Differences in etching characteristics of TMAH and KOH on preparing inverted pyramids for silicon solar cells. *Applied Surface Science*, 264:761–766, 2013. doi:10.1016/j.apsusc.2012.10.117.

[89] H. A. Fonseka, P. Caroff, J. Wong-Leung, A. S. Ameruddin, H. H. Tan, and C. Jagadish. Nanowires grown on InP (100): growth directions, facets, crystal structures, and relative yield control. *ACS nano*, 8(7):6945–54, 2014. doi:10.1021/nn5017428.

[90] A. Fontcuberta i Morral, C. Colombo, G. Abstreiter, J. Arbiol, and J. R. Morante. Nucleation mechanism of gallium-assisted molecular beam epitaxy growth of gallium arsenide nanowires. *Applied Physics Letters*, 92(6):063112, 2008. doi:10.1063/1.2837191.

[91] A. Fontcuberta i Morral, D. Spirkoska, J. Arbiol, M. Heigoldt, J. Ramon Morante, and G. Abstreiter. Prismatic quantum heterostructures synthesized on molecular-beam epitaxy GaAs nanowires. *Small (Weinheim an der Bergstrasse, Germany)*, 4(7):899–903, 2008. doi:10.1002/smll.200701091.

[92] F. C. Frank and J. H. van der Merwe. One-Dimensional Dislocations. I. Static Theory. *Proceedings of the Royal Society A: Mathematical, Physical and Engineering Sciences*, 198(1053):205–216, 1949. doi:10.1098/rspa.1949.0095.

[93] F. C. Frank and J. H. van der Merwe. One-Dimensional Dislocations. II. Misfitting Monolayers and Oriented Overgrowth. *Proceedings of the Royal Society A: Mathematical, Physical and Engineering Sciences*, 198(1053):216–225, 1949. doi:10.1098/rspa.1949.0096.

[94] S. Fujii, N. Miyata, S. Migita, T. Horikawa, and A. Toriumi. Nanometer-scale crystallization of thin HfO_2 films studied by HF-chemical etching. *Applied Physics Letters*, 86(21):212907, 2005. doi:10.1063/1.1939073.

[95] S. Furthmeier, F. Dirnberger, J. Hubmann, B. Bauer, T. Korn, C. Schüller, J. Zweck, E. Reiger, and D. Bougeard. Long exciton lifetimes in stacking-fault-free wurtzite GaAs nanowires. *Applied Physics Letters*, 105(22):222109, 2014. doi:10.1063/1.4903482.

[96] B. Galiana, M. Benedicto, L. Vázquez, J. M. Molina-Aldareguia, and P. Tejedor. Thermal stability of HfO_2-on-GaAs nanopatterns. *Nanoscale*, 4(12):3734–8, 2012. doi:10.1039/c2nr30190c.

[97] M. Galicka, M. Bukala, R. Buczko, and P. Kacman. Modelling the structure of GaAs and InAs nanowires. *Journal of Physics: Condensed Matter*, 20(45):454226, 2008. doi:10.1088/0953-8984/20/45/454226.

[98] B. Ganjipour, A. W. Dey, B. M. Borg, M. Ek, M.-E. Pistol, K. A. Dick, L.-E. Wernersson, and C. Thelander. High current density Esaki tunnel diodes based on GaSb-InAsSb heterostructure nanowires. *Nano letters*, 11(10):4222–6, 2011. doi:10.1021/nl202180b.

[99] B. Ganjipour, M. Ek, B. Mattias Borg, K. A. Dick, M.-E. Pistol, L.-E. Wernersson, and C. Thelander. Carrier control and transport modulation in GaSb/InAsSb core/shell nanowires. *Applied Physics Letters*, 101(10):103501, 2012. doi:10.1063/1.4749283.

[100] H. Geng, X. Yan, X. Zhang, J. Li, Y. Huang, and X. Ren. Analysis of critical dimensions for axial double heterostructure nanowires. *Journal of Applied Physics*, 112(11):114307, 2012. doi:10.1063/1.4767927.

[101] S. G. Ghalamestani, A. Mazid Munshi, D. L. Dheeraj, B.-O. Fimland, H. Weman, and K. A. Dick. Self-catalyzed MBE grown GaAs/$GaAs_xSb_{1-x}$ core-shell nanowires in ZB and WZ crystal structures. *Nanotechnology*, 24(40):405601, 2013. doi:10.1088/0957-4484/24/40/405601.

[102] S. Gibson and R. LaPierre. Study of radial growth in patterned self-catalyzed GaAs nanowire arrays by gas source molecular beam epitaxy. *physica status solidi (RRL) - Rapid Research Letters*, 7(10):845–849, 2013. doi:10.1002/pssr.201307142.

[103] S. J. Gibson and R. R. LaPierre. Model of patterned self-assisted nanowire growth. *Nanotechnology*, 25(41):415304, 2014. doi:10.1088/0957-4484/25/41/415304.

[104] F. Glas. Critical dimensions for the plastic relaxation of strained axial heterostructures in free-standing nanowires. *Physical Review B*, 74(12):121302, 2006. doi:10.1103/PhysRevB.74.121302.

[105] F. Glas and J.-C. Harmand. Calculation of the temperature profile in nanowhiskers growing on a hot substrate. *Physical Review B*, 73(15):155320, 2006. doi:10.1103/PhysRevB.73.155320.

[106] F. Glas, J.-C. Harmand, and G. Patriarche. Why Does Wurtzite Form in Nanowires of III-V Zinc Blende Semiconductors? *Physical Review Letters*, 99(14):3–6, 2007. doi:10.1103/PhysRevLett.99.146101.

[107] S. Gorji Ghalamestani, M. Heurlin, L.-E. Wernersson, S. Lehmann, and K. A. Dick. Growth of InAs/InP core-shell nanowires with various pure crystal structures. *Nanotechnology*, 23(28):285601, 2012. doi:10.1088/0957-4484/23/28/285601.

[108] J. Grandal, M. Wu, X. Kong, M. Hanke, E. Dimakis, L. Geelhaar, H. Riechert, and A. Trampert. Plan-view transmission electron microscopy investigation of GaAs/(In,Ga)As core-shell nanowires. *Applied Physics Letters*, 105(12):121602, 2014. doi:10.1063/1.4896505.

[109] T. Grap, T. Rieger, C. Blömers, T. Schäpers, D. Grützmacher, and M. I. Lepsa. Self-catalyzed VLS grown InAs nanowires with twinning superlattices. *Nanotechnology*, 24(33):335601, 2013. doi:10.1088/0957-4484/24/33/335601.

[110] D. Grützmacher, S. Wirths, T. Rieger, D. Buca, T. Stoica, M. I. Lepsa, Q.-T. Zhao, and S. Mantl. (Keynote) Epitaxy-Based Strain-Engineering Methods for Advanced Devices. *ECS Transactions*, 64(11):85–96, 2014. doi:10.1149/06411.0085ecst.

[111] O. Gül, N. Demarina, C. Blömers, T. Rieger, H. Lüth, M. I. Lepsa, D. Grützmacher, and T. Schäpers. Flux periodic magnetoconductance oscillations in GaAs/InAs core/shell nanowires. *Physical Review B*, 89(4):045417, 2014. doi:10.1103/PhysRevB.89.045417.

[112] O. Gül, H. Y. Günel, H. Lüth, T. Rieger, T. Wenz, F. Haas, M. I. Lepsa, G. Panaitov, D. Grützmacher, and T. Schäpers. Giant Magnetoconductance Oscillations in Hybrid Superconductor-Semiconductor Core/Shell Nanowire Devices. *Nano letters*, 14(11):6269–6274, 2014. doi:10.1021/nl502598s.

[113] O. Gül, D. J. van Woerkom, I. van Weperen, D. Car, S. R. Plissard, E. P. A. M. Bakkers, and L. P. Kouwenhoven. Towards high mobility InSb nanowire devices. *arXiv*, 2014. URL: http://arxiv.org/abs/1411.7285, arXiv:1411.7285.

[114] Y. N. Guo, J. Zou, M. Paladugu, H. Wang, Q. Gao, H. H. Tan, and C. Jagadish. Structural characteristics of GaSb-GaAs nanowire heterostructures grown by metal-organic chemical vapor deposition. *Applied Physics Letters*, 89(23):231917, 2006. doi:10.1063/1.2402234.

[115] A. Haab, M. Mikulics, E. Sutter, J. Jin, T. Stoica, B. Kardynal, T. Rieger, D. Grützmacher, and H. Hardtdegen. Evolution and characteristics of GaN nanowires produced via maskless reactive ion etching. *Nanotechnology*, 25(25):255301, 2014. doi:10.1088/0957-4484/25/25/255301.

[116] C. M. Haapamaki, J. Baugh, and R. R. LaPierre. Critical shell thickness for InAs-$Al_xIn_{1-x}As$(P) core-shell nanowires. *Journal of Applied Physics*, 112(12):124305, 2012. doi:10.1063/1.4769735.

[117] F. Haas, K. Sladek, A. Winden, M. von der Ahe, T. E. Weirich, T. Rieger, H. Lüth, D. Grützmacher, T. Schäpers, and H. Hardtdegen. Nanoimprint and selective-area MOVPE for growth of GaAs/InAs core/shell nanowires. *Nanotechnology*, 24(8):085603, 2013. doi:10.1088/0957-4484/24/8/085603.

[118] F. J. Hackemüller. Selektives Ätzen von Kern-Hülle-Nanodrähten aus InAs-GaSb. Ausarbeitung zum Forschungspraktikum, September 2014.

[119] F. J. Hackemüller. Halbleiternanodrähte für die Elektronenholographie: Präparation und Transportmessungen. Master's thesis, Forschungszentrum Jülich, 2015.

[120] R. Hao, Y. Xu, Z. Zhou, Z. Ren, H. Ni, Z. He, and Z. Niu. MBE growth of very short period InAs/GaSb type-II superlattices on (001)GaAs substrates. *Journal of Physics D: Applied Physics*, 40(21):6690–6693, 2007. doi:10.1088/0022-3727/40/21/031.

[121] D. M. Hausmann and R. G. Gordon. Surface morphology and crystallinity control in the atomic layer deposition (ALD) of hafnium and zirconium oxide thin films. *Journal of Crystal Growth*, 249(1-2):251–261, 2003. doi:10.1016/S0022-0248(02)02133-4.

[122] M. Heigoldt, J. Arbiol, D. Spirkoska, J. M. Rebled, S. Conesa-Boj, G. Abstreiter, F. Peiró, J. R. Morante, and A. Fontcuberta i Morral. Long range epitaxial growth of prismatic heterostructures on the facets of catalyst-free GaAs nanowires. *Journal of Materials Chemistry*, 19(7):840, 2009. doi:10.1039/b816585h.

[123] M. Heiss, S. Conesa-Boj, J. Ren, H.-H. Tseng, A. Gali, A. Rudolph, E. Uccelli, F. Peiró, J. R. Morante, D. Schuh, E. Reiger, E. Kaxiras, J. Arbiol, and A. Fontcuberta i Morral. Direct correlation of crystal structure and optical properties in wurtzite/zinc-blende GaAs nanowire heterostructures. *Physical Review B*, 83(4):045303, 2011. doi:10.1103/PhysRevB.83.045303.

[124] M. Heiss, Y. Fontana, A. Gustafsson, G. Wüst, C. Magen, D. D. O'Regan, J. W. Luo, B. Ketterer, S. Conesa-Boj, A. V. Kuhlmann, J. Houel, E. Russo-Averchi, J. R. Morante, M. Cantoni, N. Marzari, J. Arbiol, A. Zunger, R. J. Warburton, and A. Fontcuberta i Morral. Self-assembled quantum dots in a nanowire system for quantum photonics. *Nature materials*, 12(5):439–44, 2013. doi:10.1038/nmat3557.

[125] M. Heiss, A. Gustafsson, S. Conesa-Boj, F. Peiró, J. R. Morante, G. Abstreiter, J. Arbiol, L. Samuelson, and A. Fontcuberta i Morral. Catalyst-free nanowires with axial $In_xGa_{1-x}As$/GaAs heterostructures. *Nanotechnology*, 20(7):075603, 2009. doi:10.1088/0957-4484/20/7/075603.

[126] S. Hertenberger, D. Rudolph, J. Becker, M. Bichler, J. J. Finley, G. Abstreiter, and G. Koblmüller. Rate-limiting mechanisms in high-temperature growth of catalyst-free InAs nanowires with large thermal stability. *Nanotechnology*, 23(23):235602, 2012. doi:10.1088/0957-4484/23/23/235602.

[127] S. Hertenberger, D. Rudolph, M. Bichler, J. J. Finley, G. Abstreiter, and G. Koblmüller. Growth kinetics in position-controlled and catalyst-free InAs nanowire arrays on Si(111) grown by selective area molecular beam epitaxy. *Journal of Applied Physics*, 108(11):114316, 2010. doi:10.1063/1.3525610.

[128] S. Hertenberger, D. Rudolph, S. Bolte, M. Döblinger, M. Bichler, D. Spirkoska, J. J. Finley, G. Abstreiter, and G. Koblmüller. Absence of vapor-liquid-solid growth during molecular beam epitaxy of self-induced InAs nanowires on Si. *Applied Physics Letters*, 98(12):123114, 2011. doi:10.1063/1.3567496.

[129] C. Heyn. Kinetic model of local droplet etching. *Physical Review B*, 83(16):165302, 2011. doi:10.1103/PhysRevB.83.165302.

[130] C. Heyn, T. Bartsch, S. Sanguinetti, D. Jesson, and W. Hansen. Dynamics of mass transport during nanohole drilling by local droplet etching. *Nanoscale Research Letters*, 10(1):67, 2015. doi:10.1186/s11671-015-0779-5.

[131] D. G. Hill. Two Selective Etching Solutions for GaAs on InGaAs and GaAs/AlGaAs on InGaAs. *Journal of The Electrochemical Society*, 137(9):2912, 1990. doi:10.1149/1.2087098.

[132] K. Hillerich, D. S. Ghidini, K. A. Dick, K. Deppert, and J. Johansson. Cu particle seeded InP-InAs axial nanowire heterostructures. *physica status solidi (RRL) - Rapid Research Letters*, 7(10):850–854, 2013. doi:10.1002/pssr.201307241.

[133] C. L. Hinkle, A. M. Sonnet, E. M. Vogel, S. McDonnell, G. J. Hughes, M. Milojevic, B. Lee, F. S. Aguirre-Tostado, K. J. Choi, H. C. Kim, J. Kim, and R. M. Wallace. GaAs interfacial self-cleaning by atomic layer deposition. *Applied Physics Letters*, 92(7):071901, 2008. doi:10.1063/1.2883956.

[134] K. Hiruma, M. Yazawa, T. Katsuyama, K. Ogawa, K. Haraguchi, M. Koguchi, and H. Kakibayashi. Growth and optical properties of nanometer-scale GaAs and InAs whiskers. *Journal of Applied Physics*, 77(2):447, 1995. doi:10.1063/1.359026.

[135] M. Hjort, S. Lehmann, J. Knutsson, R. Timm, D. Jacobsson, E. Lundgren, K. A. Dick, and A. Mikkelsen. Direct imaging of atomic scale structure and electronic properties of GaAs wurtzite and zinc blende nanowire surfaces. *Nano letters*, 13(9):4492–8, 2013. doi:10.1021/nl402424x.

[136] M.-Y. Ho, H. Gong, G. D. Wilk, B. W. Busch, M. L. Green, P. M. Voyles, D. A. Muller, M. Bude, W. H. Lin, A. See, M. E. Loomans, S. K. Lahiri, and P. I. Räisänen. Morphology and crystallization kinetics in HfO_2 thin films grown by atomic layer deposition. *Journal of Applied Physics*, 93(3):1477, 2003. doi:10.1063/1.1534381.

[137] F. Huang. Theory of Strain Relaxation for Epitaxial Layers Grown on Substrate of a Finite Dimension. *Physical Review Letters*, 85(4):784–787, 2000. doi:10.1103/PhysRevLett.85.784.

[138] S. H. Huang, G. Balakrishnan, A. Khoshakhlagh, A. Jallipalli, L. R. Dawson, and D. L. Huffaker. Strain relief by periodic misfit arrays for low defect density GaSb on GaAs. *Applied Physics Letters*, 88(13):131911, 2006. doi:10.1063/1.2172742.

[139] D. Hull and D. Bacon. *Introduction to Dislocations*. Elsevier, 2011. doi:10.1016/B978-0-08-096672-4.00011-6.

[140] A.-M. Huntz, M. Andrieux, C. Vahlas, M.-M. Sovar, D. Samelor, and A. N. Gleizes. Phase Transformations of Metallorganic Chemical Vapor Deposition Processed Alumina Coatings Investigated by In Situ Deflection. *Journal of The Electrochemical Society*, 154(5):P63, 2007. doi:10.1149/1.2715314.

[141] P. K. Hurley, E. O'Connor, S. Monaghan, R. Long, A. O'Mahony, I. M. Povey, K. Cherkaoui, J. MacHale, A. Quinn, G. Brammertz, M. M. Heyns, S. Newcomb, V. V. Afanas'ev, A. Sonnet, R. Galatage, N. Jivani, E. Vogel, R. M. Wallace, and M. Pemble. Structural and Electrical Properties of HfO_2/n-$In_xGa_{1-x}As$ structures (x: 0, 0.15, 0.3 and 0.53) . In *ECS Transactions*, volume 25, pages 113–127. ECS, 2009. doi:10.1149/1.3206612.

[142] M. Hÿtch, E. Snoeck, and R. Kilaas. Quantitative measurement of displacement and strain fields from HREM micrographs. *Ultramicroscopy*, 74(3):131–146, 1998. doi:10.1016/S0304-3991(98)00035-7.

[143] M. J. Hÿtch. Analysis of Variations in Structure from High Resolution Electron Microscope Images by Combining Real Space and Fourier Space Information. *Microscopy Microanalysis Microstructures*, 8(1):41–57, 1997. doi:10.1051/mmm:1997105.

[144] H. Ikeda, T. Goto, M. Sakashita, A. Sakai, S. Zaima, and Y. Yasuda. Local Leakage Current of HfO_2 Thin Films Characterized by Conducting Atomic Force Microscopy. *Japanese Journal of Applied Physics*, 42(Part 1, No. 4B):1949–1953, 2003. doi:10.1143/JJAP.42.1949.

[145] Ioffe Institute. New Semiconductor Materials. Characteristics and Properties. April 2015. URL: http://www.ioffe.ru/SVA/NSM/.

[146] A. M. Ionescu and H. Riel. Tunnel field-effect transistors as energy-efficient electronic switches. *Nature*, 479(7373):329–37, 2011. doi:10.1038/nature10679.

[147] R. Isaacson. Electron Spin Resonance in n-Type InSb. *Physical Review*, 169(2):312–314, 1968. doi:10.1103/PhysRev.169.312.

[148] A. Jallipalli, G. Balakrishnan, S. Huang, T. Rotter, K. Nunna, B. Liang, L. Dawson, and D. Huffaker. Structural Analysis of Highly Relaxed GaSb Grown on GaAs Substrates with Periodic Interfacial Array of 90° Misfit Dislocations. *Nanoscale research letters*, 4(12):1458–62, 2009. doi:10.1007/s11671-009-9420-9.

[149] M. Jeppsson, K. A. Dick, J. B. Wagner, P. Caroff, K. Deppert, L. Samuelson, and L.-E. Wernersson. GaAs/GaSb nanowire heterostructures grown by MOVPE. *Journal of Crystal Growth*, 310(18):4115–4121, 2008. doi:10.1016/j.jcrysgro.2008.06.066.

[150] L. Jeurgens, W. Sloof, F. Tichelaar, and E. Mittemeijer. Thermodynamic stability of amorphous oxide films on metals: Application to aluminum oxide films on aluminum substrates. *Physical Review B*, 62(7):4707–4719, 2000. doi:10.1103/PhysRevB.62.4707.

[151] X. Jiang, Q. Xiong, S. Nam, F. Qian, Y. Li, and C. M. Lieber. InAs/InP radial nanowire heterostructures as high electron mobility devices. *Nano letters*, 7(10):3214–8, 2007. doi:10.1021/nl072024a.

[152] J. Johansson, L. S. Karlsson, C. P. T. Svensson, T. Mårtensson, B. A. Wacaser, K. Deppert, L. Samuelson, and W. Seifert. Structural properties of ⟨111⟩B -oriented III-V nanowires. *Nature materials*, 5(7):574–80, 2006. doi:10.1038/nmat1677.

[153] A. Jordan. An evaluation of the thermal and elastic constants affecting GaAs crystal growth. *Journal of Crystal Growth*, 49(4):631–642, 1980. doi:10.1016/0022-0248(80)90287-0.

[154] T. Jörres. Atomlagenabscheidung von high-k Oxiden für nanoelektronische Bauelemente. Diploma thesis, 2013.

[155] H. J. Joyce, J. Wong-Leung, Q. Gao, H. H. Tan, and C. Jagadish. Phase perfection in zinc Blende and Wurtzite III-V nanowires using basic growth parameters. *Nano letters*, 10(3):908–15, 2010. doi:10.1021/nl903688v.

[156] A. Kahn. Surface and near-surface atomic structure of GaAs (110). *Journal of Vacuum Science and Technology*, 15(4):1223, 1978. doi:10.1116/1.569697.

[157] J.-H. Kang, Y. Cohen, Y. Ronen, M. Heiblum, R. Buczko, P. Kacman, R. Popovitz-Biro, and H. Shtrikman. Crystal structure and transport in merged InAs nanowires MBE grown on (001) InAs. *Nano letters*, 13(11):5190–6, 2013. doi:10.1021/nl402571s.

[158] Y. S. Kang, C. Y. Kim, M. H. Cho, K. B. Chung, C. H. An, H. Kim, H. J. Lee, C. S. Kim, and T. G. Lee. Thickness dependence on crystalline structure and interfacial reactions in HfO_2 films on InP (001) grown by atomic layer deposition. *Applied Physics Letters*, 97(17):172108, 2010. doi:10.1063/1.3506695.

[159] Y.-S. Kang, D.-K. Kim, M.-H. Cho, J.-H. Seo, H. K. Shon, T. G. Lee, Y. D. Cho, S.-W. Kim, D.-H. Ko, and H. Kim. Change in crystalline structure and band alignment in atomic-layer-deposited HfO_2 on InP using an annealing treatment. *physica status solidi (a)*, 210(8):1612–1617, 2013. doi:10.1002/pssa.201228628.

[160] P. D. Kanungo, H. Schmid, M. T. Björk, L. M. Gignac, C. Breslin, J. Bruley, C. D. Bessire, and H. Riel. Selective area growth of III-V nanowires and their heterostructures on silicon in a nanotube template: towards monolithic integration of nano-devices. *Nanotechnology*, 24(22):225304, 2013. doi:10.1088/0957-4484/24/22/225304.

[161] S. Kato, M. Bielmann, K. Ikeda, S.-i. Orimo, A. Borgschulte, and A. Zuüttel. Surface changes on AlH_3 during the hydrogen desorption. *Applied Physics Letters*, 96(5):051912, 2010. doi:10.1063/1.3269598.

[162] H. Kauko, T. Grieb, R. Bjørge, M. Schowalter, A. M. Munshi, H. Weman, A. Rosenauer, and A. T. J. van Helvoort. Compositional characterization of GaAs/GaAsSb nanowires by quantitative HAADF-STEM. *Micron (Oxford, England : 1993)*, 44:254–60, 2013. doi:10.1016/j.micron.2012.07.002.

[163] K. L. Kavanagh. Misfit dislocations in nanowire heterostructures. *Semiconductor Science and Technology*, 25(2):024006, 2010. doi:10.1088/0268-1242/25/2/024006.

[164] K. L. Kavanagh, J. Salfi, I. Savelyev, M. Blumin, and H. E. Ruda. Transport and strain relaxation in wurtzite InAs-GaAs core-shell heterowires. *Applied Physics Letters*, 98(15):152103, 2011. doi:10.1063/1.3579251.

[165] K. L. Kavanagh, I. Saveliev, M. Blumin, G. Swadener, and H. E. Ruda. Faster radial strain relaxation in InAs-GaAs core-shell heterowires. *Journal of Applied Physics*, 111(4):044301, 2012. doi:10.1063/1.3684964.

[166] P. Keck and J. Broder. The Solubility of Silicon and Germanium in Gallium and Indium. *Physical Review*, 90(4):521–522, 1953. doi:10.1103/PhysRev.90.521.

[167] B. Ketterer, M. Heiss, M. J. Livrozet, A. Rudolph, E. Reiger, and A. Fontcuberta i Morral. Determination of the band gap and the split-off band in wurtzite GaAs using Raman and photoluminescence excitation spectroscopy. *Physical Review B*, 83(12):125307, 2011. doi:10.1103/PhysRevB.83.125307.

[168] B. Ketterer, E. Mikheev, E. Uccelli, and A. Fontcuberta i Morral. Compensation mechanism in silicon-doped gallium arsenide nanowires. *Applied Physics Letters*, 97(22):223103, 2010. doi:10.1063/1.3517254.

[169] C. Y. Kim, S. W. Cho, M.-H. Cho, K. B. Chung, D. C. Suh, D.-H. Ko, C.-H. An, H. Kim, and H. J. Lee. Changes in the structure of an atomic-layer-deposited HfO_2 film on a GaAs (100) substrate as a function of postannealing temperature. *Applied Physics Letters*, 95(4):042903, 2009. doi:10.1063/1.3182702.

[170] S. K. Kim, S. Hoffmann-Eifert, M. Reiners, and R. Waser. Relation Between Enhancement in Growth and Thickness-Dependent Crystallization in ALD TiO_2 Thin Films. *Journal of The Electrochemical Society*, 158(1):D6, 2011. doi:10.1149/1.3507258.

[171] W. D. Kingery, H. K. Bowen, and D. R. Uhlmann. *Introduction to ceramics*. JohnWiley & Sons, Inc., 2nd ed. edition, 1976.

[172] A. Kingon, J. Maria, and S. Streiffer. Alternative dielectrics to silicon dioxide for memory and logic devices. *Nature*, 406(6799):1032–8, 2000. doi:10.1038/35023243.

[173] V. V. R. Kishore, B. Partoens, and F. M. Peeters. Electronic structure of InAs/GaSb core-shell nanowires. *Physical Review B*, 86(16):165439, 2012. doi:10.1103/PhysRevB.86.165439.

[174] J. Klaus, S. Ferro, and S. George. Atomic layer deposition of tungsten using sequential surface chemistry with a sacrificial stripping reaction. *Thin Solid Films*, 360(1-2):145–153, 2000. doi:10.1016/S0040-6090(99)01076-7.

[175] I. Knez, R.-R. Du, and G. Sullivan. Evidence for Helical Edge Modes in Inverted InAs/GaSb Quantum Wells. *Physical Review Letters*, 107(13):136603, 2011. doi:10.1103/PhysRevLett.107.136603.

[176] J. Knoch and J. Appenzeller. Modeling of High-Performance p-Type III-V Heterojunction Tunnel FETs. *IEEE Electron Device Letters*, 31(4):305–307, 2010. doi:10.1109/LED.2010.2041180.

[177] G. Koblmüller, S. Hertenberger, K. Vizbaras, M. Bichler, F. Bao, J.-P. Zhang, and G. Abstreiter. Self-induced growth of vertical free-standing InAs nanowires on Si(111) by molecular beam epitaxy. *Nanotechnology*, 21(36):365602, 2010. doi:10.1088/0957-4484/21/36/365602.

[178] M. Köhl, P. Schroth, A. A. Minkevich, J. W. Hornung, E. Dimakis, C. Somaschini, L. Geelhaar, T. Aschenbrenner, S. Lazarev, D. Grigoriev, U. Pietsch, and T. Baumbach. Polytypism in GaAs nanowires: determination of the interplanar spacing of wurtzite GaAs by X-ray diffraction. *Journal of synchrotron radiation*, 22(Pt 1):67–75, 2015. doi:10.1107/S1600577514023480.

[179] P. Komninou, J. Kioseoglou, G. P. Dimitrakopulos, T. Kehagias, and T. Karakostas. Partial dislocations in wurtzite GaN. *physica status solidi (a)*, 202(15):2888–2899, 2005. doi:10.1002/pssa.200521263.

[180] D. Kriegner, C. Panse, B. Mandl, K. A. Dick, M. Keplinger, J. M. Persson, P. Caroff, D. Ercolani, L. Sorba, F. Bechstedt, J. Stangl, and G. Bauer. Unit cell structure of crystal polytypes in InAs and InSb nanowires. *Nano letters*, 11(4):1483–9, 2011. doi:10.1021/nl1041512.

[181] H. Kroemer. The 6.1 Å family (InAs, GaSb, AlSb) and its heterostructures: a selective review. *Physica E: Low-dimensional Systems and Nanostructures*, 20(3-4):196–203, 2004. doi:10.1016/j.physe.2003.08.003.

[182] P. Krogstrup, S. Curiotto, E. Johnson, M. Aagesen, J. Nygård, and D. Chatain. Impact of the Liquid Phase Shape on the Structure of III-V Nanowires. *Physical Review Letters*, 106(12):125505, 2011. doi:10.1103/PhysRevLett.106.125505.

[183] P. Krogstrup, M. Hannibal Madsen, W. Hu, M. Kozu, Y. Nakata, J. Nygård, M. Takahasi, and R. Feidenhans'l. In-situ x-ray characterization of wurtzite formation in GaAs nanowires. *Applied Physics Letters*, 100(9):093103, 2012. doi:10.1063/1.3688489.

[184] P. Krogstrup, H. I. Jørgensen, M. Heiss, O. Demichel, J. V. Holm, M. Aagesen, J. Nygård, and A. Fontcuberta i Morral. Single-nanowire solar cells beyond the Shockley-Queisser limit. *Nature Photonics*, 7(4):306–310, 2013. doi:10.1038/nphoton.2013.32.

[185] P. Krogstrup, H. I. Jørgensen, E. Johnson, M. H. Madsen, C. B. Sørensen, A. F. i. Morral, M. Aagesen, J. Nygård, and F. Glas. Advances in the theory of III-V nanowire growth dynamics. *Journal of Physics D: Applied Physics*, 46(31):313001, 2013. doi:10.1088/0022-3727/46/31/313001.

[186] P. Krogstrup, R. Popovitz-Biro, E. Johnson, M. H. Madsen, J. Nygård, and H. Shtrikman. Structural Phase Control in Self-Catalyzed Growth of GaAs Nanowires on Silicon (111). *Nano Letters*, 10(11):4475–4482, 2010. doi:10.1021/nl102308k.

[187] K. Kukli, J. Aarik, M. Ritala, T. Uustare, T. Sajavaara, J. Lu, J. Sundqvist, A. Aidla, L. Pung, A. Hårsta, and M. Leskelaä. Effect of selected atomic layer deposition parameters on the structure and dielectric properties of hafnium oxide films. *Journal of Applied Physics*, 96(9):5298, 2004. doi:10.1063/1.1796513.

[188] K. Kukli, M. Ritala, J. Lu, A. Hårsta, and M. Leskelö. Properties of HfO_2 Thin Films Grown by ALD from Hafnium tetrakis(ethylmethylamide) and Water. *Journal of The Electrochemical Society*, 151(8):F189, 2004. doi:10.1149/1.1770934.

[189] P. Kusch, S. Breuer, M. Ramsteiner, L. Geelhaar, H. Riechert, and S. Reich. Band gap of wurtzite GaAs: A resonant Raman study. *Physical Review B*, 86(7):075317, 2012. doi:10.1103/PhysRevB.86.075317.

[190] M. W. Larsson, J. B. Wagner, M. Wallin, P. Håkansson, L. E. Fröberg, L. Samuelson, and L. R. Wallenberg. Strain mapping in free-standing heterostructured wurtzite InAs/InP nanowires. *Nanotechnology*, 18(1):015504, 2007. doi:10.1088/0957-4484/18/1/015504.

[191] H. D. Lee, T. Feng, L. Yu, D. Mastrogiovanni, A. Wan, T. Gustafsson, and E. Garfunkel. Reduction of native oxides on GaAs during atomic layer growth of Al_2O_3. *Applied Physics Letters*, 94(22):222108, 2009. doi:10.1063/1.3148723.

[192] P. F. Lee, J. Y. Dai, K. H. Wong, H. L. W. Chan, and C. L. Choy. Growth and characterization of Hf-aluminate high-k gate dielectric ultrathin films with equivalent oxide thickness less than 10 Å. *Journal of Applied Physics*, 93(6):3665, 2003. doi:10.1063/1.1554764.

[193] J. Leger, A. Atouf, P. Tomaszewski, and A. Pereira. Pressure-induced phase transitions and volume changes in HfO_2 up to 50 GPa. *Physical Review B*, 48(1):93–98, 1993. doi:10.1103/PhysRevB.48.93.

[194] S. Lehmann, D. Jacobsson, K. Deppert, and K. A. Dick. High crystal quality wurtzite-zinc blende heterostructures in metal-organic vapor phase epitaxy-grown GaAs nanowires. *Nano Research*, 5(7):470–476, 2012. doi:10.1007/s12274-012-0232-3.

[195] M. Lexholm, I. Karlsson, F. Boxberg, and D. Hessman. Optical determination of Young's modulus of InAs nanowires. *Applied Physics Letters*, 95(11):113103, 2009. doi:10.1063/1.3225150.

[196] R. Li, Y. Lu, S. D. Chae, G. Zhou, Q. Liu, C. Chen, M. Shahriar Rahman, T. Vasen, Q. Zhang, P. Fay, T. Kosel, M. Wistey, H. G. Xing, S. Koswatta, and A. Seabaugh. InAs/AlGaSb heterojunction tunnel field-effect transistor with tunnelling in-line with the gate field. *physica status solidi (c)*, 9(2):389–392, 2012. doi:10.1002/pssc.201100241.

[197] R. Li, Y. Lu, G. Zhou, Q. Liu, S. D. Chae, T. Vasen, W. S. Hwang, Q. Zhang, P. Fay, T. Kosel, M. Wistey, H. Xing, and A. Seabaugh. AlGaSb/InAs Tunnel Field-Effect Transistor With On-Current of 78 μA/ μm at 0.5 V. *IEEE Electron Device Letters*, 33(3):363–365, 2012. doi:10.1109/LED.2011.2179915.

[198] Y. C. Lin, H. Yamaguchi, E. Y. Chang, Y. C. Hsieh, M. Ueki, Y. Hirayama, and C. Y. Chang. Growth of very-high-mobility AlGaSb/InAs high-electron-mobility transistor structure on si substrate for high speed electronic applications. *Applied Physics Letters*, 90(2):023509, 2007. doi:10.1063/1.2431567.

[199] X. Liu, S. Ramanathan, A. Longdergan, A. Srivastava, E. Lee, T. E. Seidel, J. T. Barton, D. Pang, and R. G. Gordon. ALD of Hafnium Oxide Thin Films from Tetrakis(ethylmethylamino)hafnium and Ozone. *Journal of The Electrochemical Society*, 152(3):G213, 2005. doi:10.1149/1.1859631.

[200] H. Lüth. *Solid Surfaces, Interfaces and Thin Films*. Graduate Texts in Physics. Springer International Publishing, Cham, 2015. doi:10.1007/978-3-319-10756-1.

[201] O. Madelung. *Semiconductors: Data Handbook*. Springer Berlin Heidelberg, Berlin, Heidelberg, 2004. doi:10.1007/978-3-642-18865-7.

[202] M. H. Madsen, M. Aagesen, P. Krogstrup, C. Sørensen, and J. Nygård. Influence of the oxide layer for growth of self-assisted InAs nanowires on Si(111). *Nanoscale research letters*, 6(1):516, 2011. doi:10.1186/1556-276X-6-516.

[203] T. Maemoto, H. Dobashi, S. Izumiya, K. Yoh, and M. Inoue. Fabrication of Superconducting Transistors using InAs/(AlGa)Sb Quantum Wells. *Japanese Journal of Applied Physics*, 33(Part 1, No. 12B):7204–7209, 1994. doi:10.1143/JJAP.33.7204.

[204] B. Mandl, K. a. Dick, D. Kriegner, M. Keplinger, G. Bauer, J. Stangl, and K. Deppert. Crystal structure control in Au-free self-seeded InSb wire growth. *Nanotechnology*, 22(14):145603, 2011. doi:10.1088/0957-4484/22/14/145603.

[205] B. Mandl, J. Stangl, E. Hilner, A. A. Zakharov, K. Hillerich, A. W. Dey, L. Samuelson, G. Bauer, K. Deppert, and A. Mikkelsen. Growth mechanism of self-catalyzed group III-V nanowires. *Nano letters*, 10(11):4443–9, 2010. doi:10.1021/nl1022699.

[206] R. Martin. Relation between Elastic Tensors of Wurtzite and Zinc-Blende Structure Materials. *Physical Review B*, 6(12):4546–4553, 1972. doi:10.1103/PhysRevB.6.4546.

[207] R. Martin. Erratum: Relation between elastic tensors of wurtzite and zinc-blende structure materials. *Physical Review B*, 20(2):818–818, 1979. doi:10.1103/PhysRevB.20.818.2.

[208] J. Matthews and A. Blakeslee. Defects in epitaxial multilayers. *Journal of Crystal Growth*, 27:118–125, 1974. doi:10.1016/S0022-0248(74)80055-2.

[209] B. Mattias Borg and L.-E. Wernersson. Synthesis and properties of antimonide nanowires. *Nanotechnology*, 24(20):202001, 2013. doi:10.1088/0957-4484/24/20/202001.

[210] B. Mayer, D. Rudolph, J. Schnell, S. Morkötter, J. Winnerl, J. Treu, K. Müller, G. Bracher, G. Abstreiter, G. Koblmüller, and J. J. Finley. Lasing from individual GaAs-AlGaAs core-shell nanowires up to room temperature. *Nature communications*, 4:2931, 2013. doi:10.1038/ncomms3931.

[211] K. McKenna, A. Shluger, V. Iglesias, M. Porti, M. Nafría, M. Lanza, and G. Bersuker. Grain boundary mediated leakage current in polycrystalline HfO_2 films. *Microelectronic Engineering*, 88(7):1272–1275, 2011. doi:10.1016/j.mee.2011.03.024.

[212] P. A. Midgley and R. E. Dunin-Borkowski. Electron tomography and holography in materials science. *Nature materials*, 8(4):271–80, 2009. doi:10.1038/nmat2406.

[213] T. D. Mishima, M. Edirisooriya, and M. B. Santos. Reduction of microtwin defects for high-electron-mobility InSb quantum wells. *Applied Physics Letters*, 91(6):062106, 2007. doi:10.1063/1.2768033.

[214] T.-a. Miura, M. Niwano, D. Shoji, and N. Miyamoto. Kinetics of oxidation on hydrogen-terminated Si(100) and (111) surfaces stored in air. *Journal of Applied Physics*, 79(8):4373, 1996. doi:10.1063/1.362670.

[215] K. Momma and F. Izumi. VESTA 3 for three-dimensional visualization of crystal, volumetric and morphology data. *Journal of Applied Crystallography*, 44(6):1272–1276, 2011. doi:10.1107/S0021889811038970.

[216] M. Morita, T. Ohmi, E. Hasegawa, M. Kawakami, and M. Ohwada. Growth of native oxide on a silicon surface. *Journal of Applied Physics*, 68(3):1272, 1990. doi:10.1063/1.347181.

[217] S. Morkötter, S. Funk, M. Liang, M. Döblinger, S. Hertenberger, J. Treu, D. Rudolph, A. Yadav, J. Becker, M. Bichler, G. Scarpa, P. Lugli, I. Zardo, J. J. Finley, G. Abstreiter, and G. Koblmüller. Role of microstructure on optical properties in high-uniformity $In_{1-x}Ga_xAs$ nanowire arrays: Evidence of a wider wurtzite band gap. *Physical Review B*, 87(20):205303, 2013. doi:10.1103/PhysRevB.87.205303.

[218] V. Mourik, K. Zuo, S. M. Frolov, S. R. Plissard, E. P. A. M. Bakkers, and L. P. Kouwenhoven. Signatures of Majorana fermions in hybrid superconductor-semiconductor nanowire devices. *Science*, 336(6084):1003–7, 2012. doi:10.1126/science.1222360.

[219] D. Muñoz, P. Carreras, J. Escarré, D. Ibarz, S. Martín de Nicolás, C. Voz, J. Asensi, and J. Bertomeu. Optimization of KOH etching process to obtain textured substrates suitable for heterojunction solar cells fabricated by HWCVD. *Thin Solid Films*, 517(12):3578–3580, 2009. doi:10.1016/j.tsf.2009.01.024.

[220] A. M. Munshi, D. L. Dheeraj, J. Todorovic, A. T. van Helvoort, H. Weman, and B.-O. Fimland. Crystal phase engineering in self-catalyzed GaAs and GaAs/GaAsSb nanowires grown on Si(111). *Journal of Crystal Growth*, 372:163–169, 2013. doi:10.1016/j.jcrysgro.2013.03.004.

[221] S. Nadj-Perge, V. S. Pribiag, J. W. G. van den Berg, K. Zuo, S. R. Plissard, E. P. A. M. Bakkers, S. M. Frolov, and L. P. Kouwenhoven. Spectroscopy of Spin-Orbit Quantum Bits in Indium Antimonide Nanowires. *Physical Review Letters*, 108(16):166801, 2012. doi:10.1103/PhysRevLett.108.166801.

[222] U. Neuwald, A. Feltz, U. Memmert, and R. J. Behm. Chemical oxidation of hydrogen passivated Si(111) surfaces in H_2O_2. *Journal of Applied Physics*, 78(6):4131, 1995. doi:10.1063/1.359872.

[223] C. B. Nielsen, C. Christensen, C. Pedersen, and E. V. Thomsen. Particle Precipitation in Connection with KOH Etching of Silicon. *Journal of The Electrochemical Society*, 151(5):G338, 2004. doi:10.1149/1.1688802.

[224] H. A. Nilsson, P. Caroff, C. Thelander, M. Larsson, J. B. Wagner, L.-E. Wernersson, L. Samuelson, and H. Q. Xu. Giant, level-dependent g factors in InSb nanowire quantum dots. *Nano letters*, 9(9):3151–6, 2009. doi:10.1021/nl901333a.

[225] Y. K. Noh. Strucrural Properties of GaSb Layers Grown on InAs, AlSb, and GaSb Buffer Layers on GaAs (001) Substrates. *Journal of the Korean Physical Society*, 50(6):1929, 2007. doi:10.3938/jkps.50.1929.

[226] B. Z. Nosho, B. R. Bennett, L. J. Whitman, and M. Goldenberg. Effects of As_2 versus As_4 on InAs/GaSb heterostructures: As-for-Sb exchange and film stability. *Journal of Vacuum Science & Technology B: Microelectronics and Nanometer Structures*, 19(4):1626, 2001. doi:10.1116/1.1386377.

[227] J. E. Oh, P. K. Bhattacharya, Y. C. Chen, and S. Tsukamoto. Molecular-beam epitaxial growth of high-quality InSb on InP and GaAs substrates. *Journal of Applied Physics*, 66(8):3618, 1989. doi:10.1063/1.344069.

[228] M. Oloumi and C. C. Matthai. Band offset at InAs/GaAs interfaces. *Journal of Physics: Condensed Matter*, 1(SB):SB211–SB212, 1989. doi:10.1088/0953-8984/1/SB/046.

[229] Y. A. Osipiyan and I. S. Smirnova. Perfect Dislocations in the Wurtzite Lattice. *Physica Status Solidi (b)*, 30(1):19–29, 1968. doi:10.1002/pssb.19680300103.

[230] Y. Osipyan and I. Smirnova. Partial dislocations in the wurtzite lattice. *Journal of Physics and Chemistry of Solids*, 32(7):1521–1530, 1971. doi:10.1016/S0022-3697(71)80046-X.

[231] J. H. Paek, T. Nishiwaki, M. Yamaguchi, and N. Sawaki. MBE-VLS growth of GaAs nanowires on (111)Si substrate. *Physica Status Solidi (C)*, 5(9):2740–2742, 2008. doi:10.1002/pssc.200779248.

[232] S.-J. Paik, J. Kim, S. Park, S. Kim, C. Koo, S.-K. Lee, and D. Cho. A Novel Micromachining Technique to Fabricate Released GaAs Microstructures with a Rectangular Cross Section. *Japanese Journal of Applied Physics*, 42(Part 1, No. 1):326–332, 2003. doi:10.1143/JJAP.42.326.

[233] M. Paladugu, J. Zou, Y.-N. Guo, X. Zhang, Y. Kim, H. J. Joyce, Q. Gao, H. H. Tan, and C. Jagadish. Nature of heterointerfaces in GaAs/InAs and InAs/GaAs axial nanowire heterostructures. *Applied Physics Letters*, 93(10):101911, 2008. doi:10.1063/1.2978959.

[234] L. Pan, K.-K. Lew, J. M. Redwing, and E. C. Dickey. Stranski-Krastanow growth of germanium on silicon nanowires. *Nano letters*, 5(6):1081–5, 2005. doi:10.1021/nl050605z.

[235] C. Panse, D. Kriegner, and F. Bechstedt. Polytypism of GaAs, InP, InAs, and InSb: An ab initio study. *Physical Review B*, 84(7):075217, 2011. doi:10.1103/PhysRevB.84.075217.

[236] E. Parton and P. Verheyen. Strained silicon – the key to sub-45 nm CMOS. *III-Vs Review*, 19(3):28–31, 2006. doi:10.1016/S0961-1290(06)71590-3.

[237] G. Patriarche, F. Glas, M. Tchernycheva, C. Sartel, L. Largeau, J.-C. Harmand, and G. E. Cirlin. Wurtzite to zinc blende phase transition in GaAs nanowires induced by epitaxial burying. *Nano letters*, 8(6):1638–43, 2008. doi:10.1021/nl080319y.

[238] P. Paulitschke, N. Seltner, A. Lebedev, H. Lorenz, and E. M. Weig. Size-independent Young's modulus of inverted conical GaAs nanowire resonators. *Applied Physics Letters*, 103(26):261901, 2013. doi:10.1063/1.4851897.

[239] E. Pehlke, N. Moll, A. Kley, and M. Scheffler. Shape and stability of quantum dots. *Applied Physics A: Materials Science & Processing*, 65(6):525–534, 1997. doi:10.1007/s003390050619.

[240] R. People and J. C. Bean. Calculation of critical layer thickness versus lattice mismatch for Ge_xSi_{1-x}/Si strained-layer heterostructures. *Applied Physics Letters*, 47(3):322, 1985. doi:10.1063/1.96206.

[241] O. Pirrotta, L. Larcher, M. Lanza, A. Padovani, M. Porti, M. Nafría, and G. Bersuker. Leakage current through the poly-crystalline HfO_2: Trap densities at grains and grain boundaries. *Journal of Applied Physics*, 114(13):134503, 2013. doi:10.1063/1.4823854.

[242] M.-E. Pistol and C. Pryor. Band structure of core-shell semiconductor nanowires. *Physical Review B*, 78(11):115319, 2008. doi:10.1103/PhysRevB.78.115319.

[243] M.-E. Pistol and C. Pryor. Band structure of segmented semiconductor nanowires. *Physical Review B*, 80(3):035316–, 2009. doi:10.1103/PhysRevB.80.035316.

[244] S. Plissard, K. A. Dick, X. Wallart, and P. Caroff. Gold-free GaAs/GaAsSb heterostructure nanowires grown on silicon. *Applied Physics Letters*, 96(12):121901, 2010. doi:10.1063/1.3367746.

[245] S. R. Plissard, D. R. Slapak, M. A. Verheijen, M. Hocevar, G. W. G. Immink, I. van Weperen, S. Nadj-Perge, S. M. Frolov, L. P. Kouwenhoven, and E. P. A. M. Bakkers. From InSb nanowires to nanocubes: looking for the sweet spot. *Nano letters*, 12(4):1794–8, 2012. doi:10.1021/nl203846g.

[246] S. R. Plissard, I. van Weperen, D. Car, M. A. Verheijen, G. W. G. Immink, J. Kammhuber, L. J. Cornelissen, D. B. Szombati, A. Geresdi, S. M. Frolov, L. P. Kouwenhoven, and E. P. A. M. Bakkers. Formation and electronic properties of InSb nanocrosses. *Nature nanotechnology*, 8(11):859–64, 2013. doi:10.1038/nnano.2013.198.

[247] R. Popovitz-Biro, A. Kretinin, P. Von Huth, and H. Shtrikman. InAs/GaAs Core/Shell Nanowires. *Crystal Growth & Design*, 11(9):3858–3865, 2011. doi:10.1021/cg200393y.

[248] G. Priante, S. Ambrosini, V. G. Dubrovskii, A. Franciosi, and S. Rubini. Stopping and Resuming at Will the Growth of GaAs Nanowires. *Crystal Growth & Design*, 13(9):3976–3984, 2013. doi:10.1021/cg400701w.

[249] S. I. Raider. Oxide Growth on Etched Silicon in Air at Room Temperature. *Journal of The Electrochemical Society*, 122(3):413, 1975. doi:10.1149/1.2134225.

[250] M. R. Ramdani, J. C. Harmand, F. Glas, G. Patriarche, and L. Travers. Arsenic Pathways in Self-Catalyzed Growth of GaAs Nanowires. *Crystal Growth & Design*, 13(1):91–96, 2013. doi:10.1021/cg301167g.

[251] S. Raychaudhuri. *Toward nanowire devices and systems : heterostructure design and dielectrophoretic integration*. PhD thesis, University of California, San Diego, Jan. 2009. URL: https://escholarship.org/uc/item/9mj8c88v.

[252] S. Raychaudhuri and E. T. Yu. Calculation of critical dimensions for wurtzite and cubic zinc blende coaxial nanowire heterostructures. *Journal of Vacuum Science & Technology B: Microelectronics and Nanometer Structures*, 24(4):2053, 2006. doi:10.1116/1.2216715.

[253] S. Raychaudhuri and E. T. Yu. Critical dimensions in coherently strained coaxial nanowire heterostructures. *Journal of Applied Physics*, 99(11):114308, 2006. doi:10.1063/1.2202697.

[254] M. E. Reimer, G. Bulgarini, N. Akopian, M. Hocevar, M. B. Bavinck, M. A. Verheijen, E. P. A. M. Bakkers, L. P. Kouwenhoven, and V. Zwiller. Bright single-photon sources in bottom-up tailored nanowires. *Nature communications*, 3:737, 2012. doi:10.1038/ncomms1746.

[255] T. Rieger. Growth and characterization of GaAs and GaAs-based heterostructure nanowires. Master's thesis, Forschungszentrum Jülich, 2011.

[256] T. Rieger, D. Grützmacher, and M. I. Lepsa. Si substrate preparation for the VS and VLS growth of InAs nanowires. *physica status solidi (RRL) - Rapid Research Letters*, 7(10):840–844, 2013. doi:10.1002/pssr.201307229.

[257] T. Rieger, D. Grützmacher, and M. I. Lepsa. InAs nanowires with AlxGa1-xSb shells for band alignment engineering. *Journal of Crystal Growth*, 425:80–84, May 2015. doi:10.1016/j.jcrysgro.2015.03.043.

[258] T. Rieger, D. Grützmacher, and M. I. Lepsa. Misfit dislocation free InAs/GaSb core-shell nanowires grown by molecular beam epitaxy. *Nanoscale*, 7(1):356–64, 2015. doi:10.1039/c4nr05164e.

[259] T. Rieger, S. Heiderich, S. Lenk, M. I. Lepsa, and D. Grützmacher. Ga-assisted MBE growth of GaAs nanowires using thin HSQ layer. *Journal of Crystal Growth*, 353(1):39–46, 2012. doi:10.1016/j.jcrysgro.2012.05.006.

[260] T. Rieger, T. Jörres, J. Vogel, A. Biermanns, U. Pietsch, D. Grützmacher, and M. I. Lepsa. Crystallization of HfO_2 in InAs/HfO_2 core-shell nanowires. *Nanotechnology*, 25(40):405701, 2014. doi:10.1088/0957-4484/25/40/405701.

[261] T. Rieger, M. I. Lepsa, T. Schäpers, and D. Grützmacher. Controlled wurtzite inclusions in self-catalyzed zinc blende III-V semiconductor nanowires. *Journal of Crystal Growth*, 378:506–510, 2013. doi:10.1016/j.jcrysgro.2012.12.035.

[262] T. Rieger, M. Luysberg, T. Schäpers, D. Grützmacher, and M. I. Lepsa. Molecular beam epitaxy growth of GaAs/InAs core-shell nanowires and fabrication of InAs nanotubes. *Nano letters*, 12(11):5559–64, 2012. doi:10.1021/nl302502b.

[263] T. Rieger, D. Rosenbach, G. Mussler, T. Schäpers, D. Grützmacher, and M. I. Lepsa. Simultaneous Integration of Different Nanowires on Single Textured Si (100) Substrates. *Nano Letters*, 15(3):1979–1986, 2015. doi:10.1021/nl504854v.

[264] T. Rieger, T. Schäpers, D. Grützmacher, and M. I. Lepsa. Crystal Phase Selective Growth in GaAs/InAs Core-Shell Nanowires. *Crystal Growth & Design*, 14(3):1167–1174, 2014. doi:10.1021/cg401667v.

[265] M. Ritala, M. Leskelä, L. Niinistö, T. Prohaska, G. Friedbacher, and M. Grasserbauer. Development of crystallinity and morphology in hafnium dioxide thin films grown by atomic layer epitaxy. *Thin Solid Films*, 250(1):72–80, 1994. doi:10.1016/0040-6090(94)90168-6.

[266] J. Rodriguez, P. Christol, L. Cerutti, F. Chevrier, and A. Joullié. MBE growth and characterization of type-II InAs/GaSb superlattices for mid-infrared detection. *Journal of Crystal Growth*, 274(1-2):6–13, 2005. doi:10.1016/j.jcrysgro.2004.09.088.

[267] D. Rosenbach. Prozessierung und Charakterisierung von InAs-Nanodrahtstrukturen auf Si (100) Substraten. Bachelors Thesis, 2014.

[268] M. Rosien. Prozessierung und Charakterisierung von InAs Nanodrähten mit HfO_2 als Gate Dielektrikum. Master's thesis, Forschungszentrum Jülich, 2014.

[269] A. Rudolph, M. Soda, M. Kiessling, T. Wojtowicz, D. Schuh, W. Wegscheider, J. Zweck, C. Back, and E. Reiger. Ferromagnetic GaAs/GaMnAs core-shell nanowires grown by molecular beam epitaxy. *Nano letters*, 9(11):3860–6, 2009. doi:10.1021/nl9020717.

[270] D. Rudolph, S. Hertenberger, S. Bolte, W. Paosangthong, D. Spirkoska, M. Döblinger, M. Bichler, J. J. Finley, G. Abstreiter, and G. Koblmüller. Direct observation of a

noncatalytic growth regime for GaAs nanowires. *Nano Letters*, 11(9):3848–3854, 2011. doi:10.1021/nl2019382.

[271] D. Rüffer. *Magnetic states and spin-wave modes in single ferromagnetic nanotubes*. PhD thesis, EPFL, 2014. doi:10.5075/epfl-thesis-6316.

[272] E. Russo-Averchi, A. Dalmau-Mallorquí, I. Canales-Mundet, G. Tütüncüoğlu, E. Alarcon-Llado, M. Heiss, D. Rüffer, S. Conesa-Boj, P. Caroff, and A. Fontcuberta i Morral. Growth mechanisms and process window for InAs V-shaped nanoscale membranes on Si[001]. *Nanotechnology*, 24(43):435603, 2013. doi:10.1088/0957-4484/24/43/435603.

[273] E. Russo-Averchi, M. Heiss, L. Michelet, P. Krogstrup, J. Nygard, C. Magen, J. R. Morante, E. Uccelli, J. Arbiol, and A. Fontcuberta i Morral. Suppression of three dimensional twinning for a 100% yield of vertical GaAs nanowires on silicon. *Nanoscale*, 4(5):1486–90, 2012. doi:10.1039/c2nr11799a.

[274] O. Salehzadeh, K. L. Kavanagh, and S. P. Watkins. Growth and strain relaxation of GaAs and GaP nanowires with GaSb shells. *Journal of Applied Physics*, 113(13):134309, 2013. doi:10.1063/1.4799065.

[275] C. Sartel, D. L. Dheeraj, F. Jabeen, and J. C. Harmand. Effect of arsenic species on the kinetics of GaAs nanowires growth by molecular beam epitaxy. *Journal of Crystal Growth*, 312(14):2073–2077, 2010. doi:10.1016/j.jcrysgro.2010.04.027.

[276] K. Sato, M. Shikida, Y. Matsushima, T. Yamashiro, K. Asaumi, Y. Iriye, and M. Yamamoto. Characterization of orientation-dependent etching properties of single-crystal silicon: effects of KOH concentration. *Sensors and Actuators A: Physical*, 64(1):87–93, 1998. doi:10.1016/S0924-4247(97)01658-0.

[277] H. Seidel. Anisotropic Etching of Crystalline Silicon in Alkaline Solutions. *Journal of The Electrochemical Society*, 137(11):3612, 1990. doi:10.1149/1.2086277.

[278] M. Shandalov and P. C. McIntyre. Size-dependent polymorphism in HfO_2 nanotubes and nanoscale thin films. *Journal of Applied Physics*, 106(8):084322, 2009. doi:10.1063/1.3243077.

[279] R. C. Sharma, T. L. Ngai, and Y. A. Chang. The In-Sb (Indium-Antimony) system. *Bulletin of Alloy Phase Diagrams*, 10(6):657–664, 1989. doi:10.1007/BF02877639.

[280] K. Shim. Composition dependence of band alignments in $Ga_xIn_{1-x}As_ySb_{1-y}$ heterojunctions lattice matched to GaSb and InAs. *Journal of Applied Physics*, 114(20):203703, 2013. doi:10.1063/1.4834536.

[281] H. Shtrikman, R. Popovitz-Biro, A. Kretinin, L. Houben, M. Heiblum, M. Bukala, M. Galicka, R. Buczko, and P. Kacman. Method for suppression of stacking faults in Wurtzite III-V nanowires. *Nano letters*, 9(4):1506–10, 2009. doi:10.1021/nl803524s.

[282] S. Sivasubramaniam and M. M. Alkaisi. Inverted nanopyramid texturing for silicon solar cells using interference lithography. *Microelectronic Engineering*, 119:146–150, 2014. doi:10.1016/j.mee.2014.04.004.

[283] K. Sladek. *Realization of III-V semiconductor nano structures towards more efficient (opto-)electronic devices*. PhD thesis, RWTH Aachen University, 2013. URL: http://publications.rwth-aachen.de/record/229511.

[284] K. Sladek, V. Klinger, J. Wensorra, M. Akabori, H. Hardtdegen, and D. Grützmacher. MOVPE of n-doped GaAs and modulation doped GaAs/AlGaAs nanowires. *Journal of Crystal Growth*, 312(5):635–640, 2010. doi:10.1016/j.jcrysgro.2009.11.026.

[285] J. R. Soderstrom, M. M. Cumming, J. Y. Yao, and T. G. Andersson. Molecular beam epitaxy growth and characterization of InSb layers on GaAs substrates. *Semiconductor Science and Technology*, 7(3):337–343, 1992. doi:10.1088/0268-1242/7/3/010.

[286] C. Somaschini, A. Biermanns, S. Bietti, G. Bussone, A. Trampert, S. Sanguinetti, H. Riechert, U. Pietsch, and L. Geelhaar. Axial InAs/GaAs heterostructures on silicon in a nanowire geometry. *Nanotechnology*, 25(48):485602, 2014. doi:10.1088/0957-4484/25/48/485602.

[287] C. Somaschini, S. Bietti, A. Trampert, U. Jahn, C. Hauswald, H. Riechert, S. Sanguinetti, and L. Geelhaar. Control over the number density and diameter of GaAs nanowires on Si(111) mediated by droplet epitaxy. *Nano letters*, 13(8):3607–13, 2013. doi:10.1021/nl401404w.

[288] M. J. L. Sourribes, I. Isakov, M. Panfilova, H. Liu, and P. A. Warburton. Mobility enhancement by Sb-mediated minimisation of stacking fault density in InAs nanowires grown on silicon. *Nano letters*, 14(3):1643–50, 2014. doi:10.1021/nl5001554.

[289] M. J. L. Sourribes, I. Isakov, M. Panfilova, and P. A. Warburton. Minimization of the contact resistance between InAs nanowires and metallic contacts. *Nanotechnology*, 24(4):045703, 2013. doi:10.1088/0957-4484/24/4/045703.

[290] W. Sparber, O. Schultz, D. Biro, G. Emanuel, R. Preu, A. Poddey, and D. Borchert. Comparison of texturing methods for monocrystalline silicon solar cells using KOH and Na_2CO_3. *Photovoltaic Energy Conversion, 2003. Proceedings of 3rd World Conference on*, 2:1372–1375, 2003.

[291] S. Spiga, C. Wiemer, G. Tallarida, G. Scarel, S. Ferrari, G. Seguini, and M. Fanciulli. Effects of the oxygen precursor on the electrical and structural properties of HfO_2 films grown by atomic layer deposition on Ge. *Applied Physics Letters*, 87(11):112904, 2005. doi:10.1063/1.2042631.

[292] D. Spirkoska, J. Arbiol, A. Gustafsson, S. Conesa-Boj, F. Glas, I. Zardo, M. Heigoldt, M. H. Gass, A. L. Bleloch, S. Estrade, M. Kaniber, J. Rossler, F. Peiro, J. R. Morante, G. Abstreiter, L. Samuelson, and A. Fontcuberta i Morral. Structural and optical properties of high quality zinc-blende/wurtzite GaAs nanowire heterostructures. *Physical Review B*, 80(24):245325, 2009. doi:10.1103/PhysRevB.80.245325.

[293] D. Spirkoska, A. Fontcuberta i Morral, J. Dufouleur, Q. Xie, and G. Abstreiter. Free standing modulation doped core-shell GaAs/AlGaAs hetero-nanowires. *physica status solidi (RRL) - Rapid Research Letters*, 5(9):353–355, 2011. doi:10.1002/pssr.201105338.

[294] N. Stranski and L. Krastanov. Zur Theorie der orientierten Ausscheidung von Ionenkristallen aufeinander. *Abhandlungen der Mathematisch-Naturwissenschaftlichen Klasse IIb. Akademie der Wissenschaften Wien*, 146:797–810, 1938.

[295] R. Suri, D. J. Lichtenwalner, and V. Misra. Interfacial self cleaning during atomic layer deposition and annealing of HfO_2 films on native (100)-GaAs substrates. *Applied Physics Letters*, 96(11):112905, 2010. doi:10.1063/1.3357422.

[296] D. B. Suyatin, J. Sun, A. Fuhrer, D. Wallin, L. E. Fröberg, L. S. Karlsson, I. Maximov, L. R. Wallenberg, L. Samuelson, and H. Q. Xu. Electrical properties of self-assembled branched InAs nanowire junctions. *Nano letters*, 8(4):1100–4, 2008. doi:10.1021/nl073193y.

[297] T. Tanaka, K. Tomioka, S. Hara, J. Motohisa, E. Sano, and T. Fukui. Vertical Surrounding Gate Transistors Using Single InAs Nanowires Grown on Si Substrates. *Applied Physics*, 3:3–5, 2010. doi:10.1143/APEX.3.025003.

[298] M. Tchernycheva, J. C. Harmand, G. Patriarche, L. Travers, and G. E. Cirlin. Temperature conditions for GaAs nanowire formation by Au-assisted molecular beam epitaxy. *Nanotechnology*, 17(16):4025–30, 2006. doi:10.1088/0957-4484/17/16/005.

[299] J. Tersoff, A. Denier van der Gon, and R. Tromp. Shape oscillations in growth of small crystals. *Physical Review Letters*, 70(8):1143–1146, 1993. doi:10.1103/PhysRevLett.70.1143.

[300] C. Thelander, P. Caroff, S. Plissard, A. W. Dey, and K. A. Dick. Effects of crystal phase mixing on the electrical properties of InAs nanowires. *Nano letters*, 11(6):2424–9, 2011. doi:10.1021/nl2008339.

[301] R. Timm, A. Fian, M. Hjort, C. Thelander, E. Lind, J. N. Andersen, L.-E. Wernersson, and A. Mikkelsen. Reduction of native oxides on InAs by atomic layer deposited Al_2O_3 and HfO_2. *Applied Physics Letters*, 97(13):132904, 2010. doi:10.1063/1.3495776.

[302] R. Timm, M. Hjort, A. Fian, B. M. Borg, C. Thelander, J. N. Andersen, L.-E. Wernersson, and A. Mikkelsen. Interface composition of InAs nanowires with Al_2O_3 and HfO_2 thin films. *Applied Physics Letters*, 99(22):222907, 2011. doi:10.1063/1.3664399.

[303] K. Tomioka and T. Fukui. Tunnel field-effect transistor using InAs nanowire/Si heterojunction. *Applied Physics Letters*, 98(8):083114, 2011. doi:10.1063/1.3558729.

[304] K. Tomioka, M. Yoshimura, and T. Fukui. Sub 60 mV/decade switch using an InAs nanowire-Si heterojunction and turn-on voltage shift with a pulsed doping technique. *Nano letters*, 13(12):5822–6, 2013. doi:10.1021/nl402447h.

[305] S. Tong, A. Lubinsky, B. Mrstik, and M. Van Hove. Surface bond angle and bond lengths of rearranged As and Ga atoms on GaAs(110). *Physical Review B*, 17(8):3303–3309, 1978. doi:10.1103/PhysRevB.17.3303.

[306] T. L. Tran, F. Hatami, W. T. Masselink, V. P. Kunets, and G. Salamo. Comparison of MBE Growth of InSb on Si (001) and GaAs (001). *Journal of Electronic Materials*, 37(12):1799–1805, 2008. doi:10.1007/s11664-008-0558-5.

[307] J. Treu, M. Bormann, H. Schmeiduch, M. Döblinger, S. Morkötter, S. Matich, P. Wiecha, K. Saller, B. Mayer, M. Bichler, M.-C. Amann, J. J. Finley, G. Abstreiter, and G. Koblmüller. Enhanced luminescence properties of InAs-InAsP core-shell nanowires. *Nano letters*, 13(12):6070–7, 2013. doi:10.1021/nl403341x.

[308] D. Triyoso, R. Liu, D. Roan, M. Ramon, N. V. Edwards, R. Gregory, D. Werho, J. Kulik, G. Tam, E. Irwin, X.-D. Wang, L. B. La, C. Hobbs, R. Garcia, J. Baker, B. E. White, and P. Tobin. Impact of Deposition and Annealing Temperature on Material and Electrical Characteristics of ALD HfO_2. *Journal of The Electrochemical Society*, 151(10):F220, 2004. doi:10.1149/1.1784821.

[309] F. Turco and J. Massies. Strain-induced In incorporation coefficient variation in the growth of $Al_{1-x}In_xAs$ alloys by molecular beam epitaxy. *Applied Physics Letters*, 51(24):1989, 1987. doi:10.1063/1.98320.

[310] G. Tuttle, H. Kroemer, and J. H. English. Electron concentrations and mobilities in AlSb/InAs/AlSb quantum wells. *Journal of Applied Physics*, 65(12):5239, 1989. doi:10.1063/1.343167.

[311] A. Twitchett, R. Dunin-Borkowski, and P. Midgley. Quantitative Electron Holography of Biased Semiconductor Devices. *Physical Review Letters*, 88(23):238302, 2002. doi:10.1103/PhysRevLett.88.238302.

[312] E. Uccelli, J. Arbiol, C. Magen, P. Krogstrup, E. Russo-Averchi, M. Heiss, G. Mugny, F. Morier-Genoud, J. Nygård, J. R. Morante, and A. Fontcuberta I Morral. Three-dimensional multiple-order twinning of self-catalyzed GaAs nanowires on Si substrates. *Nano letters*, 11(9):3827–32, 2011. doi:10.1021/nl201902w.

[313] E. Uccelli, J. Arbiol, J. R. Morante, and A. Fontcuberta i Morral. InAs quantum dot arrays decorating the facets of GaAs nanowires. *ACS nano*, 4(10):5985–93, 2010. doi:10.1021/nn101604k.

[314] O. Ueda and S. J. Pearton. *Materials Fundamentals of Gate Dielectrics*. Springer-Verlag, Berlin/Heidelberg, 2005. doi:10.1007/1-4020-3078-9.

[315] O. Ueda and S. J. Pearton. *Materials and Reliability Handbook for Semiconductor Optical and Electron Devices*. Springer New York, New York, NY, 2013. doi:10.1007/978-1-4614-4337-7.

[316] J. van den Berg, S. Nadj-Perge, V. Pribiag, S. Plissard, E. Bakkers, S. Frolov, and L. Kouwenhoven. Fast Spin-Orbit Qubit in an Indium Antimonide Nanowire. *Physical Review Letters*, 110(6):066806, 2013. doi:10.1103/PhysRevLett.110.066806.

[317] W. Van den Broek, A. Rosenauer, B. Goris, G. Martinez, S. Bals, S. Van Aert, and D. Van Dyck. Correction of non-linear thickness effects in HAADF STEM electron tomography. *Ultramicroscopy*, 116:8–12, 2012. doi:10.1016/j.ultramic.2012.03.005.

[318] J. H. Van Der Merwe. Crystal Interfaces. Part II. Finite Overgrowths. *Journal of Applied Physics*, 34(1):123, 1963. doi:10.1063/1.1729051.

[319] J. W. W. van Tilburg, R. E. Algra, W. G. G. Immink, M. Verheijen, E. P. A. M. Bakkers, and L. P. Kouwenhoven. Surface passivated InAs/InP core/shell nanowires. *Semiconductor Science and Technology*, 25(2):024011, 2010. doi:10.1088/0268-1242/25/2/024011.

[320] M. Volmer and A. Weber. Keimbildung in übersättigten Gebilden. *Z. phys. Chem.*, 119:277–301, 1926.

[321] R. S. Wagner and W. C. Ellis. VAPOR-LIQUID-SOLID MECHANISM OF SINGLE CRYSTAL GROWTH. *Applied Physics Letters*, 4(5):89, 1964. doi:10.1063/1.1753975.

[322] H. Wang, J. Yuan, T. Rieger, P. J. van Veldhoven, P. Nouwens, T. J. Eijkemans, T. de Vries, B. Smalbrugge, E. J. Geluk, and R. Nötzel. Distribution control of 1.55 μm InAs quantum dots down to small numbers on truncated InP pyramids grown by selective area metal organic vapor phase epitaxy. *Applied Physics Letters*, 94(14):143103, 2009. doi:10.1063/1.3116146.

[323] J. Wang, S. Plissard, M. Hocevar, T. T. T. Vu, T. Zehender, G. G. W. Immink, M. A. Verheijen, J. Haverkort, and E. P. A. M. Bakkers. Position-controlled [100] InP nanowire arrays. *Applied Physics Letters*, 100(5):053107, 2012. doi:10.1063/1.3679136.

[324] L. Wang, P. Kratzer, N. Moll, and M. Scheffler. Size, shape, and stability of InAs quantum dots on the GaAs(001) substrate. *Physical Review B*, 62(3):1897–1904, 2000. doi:10.1103/PhysRevB.62.1897.

[325] S. Q. Wang and H. Q. Ye. First-principles study on elastic properties and phase stability of III-V compounds. *physica status solidi (b)*, 240(1):45–54, 2003. doi:10.1002/pssb.200301861.

[326] Y. Wang, A. S. Özcan, K. F. Ludwig, and A. Bhattacharyya. Real-time studies of gallium adsorption and desorption kinetics on sapphire (0001) by grazing incidence small-angle x-ray scattering and x-ray fluorescence. *Journal of Applied Physics*, 103(10):103538, 2008. doi:10.1063/1.2936969.

[327] Y.-B. Wang, L.-F. Wang, H. J. Joyce, Q. Gao, X.-Z. Liao, Y.-W. Mai, H. H. Tan, J. Zou, S. P. Ringer, H.-J. Gao, and C. Jagadish. Super deformability and Young's modulus of GaAs nanowires. *Advanced materials (Deerfield Beach, Fla.)*, 23(11):1356–60, 2011. doi:10.1002/adma.201004122.

[328] H. Wen, Z. Wang, J. Shultz, B. Liang, and G. Salamo. Growth and characterization of InAs epitaxial layer on GaAs(111)B. *Physical Review B*, 70(20):205307, 2004. doi:10.1103/PhysRevB.70.205307.

[329] T. Wenz, M. Rosien, F. Haas, T. Rieger, N. Demarina, M. I. Lepsa, H. Lüth, D. Grützmacher, and T. Schäpers. Phase coherent transport in hollow InAs nanowires. *Applied Physics Letters*, 105(11):113111, 2014. doi:10.1063/1.4896286.

[330] J. Werking, C. Bolognesi, L.-D. Chang, C. Nguyen, E. Hu, and H. Kroemer. High-transconductance InAs/AlSb heterojunction field-effect transistors with delta - doped AlSb upper barriers. *IEEE Electron Device Letters*, 13(3):164–166, 1992. doi:10.1109/55.144998.

[331] T. E. Whall and E. H. C. Parker. SiGe heterostructures for FET applications. *Journal of Physics D: Applied Physics*, 31(12):1397–1416, 1998. doi:10.1088/0022-3727/31/12/003.

[332] D. B. Williams and C. B. Carter. *Transmission Electron Microscopy*. Springer US, Boston, MA, 2009. doi:10.1007/978-0-387-76501-3.

[333] S. Wirths, R. Geiger, N. V. D. Driesch, G. Mussler, T. Stoica, S. Mantl, Z. Ikonic, M. Luysberg, S. Chiussi, J. M. Hartmann, H. Sigg, J. Faist, D. Buca, and D. Grützmacher. Lasing in direct-bandgap GeSn alloy grown on Si. *Nature Photonics*, 9(2):88–92, 2015. doi:10.1038/nphoton.2014.321.

[334] S. Wirths, K. Weis, A. Winden, K. Sladek, C. Volk, S. Alagha, T. E. Weirich, M. von der Ahe, H. Hardtdegen, H. Lüth, N. Demarina, D. Grützmacher, and T. Schäpers. Effect of Si-doping on InAs nanowire transport and morphology. *Journal of Applied Physics*, 110(5):053709, 2011. doi:10.1063/1.3631026.

[335] A. Wolkenberg. A Mechanism for the Effect of Doping on the Silicon Native Oxide Thickness. *Physica Status Solidi (a)*, 79(1):313–322, 1983. doi:10.1002/pssa.2210790135.

[336] H. Yamaguchi, J. G. Belk, X. M. Zhang, J. L. Sudijono, M. R. Fahy, T. S. Jones, D. W. Pashley, and B. A. Joyce. Atomic-scale imaging of strain relaxation via misfit dislocations in highly mismatched semiconductor heteroepitaxy: InAs/GaAs(111)A. *Physical Review B*, 55(3):1337–1340, 1997. doi:10.1103/PhysRevB.55.1337.

[337] H. Yamaguchi, R. Dreyfus, Y. Hirayama, and S. Miyashita. Excellent electric properties of free-standing InAs membranes. *Applied Physics Letters*, 78(16):2372, 2001. doi:10.1063/1.1365946.

[338] T. Yamashita, T. Akiyama, K. Nakamura, and T. Ito. Effects of Facet Orientation on Relative Stability between Zinc Blende and Wurtzite Structures in Group III-V Nanowires. *Japanese Journal of Applied Physics*, 49(5):055003, 2010. doi:10.1143/JJAP.49.055003.

[339] X. Yan, X. Zhang, X. Ren, J. Li, X. Lv, Q. Wang, and Y. Huang. Growth and photoluminescence of $In_xGa_{1-x}As$ quantum dots on the surface of GaAs nanowires by metal organic chemical vapor deposition. *Applied Physics Letters*, 101(2):023106, 2012. doi:10.1063/1.4734391.

[340] T. Yang, Y. Xuan, D. Zemlyanov, T. Shen, Y. Q. Wu, J. M. Woodall, P. D. Ye, F. S. Aguirre-Tostado, M. Milojevic, S. McDonnell, and R. M. Wallace. Interface studies of GaAs metal-oxide-semiconductor structures using atomic-layer-deposited HfO_2/Al_2O_3 nanolaminate gate dielectric. *Applied Physics Letters*, 91(14):142122, 2007. doi:10.1063/1.2798499.

[341] M. Yao, N. Huang, S. Cong, C.-Y. Chi, M. A. Seyedi, Y.-T. Lin, Y. Cao, M. L. Povinelli, P. D. Dapkus, and C. Zhou. GaAs nanowire array solar cells with axial p-i-n junctions. *Nano letters*, 14(6):3293–303, 2014. doi:10.1021/nl500704r.

[342] H. Ye and Z. Yu. Plastic relaxation of mixed dislocation in axial nanowire heterostructures using Peach-Koehler approach. *physica status solidi (RRL) - Rapid Research Letters*, 8(5):445–448, 2014. doi:10.1002/pssr.201409072.

[343] P. D. Ye, G. D. Wilk, B. Yang, J. Kwo, S. N. G. Chu, S. Nakahara, H.-J. L. Gossmann, J. P. Mannaerts, M. Hong, K. K. Ng, and J. Bude. GaAs metal-oxide-semiconductor field-effect transistor with nanometer-thin dielectric grown by atomic layer deposition. *Applied Physics Letters*, 83(1):180, 2003. doi:10.1063/1.1590743.

[344] K. Yoh, K. Kiyomi, A. Nishida, and M. Inoue. Indium Arsenide Quantum Wires Fabricated by Electron Beam Lithography and Wet-Chemical Etching. *Japanese Journal of Applied Physics*, 31(Part 1, No. 12B):4515–4519, 1992. doi:10.1143/JJAP.31.4515.

[345] X. Yu, H. Wang, J. Lu, J. Zhao, J. Misuraca, P. Xiong, and S. von Molnár. Evidence for structural phase transitions induced by the triple phase line shift in self-catalyzed GaAs nanowires. *Nano letters*, 12(10):5436–42, 2012. doi:10.1021/nl303323t.

[346] J. Yuan, H. Wang, P. J. van Veldhoven, T. Rieger, P. Nouwens, T. J. Eijkemans, T. de Vries, B. Smalbrugge, E. J. Geluk, and R. Nötzel. 1.55 μm InAs quantum dot distribution on truncated InP pyramids and regrowth by selective area epitaxy. *IOP Conference Series: Materials Science and Engineering*, 6(1):012004, 2009. doi:10.1088/1757-899X/6/1/012004.

[347] Z. Zanolli, F. Fuchs, J. Furthmüller, U. von Barth, and F. Bechstedt. Model GW band structure of InAs and GaAs in the wurtzite phase. *Physical Review B*, 75(24):245121, 2007. doi:10.1103/PhysRevB.75.245121.

[348] L. A. Zepeda-Ruiz, B. Z. Nosho, R. I. Pelzel, W. Weinberg, and D. Maroudas. Kinetics of strain relaxation through misfit dislocation formation in InAs/GaAs(111)A heteroepitaxy. *Surface Science*, 441(2-3):L911–L916, 1999. doi:10.1016/S0039-6028(99)00852-3.

[349] L. Zhao, Y. Xuan, and M. Qi. Generating integrated-circuit patterns via cutting and stitching of gratings. *Journal of Vacuum Science & Technology B: Microelectronics and Nanometer Structures*, 27(6):2750, 2009. doi:10.1116/1.3264677.

[350] X. Zhao and D. Vanderbilt. First-principles study of structural, vibrational, and lattice dielectric properties of hafnium oxide. *Physical Review B*, 65(23):233106, 2002. doi:10.1103/PhysRevB.65.233106.

[351] H. Zheng, J. Wang, J. Y. Huang, J. Wang, Z. Zhang, and S. X. Mao. Dynamic process of phase transition from wurtzite to zinc blende structure in InAs nanowires. *Nano letters*, 13(12):6023–7, 2013. doi:10.1021/nl403240r.

[352] L. Zheng, M. Xie, and S. Tong. Adsorption and desorption kinetics of gallium atoms on 6H-SiC(0001) surfaces. *Physical Review B*, 61(7):4890–4893, 2000. doi:10.1103/PhysRevB.61.4890.

[353] Q. D. Zhuang, E. A. Anyebe, R. Chen, H. Liu, A. M. Sanchez, M. K. Rajpalke, T. D. Veal, Z. M. Wang, Y. Z. Huang, and H. D. Sun. Sb-Induced Phase Control of InAsSb Nanowires Grown by Molecular Beam Epitaxy. *Nano Letters*, 15(2):1109–1116, 2015. doi:10.1021/nl5040946.

[354] I. Zubel, K. Rola, and M. Kramkowska. The effect of isopropyl alcohol concentration on the etching process of Si-substrates in KOH solutions. *Sensors and Actuators A: Physical*, 171(2):436–445, 2011. doi:10.1016/j.sna.2011.09.005.

Appendix A.

A Appendix

A.1. Substrate preparation and growth parameters for the presented nanowire structures

Substrate preparation:

- **GaAs (111)B substrates for the VLS growth of GaAs and InAs NWs:** Spin coating a layer of HSQ diluted with MIBK 1:7 - 1:9 on the substrate, baking at 300°C for at least 10 min.
- **GaAs (111)B substrates for the VS grown of InAs NWs:** Spin coating a layer of HSQ diluted with MIBK 1:40 on the substrate, baking at 300°C for at least 10 min.
- **Si (111) substrates for the VS growth of InAs NWs:** Cleaning of the substrate with piranha and removal of the native oxide by HF. Subsequently, building up a new oxide layer with H_2O_2 (1 min).
- **Si (111) substrates for the VLS growth of InAs NWs:** Ga pretreatment of the substrate (native oxide) in the MBE. Few layers of Ga (no As!) deposited at high temperature ($\sim$ 600°C) etch the oxide and form pinholes. Thermal desorption of the Ga.
- **Si (111) substrates for the VLS growth of GaAs NWs:** Several substrate preparations can be used, e.g. native oxides (out of the box), cleaning with piranha and HF and subsequent wet chemical oxide (H_2O_2) or oxidation in ambient air.
- **Textured Si (100) substrates:** Piranha and HF cleaning, etching in KOH solution of 1 wt% KOH and 7 vol% IPA at 80°C for $\sim$ 40 min. Subsequently, cleaning in piranha and HF and rebuilding a new oxide (H_2O_2).
- **Si (100) substrates with V-grooves:** spin coating 200 nm of HSQ, writing lines and spaces by electron beam lithography, development in MF CD-26. Hard bake at 450°C. KOH etching in 33 wt% KOH with 7 vol% IPA at 40°C for 40 min. Cleaning with diluted HCl (supersonic), piranha and HF. Rebuilding a new oxide in H_2O_2.

Nanowire growth: F_i denotes the flux of the element i, T_{sub} the substrate temperature. Pressures are valid for the GenII system.

- **VLS GaAs nanowires:** $T_{sub} \approx 600$°C, $F_{Ga} = 0.05$ – 0.3 µm/h, $F_{As} = 0.5$ – $10 \cdot 10^{-6}$ Torr. Large variety of growth parameters, general rule: the higher the Ga flux, the higher the As flux

  - *WZ inclusions:* Ga supply interruptions between 3 and $\sim$ 15 min depending on the droplet diameter and contact angle (for an As flux of $F_{As} = 1 \cdot 10^{-6}$ Torr)

- **VLS InAs nanowires:** $T_{sub} \approx 530$°C, $F_{In} = 0.05$ – 0.1 µm/h, $F_{As} = 1.2$ – $2.5 \cdot 10^{-6}$ Torr.
  - *WZ inclusions:* In supply interruptions between 1 and $\sim$ 3 min depending on the droplet diameter and contact angle (for an As flux of $F_{As} = 1.2 \cdot 10^{-6}$ Torr)

- **VS InAs nanowires:** $T_{sub} \approx 480$°C, $F_{In} = 0.005$ – 0.2 µm/h, $F_{As} \approx 0.8$ – $3 \cdot 10^{-5}$ Torr. The higher the In flux, the higher the NW density.

- **GaAs/InAs core-shell nanowires:** GaAs nanowires as shown above, followed by Ga droplet consumption. InAs shell: $T_{sub} \leq 490$°C, $F_{In} = 0.1$ - 0.2 µm/h, $F_{As} = 1.2$ – $2.5 \cdot 10^{-6}$ Torr.

- **InAs/GaSb core-shell nanowires:** VS InAs nanowires as shown above. Tapered GaSb shell: $T_{sub} = 490$°C, $F_{Ga} = 0.1$ µm/h, $F_{As} = 7 \cdot 10^{-7}$ mbar. Conformal GaSb shell: $T_{sub} \leq 360$°C, $F_{Ga} = 0.1$ µm/h, $F_{As} = 7 \cdot 10^{-7}$ mbar.

- **InAs/$\mathbf{Al_xGa_{1-x}Sb}$ core-shell nanowires:** VS InAs nanowires as shown above. $Al_xGa_{1-x}Sb$ shell: $T_{sub} \approx 360$°C, $F_{Ga} + F_{Al} = 0.1$ µm/h, $F_{As} = 7 \cdot 10^{-7}$ mbar. 15 min GaSb cap ($T_{sub} \approx 360$°C, $F_{Ga} = 0.1$ µm/h, $F_{As} = 7 \cdot 10^{-7}$ mbar) for shells with $x \geq 0.4$

- **GaAs/InSb axial nanowires:** GaAs nanowires as shown above, followed by Ga droplet consumption. Axial InSb segment: $T_{sub} \approx 460$°C, $F_{In} = 0.1$ µm/h, $F_{Sb} = 2$ – $4 \cdot 10^{-7}$ mbar.

- **GaAs/InSb core-shell nanowires:** GaAs nanowires as shown above, followed by Ga droplet consumption. InSb core: $T_{sub} \approx 280$ – 300°C, $F_{In} = 0.1$ µm/h, $F_{Sb} = 2 \cdot 10^{-7}$ mbar.

A.2. Critical thickness in core-shell nanowires

The calculation of the critical dimensions in core-shell NWs is based on the model developed by Raychaudhuri and Yu [251, 252, 253]. In the following, this model is presented. Further details of the model are found in the corresponding publications, i.e. Refs. [251], [252] and [253].

A.2.1. Zinc blende core-shell nanowires

The coherent strain energy in the core U^c_{zb} and the shell U^s_{zb} is given by

$$U^c_{zb} = \frac{A^c (f^c_l)^2 + B^c f^c_l f^c_t + C^c (f^c_t)^2}{D^c} L\pi r^2 \tag{A.1}$$

$$U^s_{zb} = \frac{A^s (f^s_l)^2 + B^s f^s_l f^s_t + C^s (f^s_t)^2}{D^s} L\pi ((r+h)^2 - r^2) \tag{A.2}$$

A^i, B^i, C^i and D^i are material dependent constants which are given by

$$A^i = {c^i_{11}}^2 - 2{c^i_{12}}^2 + 40 c^i_{12} c^i_{44} + 16 {c^i_{44}}^2 + c^i_{11}(c^i_{12} + 26 c^i_{44}) \tag{A.3}$$

$$B^i = 4(c^i_{11} - 2c^i_{12} - 2c^i_{44})(c^i_{11} - c^i_{12} + 4c^i_{44}) \tag{A.4}$$

$$C^i = 4(c^i_{11} + 2c^i_{12} + c^i_{44})(c^i_{11} - c^i_{12} + 4c^i_{44}) \tag{A.5}$$

$$D^i = 18(c^i_{11} + c^i_{12} + 2c^i_{44}) \tag{A.6}$$

c^i_{11}, c^i_{12} and c^i_{44} are the elastic constants of the materials. The strain components in core and shell are subdivided in tangential f^i_t and longitudinal f^i_l components, i.e.

$$f^i_t = \frac{a - a^i}{a^i} \tag{A.7}$$

$$f^i_l = \frac{a - a^i}{a^i} \tag{A.8}$$

a^i represents the lattice constant of the core and shell, respectively. a is the equilibrium lattice constant (without the presence of dislocations/strain relaxation):

$$a = \frac{a^s a^c (a^s r^2 \chi^c_{zb} + a^c h(h + 2r)\chi^s_{zb})}{a^{s2} r^2 \chi^c_{zb} + a^{c2} h(h + 2r)\chi^s_{zb}} \tag{A.9}$$

χ^i_{zb} is given by

$$\chi^i_{zb} = \frac{(c^i_{11} + 2c^i_{12})(c^i_{11} - c^i_{12} + 6c^i_{44})}{2(c^i_{11} + c^i_{12} + 2c^i_{44}} \tag{A.10}$$

If the strain is relaxed by misfit dislocations at the interface, the energy of these dislocations has to be considered as well. The energy of a loop dislocation U^{loop}_{zb} is given by

$$U^{loop}_{zb} = \frac{2\pi r}{6} \left(c^s_{11} - c^s_{12} + 4c^s_{44}\right) \frac{b^2}{4\pi} \cdot \ln\left[\frac{32r}{b} - 1\right] \tag{A.11}$$

Depending on the type of dislocations, perfect or partial, an additional energy due to a stacking fault exists. This is

$$U_{SF} = \gamma A_{SF} \tag{A.12}$$

where γ is the stacking fault energy (per unit area) and A_{SF} is the area of the stacking fault. The stacking fault can be located either in the core or in the shell.
When dislocations with a density n are present, the strain is relaxed. Consequently, the longitudinal strain components from Eq. A.8 are changed to

$$f^c_l = \frac{a - a^c}{a^c} - \left(\frac{a - a^c}{|a^c - a^s|}\right) nb \tag{A.13}$$

and

$$f^s_l = \frac{a - a^s}{a^s} - \left(\frac{a - a^s}{|a^c - a^s|}\right) nb \tag{A.14}$$

Then, the total energy of the core-shell system is given by

$$U_{total} = U^c_{zb} + U^s_{zb} + nL\left(U^{loop}_{zb} + U_{SF}\right) \tag{A.15}$$

Whether the core-shell system is coherent or relaxed is determined by the boundary given by

$$\left.\frac{\delta U_{total}}{\delta n}\right|_{n=0} = 0 \tag{A.16}$$

semiconductor	c_{11}^{zb}	c_{12}^{zb}	c_{44}^{zb}
AlAs	1.199	0.575	0.566
AlSb	0.894	0.443	0.416
GaAs	1.181	0.532	0.592
GaSb	0.884	0.403	0.432
InAs	0.833	0.453	0.396
InSb	0.667	0.365	0.302

Table A.1.: *Elastic constants of zinc blende III-V semiconductors. All values are given in Mbar. [325]*

A.2.2. Wurtzite core-shell nanowires

For WZ core-shell NWs, the calculations follow the same mechanism as for the ZB ones. The coherent strain energies in the WZ core and shell are given by

$$U_{wz}^{c} = \frac{(c_{11}^{c} f_t^{c})^2 - (c_{12}^{c} f_t^{c} + c_{13}^{c} f_l^{c})^2 + c_{11}^{c} f_l^{c} (c_{13}^{c} f_t^{c} + c_{33}^{c} f_l^{c})}{2c_{11}^{c}} \cdot L\pi r^2 \tag{A.17}$$

and

$$U_{wz}^{s} = \frac{(c_{11}^{s} f_t^{s})^2 - (c_{12}^{s} f_t^{s} + c_{13}^{s} f_l^{s})^2 + c_{11}^{s} f_l^{s} (c_{13}^{s} f_t^{s} + c_{33}^{s} f_l^{s})}{2c_{11}^{s}} \cdot L\pi((r+h)^2 - r^2 \tag{A.18}$$

Here, c_{11}^{i}, c_{12}^{i}, c_{13}^{i} and c_{33}^{i} are the elastic constants of the semiconductors in the WZ phase. In the coherent case, the tangential strain is

$$f_t^{i} = \frac{a - a^{i}}{a^{i}} \tag{A.19}$$

and the longitudinal strain is given by

$$f_t^{i} = \frac{c - c^{i}}{c^{i}} \tag{A.20}$$

The equilibrium lattice constants a and c are calculated in the same way as in Eq. A.9 with

$$\chi_{wz}^{i} = \frac{(c_{11}^{i})^2 - (c_{12}^{i} + c_{13}^{i})^2 + c_{11}^{i}(2c_{13}^{i} + c_{33}^{i})}{2c_{11}^{i}} \tag{A.21}$$

A.2.3. Elastic constants and Martin transformation

In order to calculate both the coherent strain energy and the dislocation energy, elastic constants of the different materials have to be known. For ZB III-V semiconductors, the elastic constants are known. These elastic constants are listed in Table A.1 for the III-V semiconductors used here.

Experimentally determined values of the WZ elastic constants are not yet reported. However, there are two ways to get access to the WZ elastic constants: first principle calculations and the Martin transformation of the ZB values. Wang and Ye calculated the elastic constants of various III-V semiconductors in the ZB and WZ crystal phases using first principle calculations [325]. The results are listed in Tab. A.2. An alternative approach is the Martin transformation presented in Eq. A.22 [190, 206, 207]. The first term is a rotation whereas the second term is a correction for internal strain.

semiconductor	method	c_{11}^{wz}	c_{12}^{wz}	c_{13}^{wz}	c_{33}^{wz}	c_{44}^{wz}
AlAs	FPC	1.350	0.508	0.382	1.476	0.342
	MT	1.447	0.496	0.406	1.538	0.392
AlSb	FPC	1.008	0.380	0.295	1.093	0.259
	MT	1.080	0.384	0.316	1.148	0.285
GaAs	FPC	1.476	0.460	0.334	1.602	0.424
	MT	1.442	0.449	0.354	1.538	0.408
GaSb	FPC	1.094	0.348	0.259	1.183	0.313
	MT	1.071	0.344	0.275	1.139	0.301
InAs	FPC	1.103	0.428	0.321	1.209	0.273
	MT	1.032	0.390	0.316	1.108	0.254
InSb	FPC	0.854	0.325	0.249	0.931	0.216
	MT	0.814	0.319	0.264	0.868	0.198

Table A.2.: *Elastic constants of wurtzite III-V semiconductors based on first principle calculations (FPC) and Martin transformation (MT). All values are given in Mbar. [190, 206, 207, 325]*

$$\begin{pmatrix} c_{11}^{wz} \\ c_{12}^{wz} \\ c_{13}^{wz} \\ c_{33}^{wz} \\ c_{44}^{wz} \\ c_{66}^{wz} \end{pmatrix} = \frac{1}{6} \begin{pmatrix} 3 & 3 & 6 \\ 1 & 5 & -2 \\ 2 & 4 & -4 \\ 2 & 4 & 8 \\ 2 & -2 & 2 \\ 1 & -1 & 4 \end{pmatrix} \begin{pmatrix} c_{11}^{zb} \\ c_{12}^{zb} \\ c_{44}^{zb} \end{pmatrix} - \begin{pmatrix} \Delta^2/\bar{c}_{44}^{wz} \\ -\Delta^2/\bar{c}_{44}^{wz} \\ 0 \\ 0 \\ \Delta^2/\bar{c}_{66}^{wz} \\ \Delta^2/\bar{c}_{44}^{wz} \end{pmatrix} \tag{A.22}$$

with

$$\Delta = \sqrt{2}/6 \left(c_{11}^{zb} - c_{12}^{zb} - 2c_{44}^{zb} \right) \tag{A.23}$$

$\bar{c}_{44}^{w}z$ and $\bar{c}_{66}^{wz}$ are given by a pure rotation, thus

$$\bar{c}_{44}^{wz} = \left(2c_{11}^{zb} - 2c_{12}^{zb} + 2c_{44}^{zb} \right) \tag{A.24}$$

and

$$\bar{c}_{66}^{wz} = \left(c_{11}^{zb} - c_{12}^{zb} + 4c_{44}^{zb} \right) \tag{A.25}$$

The elastic constants obtained via Martin transformation are also given in Tab. A.2. As seen, the values obtained by first principle calculations and by the Martin transformation are in a good agreement.

A.3. InAs/Al$_x$Ga$_{1-x}$Sb based core-multiple shell nanowires

A.3.1. InAs/Al$_x$Ga$_{1-x}$Sb/InAs core-multiple shell nanowires

In Section 6.1, InAs/Al$_x$Ga$_{1-x}$Sb core-shell NWs have been described being of interest for e.g. TFETs, 2D topological insulators or passivated NWs. Covering these NWs with another InAs shell further enhances the device possibilities. InAs/GaSb/InAs systems actually have two interfaces that should exhibit properties of two dimensional topological insulators. Electrical

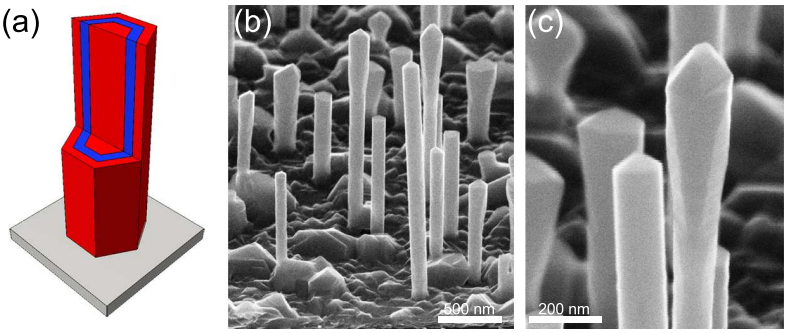

Figure A.1: *InAs/GaSb/InAs core-shell NWs. (a) schematic illustration and (b,c) SEM images showing two different top morphologies: a flat and a tapered tip.*

transport vertically trough the layered structured can show band to band tunneling at both interfaces. InAs/GaSb superlattices are commonly regarded as optimal structures for mid infrared detectors or lasers. Transferring these superlattices into a quasi one dimensional NW structure may e.g. enhance the sensitivity of the detectors. A NW with an InAs core covered by an AlSb as well as an InAs shell can replace GaAs/InAs core-shell NWs whch have been described in Section 5.1. The AlSb separates the conductive InAs core from the InAs shell, thus the InAs core solely acts as the host material. InAs and AlSb are almost lattice matched and it was shown in Sec. 6.1 that misfit dislocation free core-shell NWs can be obtained. While the electron mobility is very low in GaAs/InAs core-shell NWs due to scattering at the dislocation, these dislocation are not present in InAs/AlSb/InAs core-shell NWs.

Figure A.1a schematically shows the structure of InAs/GaSb/InAs core-shell NWs. The GaSb shell was grown using the optimal conditions described above, the InAs shell was grown at the same substrate temperature ($\sim 360°$C) with an In rate of 0.1 µm/h and an As_4 flux of $1.2 \cdot 10^{-6}$ mbar. The As and In fluxes are taken from the growth on GaAs/InAs core-shell NWs. SEM micrographs of the grown InAs/GaSb/InAs core-shell NWs are depicted in Fig. A.1b,c. Two principle structures are observed: (1) a tapered top and (2) a flat top region. The origin as well as the structural properties of these two different top regions are discussed in the following.

TEM micrographs of the first type having the tapered top are shown in Fig. A.2. In Fig. A.2a,b the top region is shown from the $\langle 110 \rangle$ and the $\langle 211 \rangle$ zone axes, respectively. The $\langle 110 \rangle$ zone axis reveals a high density of stacking faults in the lower part of the NW while the upper region is almost free of stacking faults. As discussed in Sec. 4.1.3, the InAs core has a high density of stacking faults. Consequently, the upper, almost defect free region is either caused by the growth of the GaSb or the InAs shell. In Section 6.1 it was shown that the axial growth of GaSb occurs with a very low density of twins or stacking faults. Often, the twins were not perpendicular to the growth direction but to $\langle 111 \rangle$A directions. Such twins are also seen in Fig. A.2a, indicating that axial growth of GaSb took place. This has also been confirmed by an EDX line scan, shown superimposed on the TEM micrograph. Aligning the NW to the $\langle 211 \rangle$ zone axis (Fig. A.2b) reveals the presence of multiple shells. In the upper part (axial growth of GaSb and InAs), contrast not solely arising from the presence of the different layers is seen. Rather, it seems that Moiré fringes are present (due to the twin boundaries seen in Fig. A.2a). The twins in $\langle 111 \rangle$A directions in the GaSb platform may cause defects below the platform, which are seen as lines in Fig. A.2a. These defects may either be anti-phase or grain boundaries. However, similar as for InAs/GaSb core-shell NWs, the defects are located only in the short upper part of the NW, the NW is free of such defects along the entire length of the InAs core. This is seen by the HRTEM image in Fig, A.2c, acquired from the $\langle 211 \rangle$ zone axis. A clear contrast from the InAs core, the AlSb shell as well as the InAs shell are observed, the interfaces are smooth. The FFT-filtered

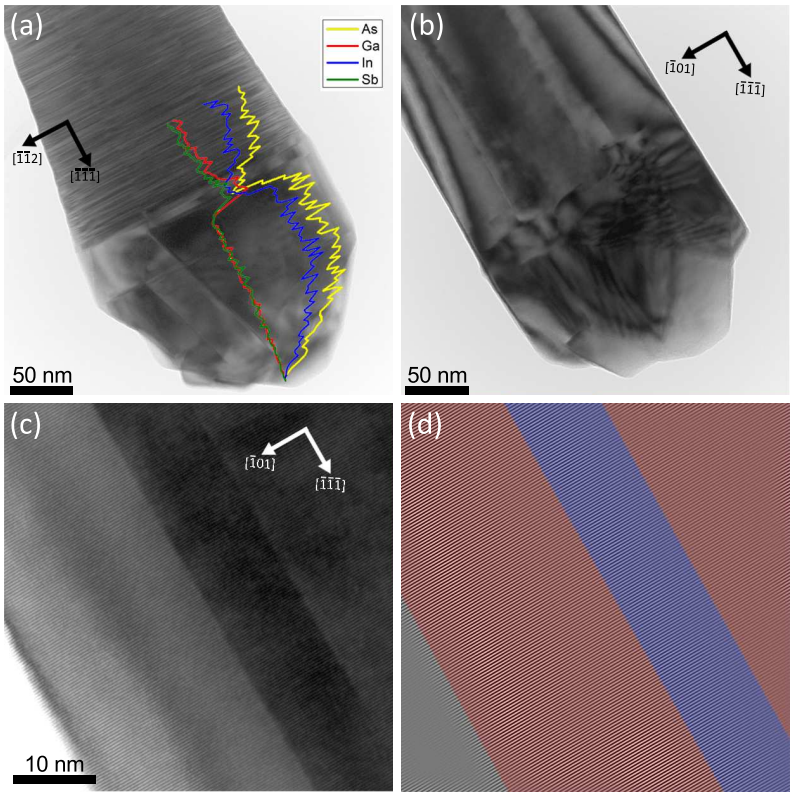

Figure A.2: *InAs/GaSb/InAs core-shell NWs of type I, i.e. a tapered tip. (a) TEM image from the ⟨110⟩ zone axis. (b) TEM image from the ⟨211⟩ zone axis. (c) HRTEM image from the ⟨110⟩ zone axis showing the different layers. (d) FFT filtered image of (c). Colored overlays denote the different materials.*

image in Fig. A.2d reveals no misfit dislocation.

The second type of InAs/GaSb/InAs core-shell NWs is shown detailed in Fig. A.3, in a,b from the ⟨110⟩ and in c,d from the ⟨211⟩ zone axis. As it has already been seen in the SEM image (Fig. A.1b,c), the top is flat. The TEM images (Fig. A.3a,c) display that only a slight axial growth took place, without any twin in the ⟨111⟩A directions. The interfaces between GaSb and InAs are relatively smooth, both from the ⟨110⟩ and ⟨211⟩ zone axes (Fig. A.3c,d). The growth of both shells is epitaxial, as evident by the HRTEM image shown in Fig. A.3b where all stacking faults and twins being present in the InAs core are adopted by both shells.

To summarize, InAs/GaSb/InAs core-shell NWs with smooth interfaces can be grown, but the shape and crystalline quality of the upper part strongly depend on the growth of the GaSb. Twins in ⟨111⟩A directions favor a tapered, defective tip. Based on these results, the growth of radial InAs/GaSb superlattices was investigated. Five shells of each semiconductor were grown, each one at a substrate temperature of 360°C. In Fig. A.4a, a SEM micrograph of the as-grown sample is displayed. The NWs have a uniform diameter, except for the top where a bulge is formed, possibly due to twins in the ⟨111⟩A directions. The TEM micrographs depicted in Fig. A.4c,d show smooth surfaces being in qualitative agreement with the SEM images. Although the thick NW results in a low contrast, all ten shells as well as the InAs core are found. These shells are seen more clearly in the EDX line scan in Fig. A.4b. As obvious from both TEM and EDX, not all shells have the same thickness. According to the growth sequence, the growth time for all InAs and GaSb shells were equal and, consequently, all shells should have almost the same thickness. Especially the thicknesses of the InAs shells vary strongly. This may be caused by the lower sticking coefficient of In adatoms compared to Ga adatoms, either resulting in a lower growth rate (due to desorption) or a higher growth rate (due to secondary adsorption).

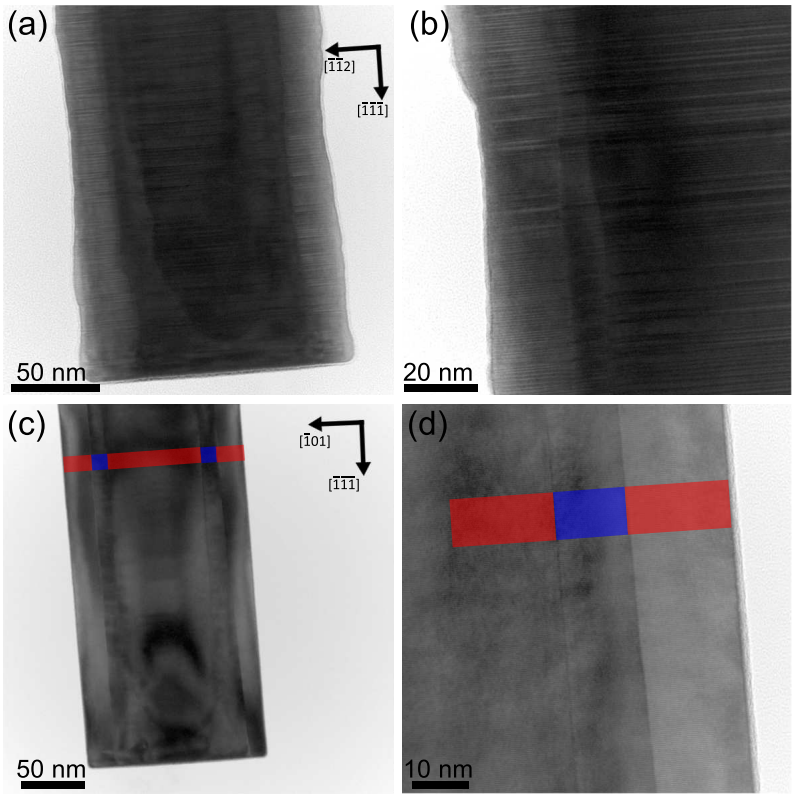

Figure A.3: *InAs/GaSb/InAs core-shell NWs of type II, i.e. a flat tip. (a) TEM image from the* ⟨110⟩ *zone axis. (b) Detailed TEM image from the* ⟨110⟩ *zone axis. (c) TEM image from the* ⟨211⟩ *zone axis. (d) Detailed TEM image from the* ⟨211⟩ *zone axis. Colored overlays denote the different materials.*

Both can strongly depend on the surface of the NW and may change during the growth of the radial superlattice. The high NW density seen in Fig. A.4a may have an additional impact due to shadowing. Nonetheless, the interfaces between InAs and GaSb still seem to be rather smooth without any interdiffusion. Substantial improvement regarding the homogeneity of the shell thicknesses should be achieved by growing the NWs on predefined position with uniform distances between neighboring NWs.

Replacing the GaSb shell with AlSb changes the band alignment as it has been described above, i.e. a conductive InAs shell covers an insulating AlSb shell. The principle structure is shown in Fig. A.5a. Analyzing these NWs by (HR)TEM reveals a surprisingly rough interface between the AlSb shell and the InAs shell. The interface between the AlSb and the InAs core is smooth as described in Sec. 6.1. Figure A.5b,c show TEM micrographs acquired from the ⟨110⟩ zone axis. Two interfaces are seen, the first one is present between the InAs core and the AlSb shell and the second one between the AlSb shell and the InAs shell. The first interface is smooth, while the second one exhibits a substantial roughness. This roughness often has the shape of a saw tooth. The ($\bar{1}\bar{1}\bar{1}$) planes represent one part of the saw tooth while the second part draws an angle of about $\sim 50°$, possibly being the $\{00\bar{1}\}$ (ZB) or $\{\bar{1}01\bar{1}\}$B (WZ) facets. The saw tooth profile has always the same arrangement. This suggests a choreographically defined roughness being independent on the high density of stacking faults. Diffraction patterns from the ⟨110⟩ and the ⟨211⟩ zone axes shown in Fig. A.5d,e do not display any splitting of diffraction spots. First of all, this indicates a mistfit dislocation free core-shell NW. Secondly, the origin of the roughness should not be an intermixing between the InAs and AlSb forming AlInAsSb which may differ in lattice constant. From the ⟨211⟩ zone axis, the roughness between the AlSb shell and the InAs shell is less pronounced but still visible. This is seen very well by both the HAADF image (Fig. A.5f) and the bright field TEM micrographs (Fig. A.5g,h). The chemical

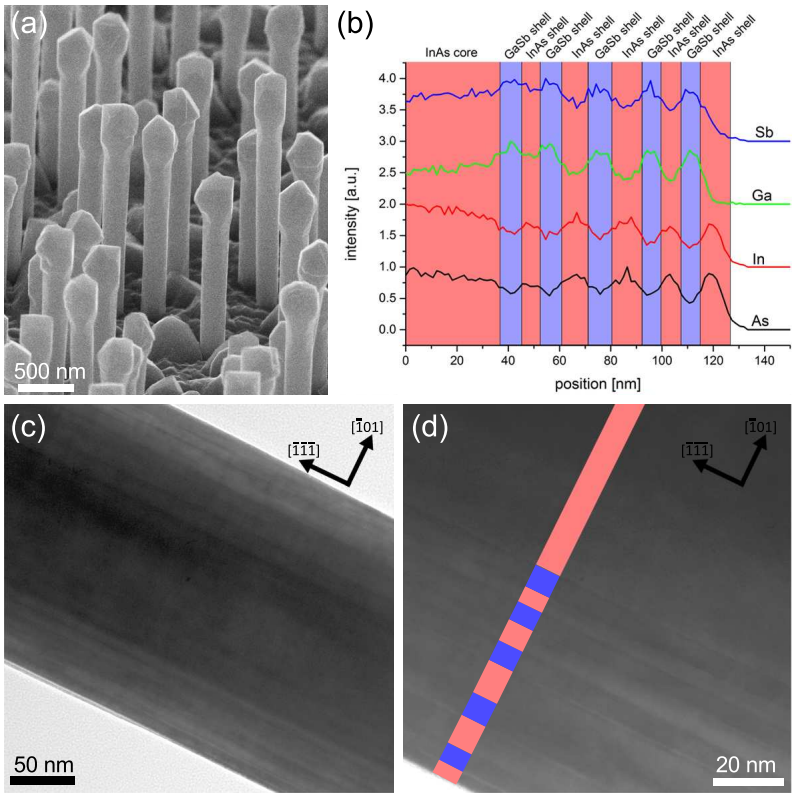

Figure A.4: *Radial InAs/GaSb super lattice with five shells of each semiconductor. (a) SEM micrograph. (b) EDX line scan. (c) TEM image from the ⟨211⟩ zone axis. (d) Detailed TEM image from the ⟨211⟩ zone axis. Colored overlays denote the different materials.*

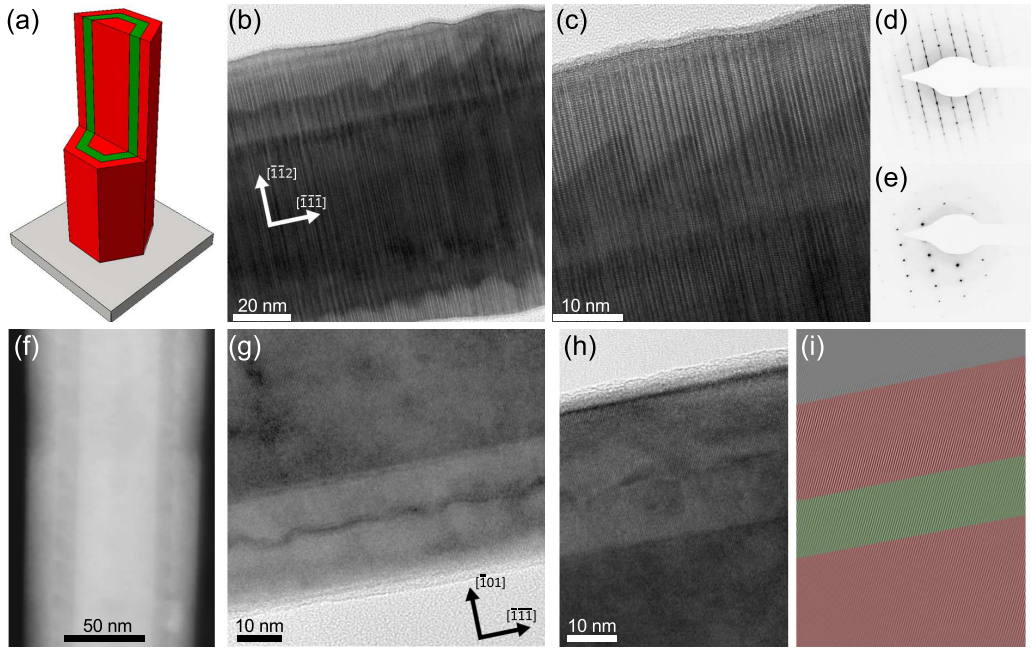

Figure A.5.: *InAs/AlSb/InAs core-shell NW. (a) Schematic illustration. (b,c) TEM image from the ⟨110⟩ zone axis. (d,e) Diffraction pattern from the ⟨110⟩ and ⟨211⟩ zone axes. (f) HAADF image from the ⟨211⟩ zone axis. (g,h) TEM images from the ⟨211⟩ zone axis. (i) FFT filtered image of (h). Colored overlays denote the different materials. All TEM images show the rough interface from the AlSb shell to the InAs shell.*

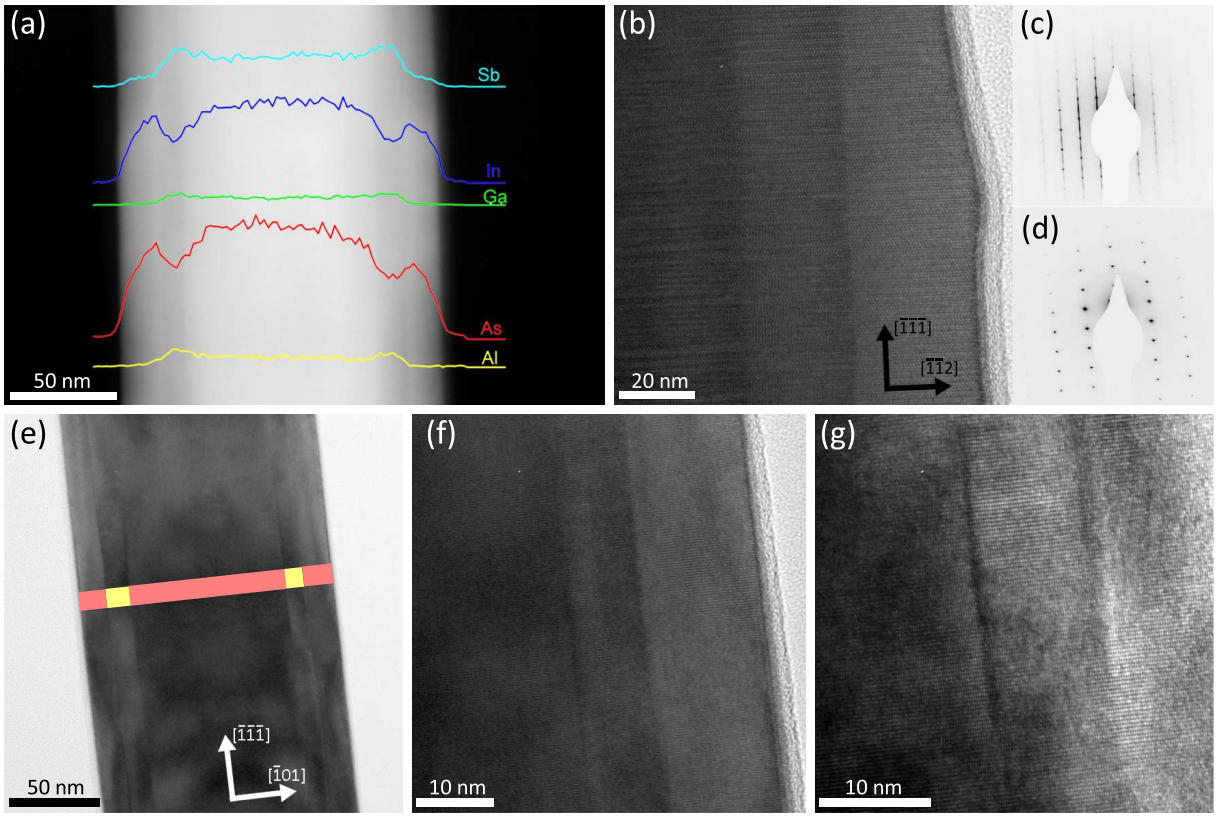

Figure A.6.: *InAs/AlGaSb/InAs core-shell NW with about 60% Al. (a) HAADF image from the* ⟨211⟩ *zone axis with superimposed EDX line scan. (b) TEM image from the* ⟨110⟩ *zone axis. (c,d) diffraction pattern from the* ⟨110⟩ *and* ⟨211⟩ *zone axes. (e-g) TEM images from the* ⟨110⟩ *zone axis. Colored overlays denote the different materials.*

sensitivity of the HAADF image further proofs the absence of intermixing or phase separation. The interface between the InAs core and the AlSb shell is smooth, similar as analyzed from the ⟨110⟩ zone axis. As it was discussed before, the ⟨211⟩ zone axis is beneficial to analyze core-shell NWs and since the roughness is still visible from this zone axis, it can also be used for InAs/AlSb/InAs-based core-shell structures. The diffraction patterns already indicated the absence of misfit dislocations, however, due to the low lattice mismatch of $\sim 1.2\%$ a second method to prove this assumption is useful. Figure A.5i displays the FFT-filtered HRTEM micrograph of Fig. A.5h. The absence of terminating lattice planes in the entire image demonstrates coherent growth of both shells, independent on the interfacial roughness.

The origin of the roughness between the AlSb shell and the InAs shell is not yet understood. The roughness between the InAs core and the AlSb shell, i.e. the same material combination but reverse growth order, is very small. Similarly also the roughness between the AlSb shell and the GaSb discussed in Sec. 6.1 is small. Consequently, only the material combination AlSb/InAs with this specific growth order seems to exhibit the interfacial roughness. To prove this assumption, Fig. A.6 displays TEM micrographs of an InAs/AlGaSb/InAs core-shell NW with about 60% Al. Figure A.6a shows the HAADF image acquired from the ⟨211⟩ zone axis with superimposed EDX line scans. An outer InAs shell as well as an inner AlGaSb shell covering an InAs core NW is clearly detected. The roughness is low. In the HRTEM micrograph in Fig. A.6b the presence of the two different shells is evident by the contrast changes. The

roughness between the InAs core and the AlGaSb shell as well as between the two shells are equally small. This very small roughness is also observed by rotating the NW by 30° to the ⟨211⟩ zone axis (Fig. A.6e,f,g). These images show uniform thicknesses of the AlGaSb and InAs shells as well as smooth interfaces. In the HRTEM images (Fig. A.6f,g) no misfit dislocation are found. In Fig. A.6g it seems that the interfaces exhibit a slight intermixing. This, however, is only caused by Fresnel fringes due to the fact that the image is not perfectly in focus. The high crystalline quality is further evidenced by the diffraction patterns shown in Fig. A.6c,d.

To conclude, pure AlSb shells result in a roughening of the AlSb/InAs interface while AlGaSb shells have smooth interfaces to InAs. Several attempts to obtain smoother interfaces between AlSb and InAs by slightly changing the InAs growth temperature failed. Accordingly, neither the In nor the As flux were varied and also the Sb/As exchange in the growth chamber was not optimized.

A.3.2. InAs cores as host materials for radial structures

Already in the previous section the possibility to use the InAs NWs as pure host material for a radial heterostructure forming an InAs tube was introduced. The fact that InAs, GaSb and AlSb belong to the 6.1 Å family, however, also enables more complex structures. Two of these structures are presented in the following.

A.3.2.1. InAs/GaSb tubes

Using an InAs/AlSb core-shell NW as the host material, two shells with a broken gap band alignment can be grown. The shells are then InAs and GaSb, forming InAs/GaSb tubes. These structures can either be used for TFETs or for two dimensional topological insulators. For both applications, electronic transport will only take place in the two outer shells and especially for two dimensional topological insulators, thin shells reduce the parasitic bulk transport.
Two possibilities exist to obtain such tubes: either InAs or GaSb represent the inner tube. The latter is displayed schematically in Fig. A.7a. TEM micrographs from the ⟨110⟩ zone axis do not clearly resolve the different shells (Fig. A.7b). Images acquired from the ⟨211⟩ zone axis shown in Fig. A.7c,d evidence the three shells, namely AlSb, GaSb and InAs. The interfaces are smooth, similar it has been also observed in the previous sections. HRTEM micrographs from both zone axes do not exhibit any misfit dislocations (Fig. A.7b,d) and also the diffraction patterns are either streaky (due stacking faults and twins seen from the ⟨110⟩ zone axis, inset in Fig. A.7b) or spotty (⟨211⟩ zone axis, inset in Fig. A.7c). Neither a splitting nor an elongation of the spots is observed, indicating coherent growth. Regarding two dimensional topological insulators, this arrangement of the shells is advantageous since ohmic contacts to InAs are easily obtained.

For TFETs the reverse arrangement of the InAs and GaSb shells is preferable since both the InAs and the GaSb need to be contacted. Thus, the outer shell, i.e. either InAs or GaSb, has to be etched locally with a high selectivity to the other material. Typically, InAs is etched with a solution based on citric acid while GaSb is etched with developers used for optical lithography, e.g. MIF316. The etching component is TMAH. Citric acid, however, also etches the GaSb and accordingly, the selectivity if too low. TMAH-based developers only attack the GaSb while InAs is not affected. Apparently, the structure suitable for TFETs needs to be InAs/AlSb/InAs/GaSb, schematically depicted in Fig. A.8a. EDX line scans were acquired from both zone axes and are depicted in Fig. A.8b,c. In both cases, all three shells are clearly identified, indicating conformal growth of all materials. Low resolution TEM and HAADF images acquired from the ⟨110⟩ are

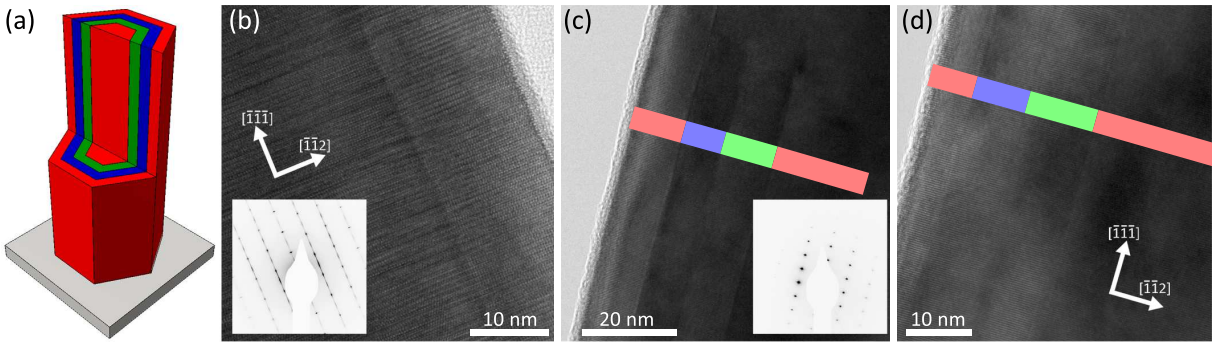

Figure A.7.: *InAs/AlSb/GaSb/InAs core-shell NW. (a) Schematic illustration. (b) TEM image from the* ⟨110⟩ *zone axis. (c,d) TEM images from the* ⟨211⟩ *zone axis. Insets in (b) and (c) show the diffraction pattern (inverted colors). Colored overlays denote the different materials.*

shown in Fig. A.8d,e, respectively. The entire NW exhibits a slight roughness. In the bright field image, the core is seen clearly, while the different shells do not exhibit a strong contrast. In the HAADF image (Fig. A.8e), the AlSb is observed due to the lower mass of the AlSb compared to InAs and GaSb. Similar as before, the interface between the InAs core and the AlSb is smooth and abrupt while the interface from the AlSb shell to the InAs shell is rough. This roughness has been discussed extensively in the previous section. The InAs and GaSb shells cannot be distinguished by HAADF (see Sec. 6.1). In the HRTEM image (⟨110⟩ zone axis) depicted in Fig. A.8f the InAs core and AlSb shell are seen, similar as the roughness between the AlSb and InAs shell. Only a slight change in contrast between the InAs and GaSb is found, making it difficult to identify the interface or its roughness. All interfaces as well as all three shells and the core are seen more clearly when analyzed from the ⟨211⟩ zone axis, see Fig. A.8g. The interface between the AlSb shell and the InAs shell exhibits a slight roughness while all other interfaces are smooth.
In general, the InAs shell seems to be thinner when analyzed from the ⟨110⟩ zone axes than from the ⟨211⟩ zone axis. In the first case, InAs grown in the ⟨211⟩ direction is seen while the thickness in the ⟨110⟩ is measured when seen from the ⟨211⟩ zone axis. This non-uniformity may either be caused by the NW cross-section making it hard to measure the shell thicknesses from the ⟨110⟩ zone axis (see Sec. 6.1.1) or different growth rates of InAs in the ⟨110⟩ and ⟨211⟩ directions. The latter is reasonable as the presence of both {110} and {211} side facets was clearly observed for InAs/GaSb core-shell NWs (see Sec. 6.1).

A.3.2.2. AlSb/InAs/AlSb radial quantum wells

The last presented possibility of 6.1Å-based core-shells NWs is an InAs quantum well. The required structure is the following: an InAs core acts as the host material being covered by AlSb. A subsequent InAs shell is again covered by AlSb and finally, a thin GaSb cap is used to prevent oxidation of the AlSb. The conduction band of the AlSb is more than 1 eV above that one of the InAs. Consequently, electrons are confined in the InAs shell. High mobility InAs-based devices are typically InAs quantum wells embedded in AlSb [181]. The structure is displayed schematically in Fig. A.9a, a typical SEM micrograph in Fig. A.9b. The NWs are macroscopically smooth, HRTEM images from the ⟨110⟩ zone axis (Fig. A.9c) exhibit a slight roughness either of the AlSb or the thin GaSb cap. No contrast from the different shells is seen. The shells are identified only when viewed from the ⟨211⟩ zone axis, as seen in Fig. A.9d-g. No tapering is observed, indicating growth temperatures low enough to limit adatom diffusion. The presence of the four different shells is obvious from the HAADF image in Fig. A.9e where bright

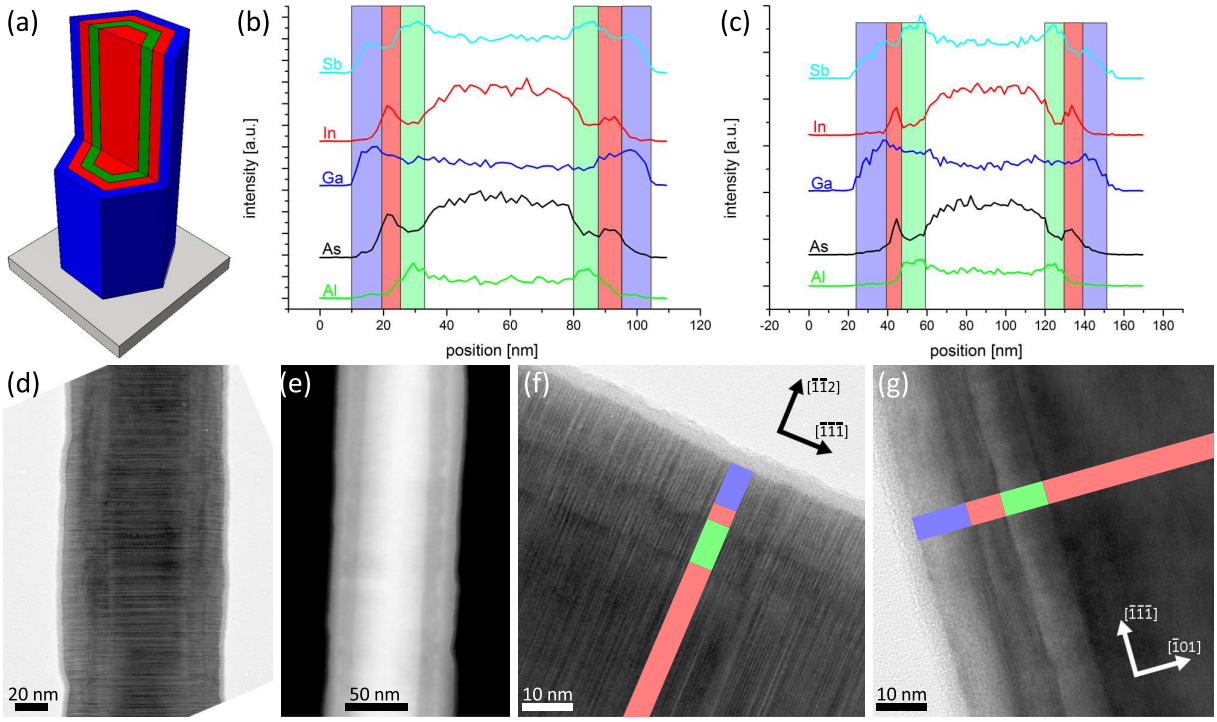

Figure A.8.: *InAs/AlSb/InAs/GaSb core-shell NWs. (a) Schematic illustration. (b,c) EDX line scans from the* ⟨110⟩ *and* ⟨211⟩ *zone axes. (d) Low magnification TEM image from the* ⟨110⟩ *zone axis. (e) HAADF image from the* ⟨211⟩ *zone axis. (f) TEM image from the* ⟨110⟩ *zone axis. (g) TEM image from the* ⟨211⟩ *zone axis. Colored overlays denote the different materials.*

regions correspond to InAs or GaSb and darker areas to AlSb. Figure A.9f,g display bright field TEM images from the ⟨211⟩ zone axis. The AlSb and InAs shells are uniform on both sides of the NW, the AlSb is not oxidized. The interface from the first AlSb shell to the InAs quantum well shows the expected roughness, whereas the interface between InAs and AlSb is always smooth (Fig. A.9g). No misfit dislocations are detected along the entire heterostructure. Here, the InAs core is only considered as the host material for the radial heterostructure, not having a direct function. By doping the InAs to high values, i.e. having a highly conductive core, it can be considered as metallic and may therefore act as an inner gate electrode. Then, the AlSb shell not only confines the electrons into the InAs but also acts as a gate dielectric. Such an inner gate cannot only be used for the InAs quantum wells but e.g. also for radial TFETs.

A.4. GaAs nanowires with a flat top facet

Figure A.10 displays a GaAs NW with a rather flat $(\overline{111})$B top facet obtained by growing at a substrate temperature of $\sim 600°C$, Ga rate of 0.1 µm/h and an As_4 flux of $2.5{\cdot}10^{-6}$ mbar. After the growth, the Ga droplet was consumed.

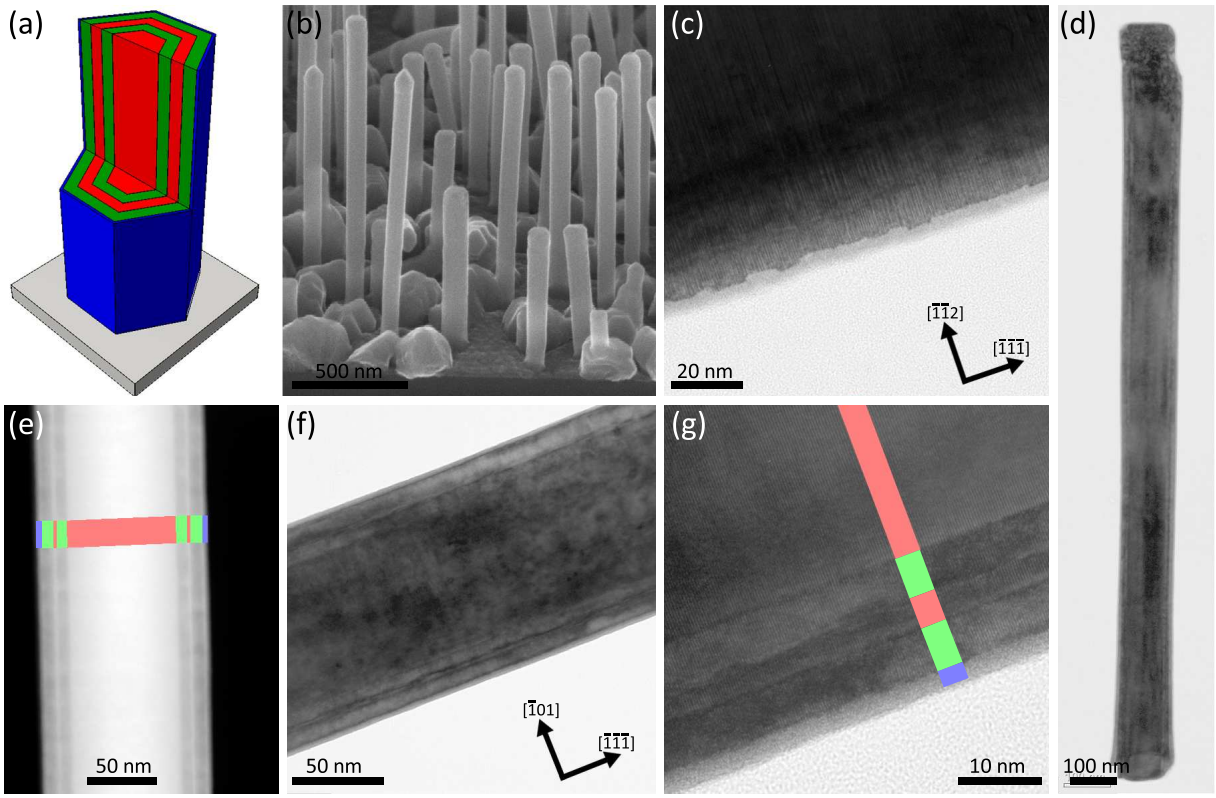

Figure A.9.: *Radial InAs quantum wells. (a) Schematic illustration. (b) SEM image. (c) TEM image from the ⟨110⟩ zone axis. (d) Low magnification TEM image from the ⟨211⟩ zone axis. (e) HAADF image from the ⟨211⟩ zone axis. (f,g) TEM images from the ⟨211⟩ zone axis. Colored overlays denote the different materials.*

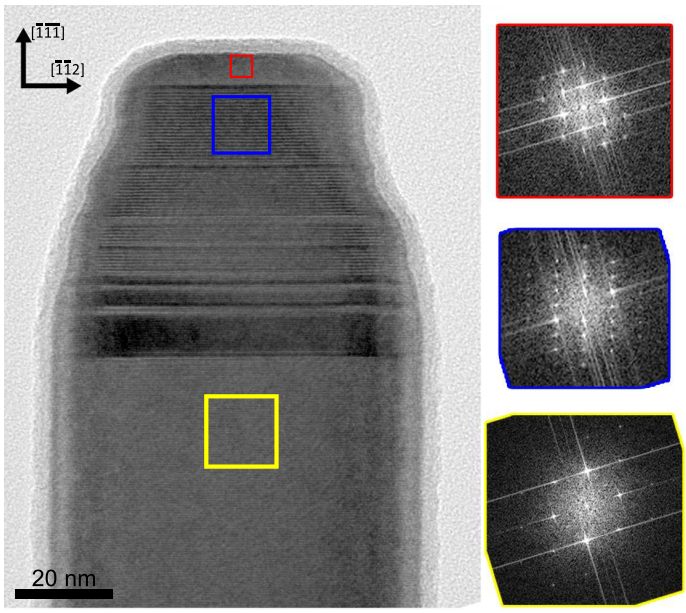

Figure A.10: *TEM micrograph of a GaAs NWs with a flat top facet. FFTs obtained from the marked regions are shown as insets and indicate the different crystal structures at the NW top: ZB (red), WZ (blue) and ZB (yellow).*

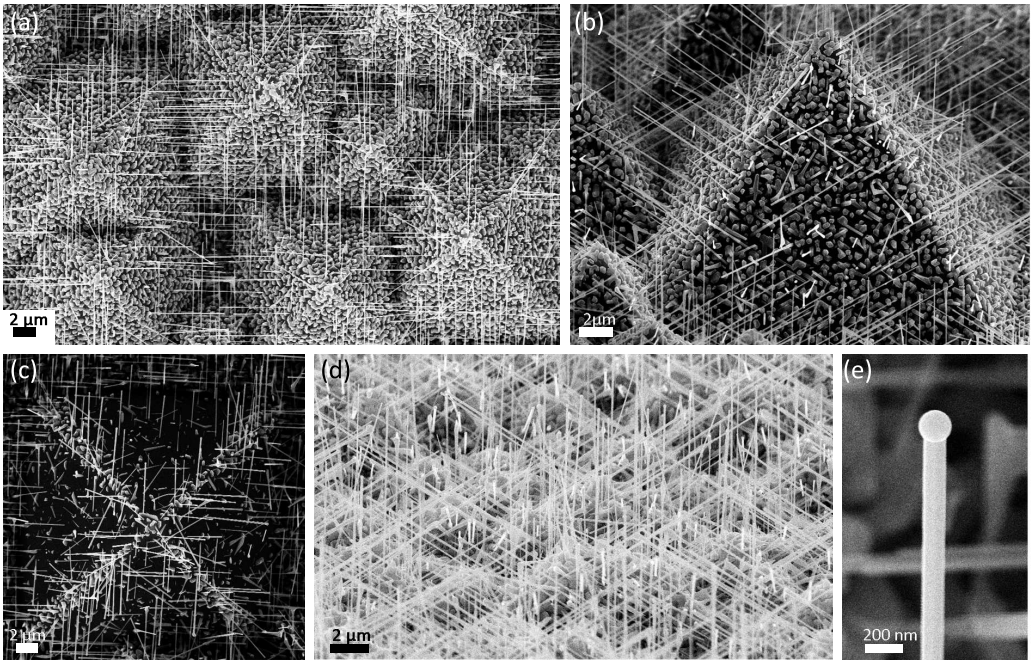

Figure A.11.: *GaAs NWs grown rotated and textured Si (100) substrates. (a,b) top and side view images of GaAs NWs on Si pyramids with strong parasitic growth. (c) top view image demonstrating the preferred nucleation of GaAs NWs at the pyramids edges. (d) Optimized growth of GaAs NWs on textured Si substrates with small, high density pyramids. (e) Ga droplet on top of the NW.*

A.5. GaAs nanowires on textured substrates[1]

A.5.1. Growth on rotating textured substrates

Figure A.11 displays SEM micrographs of GaAs NWs grown on textured Si (100) substrates being rotated during the growth. In Fig. A.11a and b, top and side view images are seen. Due to non-optimized growth conditions, strong parasitic growth occurs. Nonetheless, GaAs NWs grow mainly perpendicular to the pyramid side facets. In few cases, NW growth in non-$\langle 111 \rangle$ directions of the substrate is observed [312]. Similar as for InAs NWs, a preferred nucleation of GaAs NWs at the edges of the pyramids side facets occurs (see Fig. A.11c). Contrary to the InAs NWs, GaAs NWs are found to grow also on remaining Si (100) surfaces. Optimized growth on high density, small pyramids results in GaAs NWs as depicted in Fig. A.11d,e. A high density of GaAs NWs is observed, only growing in the $\langle 111 \rangle$ directions of the substrate. The density of parasitic crystallites is low. As seen in Fig. A.11e, the GaAs NW growth is catalyzed by a Ga droplet.

A.5.2. Control of the GaAs nanowire growth direction

For the supply of Ga and As adatoms, the corresponding effusion cells are mounted differently than for In and As. In the GEN II system, the In and As effusion cell are mounted with an angle of 90° between them. For the Ga and As effusion cells, the angle is 45°. Consequently, the impingement types are different than for In and As. When the sample is aligned as depicted in Fig. A.12a, the impingement types are as listed in Tab. A.3. A rotation of the sample by 45° changes the impingement types (see Fig. A.14a). The impingement types are then as given in

[1] Results of this part were published as Supporting Information in [263].

facet	Ga adatoms	As adatoms
A	direct impingement	direct impingement
B	grazing incidence	grazing incidence
C	shadowed facet	grazing incidence
D	direct impingement	direct impingement

Table A.3.: *Impingement types of Ga and As adatoms when the pyramids are aligned as shown in Fig. A.12a*

facet	Ga adatoms	As adatoms
A	direct impingement	grazing incidence
B	grazing incidence	shadowed facet
C	grazing incidence	grazing incidence
D	direct impingement	direct impingement

Table A.4.: *Impingement types of Ga and As adatoms when the pyramids are aligned as shown in Fig. A.14a*

Tab. A.4.

The incoming Ga and As fluxes are partially shadowed when the substrate rotation is stopped. Figure A.12a displays the schematic of the substrate alignment relative to the Ga and As effusion cells. Ga adatoms impinge directly on the A facet of the pyramid while the C facet is shadowed from the incident Ga flux. As impinges directly on the A and D facets. An overview image after GaAs NW growth is displayed in Fig. A.12b. Higher resolution images are plotted in Fig. A.12c-e. The growth clearly occurs only on three facets while growth is absent on the remaining shadowed facet (Facet C).

A top view image of the sample is displayed in Fig. A.13. The NW dimensions on the different facets are different, reflecting the incoming fluxes. NWs grown on facet A have an average length of about 1.5 ± 0.1 µm and exhibit only a small tapering. The NWs on facet D have the same average length but have a significant tapering with a larger top than bottom diameter. A similar tapering is found for the NWs on facet B, however, these NWs are shorter ($\sim 1.1 \pm 0.1$ µm). These different NW dimensions are explained by the different impingement types of Ga and As adatoms. The As flux controls the growth rate of VLS grown GaAs NWs. The As impingement is identical on facets A and D (direct impingement) and therefore also the growth rates are the same. On facet B, the impingement type is different resulting in a reduced As flux, i.e. shorter NWs. The impingement of Ga adatoms is identical on the facets B and D. Once the NWs nucleated, rather the impingement of Ga adatoms on the NWs than on the pyramids facets is important. For NWs grown on the facet A, Ga adatoms mainly impinge on the droplet. For the NWs on the facets B and D, the Ga adatoms also impinge on the side facets of the NWs and can diffuse to the droplet. Consequently, the effective Ga flux arriving at the droplet is higher on facets B and D than on facet A. The higher Ga flux gives rise to an increase of the Ga droplet, i.e. a tapering.

A rotation of the substrate by 45° modifies the impingement of Ga and As atoms as shown in Fig. A.14a and given in Table A.4. Figure A.14b displays a representative SEM top view image. GaAs NWs are grown on all four pyramidal side facets. On facet B many tilted NWs are found when the As flux is shadowed during the nucleation process, i.e. very low. Low V/III

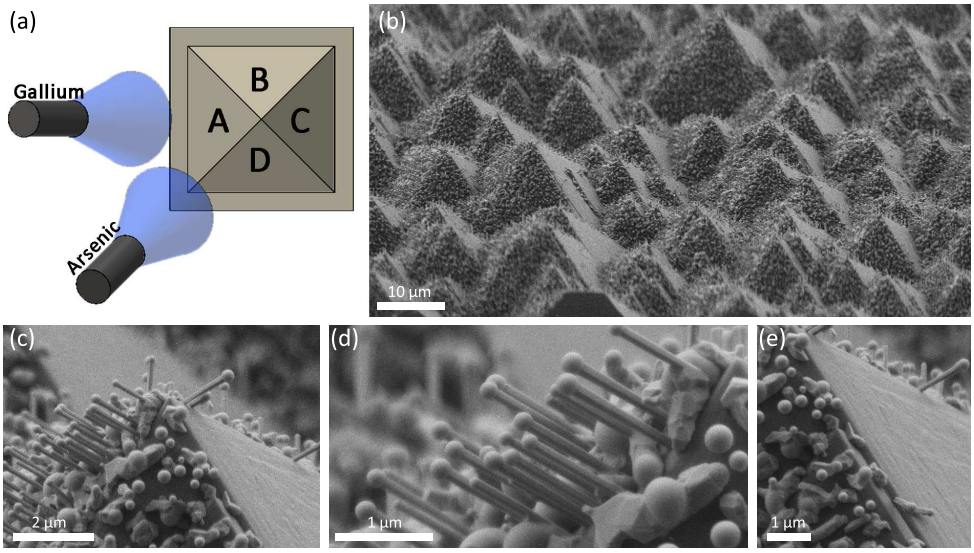

Figure A.12.: *GaAs NWs grown on non-rotating textured Si (100) substrates. (a) Schematic of the substrate alignment. (b) Overview tilted-view SEM image. (c-e) Detailed SEM images of the pyramid apex and facet A and C.*

Figure A.13: *GaAs NWs grown on non-rotating textured Si (100) substrates. Top view SEM image of a single pyramid with higher magnification images of the facets A, B and D.*

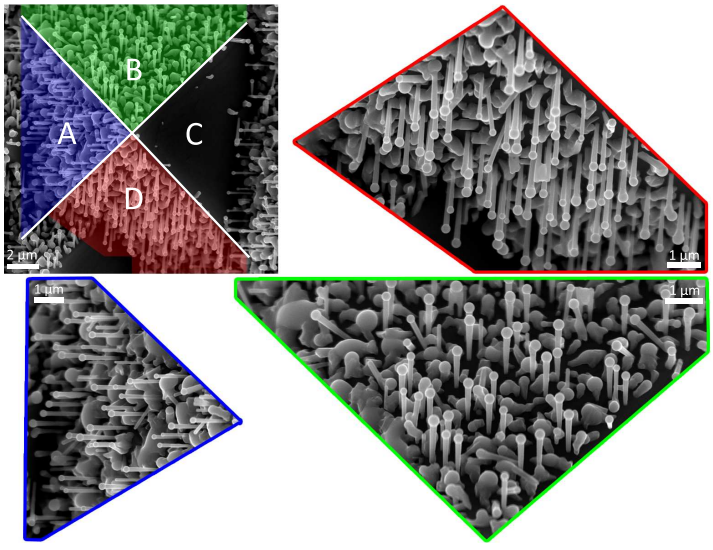

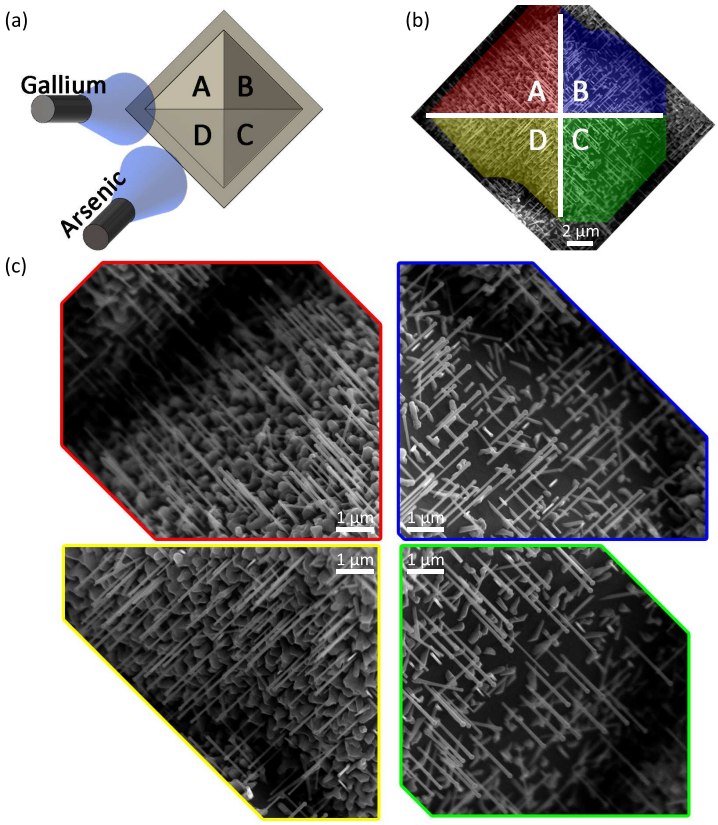

Figure A.14: *GaAs NWs grown on non-rotating textured Si (100) substrates. (a) Schematic of the substrate alignment. (b) top view SEM image of a single pyramid. (c) detailed SEM micrographs of the four different pyramidal facets.*

ratios result in three dimensional twinning during the NW nucleation process which causes tilted NWs [273]. Grazing incidence of As atoms being present on facets A and C during the nucleation results in a significant decrease of the number of tilted NWs. Finally, the number of tilted NWs is lowest on facet D having the highest amount of As adatoms during the nucleation. As seen by a comparison of facets A and C, parasitic growth is found to be increased with the Ga flux.